Time Resolved X-Ray Scattering of molecules in Solution

Approaching the Molecular Movie

Brandt van Driel, Tim; Nielsen, Martin Meedom

Publication date:
2014

Document Version
Peer reviewed version

Time Resolved X-ray scattering of molecules in solution: approaching the Molecular Movie

Tim Brandt van Driel

PhD dissertation

2014

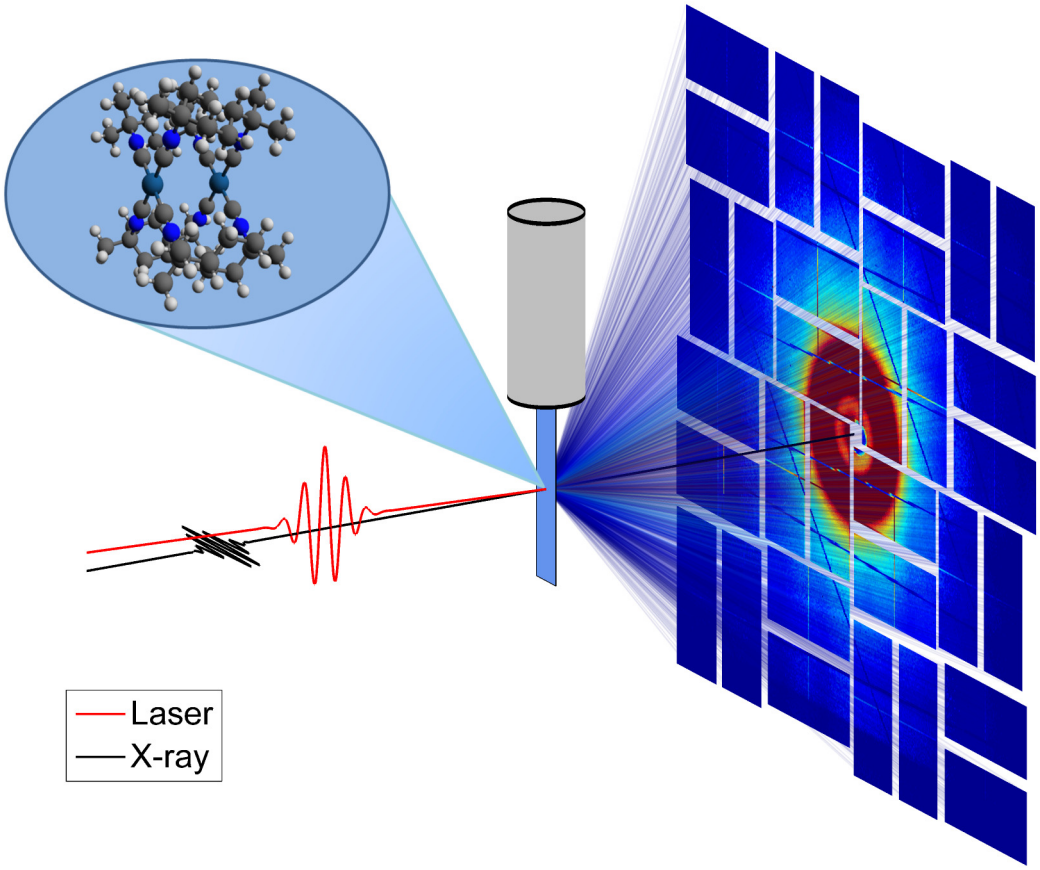

DTU Physics
Department of Physics

Time Resolved X-ray scattering of molecules in solution: approaching the Molecular Movie

Printed at DTU, Lyngby, 2014

NEXMAP - Neutrons and X-rays for materials research
Department of Physics
Technical university of Denmark
2800 Kgs. Lyngby
Denmark

http://www.fysik.dtu.dk/english/research/nexmap/

"If we knew what it was we were doing, it would not be called research, would it?"
Albert Einstein

Abstract

This dissertation describes the use of Time-Resolved X-ray Diffuse Scattering (TR-XDS) to study photo-induced structural changes in molecules in solution. The application of the technique is exemplified with experiments on two bimetallic molecules.

The main focus is on the data-flow and process of bringing the data from measurement to analysis. Bridging the experimental design and challenges of the experiments from X-ray synchrotrons to the newly available X-ray Free Electron Laser sources (XFEL).

LCLS in California is the first XFEL to come online and delivers intense 30fs X-ray pulses, orders of magnitude shorter than the 100ps X-ray pulses available from synchrotron sources. This increase in time-resolution allows for the use of X-ray techniques in a completely new time-domain, where coherent photo-induced changes in structure can be studied on their intrinsic time-scale.

Measurements on $Rh_2(dimen)_4^{2+}$obtained at European Synchrotron Radiation Facility (ESRF) are presented to exemplify TR-XDS at synchrotrons. Similarly, measurements on $Ir_2(dimen)_4^{2+}$are used to show the XFEL data-flow and how it deviates from the prior. A method to identify and account for systematic fluctuations in the purpose built CSPAD detector is presented and applied to the data to highlight the relevance of this work. Thereby showing the ability to capture a molecular movie on the sub-ps time-scale.

Resumé på dansk

Denne afhandling beskriver brugen af tidsopløst røntgenspredning (TR-XDS) til at studere fotoinducerede ændringer i molekylstruktur på molekyler i opløsning. Teknikken er eksemplificeret ved to røntgen målinger på bimetaliske molekyler.

Hoved fokus er lagt på den eksperimentelle proces, samt på den databehandling der bringer målingerne fra eksperiment til analyse. Derved kobles TR-XDS eksperimenter på synchrotroner til lignende eksperimenter på de nyligt færdigbyggede fri elektron røntgen lasere (XFEL).

LCLS i Californien er den første af slagsen der kan levere hård røntgen og producerer intense 30fs røntgenpulser, størrelsesordner kortere end de 100ps pulserder leveres af synchrotronkilder.

Den øgede tidsopløsning muliggør undersøgelser på en helt ny tidsskala, hvor fotoinducerede ændringer i molekylers struktur, kan studeres på samme tidsskale hvormed atomer bevæger sig.

Målinger på $Rh_2(dimen)_4^{2+}$ved European Synchrotron Radiation Facility (ESRF) bliver præsenteret som eksempel på tidsopløste røntgen målinger på en synchrotron. Ligeledes præsenteres målinger på $Ir_2(dimen)_4^{2+}$som eksempel på målinger ved en fri elektron røntgen laser for at illustrere forskelle og ligheder imellem eksperimenter ved de to forskellige kilder. En metode til at identificere og korrigere systematiske detektor fluktuationer præsenteres også her og anvendes på XFEL målingerne, for at vise deres potentiale. Hermed er det muligt at optage en molekylær film af hvad der sker indenfor det første picosekund efter molekyler eksiteres med en laser.

Acknowledgments

First of all I would like to thank my supervisor Martin Meedom Nielsen for giving me the chance to pursue a PhD and the freedom to immerse myself in all the many different opportunities that have arisen.

I would like to especially thank Kasper Skov Kjær who I have worked very closely with. Together with Tobias Harlang, Asmus Dohn and Robert Hartsock we have shared many experiments and late nights but also experienced the night-life and sightseeing during our travels for science. Their excellent company have made long work hours and challenging beamtimes seem more like fun than work. Additionally I would like to thank Kristoffer Haldrup, Elisa Biasin and Morten Christensen for support and discussions making the Centre for Molecular Movies (CMM) a great basis regardless of being located at Risø or DTU.

I would also like to thank Jan Kehres, Tejs Vegge, Jens Wenzel and Poul Nordby for discussions and support regarding Li-Battery studies and other projects during my time at RISØ.

A large part of the work has been done in collaborations and many of the interesting projects would not have come about without them. Also, these collaborations have made it necessary to utilise different techniques and expand my field of research. For this I thank UDECS: Lund, Hamburg, Budapest for projects on molecules in solution with the combination of many different techniques. I would especially like to thank Sophie Canton for her valuable insight into Photo-Chemistry and György Vanko for introducing me to X-ray Emission Spectroscopy.

I thank Markus Mezger and Pieter Reichert for involving us in experiments regarding charged solid-electrolyte interfaces, Dago de leeuw and his group for the opportunity to study ferroelectric devices and Richard Neutze for involving us in the ultra-fast study of proteins.

All these many projects would not be possible without the expert support from the beamline staff: Michael Wulff and Dmitry Khakulin at ID09b, Veijo Honkimäki at ID15 and Pieter Glatzel at ID26 at ESRF. Oliver Seeck and André Beerlink from p08 at Petra, Xiaoyi Zhang from 11-ID-D as well as the staff at sector 7 at APS. And most of all the staff at XPP at LCLS, Diling Zhu, Matthieu Chollet and Mike Glownia. My utmost thanks go out to Henrik Lemke as well as Kelly Gaffney and Robert Hartsock for many inspiring ongoing projects as well as making my 3 month stay in California extremely pleasant.

I would like to thank my friends and family for giving me some well needed interruptions from time to time and for supporting me and bearing with me for being away and still have time and energy to spend time together whenever I

caught a break. Finally I wish to thank my girlfriend, Stine for the support and understanding in times of stress.

All in all thanks to everyone who made it possible for me to complete my PhD project in its full expanse, it has been quite a ride.

Contents

List of Publications

This thesis is based on the following papers, which will be referred to by their Roman numerals in the text.

Attached Puplications

I **Bond shortening (1.4 Å) in the singlet and triplet excited states of [Ir2(dimen)4]2+ in solution determined by time-resolved X-ray scattering.**
Kristoffer Haldrup, Tobias Harlang, Morten Christensen, Asmus Dohn, **Tim Brandt van Driel**, Kasper Skov Kjær, Niels Harrit, Johan Vibenholt, Laurent Guerin, Michael Wulff and Martin Meedom Nielsen.
Inorganic chemistry **50 (19)**, 9329-36(2011).

II **Guest-host interactions investigated by time-resolved X-ray spectroscopies and scattering at MHz rates solvation dynamics and photoinduced spin transition in aqueous Fe(bipy)32+.**
K. Haldrup, G. Vankó, W. Gawelda, A. Galler, G. Doumy, A.M. March, E.P. Kanter, A. Bordage, A. Dohn, **T.B. van Driel**, K.S. Kjær, H.T. Lemke, S.E. Canton, J. Uhlig, V. Sundstrom, L. Young, S.H. Southworth, M. M. Nielsen and C. Bressler.
The journal of physical chemistry. A **116(40)**, 9878-87(2012).

III **Introducing a standard method for experimental determination of the solvent response in laser pump,X-ray probe time-resolved wide-angle X-ray scattering experiments on systems in solution**
Kasper Skov Kjær, **Tim Brandt van Driel**, Jan Kehres, Kristoffer Haldrup, Dmitry Khakhulin, Klaus Bechgaard, Marco Cammarata, Michael Wulff, Thomas Just Sørensen and Martin M. Nielsen.
Physical chemistry chemical physics **15(36)**, 15003-16(2013).

IV **Probing the Nonequilibrium Dynamics of Photoinduced Electron Transfer with Femtosecond X-ray Pulses**
Sophie E. Canton, Kasper S. Kjær, György Vankó, Shin-ichi Adachi, Christian Bressler, Morten Christensen, Asmus O. Dohn, **Tim B. van Driel**, Andreas Galler, Wojciech Gawelda, Kristoffer Haldrup, Tobias Harlang, Yizhu Liu, Klaus B. Møller, Zoltan Nemeth, Shunsuke Nozawa, Mátyás Pápai, Tokushi Sato, Takahiro Sato, Tadashi Togashi, Kensuke Tono, Jens Uhlig, Kenneth Wärnmark, Makina Yabashi, Jianxin Zhang, Villy Sundström and Martin M. Nielsen.
Advanced Draft.

V **Direct dynamics studies of a binuclear metal complex in solution: The interplay between vibrational relaxation, coherence decay and solvation effects.**
Asmus Ougaard Dohn, Elvar Orn Jonsson, Kasper Skov kjær, **Tim Brandt van driel**, Martin Meedom Nielsen, Karsten Wedel Jacobsen, Niels Engholm Henriksen, and Klaus Braagaard Møller.
Advanced Draft.

VI **Experimental and theoretical investigation of the photoinduced high-spin state of the $[Fe(terpy)_2]^{2+}$ complex.**
Amélie Bordage, Kristoffer Haldrup, Pieter Glatzel, Andreas Galler,Wojciech Gawelda, Gilles Doumy, Anne Marie March, Elliot P. Kanter, Asmus Dohn, **Tim B. van Driel**, Kasper S. Kjær, Klaus B. Møller, Henrik T. Lemke, Erik Gallo, Mauro Rovezzi, Mátyás Pápai, Zoltán Németh, Tamás Rozgonyi,Delphine Cabaret, Amélie Juhin, Jens Uhlig, Villy Sundström, Martin M. Nielsen, Stephen Southworth, Linda Young, Christian Bressler and György Vankó.
Advanced Draft.

VII **Fingerprinting and tracking sub-picosecond spin- and solvation dynamics of the spin-crossover complex [Fe(bpy)3]2+ by simultaneous ultrafast X-ray emission and X-ray scattering**
Kristoffer Haldrup, Kasper Skov Kjær, Sophie Canton, Robert Hartsock, Tobias Harlang, **Tim Brandt van Driel**, Wojciech Gawelda, Andreas Galler, Asmus Ougaard Dohn, Klaus Braagaard Møller, Amélie Bordage, Zoltan Nemeth, Henrik Lemke, Marco Cammarata, David Mark Fritz, Kelly J. Gaffney, Villy Sundstrom, Gyorgy Vanko, Martin Meedom Nielsen and Christian Bressler.
Advanced Draft.

Other puplications

VIII **Ligand and Solvent Manipulation of Electronic Excited State Spin Dynamics in Iron Coordination Complexes**
Wenkai Zhang, Roberto Alonso-Mori, Uwe Bergmann, Christian Bressler, Matthieu Chollet, Andreas Galler, Wojciech Gawelda, Ryan G. Hadt, Robert W. Hartsock, Thomas Kroll, Kasper S. Kjær, Katharina Kubiček, Henrik T. Lemke, Huiyang W. Liang, Drew A. Meyer, Martin M. Nielsen, Carola Purser, Joseph S. Robinson, Edward I. Solomon, Zheng Sun, Dimosthenis Sokaras, **Tim B. van Driel**, György Vankó, Tsu-Chien Weng, Diling Zhu and Kelly J. Gaffney.
Accepted, Nature.

IX **Theoretical study of the triplet excited state of PtPOP and the exciplexes M-PtPOP (M=Tl, Ag) in solution and comparison with ultrafast X-ray scattering results**
Qingyu Kong, Kasper S. Kjær, Kristoffer Haldrup, Stephan P.A. Sauer, **Tim Brandt van Driel**, Morten Christensen, Martin M. Nielsen and Michael Wulff.
Chemical Physics **393(1)**, 117-122(2012).

X **Spin-state studies with XES and RIXS: From static to ultrafast**
Gyorgy Vanko, Amelie Bordage, Pieter Glatzel, Erik Gallo, Mauro Rovezzi, Wojciech Gawelda, Andreas Galler, Christian Bressler, Gilles Doumy, Anne Marie March, Elliot P. Kanter, Linda Young, Stephen H. Southworth, Sophie E. Canton, Jens Uhlig, Grigory Smolentsev, Villy Sundstrom, Kristoffer Haldrup, **Tim Brandt van Driel**, Martin M. Nielsen, Kasper S. Kjær, Henrik T. Lemke.
Journal of Electron Spectroscopy and Related Phenomena **188**, 166-171(2013).

XI **Toward Highlighting the Ultrafast Electron Transfer Dynamics at the Optically Dark Sites of Photocatalysts**
Sophie E. Canton, Xiaoyi Zhang, Jianxin Zhang, **Tim B. van Driel**, Kasper S. Kjær, Kristoffer Haldrup, Pavel Chabera, Tobias Harlang, Karina Suarez-Alcantara, Yizhu Liu, Jorge Perez, Amelie Bordage, Matyas Papai, Gyorgy Vanko, Guy Jennings, Charles A. Kurtz, Mauro Rovezzi, Pieter Glatzel, Grigory Smolentsev, Jens Uhlig, Asmus O. Dohn, Morten Christensen, Andreas Galler, Wojciech Gawelda, Christian Bressler, Henrik T. Lemke, Klaus B. Møller, Martin M. Nielsen, Reiner Lomoth, Kenneth Warnmark and Villy Sundstrom.
The Journal of Physical Chemistry Letters **4(11)**, 1972-1976(2013).

XII **Recent development of thin diamond crystals for X-ray FEL beam-sharing**
Yiping Feng, Roberto Alonso-Mori, Vladimir Blank, Sébastien Boutet, Mathieu Chollet, **Tim B. van Driel**, David M Fritz, James M Glownia, Jerome B Hastings, Henrik Lemke, Marc Messerchmidt, Paul A Montanez, Aymeric Robert, Joseph Robinson, Liubov Samoylova, Yuri Shvyd'ko, Marcin Sikorski, Harald Sinn, Sanghoon Song, Venkat N Srinivasan, Stanislav Stoupin, Sergey Terentiev, Garth Williams, Diling Zhu.
Proc. of SPIE **8778**, 87780B–87780B–8(2013).

XIII **Performance of a beam-multiplexing diamond crystal monochromator at the Linac Coherent Light Source Recent development of thin diamond crystals for X-ray FEL beam-sharing**
Diling Zhu, Feng Yiping, Stanislav Stoupin, Sergey Terentyev, Henrik Lemke, David Fritz, Matthieu Chollet, James M. Glownia, Roberto Alonso-Mori, Marcin Sikorski, Sanghoon Song, **Tim van Driel**, Garth Williams, Marc Messerschmidt, Sebastien Boutet, Yuri Shvyd'ko, Vladimir Blank, and Aymeric Robert.
Submitted, Review of Scientific Instruments .

XIV **A protein quake through a photosynthetic reaction centre**
David Arnlund, Linda C. Johansson, Cecilia Wickstrand, Anton Barty, Garth J. Williams, Erik Malmerberg, Jan Davidsson, Despina Milathianaki, Daniel P. DePonte, Robert L. Shoeman, Dingjie Wang, Daniel James, Gergely Katona, Sebastian Westenhoff, Thomas A. White, Andrew Aquila, Sadia Bari, Peter Berntsen, Mike Bogan, **Tim Brandt van Driel**, R. Bruce Doak, Kasper Skov Kjær, Matthias Frank, Raimund Fromme, Ingo Grotjohann, Robert Henning, Mark S. Hunter, Richard A. Kirian, Irina Kosheleva, Christopher Kupitz, Mengning Liang, Andrew V. Martin, Martin Meedom Nielsen, Marc Messerschmidt, M. Marvin Seibert, Jennie Sjöhamn, Francesco Stellato, Uwe Weierstall, Nadia A. Zatsepin, John C. H. Spence, Petra Fromme, Ilme Schlichting, Sébastien Boutet, Gerrit Groenhof, Henry N. Chapman and Richard Neutze.
Submitted, Nature Chemistry.

XV **Bond shortening of Rh_2dimen$_4^{2+}$ upon excitation studied with Time-Resolved X-ray Diffuse Scattering**
T. B. van driel, Tobias Harlang, Kasper Skov Kjaer, Kristoffer Haldrup, Morten Christensen, Asmus Dohn, Niels Harrit, Dmitry Khakulin, Michael Wulff and Martin M. Nielsen.
In preparation.

XVI **Disentangling x-ray detector data at an XFEL**
T. B. van driel, Henrik T. Lemke, Kasper S. Kjaer, Robert W. Hartsock, Kelly Gaffney and Martin M. Nielsen.
In preparation.

XVII **Coherent Structural Dynamics in a Solution Phase Coordination Complex Studied with Time-Resolved X-ray Diffuse Scattering**
T. B. van driel, Robert W. Hartsock, K.Kjaer, K.Haldrup, M. Christensen, A. Dohn, K. Moller, T.Harlang, W. Zhang, Z. Sun , H. T. Lemke, D. Zhu, Martin M. Nielsen and Kelly Gaffney.
In preparation.

XVIII **Structural Characterization of Photo Induced Electron Transfer in a Bimetallic Complex**
Tobias Harlang, Sophie Canton, **Tim van driel**, Asmus Dohn, Kristoffer Haldrup, Robert Hartsock, Dmitry Khakhulin, Kasper Kjær, Jianxin Zhang, Martin Nielsen, Michael Wulff, Kenneth Wärnmark and Villy Sundström.
In preparation.

XIX **Watching a Capacitor at Work - Molecular Scale Structure and Dynamics at an Ionic Liquid/Electrode Interface**
Peter Reichert, Kasper Skov Kjær, **Tim Brandt van driel**, Jannis Ochsmann, Moshe Deutsch, Diego Pontoni, Martin Meedom Nielsen and Markus Mezger.
In preparation.

XX **Origin of piezoelectricity in ferroelectric PVDF-TrFE capacitors**
Ilias Katsouras, Mengyuan Li, Kamal Asadi, **Tim van driel**, Kasper Skov Kjær, Yun Gu, Martin Meedom Nielsen, Dago M. de Leeuw.
In preparation.

Abbreviations

ESRF	European Synchrotron Radiation Facility
LCLS	Linac Coherent Light Source
SACLA	SPring-8 Angstrom Compact free electron LAser
APS	Advanced Photon Source
TR-	Time-Resolved
XRD	X-ray Diffraction
XDS	X-ray Diffuse Scattering
XES	X-ray Emission Spectroscopy
XAS	X-ray Absorption Spectroscopy
RIXS	Resonant Inelastic X-ray Scattering
XFEL	X-ray Free Electron Laser
SASE	Self-Amplified Spontaneous Emission
ROI	Region of Interest
FOM	Figure of Merit
QM/MM	Quantum Mechanics / Molecular Mechanics
DFT	Denity Functional Theory
MD	Molecular Dynamics
FWHM	Full width at half maximum
MAD	Median Absolute Deviation
SVD	Singular Value Decomposition
UDECS	Ultrafast Dynamics Exploiting Complementary Structural Tools

Chapter 1

Introduction

Studying chemistry on ultra-fast time-scales became possible with the invention of lasers from 1960's. Optical pump-probe studies were basically limited by the laser pulse duration and therefore rapidly developed along with the improvement of lasers. The optical techniques reached ps time-resolution in the 80's and fs time-resolution in the 90's. Accessing the fs time-scale allows the technique to probe the intrinsic time-scale of atomic motion, namely the speed of atomic vibrations around $10^{12} - 10^{14}$Hz, corresponding to the sub-ps time-scale. In 1999 Ahmed H. Zewail was awarded a Nobel prize in Chemistry "for showing that it is possible with rapid laser technique to see how atoms in a molecule move during a chemical reaction" [1]. Optical techniques rely on the often tight coupling between energy levels and structure in molecules to deduce the molecular structure and energy landscape. However, this approach depends heavily on the system and falls short when the structure is not directly reflected in the absorption/emission spectrum. With the availability of short X-ray pulses from synchrotrons, the field of Time-Resolved X-ray Diffuse Scattering (TR-XDS) made it possible to use X-rays as a structural probe following photo excitation of disordered systems [2, 3, 4]. This technique allows for the determination of the molecular structure independent of its energy-landscape. In addition to these techniques several X-ray spectroscopic techniques such as X-ray absorption spectroscopy and X-ray emission spectroscopy supply additional information on the energy levels, spin, charge and structure of an investigated sample.

The primary focus of this dissertation is the recent advancements made within TR-XDS. The thesis is centred around two solution state experiments, studying photo-induced structural changes in bi-metallic molecules. The experiments are used to exemplify the challenges and possibilities faced when moving from synchrotron X-ray sources to X-ray Free Electron Laser (XFEL) sources. With typical X-ray pulse of 10^{12} photons with 30fs duration, the XFEL provides nine orders of magnitude improvement in peak brilliance and three orders of magnitude in time-resolution compared to the synchrotron. This means that applying TR-XDS at an XFEL opens for studies of molecular structural dynamics on the intrinsic time-scale of atomic movement, making it possible to directly observe structural dynamics *during* chemical reactions. However, the immense increase in flux and time-resolution of the XFEL compared to the synchrotron comes with many new challenges that need to be addressed. These challenges are both found with regards to the experimental setup and the systems studied, but also

technical issues such as significant shot-to-shot fluctuations in both X-ray energy and intensity. Furthermore the orders of magnitude increase in data acquisition rate have presented logistic challenges in the form of data extraction, treatment and analysis of very large datasets.

The work presented here focuses on the advancement of X-ray Diffuse Scattering from 100 ps resolution at synchrotrons to 100 fs resolution at the newly available XFEL sources. TR-XDS has also benefited greatly from combination with simultaneous X-ray spectroscopy techniques and has been applied at both synchrotrons and XFELs to utilise the incident X-rays to their full potential.

My PhD has been focused on these challenges making TR-XDS possible at XFELs and facilitating their use at synchrotron sources.

Chapter 2

Background

This chapter covers some of the background theory used in this dissertation. It briefly introduces visible absorption, available X-ray sources along with X-ray techniques of interest.

2.1 Visible Absorption

When a photon travels in the vicinity of a molecule it has a probability of being absorbed. Given the photon travelling at the speed of light the absorption process occurs within 10^{-18}s [5], bringing the molecule into an excited state. From the excited state the molecule has many decay pathways, both radiative and non-radiative. The two radiative processes, fluorescence and phosphorescence, arise from radiative decay to the ground-state from an excited singlet or an excited state of higher spin multiplicity. A classic Perrin-Jablonski diagram [7] shown in figure 2.1, gives a static image of the energy levels and is useful for illustrating excited states, decay pathways and time-constants. In order for the excited state to undergo inter system crossing (ISC) it must change spin, typically bringing the excited singlet to an excited triplet state. The radiative decay from the triplet state to the ground state is spin forbidden and is therefore kinetically unfavourable. This gives rise to long lived excited states (up to 1s) as opposed to the exited singlet, typically living for $10^{-10} - 10^{-7}s$. The advancement of lasers technology has allowed optical pump-probe techniques to develop rapidly, making fs transient spectroscopy, for which Zewail received the Nobel prize [1], a generally applied technique available in many labs around the world today.

In addition to the Jablonski diagram, a Franck-Condon diagram can be used to visualise the dynamic nature of the energy landscape by projecting the potential energy surfaces along a reaction coordinate. This is shown for a molecule in figure 2.2.

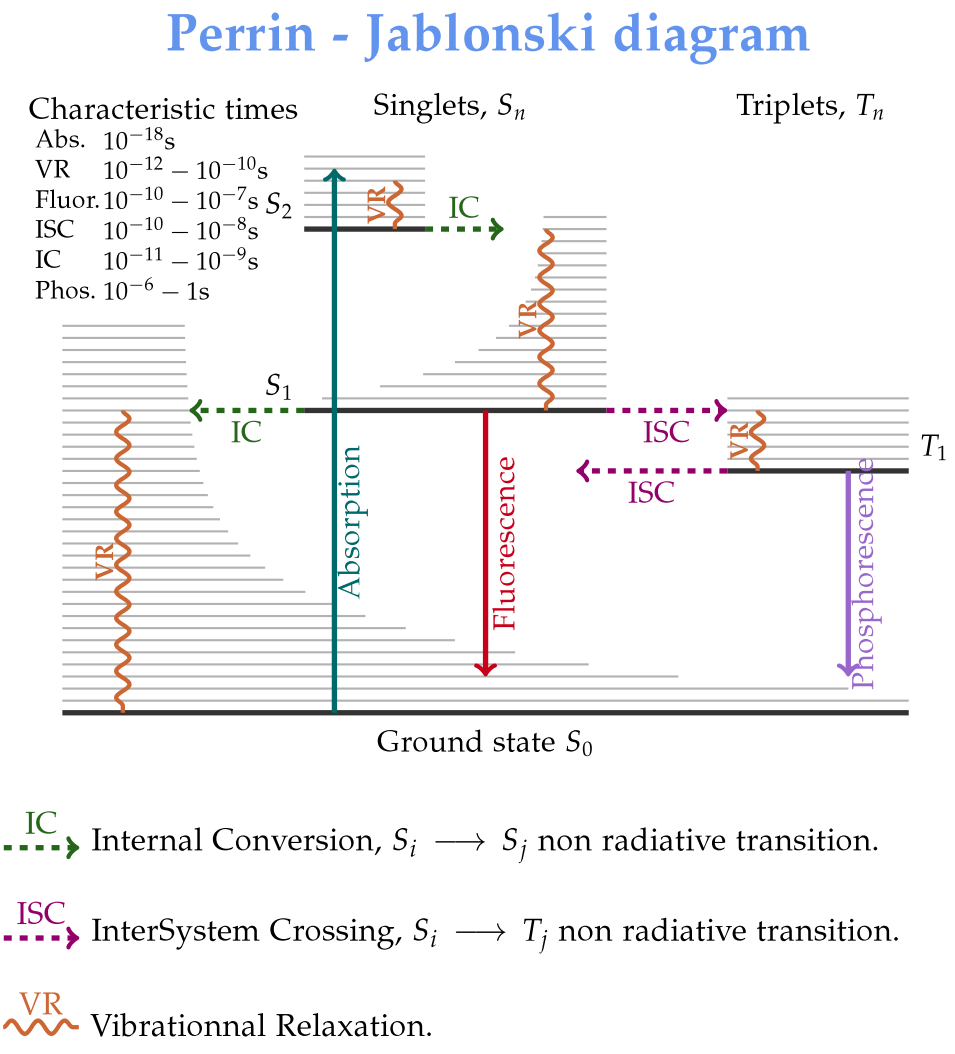

Figure 2.1: A Perrin-Jablonski digram showing the energy pathways for an excited molecule. Adapted from [6] with time-scales from [7, 5].

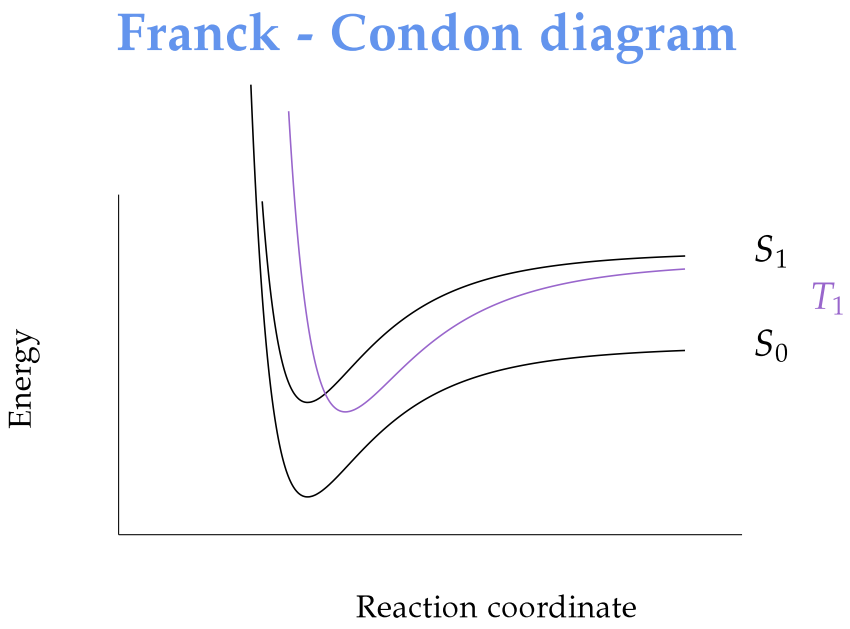

Figure 2.2: A Frank-Condon digram showing the energy levels and potential energy surfaces as a function of a reaction coordinate.

Each curve in figure 2.2 corresponds to the potential energy surface of a state. The minimum of a curve describes the energetically favoured configuration along the reaction coordinate. Excitation of a molecule promotes it to a higher laying state after which the excited wave-packet relaxes on the new potential surface.

Each point along each of the energy surfaces has different kinetics, pathways and transitions available to it. For excited state molecular dynamics the Franck - Condon diagram is a very useful interpretation tool.

2.2 X-rays and matter

Ever since their discovery in 1895 by Wilhelm Conrad Röntgen [8], X-rays have been an integral part of materials research, spanning many fields and techniques and resulting in no less than 28 Nobel prizes. Synchrotron radiation sources have made high intensity X-rays accessible to researchers around the world, making advanced setups and techniques available, facilitating the development and study of a plethora of specialised areas.

The discovery of X-rays very quickly led to medical uses, taking advantage of the difference in transmission of X-rays through flesh and bones.

Furthermore, the short wavelength of X-rays makes it possible to produce interference patterns from crystals. X-ray diffraction (XRD) was first discovered by Max von Laue in 1912 and he was awarded the Nobel prize in Physics in 1914. Further work on XRD by Sir William Lawrence Bragg and his father Sir William Henry Bragg made it possible to derive structural information with atomic resolution. The Braggs were also awarded the Nobel prize in Physics in 1915. Their work resulted in the famous Bragg's law describing diffraction conditions from crystal planes.

$$n\lambda = 2dsin(\theta) \tag{2.1}$$

where n is an integer, λ is the incident wavelength, d is the crystal plane distance and θ is the angle between the incident beam and the scattering planes. Braggs law arises from the constructive interference from scattering of crystal planes, when the phase between the waves scattered from consecutive planes is a multiple of 2π.

During an X-ray scattering process the electromagnetic wave scatters off the charged particle either elastically or inelastically. Since X-rays typically have a wavelength around 1Å, which is the typical length of a covalent bond, X-rays provide a wavelength ideal for studying molecular structures (see figure 2.3).

When an electromagnetic wave encounters an electron it can either be scattered or absorbed. These fundamental interactions lead us to the three basic techniques used here and in the attached/referenced papers; X-ray Diffuse Scattering(XDS) measuring the scattered X-ray photons, X-ray Absorption Spectroscopy (XAS) measuring the absorbed photons and X-ray Emission Spectroscopy (XES) measuring the emitted X-rays upon re-population of the core hole created during the X-ray absorption event.

2.3 X-ray sources

Since the discovery of X-rays there has been a rapid development of X-ray techniques. Much of this development has been driven by the availability of new X-ray sources. As seen in figure 2.4 the brightness of the available X-ray sources has increased exponentially since the introduction of synchrotrons. Synchrotrons are divided into generations with 1st generation synchrotrons relying on bending magnets for X-ray generation, 2nd generation synchrotrons are based on wigglers and 3rd generation use undulators to increase the X-ray output.

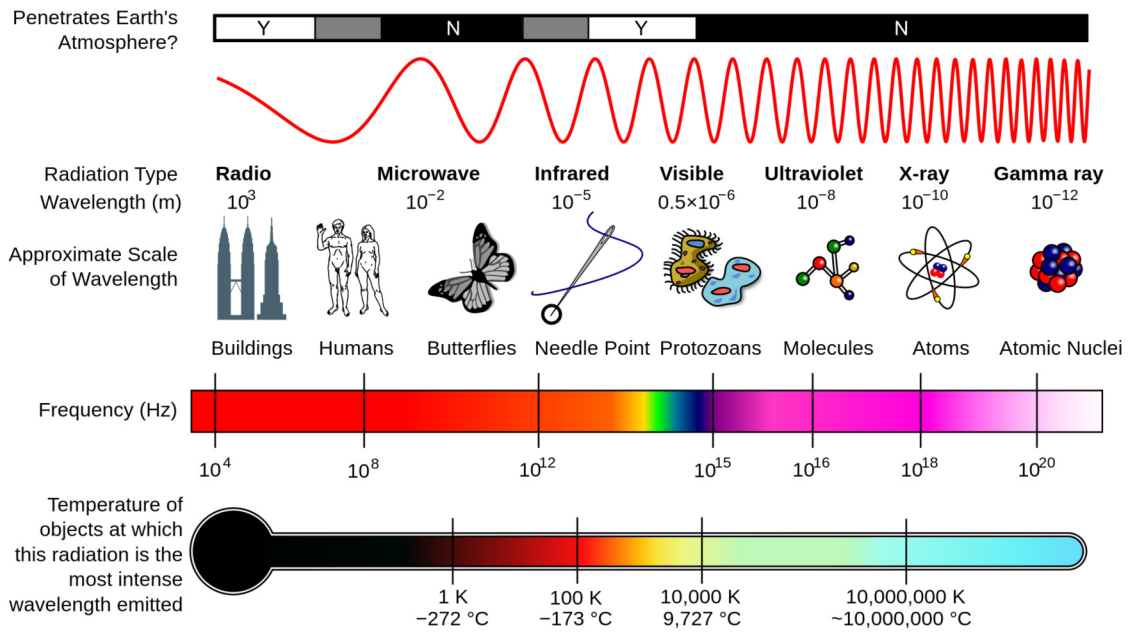

Figure 2.3: The electro-magnetic spectrum, showing the correspondence between energy, wavelength, frequency and size from [9].

Source	3rd gen. synchrotron		XFEL	
Beamline	ID09b at ESRF		XPP at LCLS	
	Polychrom.	Monochrom.	Polychrom.	Monochrom.
Flux (ph/pulse)	$5 \cdot 10^{8}$	$5 \cdot 10^{5}$	$1 \cdot 10^{12}$	$1 \cdot 10^{10}$
Flux (ph/second)	$5 \cdot 10^{11}$	$8 \cdot 10^{8}$	$1 \cdot 10^{14}$	$1 \cdot 10^{12}$
X-ray energy (keV)	$8.5 - 28$ keV		$0.2 - 11$keV	
Reprate(Hz)	$1 \cdot 10^{3}$Hz		120Hz	
MRF(ps)	$80 - 120$ps		0.1ps	

Table 2.1: This table gives an overview of the beam characteristics at a synchrotron- and XFEL beamline respectively.

The newest X-ray source is the XFEL using a linear layout and a long series of undulators to coax the electron bunch to undergo Self Amplified Spontaneous Emission (SASE), and thereby increase the brightness of the X-ray pulses by many orders of magnitude compared to 3rd generation synchrotron sources. This X-ray source improvement has drastically increased the intensity, brilliance and coherence of X-ray pulses while decreasing pulselength by orders of magnitude. Providing a natural enhancement of already available techniques and facilitating brand new areas of research.

As seen from table 2.1 the X-ray sources are continuously improving. Comparing the specific beamline statistics between the ID09b beamline at ESRF and the XPP beamline at LCLS, showing an increase of 3 orders of magnitude in photons/second at an XFEL.

XFELs have advantages for almost all X-ray techniques and have allready achieved some impressive results in protein nano-crystallography [11, 12], atomic science [13] single particle diffraction [14] as well as time-resolved diffraction

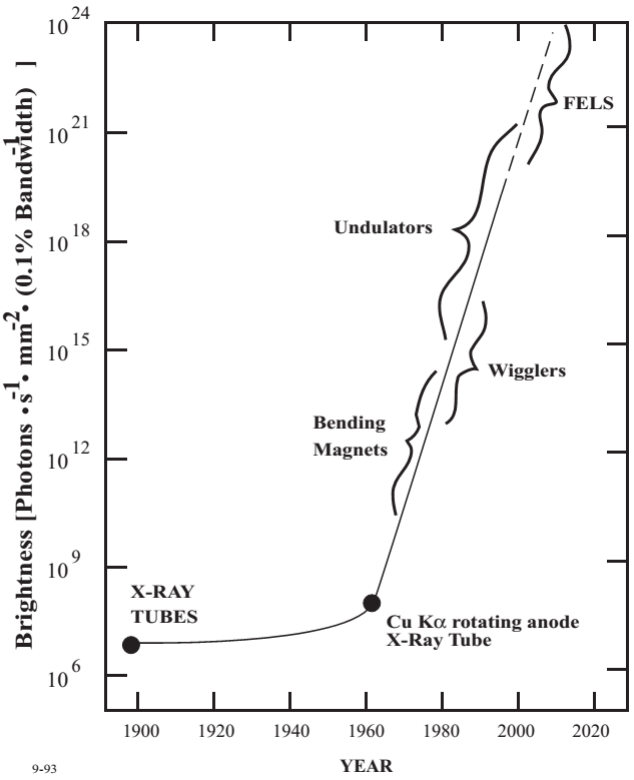

Figure 2.4: X-ray source brightness over the years since their discovery in 1895 [10]

and gold nanoparticles [15]. The interest in XFELs is reflected in the amount of planned constructions, especially given the billion € price tag. FLASH in Germany was the first XFEL to come online in 2005, delivering soft X-rays. Currently only 2 hard XFEL's are online; the LCLS in California came online in 2010[16] and SACLA in Japan came online in 2012. Additionally several XFEL's are under construction; The European XFEL in Hamburg will be online in 2015, SwissFEL in Switzerland in 2017 and PAL-XFEL in South Korea should be online in 2014. Furthermore 10 additional XFEL's are under different stages of planning along with multiple proposed upgrades for the existing facilities [17].

2.4 X-ray Diffuse Scattering - XDS

X-ray Diffuse Scattering relies on the X-ray scattering power of electrons to deduce structural information from an investigated sample. Unlike X-ray diffraction (XRD), which utilizes the long range positional order of crystalline material, XDS probes samples with almost no long-range structural order. For this reason the features in XDS are broad and weak as opposed to the bright diffraction spots typical of XRD experiments. The disorder in a system gives rise to a smearing of the scattered intensity as the Bragg condition is no longer fulfilled at single points in space. Instead the X-rays scatter off the full electron density distribution.

The elastic scattering, known as Thomson scattering, maintains the energy and wavelength of the X-ray while exchanging momentum with the electron. Inelastic scattering on the other hand, transfers energy to the electron thereby changing energy and wavelength in addition to being scattered. The inelastic scattering is known as Compton Scattering and does not contain any structural information.

The polarised X-ray plane-wave can be written as:

$$E(\vec{r},t) = \hat{\epsilon} \cdot E_0 e^{i(\vec{k}\cdot\vec{r}-\omega t)} \tag{2.2}$$

where r and t are the position and time respectively, $\hat{\varepsilon}$ is the polarisation and $\vec{k} = \frac{2\pi}{\lambda}$ is the wave-vector along the direction of propagation.
Quantum mechanically the wave becomes a string of photons with energy $e_{photon} = h\nu$ and momentum $\vec{p} = \hbar \cdot \vec{k}$.

The momentum transfer vector describing the elastic scattering process $|\vec{p}|^2 = |\vec{p'}|^2$ is given by $\vec{Q} = \vec{k} - \vec{k'}$.

The elastic scattering can be derived from the scattering of a single electron and expanding it into a larger system.

The coherent scattering from an electron can be visualised as an incident plane wave with an electric field. This field makes the encountered electron oscillate which results in an expanding spherical wave of photons oscillating in phase, with the electron at the origin.

$$\frac{E_{rad}(R,t)}{E_{in}} = \left(\frac{e^2}{4\pi\epsilon_0 mc^2}\right)\frac{e^{i\vec{k}R}}{R}cos\psi \tag{2.3}$$

$$\text{where } r_0 = (\frac{e^2}{4\pi\epsilon_0 mc^2}) = 2.82 * 10^{-5}\text{Å} \quad \text{for electrons} \tag{2.4}$$

$e^{i\vec{k}R}$ is the phase at distance R from the electron and $cos\psi$ is the polarisation factor. From the equation we get the factor r_0 known as the scattering length of an electron. When expanding the system to include several electrons the expanding spherical waves will interact, causing constructive and destructive interference corresponding to the phase difference between the radiated waves.

To find the coherent scattering of an atom the atomic wave-functions are described as electronic charge-distributions around the nucleus with a charge density $\rho(\vec{r})$. The scattering amplitude, called the form-factor f^0 is given by integrating the phase weighted scattering contribution of each infinitesimal

volume element $d\vec{r}$.
f^0 is expressed in units of r_0 the coherent scattering length of an electron and f_n the atomic form-factor including the scattering length r_0.

$$f_n = -r_0 * f^0 \tag{2.5}$$

$$f_1 = -r_0 * f_1^0 = -r_0 * \int \rho(\vec{r}) \cdot e^{i\vec{Q}\cdot\vec{r}} d\vec{r} \tag{2.6}$$

Thus the atomic form-factor f_1 is given by integrating the electron density times the phase factor over each volume element in units of $-r_0$. Where $e^{i\vec{Q}\cdot\vec{r}}$ is the phase factor from the 1 electron scattering formula and $\int \rho(\vec{r}) d\vec{r} = n_e$ the number of electrons.

As an example, the coherent scattering from a two atomic molecule can be found through the independent atom model:

$$f_{molecule} = f_1 + f_2 e^{i\vec{Q}\cdot\vec{r}} \tag{2.7}$$

where $\vec{r}$ is the position vector of atom two and atom one is placed in the origin. The Scattering intensity can be found as the absolute squared scattering of the atomic form-factor resulting in the following expression:

$$I(\vec{Q}) = f_1^2 + f_2^2 + f_1 f_2 e^{i\vec{Q}\cdot\vec{r}} + f_1 f_2 e^{-i\vec{Q}\cdot\vec{r}} \tag{2.8}$$

considering spherical symmetry of the electron density around each atom we get:

$$I(\vec{Q}) = f_1^2 + f_2^2 + 2 f_1 f_2 e^{i\vec{Q}\cdot\vec{r}} \tag{2.9}$$

The orientational averaging is found by integrating $\vec{r}$ over all possible angles and normalising. We find that the two-atomic form-factor can be expressed by the distance between the two atomic contributions:

$$I(\vec{Q}) = f_1^2 + f_2^2 + 2 f_1 f_2 \frac{sin(\vec{Q}\vec{r})}{\vec{Q}\vec{r}} \tag{2.10}$$

This can be expanded to N atom molecular scattering, still assuming spherical symmetry of the electron density and an independent atom model:

$$I(\vec{Q}) = \left[\sum_j^N f_j e^{i\vec{Q}\cdot\vec{r}_j}\right]^2 \tag{2.11}$$

$$= \sum_i^N f_i^2(\vec{Q}) + \sum_i^N \sum_{j\neq i}^N + f_i(\vec{Q}) f_j(\vec{Q}) \frac{sin(\vec{Q}\vec{r}_{ij})}{\vec{Q}\vec{r}_{ij}} \tag{2.12}$$

where the contribution of each pair of atoms is summed up. f_i is the atomic form-factor of atom i and $\vec{r_{ij}}$ is the distance between atom i and j. This is the Debye equation for the rotationally averaged scattering.

The atomic form-factor is typically approximated by the analytical expression:

$$f_{atom}(Q) = \sum_{i=1}^4 A_i exp(-B_i(\frac{Q}{4\pi})^2) + C \tag{2.13}$$

$$I(Q) = |f_{atom}(Q)|^2 \tag{2.14}$$

where A_i, B_i and C are tabulated parameters for each atom and can be found in published tables [18, 19, 8].

The inelastic scattering holds no structural information and depends solely of the number and type of atoms in a molecule. It has been studied and approximated analytically by Hajdu et al.:

$$I_{inelastic}(Q) = \left[\frac{Z - I_{elastic}(Q)}{Z}\right] \cdot \left(1 - M[e^{\frac{-KQ}{4\pi}} - e^{\frac{-LQ}{4\pi}}]\right) \tag{2.15}$$

where K,L and M are tabulated values from the best fit to the measured inelastic intensities[18]. For atoms 20-95 the form-factor can be approximated by the equation given by Palinkas et al.:

$$I_{inelastic}(Q) = Z\left(1 - \frac{a}{(1 + bQ/4\pi)^c}\right) \tag{2.16}$$

Once again a,b and c are tabulated values presented in [19]. Both expressions can be converted to intensities by taking the absolute square of the atomic form-factors $I(\vec{Q}) = |f^0(\vec{Q})|^2$
. It is noted that the inelastic scattering $I(Q) \to 0$ for $Q \to 0$ and $I(Q) \to Z$ for $Q \to \infty$. The inelastic scattering is independent of molecular structure, and is only used for normalization and scaling in a high Q interval.

2.5 X-ray Absorption Spectroscopy (XAS) and X-ray Emission Spectroscopy (XES)

As an alternative or in combination with XDS, several X-ray spectroscopic techniques are available. They are not treated in this dissertation but are briefly introduced here as many of the attached/referenced papers elaborate on the combination of techniques and greatly benefit from their inclusion. These X-ray spectroscopic techniques rely on having an absorption edge below the X-ray energy and carry local information on the charge and spin of the element in focus. For this reason XES and XAS are especially strong for Spin-Crossover and Charge-Transfer as shown in **[II]** **[IV]** **[VI]** **[VII]** **[VIII]** **[X]** **[XI]** **[XVIII]**. For the experiments here the absorption edges are located at difficult energies and the information content questionable (The edges are located at Rh:K≈ 23keV L≈ 3keV Ir: K≈ 76keV L≈ 11keV).

XAS and XES take advantage of the atomic absorption of X-rays and either measures the absorbed X-rays (through the X-ray transmission) or the re-emitted X-ray photon following the absorption process. They both rely on scanning the incoming or outgoing X-ray energies. Since the energy levels in an atom and the energies in different atoms are separated, the techniques act as local probes focused on the energies of a single type of atom with a well-defined energy window, monitoring one or more transitions of interest.

X-ray transmission decreases as the X-ray energy increases, with a jump in absorption every time an ionisation threshold is crossed. XAS uses small shifts and modulations in this spectrum to deduce chemical information. Since the ionisation threshold is element specific, XAS very conveniently spreads out

element information along the energy axis making XAS a local element-specific probe.

XAS spectra are usually divided in the X-ray Absorption Near-Edge Structure (XANES)-region and Extended X-ray Absorption Fine Structure (EXAFS)-region.

The XANES region includes the pre-edge, white-line and 50-100 eV above the edge, where the EXAFS region extends from the XANES region.

Quantitative analysis of XAS spectra is difficult, where qualitative analysis of the XANES region can be done through representative choices in reference compounds as in [**XI**] or from models of the coordination chemistry, molecular orbitals and band structure.

The EXAFS region contains information on back-scattering from the nearest neighbouring atoms and result in oscillations due to interference.

$$\chi(E) = \frac{\mu(E) - \mu_0(E)}{\Delta\mu_0(E)} \tag{2.17}$$

where $\chi(E)$ is the EXAFS fine-structure function, μ_0 is the smooth absorption of an isolated atom and $\Delta\mu_0$ is the jump in absorption at the ionisation threshold E_0.

The oscillations in the EXAFS region due to back-scatter are now interpreted as a function of k, the wave-number of the photo-electron defined as:

$$k = \sqrt{\frac{2m_e(E - E_0)}{\hbar^2}} \tag{2.18}$$

EXAFS can then be quantitatively analysed using the EXAFS equation[20]:

$$\chi(k) = \sum_j \frac{N_j f_j(k) e^{-2k^2\sigma_j^2}}{kR_j^2} sin[2kR_j + \delta_j(k)] \tag{2.19}$$

where $f(k)$ and $\delta(k)$ are scattering properties of the neighbouring atoms, N_j is the number of equivalent atoms, R is the distance and $e^{-2k^2\sigma_j^2}$ is the debye-waller term describing the thermal disorder.

XES on the other hand relies on the emission of a secondary photon upon re-population of the core hole from another filled state. The emitted energy is element specific and XES thereby works as a local element specific probe.

The energy of the emitted photon holds information on the charge and spin of the emitting atom. Due to the novelty of this technique, most of the analysis is done based on reference spectra from different spin and charge states of the targeted element [21] as in [**VIII**] and [**IV**].

2.6 Time Resolved X-ray Techniques

For all work included in this dissertation, X-ray techniques have been used to conduct time resolved experiments. In these experiments, a laser has been synchronized to the X-ray pulses, such that the sample is excited by an optical

laser (pump) pulse at time (t) with respect to the X-ray (probe) pulse. In this fashion, the photo-induced changes in the molecular system can be tracked with the X-ray techniques described in the previous chapters, with a time-resolution limited by the pulse length of the laser and X-ray pulses. Thus, difference data describes the measured changes in X-ray signal induced by the excitation event, and in many cases, the data analysis can be carried out directly on the transient data.

Chapter 3

Synchrotron experiments - Introduction

This chapter introduces some general areas in relation to the TR-XRD studies described in the following chapter. Covering thoughts on synchrotron experiments, necessary detector corrections, time-resolved solvent scattering as well as computational tools used for molecular modelling.

TR-XDS experiments at synchrotrons have gained increasing interest and support the last 10 years, with a significant amount of work put into establishing the technique and exploring the possibilities [3, 4].

An abundance of TR-XDS is carried out at the ID09b beamline at ESRF. A Large amount of work has been put into constructing a stable high quality beamline to constantly push the technical abilities of this 3rd generation synchrotron source.

Due to the lack of adaptable software at the beamline, new software was developed in MATLAB® to allow modifications of the data reduction routines and insight into applied corrections. This led to a more flexible workflow as well as verification of the applied corrections on a neat water sample as seen in chapter 3.1.This development combined with software developed for XFELs made it possible to implement a working XES setup at the beamline [**XVIII**], as an altered sample geometry is not easily implemented in the current beamline sofware.

Based on a large number of experiments at ID09b it has also been possible to evaluate structural DFT calculations in order to predict the magnitude and shape of a photo-induced response as shown in [**IX**],[**I**], [**II**],[**VII**] as well as chapter in 4.

3.1 Detector corrections

The measured scattering data needs to be corrected for any distortions introduced by the experimental setup, detector effects as well as a geometric correction accounting for the solid angle covered by each pixel.

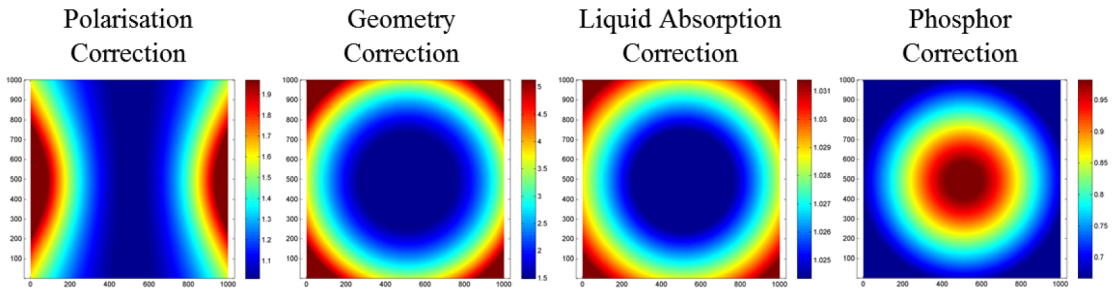

Figure 3.1: 2D Detector corrections needed at a synchrotron source (ID09b at ESRF)

The necessary corrections are applied after the dark and gain corrections have been accounted for. The full detector correction is given by:

$$I_{pixel}^{Corrected} = \frac{I_{pixel}^{measured} - Dark_{pixel}}{Gain_{pixel}} \cdot Corrections_{pixel} \tag{3.1}$$

where $Dark_{pixel}$ is the measured intensity with no incident photons and $Gain_{pixel}$ is the sensitivity of the pixels. All pixels can be treated simultaneously when all individual components are defined in a vector or array:

$$I^{Corrected} = \frac{I^{measured} - Dark}{Gain} \cdot Corrections \tag{3.2}$$

For an established beamline with a commercial detector, Dark and Gain are usually taken care of with a Dark and Flatfield measurement, yielding a partially corrected Image:

$$I_{Dark,Gain}^{measured} = \frac{I_{pixel}^{measured} - Dark_{pixel}}{Gain_{pixel}} \tag{3.3}$$

where $I_{Dark,Gain}^{measured}$ is the partially corrected images obtained from a calibrated detector e.g. the FRELON at ID09b and other commercial CCD detectors. These images still need the remaining detector corrections prior to analysis:

$$I^{Corrected} = I_{Dark,Gain}^{measured} \cdot Corrections \tag{3.4}$$

$$Corrections = C^{Polarisation} \cdot C^{Geometry} \cdot C^{Absorption} \cdot C^{Phosphor} \tag{3.5}$$

In the following the individual corrections are introduced.

X-ray polarisation - $C^{Polarisation}$

Scattering is dependent on the polarisation and is highest when the X-ray polarisation is perpendicular to the azimuthal angle to a given pixel and smallest at 90 degrees to the incoming beam along the direction of polarisation. This is why X-ray emission spectroscopy is ideally measured at this angle to avoid background scattering in the measured signal. The polarisation is given by the following equation from Hura et al. [22]:

$$C^{Polarisation} = P\left[1 - (sin(2\theta)sin(\phi))^2\right] + (1-P)\left[1 - (cos(2\theta)sin(\phi))^2\right] \quad (3.6)$$

where P is the X-ray polarisation and θ and ϕ are the X-ray scattering angle and azimuthal angle respectively.

Pixel geometry - $C^{Geometry}$

The geometry correction accounts for the relative solid angle covered by the individual pixel projected onto a sphere. The projection can be divided into the relative area of a pixel $\frac{1}{cos(t\theta)^2}$ and the relative area facing the scattering source due to the angle of the pixel given by $\frac{1}{cos(t\theta)}$.

The geometry correction is given by the ratio of a normalised spherical angle covered by a pixel in the following equation from Bosecke et al. [23]:

$$C^{Geometry} = \frac{1}{cos(2\theta)^3} \quad (3.7)$$

The geometric correction increases at large angles and results in relatively poor signal to noise at high angles, even though the higher angles cover a larger number of pixels per spherical angle.

Sample absorption - $C^{Absorption}$

The scattered X-rays on a liquid sheet will have different path-lengths through the liquid. Given the X-ray transmission of the liquid the differences in path-length result in different transmissions. This has been solved analytically for a perpendicular "plate-like sample geometry" by Pauw et al. [24].

$$C^{Absorption} = \frac{\mu D - \mu D/cos(2\theta)}{exp(\mu D)[-exp(\mu D) + exp(\mu D/cos(2\theta))]} \quad (3.8)$$

where $C^{Absorption}$ is calculated for a perpendicular liquid sheet of thickness D and only accounts for different path-lengths through the sample and not for multiple scattering. This correction has a large effect with angles larger than 2θ and when the transmission through the sample is low.

In case of a non-perpendicular liquid sheet the correction gets complicated and divides the absorption into three cases: when the scattered radiation passes through the liquid sheet, parallel to the liquid sheet and returning out the back

of the liquid sheet. This problem can be solved numerically by finding positive and negative scattering angles with regards to the liquid sheet and bounding all scattering lengths with the liquid sheet parameters (width and thickness).

Phosphor correction - $C^{Phosphor}$

The phosphor correction corrects for the probability of absorption in a detection layer. The phosphor correction is exemplified by the phosphor layer in front of X-ray CCD's, converting hard X-ray to detectable visible photons, but can also be used to account for the detection probability in the detection layer of a detector when the probability is less than unity. This correction calculates the ratio between the detection probability in the direct beam and scattered intensities of a perpendicular detector, due to differing path-lengths in the detection layer of each pixel:

$$C^{Phosphor} = \frac{1 - exp^(-\mu \cdot D_p)}{1 - exp^(-\mu \cdot D_p / cos(2\theta))} \tag{3.9}$$

where D_p is the thickness of the detection layer.

3.2 Constructing Scattering curves

The Debye equation assumes that the sample is rotationally isotropic, meaning that the scattering signal is isotropic along the azimuthal angle around the normal of the X-ray beam. Thus, after applying the corrections described in the previous chapter, the 2D images can be reduced to 1D scattering curves by azimuthal integration. This azimuthal integration collapses each 2D image into a 1D curve according to the scattering angle to each pixel $S(2\theta)$. With the relation between momentum transfer and scattering angle given by:

$$Q = \frac{4pi \cdot sin(\frac{2\theta}{2})}{\lambda} \tag{3.10}$$

where 2θ is the scattering angle and λ is the X-ray wavelength.

The scattering curves measured at ID09b at the ESRF for neat water where compared to the data published in [22] while developing reduction and analysis code, to verify the applied corrections.

The total X-ray scattering can be analysed to extract the sample structure as radial distribution functions, as done by Skinner et al. in a recent article studying neat water [25]. Since XDS is a global structural probe, a global description of the system is necessary to analyse the total scattering. For TR-XDS there are many other complication factors, so instead the data is converted into difference scattering curves, essentially cancelling out all static contributions.

Hence, when measuring TR-XDS difference scattering, static background effects can be neglected since they cancel out when taking the difference. It can however be beneficial to study the full or radially integrated images to identify and remove any sources to background, since they may fluctuate over time or increase the noise in specific regions.

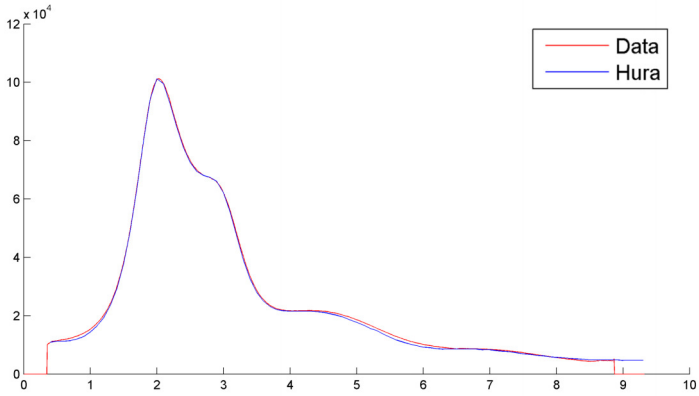

Figure 3.2: Integrated and corrected neat water Thomson scattering measured at ID09b (red) compared with Hura et al. (blue) [22]. The measured scattering (red) has been corrected for Polarisation, Geometry and Sample absorption as well as subtracted the calculated Compton scattering and the background air-scattering to compare the corrected elastic scattering from water.

3.3 Constructing difference scattering curves

As mentioned previously, TR-XDS is usually achieved using a pump-probe setup where a structural change is induced using an optical pump synchronised with the arrival time of the X-ray pulses. The difference scattering, ΔS, is extracted by subtracting scattering images taken of the un-pumped sample from images taken after the laser pumping event. The resulting difference scattering holds information about the changes in electron density and can therefore be used to extract the structural changes induced by the laser. Typically the average of the un-pumped data measured before and after the pumped data is subtracted when constructing the difference scattering curves:

$$\Delta S = S_{On} - \frac{1}{2} \cdot (S_{Off-before} + S_{Off-after}) \tag{3.11}$$

The remaining signal ΔS only contains signal from sample changes between S_{Off} and S_{On}. Given a stable setup ΔS purely consists of the scattering contribution from laser induced changes. For a controlled experimental setup measuring a laser absorbing molecule in solution, this leaves changes originating from the laser absorption in the molecule and therefore greatly reduces the amount of parameters influencing ΔS.

In general the change is described as follows:

$$\Delta S = \Delta S_{Solvent} + \Delta S_{Solute} + \Delta S_{Solvent-Solute} \tag{3.12}$$

Where $\Delta S_{Solvent}$ and ΔS_{Solute} are the changes in the scattering from the solute molecule and surrounding solvent respectively. And $\Delta S_{Solvent-Solute}$ is the Solvent-Solute cross-term.

The solvent term can be measured independently and is covered in chapter 3.4 and the solute term ΔS_{Solute} can be calculated from the molecular structures. The Solvent-Solute cross-term, $\Delta S_{Solvent-Solute}$, is highly system dependent. For some systems it is negligible ([**I**] [26]) and for other systems the cage effect can

be approximated using MD simulations of solvent around the ground-state and exited-state molecule respectively, as presented in 3.5.

The technique has been successfully applied on many different systems in solution ranging from di-atomics [2], small molecules[27, 28], large molecules[29, 26] and proteins[30]. Common for the TR-XDS experiments is that they require a good model of the system in order to extract a complete structure from the sparse $Q\Delta S$ data measured and often relies on global fitting, iterative solutions and/or model comparison [3, 31].

3.4 Solvent Response - $\Delta S_{solvent}$

In order to extract the structural information pertaining to the solute in a TR-XDS experiment the changes in the surrounding solvent need to be understood. Based on work by Cammarata et al. the scattering differentials $\frac{\partial S}{\partial T}\,|_\rho$ and $\frac{\partial S}{\partial \rho}\,|_T$ can be extracted and used to describe $\Delta S_{solvent}$ at any time assuming local thermal equilibrium [32]:

$$\Delta S_{Solvent} = \Delta T \cdot \frac{\partial S}{\partial T}|_\rho + \Delta\rho \cdot \frac{\partial S}{\partial \rho}|_T \tag{3.13}$$

This work was expanded upon in [**III**] where the method was standardised, based on a set of well suited azo-dyes. Solvent reference measurements were conducted for 7 solvents in a quasi-monochromatic (2 % BW) measurement, removing the necessity of measuring a reference solvent response in conjunction with every single experiment. Figure 3.3 shows the solvent differentials for acetonitrile, as well as the kinetics of the measured temperature ΔT and density $\Delta\rho$ for methanol measured at ID09b.

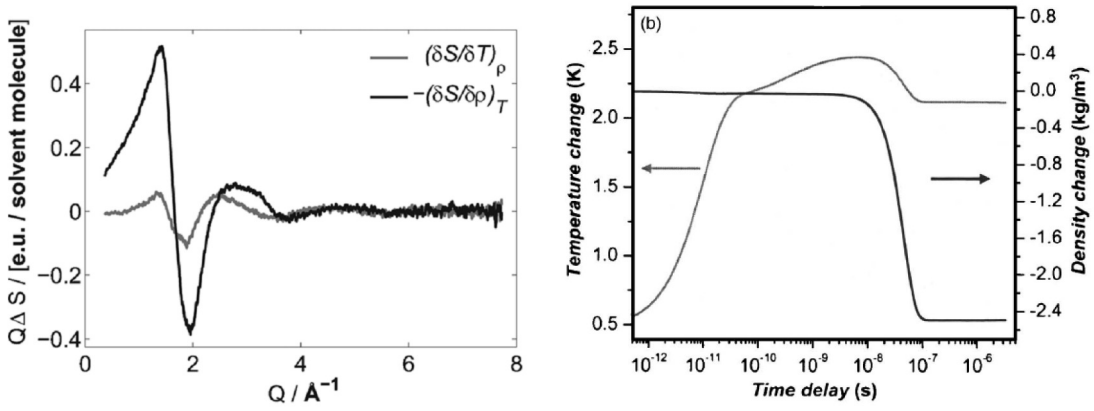

(a) Acetonitrile solvent differentials (b) Solvent kinetics in methanol

Figure 3.3: (a) Difference scattering spectra for acetonitrile heating separated into $\frac{\partial S}{\partial T}|_\rho$ and $\frac{\partial S}{\partial \rho}|_T$ from [**III**] and (b) time-scales for the respective thermal contributions in methanol showing a delayed onset of the density change $\Delta\rho$ on the $10ns$ time-scale from Cammarata et al. [32].

The solvent response is often comparable to the solute signal and therefore needs to be subtracted in order to se the signal from the naked solute. However,

the presence of the solvent signal is very useful when aligning temporal and spatial overlap in the TR-XDS experiment, since all the absorbed energy eventually ends up as heat. For a visibly absorbing sample (coloured liquid) the scattering signal at 1μs will contain large amounts of the strong $\frac{\partial S}{\partial \rho}|_T$ signal allowing for easy determination of spatial overlap. For the temporal overlap the $\frac{\partial S}{\partial T}|_\rho$ signal allows for determination of time zero (t_0), even without the presence of a solute, with a large photo-induced structural response.

3.5 Modelling

Several different approaches are utilised to understand and model the solute contributions ΔS_{Solute} and $\Delta S_{Solvent-Solute}$ to the measured scattering signal.

First of all, earlier experiences and literature may have a very good idea of which structural changes that can be expected. Since the field of time-resolved X-ray studies follows 30 years of time-resolved optical studies, many of the good research ideas are based on previous experiments and many of the thoughts and concerns have previously been contemplated by others. However, X-ray's are a structural probe and therefore we need to have a good idea of the local and global structure of the chosen system. Luckily, the availability of computational power allows us to use some computational approaches to predict and model the molecular structures and simulate the scattering from the solute ΔS_{Solute} and for the modeled Solvent-Solute interaction, $\Delta S_{Solvent-Solute}$ using the Debye equation (2.12).

3.5.1 Molecular dynamics - $\Delta S_{Solvent-Solute}$

Molecular dynamics (MD) simulations are based on classical interactions and can be used to quantify the solvent environment of the sample system, for most cases we neglect this step. However, for several experiments it has been necessary to include the solvent-cage term and/or a second order heating term for the solvent when analysing the TR-XDS data ([**II**],[**VII**],[**XVIII**] and [**IV**]).

Work is also being done on identifying the tools and computational approaches that can reproduce our pure solvent experiments [**III**]. Additionally MD relaxation around a fixed ground-state structure and excited-state structure, has also been used to yield information on the solvent packing around a solute molecule [**II**].

All in all we have found a need for classical MD simulations in order to predict and interpret the structural changes observed in the scattering data, when studying solute molecules that have a large interaction with the solvent.

3.5.2 Density Functional Theory - ΔS_{Solute}

In order to simulate the molecular structure and energy levels, a quantum mechanical description is needed. However a full complex N-electron system is too complicated to solve and therefore Density Functional Theory (DFT) is used to reduce the complexity. The Hohenberg-Kohn theorems state that a given system is uniquely described by its electron density [33]. This essentially reduces the dependency of the system from 3N spacial coordinates to 3, and allows us to calculate the energy of a system, or to minimise the energy by optimising the structure.

For use in time-resolved measurements, a description of both the ground-state and excited-state structures are needed. Since DFT calculates the lowest energetic state, it is not suitable for excited state calculations, so for this the computationally heavier TD-DFT approaches can be used [34, 35]. Luckily most of the systems investigated undergo inter-system crossing and relax to the lowest state of different spin, therefore a ground-state DFT calculation with altered spin configuration is used to calculate the excited state structure [**II**], [**IX**],[36, 37].

Finally, the XRD analysis relies on valid structural guesses to identify the structure of the molecule. The information content in the XRD signal is too low to directly determine the 3N-3 degrees of freedom in large molecules. But the information content is sufficient to distinguish between proposed structures. DFT provides a great tool for generating a series of molecular structures, either by using different optimisation parameters(functionals and approximations) or by constricting the structural optimisation to generate molecular structures along a chosen reaction coordinate. For bi-metallic d8-d8 complexes the optimisation is often constrained along the M-M axis, as this is the most important reaction coordinate upon photo-excitation. Additionally, the high electron density on the metal sites have the largest contribution to the scattering pattern.

Early TR-XDS on molecules in solution was based on perturbation of crystal structures, as for PtPOP [38] where the solute molecule is rather rigid and only deviates slightly from crystal structures. For large flexible molecules in solution, such as $Rh_2(dimen)_4^{2+}$and $Ir_2(dimen)_4^{2+}$presented in the following chapters and [**II**], crystal structures represent structural models far from reality. DFT serves as a flexible tool to both predict a structure through optimisation, but also to predict the energy landscape identifying the theoretical barrier between structures.

Future simulations will be based on much more advanced schemes such as the combination of a quantum mechanical description of the solute and solvent shell, in addition to molecular mechanics of the remaining solvent (QM/MM) in order to predict the structural dynamics as by Pham et al. [39, 40]. However, the QM/MM approach is much heavier computationally as it includes more specific interactions as presented in [**V**].

Chapter 4

Synchrotron experiments on $Rh_2dimen_4^{2+}$

This chapter covers a time-resolved X-ray diffuse scattering experiment at a synchrotron. The specific study was focused on measuring the sub-ns photo-induced structural change of a bimetallic Rhodium compound in solution, carried out at the ID09b beamline at ESRF.

After several successful measurements of the bi-metallic metal complex PtPOP ($[Pt_2(H_2P_2O_5)4]^{4-}$)[26, 38, 41, 31], $Rh_2(dimen)_4^{2+}$and $Ir_2(dimen)_4^{2+}$(dimen=$cis-1,8-diisocyano-p-menthane$) were a natural progression. $Ir_2(dimen)_4^{2+}$was studied at ID09b in [**I**] and also at XPP (see chapter 6).

$Rh_2(dimen)_4^{2+}$provided a technial challenge due to the much lighter ^{45}Rh atoms compared to the heavier ^{77}Ir atoms in $Ir_2(dimen)_4^{2+}$or ^{78}Pt in PtPOP. Additionaly, $Rh_2(dimen)_4^{2+}$has a much shorter excited state lifetime of $< 1ns$ [42] as compared to 500 ns for $Ir_2(dimen)_4^{2+}$[43] and 10μs for PtPOP [38]. The short life-time creates a smaller window of time to study the excited state structure. Both $Rh_2(dimen)_4^{2+}$and $Ir_2(dimen)_4^{2+}$show a large contraction along the M-M bond upon photo-excitation, due to the promotion of an electron from the $d\sigma*$ anti-bonding to the $p\sigma$ bonding orbital (see figure 4.1 a))

4.1 Excited state dynamics of $Rh_2dimen_4^{2+}$ in acetonitrile solution

$Rh_2(dimen)_4^{2+}$consists of two Rh atoms linked together by four dimen ligands forming a water-paddle like structure (see figure 4.1). The molecule, as well as several other $Rh_2(bridge)_4^{2+}$ molecules, were previously studied spectroscopically [45, 46, 47, 48, 49] and the crystal-structure of $Rh_2(dimen)_4^{2+}$was determined using X-ray diffraction [44]. These bimetallic d8-d8 molecules were of great interest in the 1980's due to their potential as light harvesters or two centre redox-systems [50, 51], since then the commercial use of these systems seems infeasible. However, the systems show interesting excited state dynamics [43]

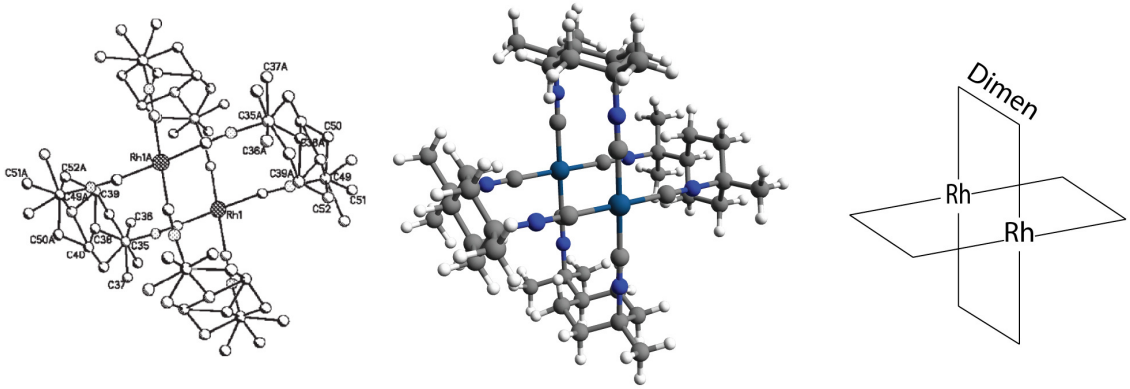

(a) (b) (c)

Figure 4.1: The molecular structure of $Rh_2(dimen)_4^{2+}$(a) Determined by X-ray diffraction [44] (b) From DFT calculations made in ORCA (see chapter 4.2) (c) A simple model-structure showing the waterwheel like structure.

and serve as great model systems for photo-induced structural and electronic changes.

From the asymmetry of the dimen ligand it is apparent that several different isomers are possible due to alternating orientation of the ligand. These isomers were first discussed by Sykes et al. [52] and given statistical distribution there are 4 possible isomers: 0:4, 1:3, 2:2-trans and 2:2-cis ligand orientation, composing $\frac{1}{8}$, $\frac{1}{2}$, $\frac{1}{4}$ and $\frac{1}{8}$ respectively. Based on the absorption spectra the 4 different $Rh_2(dimen)_4^{2+}$isomers are indistinguishable.

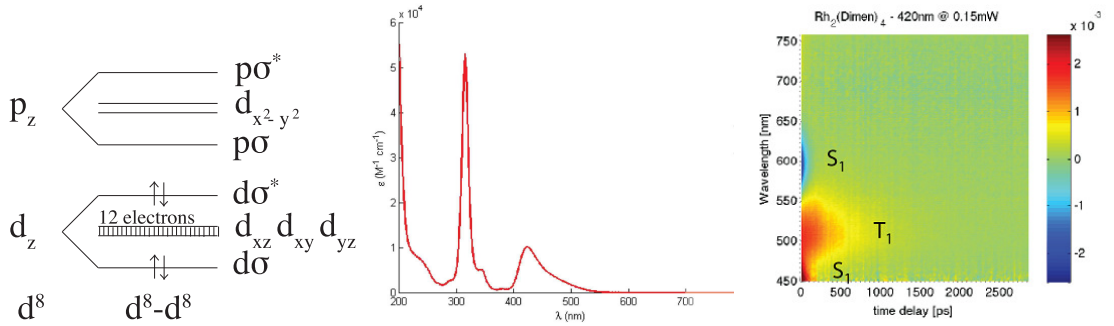

(a) (b) (c)

Figure 4.2: (a) Linear combination of Atomic Orbitals for d8-d8 metals adapted from [53] (b) Optical absorption spectrum of $Rh_2(dimen)_4^{2+}$in acetonitrile (c) Transient absorption spectrum of $Rh_2(dimen)_4^{2+}$pumped at 420 nm[43].

The optical spectroscopy of $Rh_2(dimen)_4^{2+}$and DFT calculations show a single shallow ground state energy minimum predicting one ground state structure, as well as a deeper excited state potential at a shorter Rh-Rh distance [42, 49]. The absorption feature at 400-500nm (See figure 4.1 b) corresponds to the HOMO-LUMO $4d\sigma * - > 5p\sigma$ transition [42]. The initially populated singlet state S_1 crosses into the longer lived triplet state T_1 after flipping the spin of the excited electron. The lifetimes of the populated states were determined from global fits of the transient data by T. Harlang [43] and the resulting lifetimes are $\tau S = 70ps$

and $\tau T = 590ps$. Given a synchrotron time-resolution of $100ps$ it should be possible to measure the structure of the triplet state.

4.2 Excited state structure

To determine the molecular structures of $Rh_2(dimen)_4^{2+}$ a series of good structural guesses are needed. Based on these, the maximum likelihood framework can determine the most probable structure given the measured X-ray scattering. Direct inversion of the scattering pattern is not possible due to the limited information content of the difference scattering pattern and the large number of molecular degrees of freedom.

DFT calculations on $Rh_2(dimen)_4^{2+}$ were carried out in ORCA [54], and a large number of comparisons were carried out to determine what parameters to include [55]. For the results shown here, the ground and excited state were calculated by restricting the spin configuration of the molecule allowing normal structural optimisation using DFT. Single structures were optimised for the two states using the hybrid functional PBE0 [36] in a dz basis-set. The calculations include the COnductor-like Screening MOdel (COSMO) to account for the solvent. Additionally, Effective Core Potentials (ECP) were used for the metal atoms to reduce computational time. The potential energy surfaces were accumulated by restricting the Rh-Rh bond distance, the dihedral twist of the molecule around the Rh-Rh bond and optimising the structure. The $Rh_2(dimen)_4^{2+}$ structures were optimised in steps of 0.5Å and 5 degrees twist to span out 2.5-5Å Rh-Rh distance and 0-50 degrees dihedral twist. Assuming a continuous potential energy surface additional structures and corresponding energies were interpolated from the nearest optimised structures. The resulting potential energy surfaces can be seen in figure 4.3 showing an expected ground-state Rh-Rh distance of 4.5Å and an excited-state twisted structure with 3Å Rh-Rh separation. In comparison, Mann et al. [56] achieved similar results based on DFT calculations on fractions of the molecule and symmetry constraints/arguments.

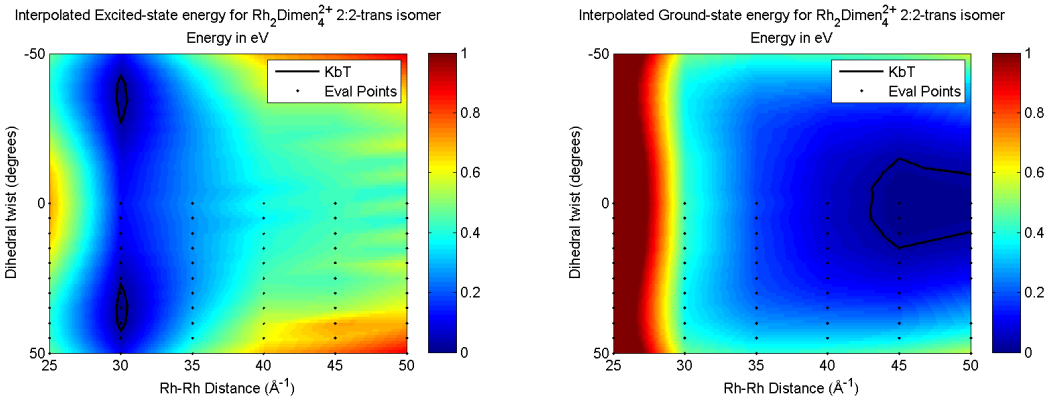

(a) Excited-state PES

(b) Ground-state PES

Figure 4.3: (a) Excited- and Ground-state Potential Energy Surfaces (PES). Calculated using DFT for a constrained singlet and triplet geometry respectively. The structures were evaluated in the grid of points superimposed on the PES.

From the calculated grid of structures an infinite amount of structures can be extrapolated as linear combinations of the nearest neighbours. This approach to generating structural guesses for the fitting of XDS data results in a series of potential molecular configurations. Traditionally structures used for the data analysis were generated by permuting either crystal structures as for PtPOP [26, 38, 41] or single DFT structures as for $Ir_2(dimen)_4^{2+}$[**I**]. For simple or rigid molecules these permutations are close to an accurate description of the possible structural configurations, but for large soft molecules in solution such as $Rh_2(dimen)_4^{2+}$the permutations will yield a poor description of the ligands. However, since XDS is dominated by the heavy scatterers, the M-M distance could probably be identified based on a set of poor guesses as long as the heavy atoms are accounted for. Using DFT together with TR-XDS allows us to benchmark the computational results. As a result, identification of a good set of computational approaches allows future experiments to be screened and simulated before applying for beamtime.

4.3 Sample Setup

The sample setup for TR-XDS requires a stable renewable target containing a solution of un-excited solute molecules. This is achieved with a circulating reservoir-pump-nozzle loop continuously pumping sample through a $300\mu m$ sapphire nozzle. This produces a thin, free-standing liquid sheet at the X-ray/laser interaction point. The liquid sheet flows into a catcher returning the exposed sample to the reservoir. Due to the small interaction volume of the X-ray and laser, most of the returned sample has never been exposed. Thus, a circulating sample can be measured for a long time, even if the exposed sample is destroyed. A larger concern is the formation of nano-particles or the destructive oxidation of the sample. To protect the sample environment the entire system is kept closed with a continuous flow of argon bubbling through the reservoir, and an over pressure of nitrogen in the sample chamber. The sample chamber is sealed with kapton windows allowing X-rays to pass onto the detector. The flow speed of the pump is set around a flow-rate of 3 m/s and tweaked to achieve the most stable liquid sheet, as the optimal speed depends on the viscosity and surface tension of the solvent.

4.4 Beamline Setup

The setup at the ID09b beamline at ESRF has been the work-horse for TR-XDS experiments for many years. The beamline uses a set of choppers to lower the X-ray frequency from 5.7 MHz to 1 kHz to match a 1 kHz laser allowing for stretched (ps) laser pulses and giving ample time for renewal of the sample interaction spot (1 ms moves the exposed sample volume 3mm at 3 m/s). The reduced repetition rate also reduces the utilised X-ray flux by 3 orders of magnitude but allows for long time-delays up to 1 ms. The X-ray pulses are generated by the 236-pole 17mm gap undulator (U17) generating an intense pink-beam in the 10-25 keV range with a maximum flux at 18 keV. The beamline also has multilayer optics available to sharpen the pink spectrum to a 2 %

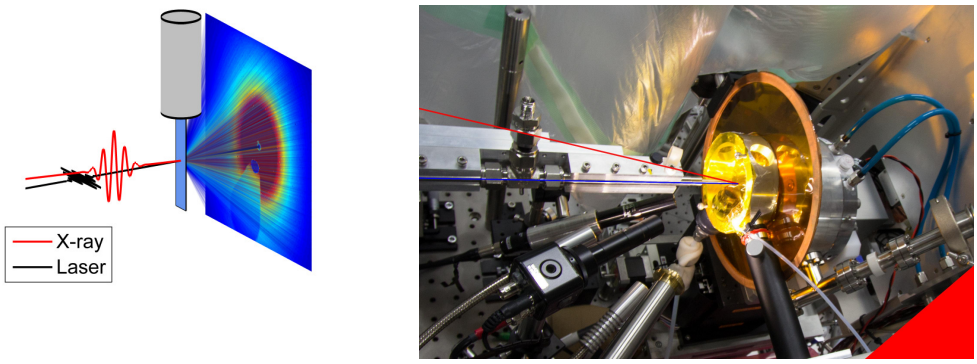

(a) TR-XDS Schematic (b) TR-XDS photograph

Figure 4.4: The TR-XDS setup at ID09b, the laser(red) and X-ray(blue) has been added to the photograph.

Bandwidth peak, however the increased flux of the pink spectrum is usually the better choice for difficult TR-XDS measurements.

The Ti-Saphire amplified laser produces $100fs$ 780nm pulses, that can be frequency tripled to the intense 250μJ 260nm pulses used for this experiment. The relatively slow repetition rate and time-resolution of the beamline makes it possible to use a pulse stretcher to create 1.2 ps optical excitation pulses. This has the huge advantage of providing much more gentle excitation conditions for the sample. The long pulses maintain the high excitation fractions, but increase the threshold for unwanted multi-photon effects as recently seen in [**VII**] and [**XIV**]. The X-rays are collimated and cleaned-up in a flight tube protruding to the upstream kapton window, and the direct beam is stopped on a small magnetic beamstop placed on the downstream kapton window. The Quasi-collinear setup allows the laser to enter the sample chamber at a slight angle to the X-ray beam and is similarly stopped by a beamstop to prevent burning holes in the detector.

The scattered X-ray images are collected on a Fast REadout Low Noise (FRELON) 2D CCD detector consisting of 2048x2048 52μm pixels. The detector is placed 45 mm downstream from the sample interaction point in order to achieve a Q-range of $0.3 - 9$ Å^{-1}. Due to the slow readout of CCD detectors, pulses are integrated until the brightest pixels are $\frac{3}{4}$ saturated, which usually corresponds to 1-10 seconds of exposure depending on sample and experimental conditions. Consecutive images are taken with varying pump-probe delay and with inter-spaced negative delays for reference subtraction, when generating difference scattering images. Having inter-spaced reference images account for drifts and changes on the longer time-scales, and random fluctuations average out during integration or when averaging many exposures. Due to the weak nature of the scattering interaction and the small fraction of the sample consisting of the solute molecule, many exposures are needed to extract a good difference scattering signal. The data presented here consists of 100 Images/time-delay of each 3000 pump-probe events with a similar number of reference images.

After a week of beamtime $\frac{1}{2}$Tb of data has been collected and can be reduced into a series of difference scattering curves that can be analysed.

4.5 Data Workflow

The established worklow for TR-XDS reduction and analysis is presented in [3, 4, 31] and is devided into steps shown in figure 4.5. The small images visualise the output of the corresponding step

Prior to the analysis the measured data needs to be reduced; extracting the information content in a controlled manner with a well defined basis for analysis. In this case the reduction conserves the structural information by transforming multiple 2D images into 1D difference scattering curves, that can be directly compared with model spectra and/or simulated scattering.

For each sample a number of scans are conducted. A scan consists of a number of images taken at different X-ray/laser delays. This series of delays is repeated a large number of times, in order to gain the statistics necessary to extract the small difference scattering signals on a noisy background. A scan series usually consist of a number of time delays of interest, as well as a reference with negative delay. The negative delay corresponds to no laser on the sample and therefore measures the steady state scattering. The reference images are used for subtraction, in order to extract the difference signal. In addition to time-delays of interest, a short (100ps) and long ($1\mu s$) delay are often included, to track the energy deposition in the solvent as mentioned in chapter 3.4 and [**III**].

Each scan is processed in the following fashion.

Raw Images

The raw .edf image files are read out and reduced one at a time, since all the 2D images take up a lot of space. For commercial detectors the detector image has been corrected for dark current and a flatfield correction has been applied. This is the case for the FRELON detector where both the corrected .edf and uncorrected .ccdraw images are supplied to the user.

Mask and correct

Initially a single image is loaded. The mask is constructed manually or identified with a threshold to remove the beamstops, as well as shadows from the beamstops, nozzle, catcher and other untrustworthy regions on the detector. From the example image the beamcentre is located and the detector distance is determined from the nominal motor position and corrected based on the location of the liquid peak position. The peak position is compared to reference solvent measurements from [**III**] to determine the actual sample-detector distance. With the beamcentre, detector layout, detector distance and known pixel-sizes the coordinates and corresponding angles can be calculated. Based on the coordinates, corrections are generated for each pixel as described in chapter 3.1 and shown in figure 4.6.

The masks and corrections are then applied to each image as it is loaded.

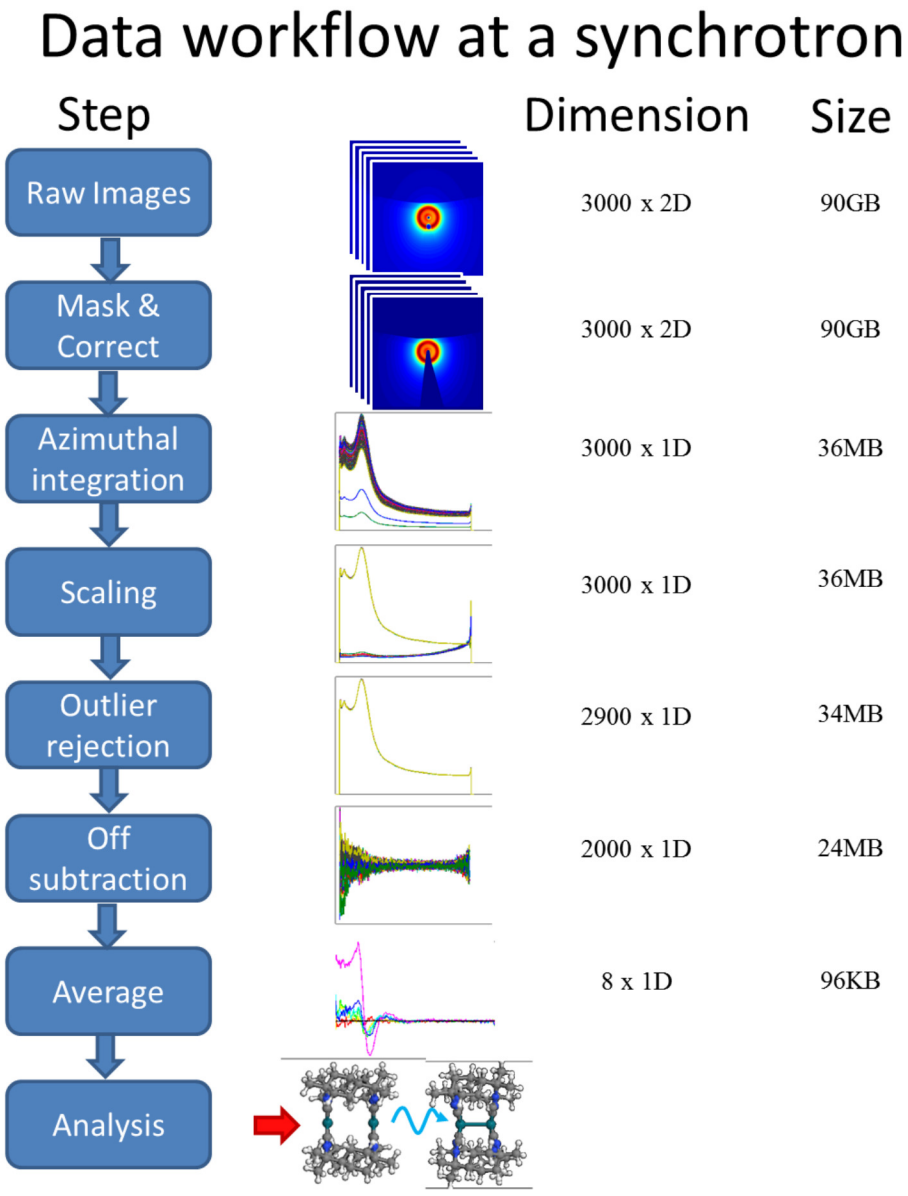

Figure 4.5: General workflow for XDS experiments at a synchrotron for beamline ID09 at ESRF

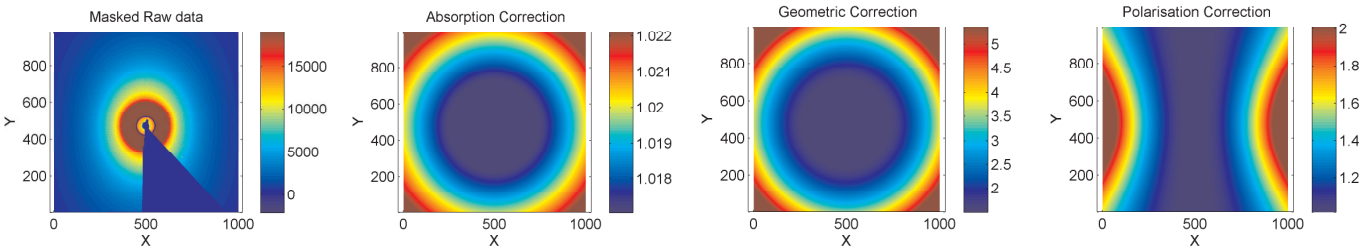

(a) Mask (b) Absorption (c) Geometry (d) Polarisation

Figure 4.6: Mask and detector corrections (a) Mask of beamstops and shadows (b) Correction for the absorption of the scattered intensity through the liquid sheet (c) Correction for the solid angle coverage of each pixel (d) Correction for the polarisation of the X-ray beam preferentially scattering perpendicular to the X-ray polarisation.

Azimuthal integration

The corrected scattering image is azimuthally isotropic and can be reduced to a 1D scattering curve. This process is referred to as either azimuthal- or radial-integration (see figure 4.7). The azimuthal integration is the data reduction step that allows us to load entire scans into memory and treat them simultaneously.

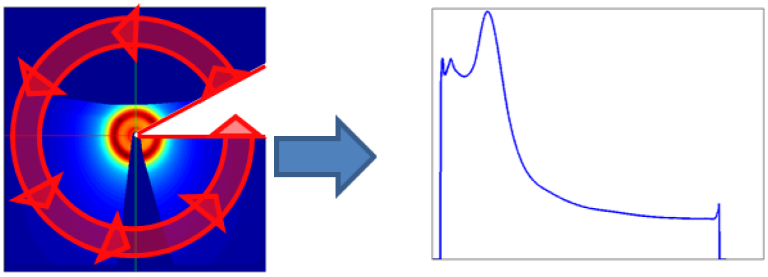

Figure 4.7: Azimuthal/Radial Integration, averaging the radially isotropic scattering signal in angular bins along the normal of the X-ray direction as descried in chapter 3.3.

Scaling

The difference curves will be affected by the fluctuations of the total intensity, as well as liquid sheet thickness and solute concentration. The intensity is somewhat stable but is constantly decreasing between top-ups. To account for all these effects the 1D scattering curves are scaled at high angles, where the structural changes have the smallest effect and the ineleastic Compton scattering dominates.

Outlier rejection

Outliers need to be identified and removed, since a single blank image will result in a difference signal 100 times stronger than the difference signal under investigation. Often the first images contain artefacts and are therefore always removed to begin with. Additional outliers can be identified by statistically comparing the entire set of scattering curves for synchrotron experiments. A rejection scheme such as the Chauvenet criterion is used to identify the significant outliers such that they can be removed before analysis [57].

Off subtraction

The X-ray difference scattering curves are constructed by subtracting the average of the neighbouring reference images. The two nearest neighbours are usually used in order to minimise effects of long term drifts/changes. In this way linear drifts or fluctuations taking longer than the time between two references are compensated for directly in the data reduction process. At 3s integration, 5 time-delays and readout time, this results in 30 seconds between references.

The subtraction is done as follows:

$$\Delta S = S_{On} - \frac{1}{2} \cdot (S_{Off-before} + S_{Off-after}) \tag{4.1}$$

Average

After subtracting off-curves, the dataset consists of a large number of 1D difference scattering curves. Averaging these curves at a given time-delay averages out the noise and other stochastic fluctuations. The result is the average difference scattering curves used for analysis (see figure 4.8). It relies on the many repetitions to increase the signal-to-noise ratio until the difference scattering signal is clearly distinguishable. Each averaged difference scattering curve contains information regarding the structural changes in the investigated sample after a laser pumping event at a given time-delay. Additionally, the data has been reduced by many orders of magnitude conserving the structural information.

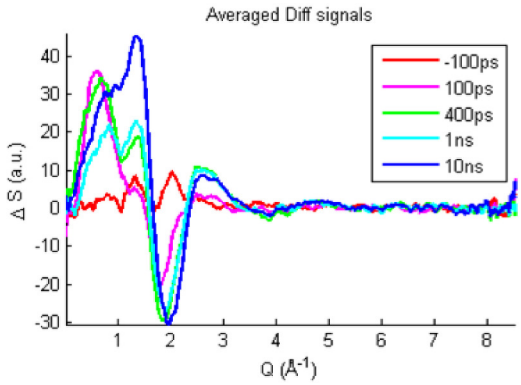

Figure 4.8: Average difference scattering curves for $Rh_2(dimen)_4^{2+}$ in acetonitrile

The averaged curves are usually produced during TR-XDS beamtimes in order to confirm apatio-temporal overlap based on the known solvent difference scattering signals at early and late times [**III**]. Additionally, simple quantitative analysis can be done based on experience, simulations, references or on the presence of a low Q peak/dip corresponding to a contraction or expansion of the solute.

Analysis

The averaged difference curves now require a model description in order to fit a model response to the measured difference scattering data.

The following model is used to fit the difference scattering signals measured from $Rh_2(dimen)_4^{2+}$:

$$\Delta S = \Delta S_{Solvent} + \Delta S_{Solute} + \Delta S_{Solvent-Solute} \tag{4.2}$$

where

$$\Delta S_{Solvent} = \Delta T \cdot \frac{\partial S}{\partial T}|_{\rho} + \Delta\rho \cdot \frac{\partial S}{\partial \rho}|_{T} \tag{4.3}$$

$$\Delta S_{Solute} = \alpha \cdot (S_{Excited-State} - S_{Ground-State}) \tag{4.4}$$

where the magnitude of $\Delta S_{Solvent}$ depends on the amount of deposited heat and α is the excitation fraction. Each of the solute scattering contributions are here parametrised as a function of the Rh-Rh separation (d) in either the ground-state (GS) or exited-state(ES).

Since $Rh_2(dimen)_4^{2+*}$ is short-lived ($\tau_P = 590$ps [43]) the measured data is taken before the solvent density change $\Delta\rho$ sets in (see chapter 3.4) and therefore $\Delta\rho \cdot \frac{\partial S}{\partial \rho}|_T$ can be neglected. Additionally we believe the solvent-solute cross-term to be small and set $\Delta S_{Solvent-Solute} = 0$.

The resulting model is then reduced to:

$$\Delta S = \alpha \cdot (S_{ES}(d_{ES}) - S_{GS}(d_{GS})) + \Delta T \cdot \frac{\partial S}{\partial T}|_{\rho} \tag{4.5}$$

The model in equation 4.5 relies on a solvent heating reference, as well as solute scattering calculated from different molecular structures. The different model structures are constructed using DFT (see chapter 4.2) and the corresponding scattering is calculated using the parametrised atomic form-factors along with the Debye equation (see chapter 2.4). The difference scattering curves corresponding to the model are shown in figure 4.9.

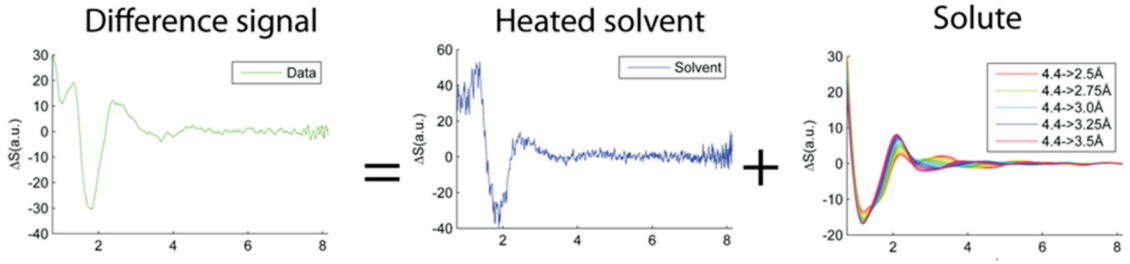

Figure 4.9: The difference scattering curves corresponding to the used model.

Given the model for the measured difference scattering it is possible to evaluate fits in a minimum χ^2 likelihood framework [31]:

$$Ł(P_1, ..., P_M) \propto exp(-\chi^2) \tag{4.6}$$

$$\chi^2(d_{GS}, d_{ES}, \alpha, \Delta T) = \sum_Q \frac{(S_{fit}(Q) - S_{exp}(Q))^2}{2\sigma(Q)^2} / (N - M - 1) \tag{4.7}$$

where $\sigma(Q)$ is the standard deviation at each Q point, N is the number of data points and M is the number of parameters in the fit. The result is a M dimensional

likelihood matrix that can be projected onto a chosen set of parameters and normalised to give the relative likelihood along the evaluated values. Likelihood fitting only evaluates the given parameter space, so a representative model is needed for the results to make sense.

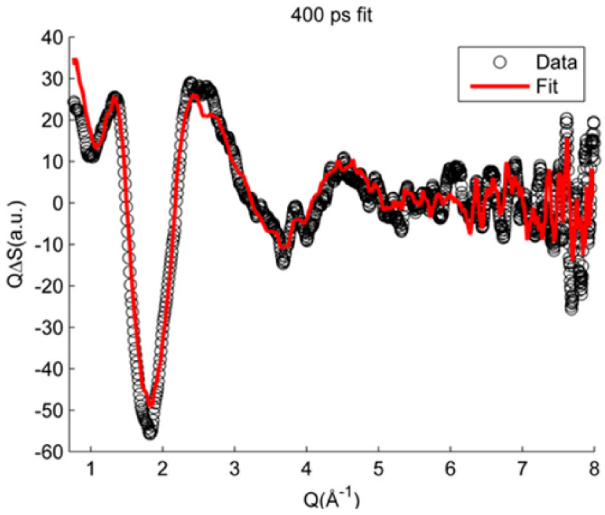

Figure 4.10: The best fit corresponding to the 400ps timedelay

Determined values from the final fits of the $Rh_2(dimen)_4^{2+}$TRXS data				
Delay	GS Rh-Rh(d_{GS})(Å)	ES Rh-Rh(d_{ES})(Å)	Exc. frac. (α)(%)	Solv. scaler (β)(a.u.)
$100ps$	4.45(±0.35)	2.85(±0.31)	0.6(±0.19)	0.35(±0.08)
$400ps$	4.20(±0.28)	2.95(±0.13)	1.0(±0.22)	0.70(±0.09)
$1000ps$	4.29(±0.28)	3.00(±0.18)	0.7(±0.24)	0.75(±0.09)

Table 4.1: The parameters from the likelihood distributions shown in figure 4.12

4.6 Results

The data is fitted for each time-delay independently based on the model, and using a 10 ns delay as $\Delta_{solvent}$. The model $Rh_2(dimen)_4^{2+}$structures were based on the calculated DFT structures. The best fit for the 400ps difference scattering curve is shown in figure 4.10 and the 400ps likelihood distribution for the GS and ES Rh-Rh seperation is shown in figure 4.11, where the 2D projection shows no correlation between the 2 parameters.

Due to a very low excitation fraction the measured difference signal is significantly weaker than the signal measured for $Ir_2(dimen)_4^{2+}$in [**I**]. However the fits identify structures similar to the DFT calculations, showing a ground-state distance between 4-4.5Å and an excited-state seperation of 2.85-3Å, with a 0.5 % excitation fraction. All the resulting likelihood distributions are shown in figure 4.12 and table 4.1 holds all the resulting parameters.

From the result of the data fits, it seems that the signal strength in the 100ps difference scattering curve is the lowest. This could very well correspond to a slightly offset time-zero where only part of the 100ps wide X-ray pulse probes after the pumping event. Appart from the slightly wider distribution at 100ps delay, the fits are in good agreement and correspond to the long contraction of around 1.5Å measured for $Ir_2(dimen)_4^{2+}$in [**I**].

4.7 Conclusion

$Rh_2(dimen)_4^{2+}$was succesfully studied at the ID09b beamline at ESRF, returning structures in agreement with DFT results in the early time-delays 100ps, 400ps

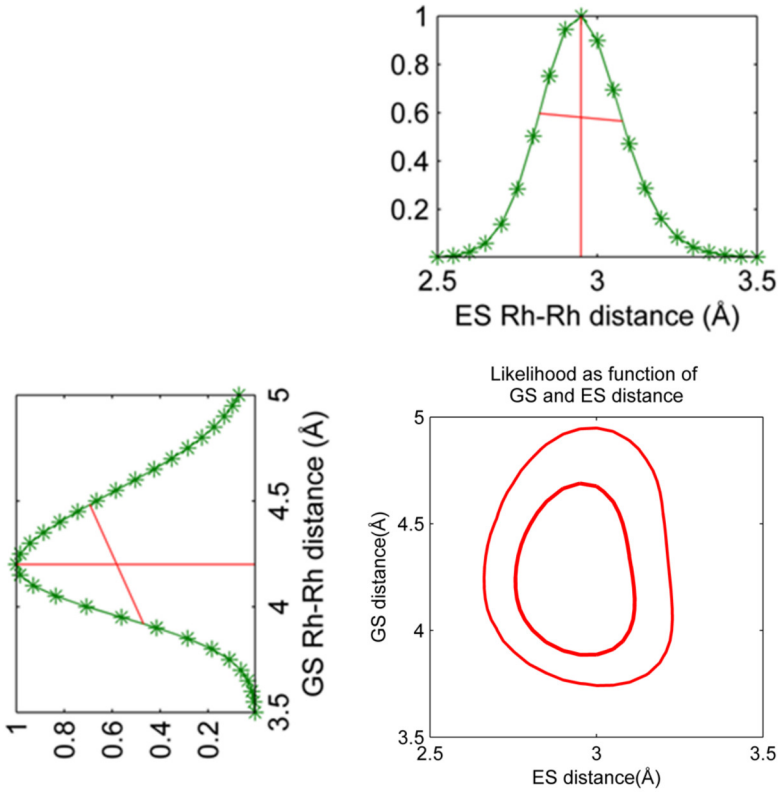

Figure 4.11: The 2D likelihood of the GS vs. ES distribution and their 1D single parameter likelihood projections.

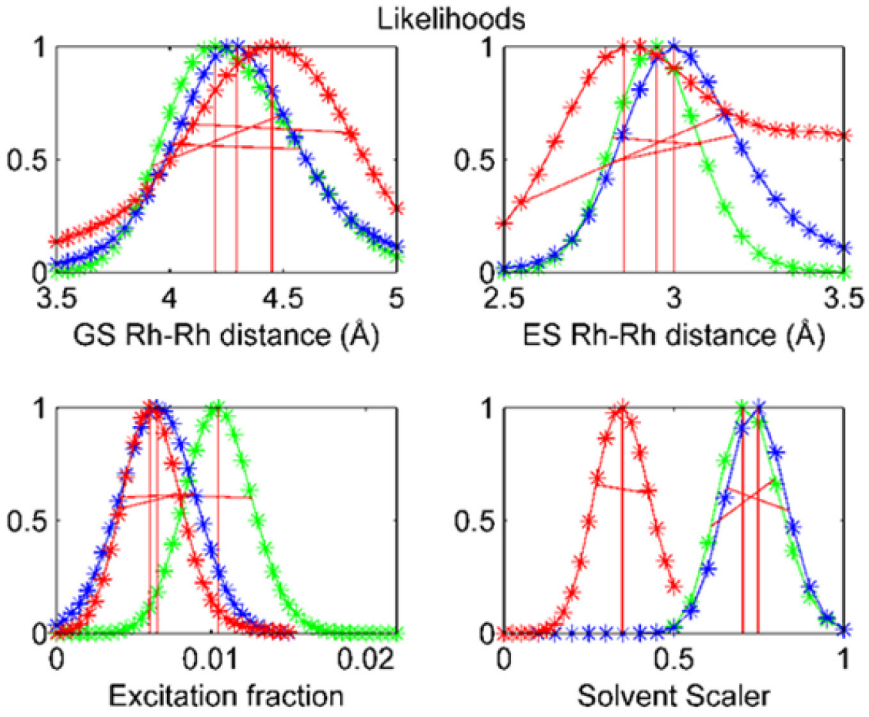

Figure 4.12: The likelihood distributions resulting from the fits, projected on to the individual parameters.

and 1ns corresponding to the triplet lifetime of 590ps observed with transient absorption[43]. However, the excitation fraction is very low compared to other d8-d8 metals with similar absorption [26] and [**I**]. The low excitation might be due to choice of 266nm excitation wavelength or excited-state absorption, exciting a uncharacterised transition instead of directly exciting the desired $d\sigma* \rightarrow p\sigma$ transition at 400-500nm. The proof-of-concept measurements were conducted at the 266nm harmonic to increase the laser output and further attempts to measure $Rh_2(dimen)_4^{2+}$at different excitation wavelengths failed.

Even though the scattering signal from $Ir_2(dimen)_4^{2+}$is more complex due to the presence of multiple ground-state structures, it was the preferred candidate for XFEL studies due to the larger scattering signal from Ir, larger excitation fraction and separation of optical spectral features (see chapter 6).

Chapter 5

XFEL experiments - introduction

This chapter introduces some of the most important aspects by which a time resolved XFEL experiment differs from a synchrotron experiment. Particular focus is given to the differences in X-ray pulse characteristics, and the adaptations of both data treatment and data analysis needed to account for this. Furthermore the available single-shot X-ray diagnostics is described, with the XPP beamline at LCLS being used for specific examples.

For TR-XDS measurements the main advantage of the XFEL source over synchrotron facilities is the increased flux and decreased pulse length (illustrated in table 2.1). The shorter X-ray pulses allow a much better time-resolution and the increased flux provides the necessary statistics faster, resulting in shorter acquisition times. Given similar experimental conditions the increased flux at an XFEL should decrease the necessary acquisition time by several orders of magnitude. However, the Self-Amplified Spontaneous Emission (SASE) process underlying the X-ray amplification at XFEL sources is an inherently stochastic process [58], meaning that the X-ray pulses produced at XFELs have a much larger pule-to-pulse variation. Thus, in an experimental approach where the signal from many X-ray pulses are averaged, the data quality suffers from this variation. For this reason, XFEL beamlines are set up for single pulse measurements such that the parameters (intensity, timing etc.) is read out for every X-ray pulse, together with the actual XDS detector images. This additional information allows for correction and scaling or filtering of the data from each single X-ray pulse of the experiment, reducing the negative impact of the intrinsic pulse-to-pulse fluctuations. Furthermore, the pulse-to-pulse nature of the experiments allows X-ray pulses and laser pulses to fire at different frequencies, making reference data available interleaved with the actual measurements(see section 5.5.3).

A complication with regards to XFEL experiments is the reduced availability of beamtime. Currently, two hard X-ray XFEL facilities exist in the world, which are designed to serve a single end-station at a time. Even though it is now possible to split the beam and conduct two simultaneous experiments at LCLS [**XII**][**XIII**], the available beamtime at XFEL sources is very limitied. In contrast to this, a synchrotron can service 30 beamlines simultaneously. Since the construction and operation expenses of a synchrotron and an XFEL are comparable, the price for one hour of beamtime at XFEL sources is significantly higher.

5.1 Time-resolution

The time-resolution at synchrotrons is limited by the X-ray pulse-length as it is much larger than the remaining time factors. At LCLS the X-ray pulses are 30fs but the time-jitter is on the order of 500fs [59]. Without correcting for the jitter in the arrival time of the X-ray pulses, this is the limiting factor in the resulting Machine Response Function (MRF). The MRF is the Full Width at Half Maximum (FWHM) of the convolution of all contributing factors to the time resolution and defines the global time-resolution of the experiment.

The timing jitter is a huge problem for XFEL experiments, preventing measurements from reaching the critical time-resolution to study the dynamics of interest [60],[**VII**] [**IV**]. The implementation of a timing tool monitors this jitter and makes it possible to correct for it (see chapter5.6).

At the XPP beamline the optical laser pulse is 70fs, the X-ray pulse is 30fs and the implemented timing tool has an accuracy of 15fs FWHM. This entails that without a timing tool correction the MRF is 500fs FWHM as opposed to the 110fs FWHM with the Timing Tool.

For TR-XDS measured through a liquid sheet the group velocity mismatch caused by the difference in speed of the optical and X-ray pulses through a 100μm liquid results in additional 150fs smearing. Therefore it is possible to reduce the effective MRF by using a thinner liquid sheet, as this is the largest contributor to the MRF after correcting for the timing jitter.

Identifying all the contributors to the MRF brings us to a current time-resolution of 160fs. It might be possible to increase the time-resolution to around 50 fs FWHM by tweeking all available parameters, but going much below 50fs would become increasingly difficult due to the origin of the limiting factors.

5.2 Difference scattering signal on the femtosecond timescale

As described in Chapter 3.3, the difference scattering signal can be regarded as comprising three terms:

$$\Delta S = \Delta S_{solvent} + \Delta S_{solute} + \Delta S_{solvent-solute} \tag{3.12}$$

On synchrotron time-scales the description of the difference scattering arising from changes in the hydrodynamic parameters of the bulk solvent $\Delta S_{solvent}$ is well understood ([32] [**III**]). However, the treatment of the hydrodynamic assumes a homogeneous temperature distribution within the sample volume. This sample-wide temperature homogeneity sets in on the 15-150 ps time-scale (depending on experimental conditions [**III**]), and the treatment of the solvent differential described in the previous chapter is thus not valid on the few- and sub picosecond time-scale. There is currently no established theoretical framework for treating the solvent response on the ultra-fast time-scales, and for this reason a lot of work was put into designing experiments that would allow for tracking of $\Delta S_{solvent}$ on the sub ps time-scale. During this work, the solvent response has been investigated on the ultra-fast time scale, using both direct excitation of intra-molecular vibrations through Near-Infrared (NIR) excitation, as well as excitation

of chromophores synthesized for ultra-short life-time and low structural response. While the analysis is still ongoing it can be noted for this work, that all measured ultra-fast solvent responses can be described by the two solvent differentials $\frac{ds}{dt}$ and $\frac{ds}{d\rho}$ exactly as on later time-scales ([32] [**III**]).

The situation is more complex for the remaining two terms of the difference scattering signal (ΔS_{solute} and $\Delta S_{solvent-solute}$). At synchrotrons the 100 ps time resolution of TR-XDS experiments usually only allows for investigation of well-defined vibrationally cooled excited state species. Thereby, the scattering from the solute ΔS_{solute} can usually be modelled by a finite number of structures (often just a single ground state and a single excited state structure). The solute-solvent cross term, $\Delta S_{solvent-solute}$, can then be modelled from MD simulations of the solvent packing around these two structures alone [**I**][**II**]. Since the time resolution of the XFEL experiment is comparable to that of the structural dynamics of the molecules as they propagate on the excited state potentials surfaces, it is necessary to be able to model both molecular structure and solvation dynamics under these conditions during structural dynamics and very far from equilibrium. While a systematic approach has not yet been established for these simulations, the experiment presented here, along with the current work within a Quantum Mechanics/Molecular Mechanics (QM/MM) framework seems to offer a very good starting point [**V**].

5.3 Anisotropy

At short timescales after an excitation event, the ensemble of excited molecules will have an anisotropic rotational distribution due to the preferential excitation of molecules with transition dipole moment parallel to the polarisation of the optical laser[7]. This preferential alignment of the excited state molecules means that the scattering signal is no longer be independent of azimuthal angle. This means that the usual assumption that the distribution of molecules is orientationally averaged is no longer valid, and thus that the scattering no longer adhere to the Debye formula.

This effect has been shown in studies of proteins on synchroton timescales having rotational diffusion lifetimes in the nanosecond regime [61]. Anisotropic scattering signals have hitherto not been observed for small molecules in solution due to their rotational lifetimes typically being in the tens of picosecond regime.

The framework necessary for treating anisotropic difference scattering signals of small molecules in solution was established by U. Lorenz and co-workers [62, 63]. Lorenz and co-workers showed that for many small molecules the scattering can be described in terms of the zeroth and second order spherical Bessel functions. They also showed that errors are introduced in the data analysis if the presence of anisotropy is not accounted for.

As described by U. Lorenz et al. the anisotropic 2D scattering image can be separated in a S_0 and S_2 component using:

$$\Delta S(Q,\tau) = S_0(Q,\tau) - P_2(cos\theta)S_2(Q,\tau) \tag{5.1}$$

$$P_2 = \frac{1}{2}(3x^2 - 1) \quad \text{ranging from -0.5 to 1} \tag{5.2}$$

Where S_0 and S_2 are the isoptropic and anisotropic contributions respectively and P_2 is the second order Legendre polynomial. S_0 is the isotropic part of the scattering and is equal to the Debye equation and S_2 accounts for the anisotropy. When anisotropy is present on the detector S_2 is non-zero and needs to be taken into account, the magnitude of the effect however, is usually small and the radially integrated images can in many cases be treated as normal with a small error depending on the system [62]. At times significantly later than the rotational lifetime of the excited molecules, the anisotropy has disappeared and only radially symmetric scattering signal described by the Debye formula will be left.

Hence, the rotational lifetime of the excited species can be readily extracted from the magnitude of the anisotropy in the data. Furthermore, since the interatomic distances of the S_2 component are weighted with their orientation along the laser polarization axis, changes in bond-distances along the laser polarization will be significantly enhanced. This means that careful consideration has to be given to the direction of the transition dipole excited by the laser, such that transition dipoles parallel with the bond distance of interest are chosen for the excitation. If there are multiple molecular bond distances of interest, multiple excitations with perpendicular transition dipoles should be chosen. Furthermore, experiments on molecules with distinct transition dipole moments parallel with the bond distance of interest should be conducted with laser and X-ray polarisations perpendicular, since the excited molecules will be parallel to the laser polarisation and the scattering power is strongest perpendicular to the X-ray polarisation.

5.4 Singular Value Decomposition - SVD

A powerful tool in matrix analysis is Singular Value Decomposition (SVD)[64, 65]. SVD seperates a given MxN dataset into U and V^T, a MxM an NxN matrix with colums containing left and right singular vectors respectively. The diagonal of Matrix S contains singular values in decreasing order.

$$[Data] = USV^T \tag{5.3}$$

For a matrix containing data with dimension MxN with measured vectors along M and steps along N, SVD seperates Data of Rank N into N independent components, U_{1-N}, the singular value $S_{i,i}$ and the amplitude in the right singular vectors V_{1-N}.

For a data set containing a noisy signal, the SVD returns the significant vectors in decreasing order with signal vectors first and noise vectors after as individual left singular vectors.

The rank of the underlying signal in a data set can be chosen by selecting a suitable cut-off based on the singular values $S_{i,i}$, that seperates the significant components from noise. In this fashion a large dataset can be reduced to a few significant components. It is noted that SVD does not identify physical components but merely separates vectors based on orthogonality.

Given large datasets SVD can be quite computationally heavy, for this reason partial algorithms are often used to only compute the first N singular vectors.

In a low rank dataset consisting of a few basis vectors, this greatly reduces the problem without loosing any information.

5.5 Beam diagnostics

Many additional diagnostics are present and supply beam characteristics on a shot-to-shot basis. All the measured diagnostics are saved together with the data and many are useful when analysing the results. However, more than 300 different values can be read out for each shot; basically every motor, detector and beam characteristic from the electron-gun to the beam-dump can be found here. With no overview of the saved parameters, what they contain or which of the final X-ray characteristics they correlate with requires some degree of understanding, discussion with LCLS employees or simply trial and error.

The many saved variables contain X-ray intensity and energy diagnostics along the accelerator path, as well as temperature measurements from outside and virtual motor positions.

The "save everything" approach is however valuable when you realise that you are missing a vital piece of information during the following analysis or if one of the used detectors proves unreliable.

The following values have been evaluated for the analysis in chapter 6 and are read out from a single scan from the experiment. The values correspond to a typical TR-XDS measurement on molecules in solution at XPP utilising 9.5 KeV X-rays at maximum flux with non-monochromatised XFEL beam.

5.5.1 X-ray intensity

There are 3 available Intensity Position Monitors(IPM) at XPP, each consisting of four diodes monitoring the X-ray back-scattering from a thin target, measured at three different locations along the beam-path; IPM3 placed closest to the sample. Each diode is read out separately, supplying information regarding the position of the beam in addition to the sum of the diodes monitoring the integrated beam intensity.

As seen in figure 5.1, the intensity has some time dependent drifts as well as a wide distribution of intensities. Additionally the temporal auto-correlation function (ACF) of the intensity shows the autocorrelation approaching 0 after 1 cycle.

As seen in figure 5.2 (a) the intensity measured by the IPM3 has a rather wide distribution when correlated with the intensity on the CSPAD area detector. The width of the distribution is attributed to both the inaccuracy of the IPMs and to fluctuations of the liquid sheet thickness, as the liquid sheet is located after IPM3 and before the CSPAD. However, this does not explain the non linearity of the correlation. But for the purpose of analysing the TR-XDS data the intensity on the CSPAD is used, as it seems to be the most reliable intensity detector. As seen from figure 5.2 (b) the IPMs also have a wide distribution making them poor intensity monitors. For future experiments a total fluorescence diode is mounted, as it monitors the intensity while taking the liquid sheet thickness into account.

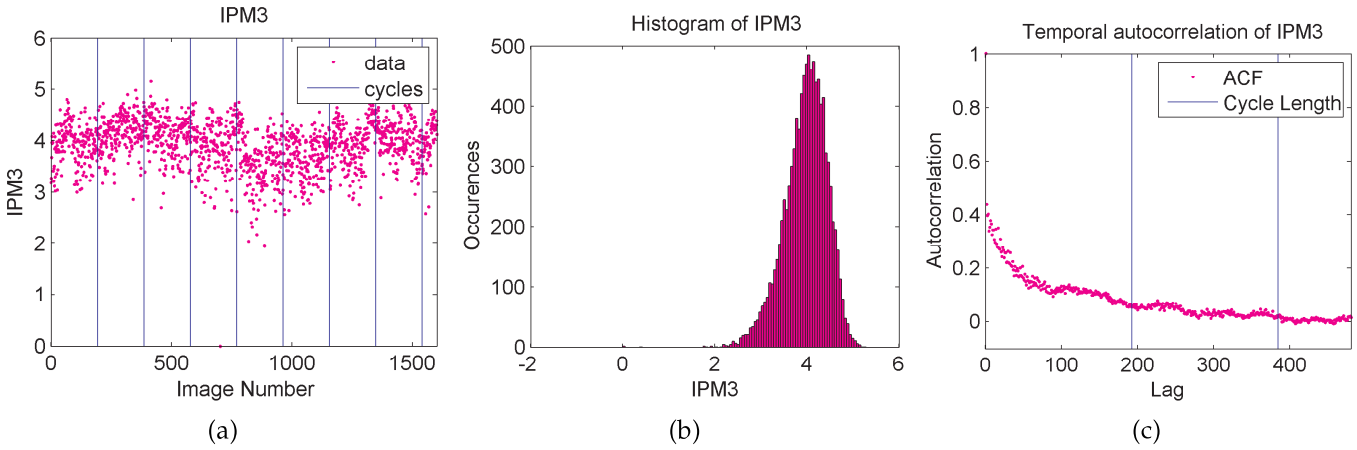

Figure 5.1: The IPM3 value measures the X-ray intensity (a)IPM3 over time (b) A histogram of IPM3 (c) The temporal autocorrelation of IPM3.

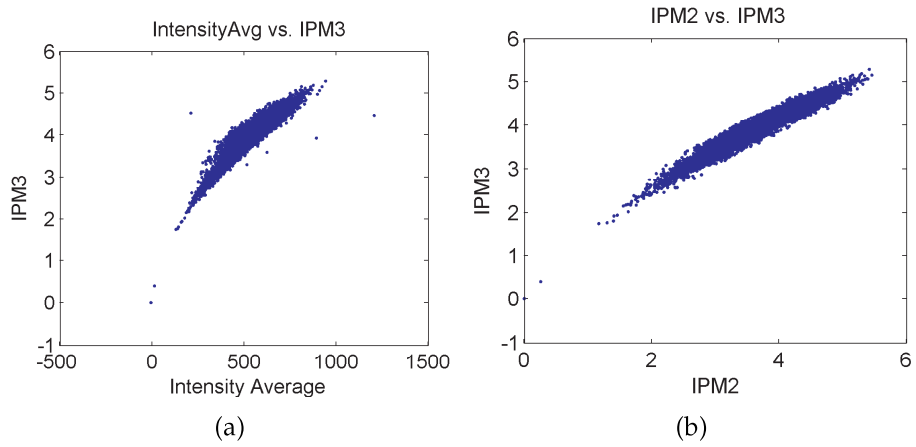

Figure 5.2: (a)Average Intensity on the CSPAD vs. IPM3 (b) IPM2 vs. IPM3.

5.5.2 X-ray energy

Due to the large fluctuations in X-ray energy, shot-to-shot information with an accurate X-ray energy reading is critical. Detection schemes are currently being developed for determining the energy or spectrum on a shot-to-shot basis [66]. Currently, no X-ray energy monitor is implemented, but at XPP the charge of the electron beam has been identified to correlate with the incoming X-ray energy.

The measured electron beam charge (Ebeam) is here shown to have a normal distribution (see figure 5.3(b)) and that the autocorrelation of the measured Ebeam is zero after approximately 100 shots.

Similarly to the IPM's the values are plotted in figure 5.3. The fluctuations over time seem to be slightly less systematic which can also be seen on the ACF.Furthermore the energy distribution is more symmetric.

The exact energy as a function of Ebeam value can be calibrated as shown in figure 5.4 where a scan is divided in Ebeam intervals, averaged and radially integrated. Plotting the peak location as a function of Ebeam returns Q scaling between each Ebeam bin and can be converted into an X-ray energy. Based on

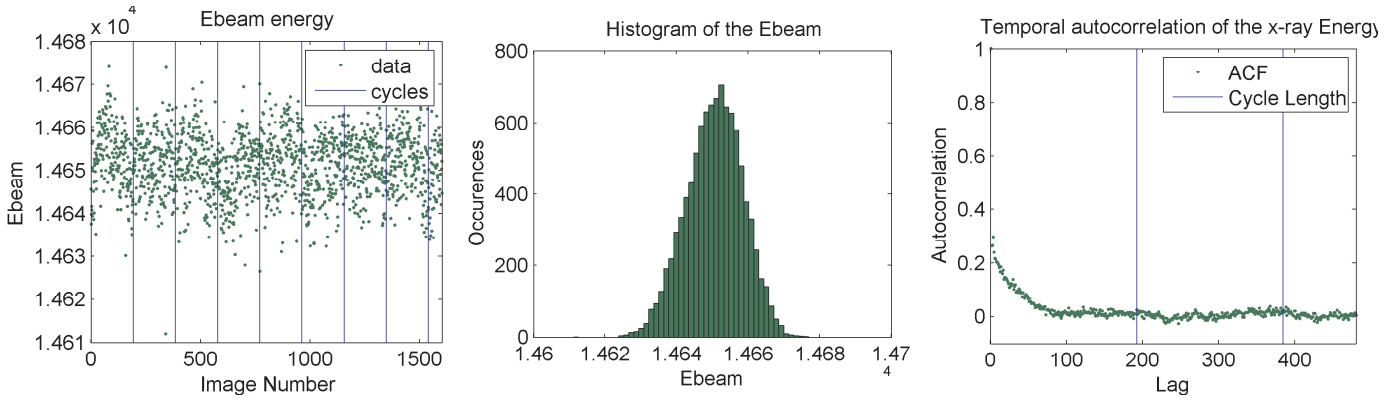

(a) (b) (c)

Figure 5.3: Electron beam charge (Ebeam) measured on the electron beam which correlates well with the resulting X-ray energy (a)Ebeam over time (b) A histogram of the Ebeam (c) The temporal autocorrelation of the Ebeam

the results of the fit shown in figure 5.4, the Ebeam distribution can now be converted to X-ray energies resulting in 32.7 eV FWHM.

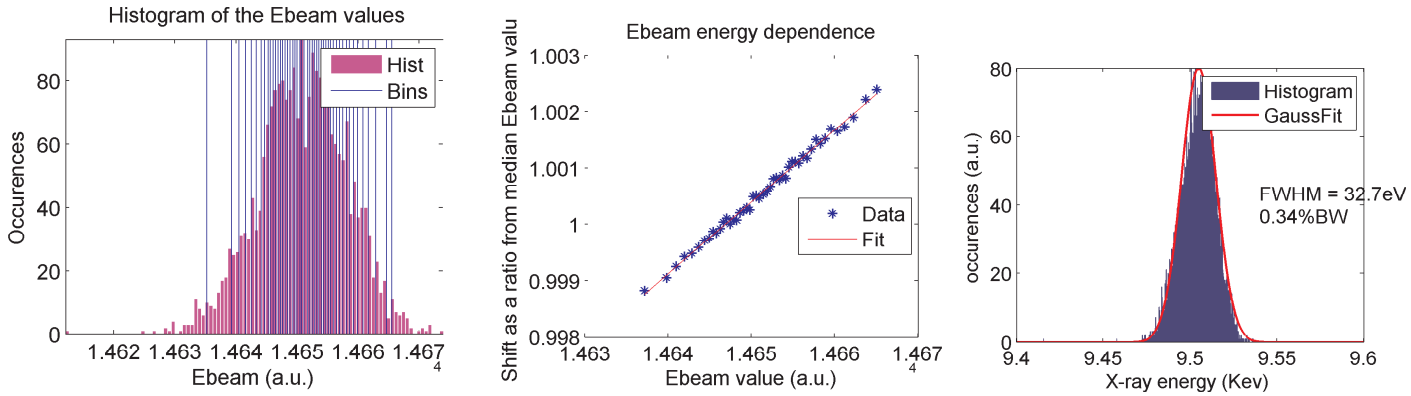

(a) (b)

Figure 5.4: The X-ray energy was callibrated by finding the liquid peak for averaged images at different Ebeam Values. (a) Histogram with bins selected to contain constant number of shots (b) The relative liquid peak position as a function of Ebeam (c) Histogram and fit of the X-ray energy distribution based on the fit in (b).

5.5.3 Event codes

The shot-to-shot based experimental conditions allow for selection of specific X-ray and laser shots and drop them entirely during the experiment. In this experiment the laser was dropped every 4th shot and the X-ray was dropped every 5th. The dropped shots allow us to account for temporal fluctuations in the off-subtraction of the TR-XRD (laser drop shots) analysis and reference subtraction for the Timing Tool (X-ray drop shots, see chapter 5.6). The events where both X-ray and laser are dropped (every 20th) provide running dark measurements read-out at experimental conditions. The dropped shots are noted in event-codes located in the data-stream and the X-ray drop shots can be

correlated with X-ray intensity monitors. However, no shot-to-shot laser intensity was measured so during this experiment we have to rely on the event-codes. As seen in figure 5.5 (a) the continuously read out event codes allows us to

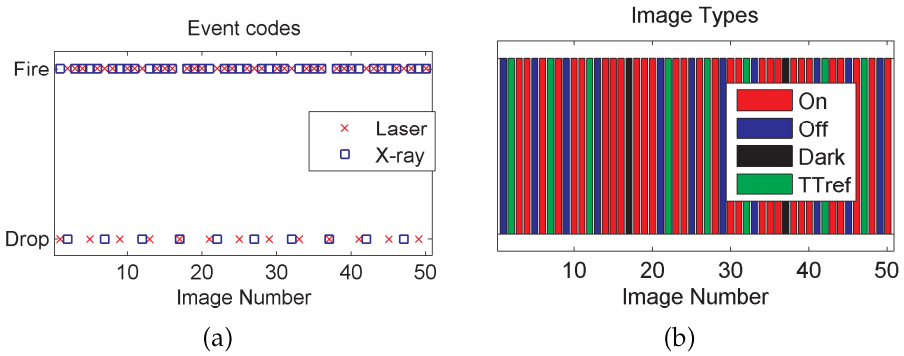

Figure 5.5: The eventcodes monitor the firing of the X-ray and Laser respectively. (a) A plot of the boolean eventcodes (b) The 4 resulting different Image types: "On" images with both laser and X-rays incident, "Off" images with only X-rays, "Dark" images with neither beam incident and the TimeTool refference "TTref" with only X-rays incident.

sort and select single shots based on the experimental conditions as the event codes monitor the firing of the X-ray and Laser respectively. In figure 5.5 (b) the resulting types of images are shown, as these are selected in diffent parts of the analysis for reference or subtraction.

5.6 Timing Tool

The timing jitter at XFELs is a large problem, preventing them from reaching their full potential. By smearing the time resolution with the uncertainty of the time-arrival of 416fs FWHM instead of being limited by the X-ray pulsewidth $\sim$ 10fs [67]. This problem was quickly realised [60][**VII**], and timing methods have been tested by Harmand et al. [67]. The timing tool correlates the arrival time of the X-ray pulse with the laser pulse. Two methods have been tested, both relying on free-carrier generation in a target material as an X-ray pulse passes through and detecting the generated carriers in the optical properties using a laser pulse transmitted or reflected of the Si_3N_4 target [68, 69].

At XPP a Si_3N_4 target is used in a transmission setup where chirped white-light from the pump pulse is used to measure the change in transmission as the X-ray pulses passes through as can be seen in figure 5.6. The timing tool is now implemented as a part of the standard setup and only requires a bit of setup-time to align the target and calibrate the timing tool.

The implemented timing tool produces a spectrally encoded X-ray arrival time on a spectrometer. After filtering and fitting the images the timing tool results in a position used for correction of the arrival time along with the amplitude and FWHM of the fit used for filtering.

At the time of the $Ir_2(dimen)_4^{2+}$experiment the timing tool was newly implemented, but the automatic fitting was not working. Therefore, the spectra needed to be analysed in order to aces the timestamps of the individual pulses.

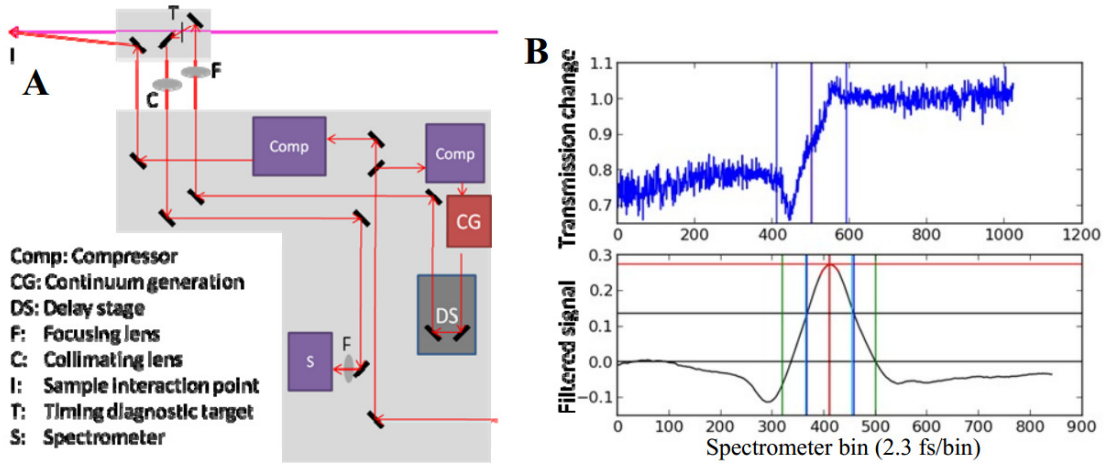

(a) (b)

Figure 5.6: The setup and output of the timing tool monitoring the arrival time of the X-ray pulses (a) A schematic of the setup (b) The transmission of the timing tool and a peak after using a peak finder filter. Figure from Lemke et al. [70]

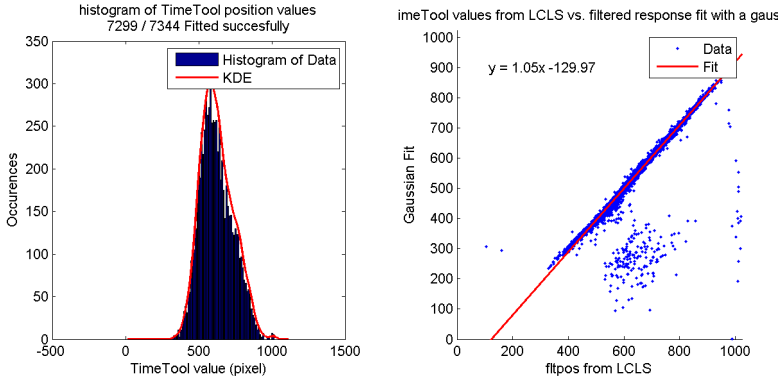

(a) (b)

Figure 5.7: (a) Histogram of the timing tool values from one scan (b)Gaussian peak-finder vs. XPP timing tool code.

The images from the timing tool camera could then be analysed in the following fashion:

A region of interest (ROI) was selected based on a cutt-off just above the background noise. Each image was then subtracted the closest timing tool reference image without X-rays and integrated to produce a single line-shape for each timing tool image.

The individual traces were filtered with an edge filter resulting in a peak at the position of the rising edge. This peak could then be robustly located with a Gaussian fit.

In order to allow further filtering based on the quality of the timing tool signal the peak position, FWHM and amplitude of the fit where saved. The resulting delays for a single scan show a FWHM jitter on the order of 500fs as also reported by [67, 70].

Figure 5.7 (a) shows the resulting filtered position on the timing tool that

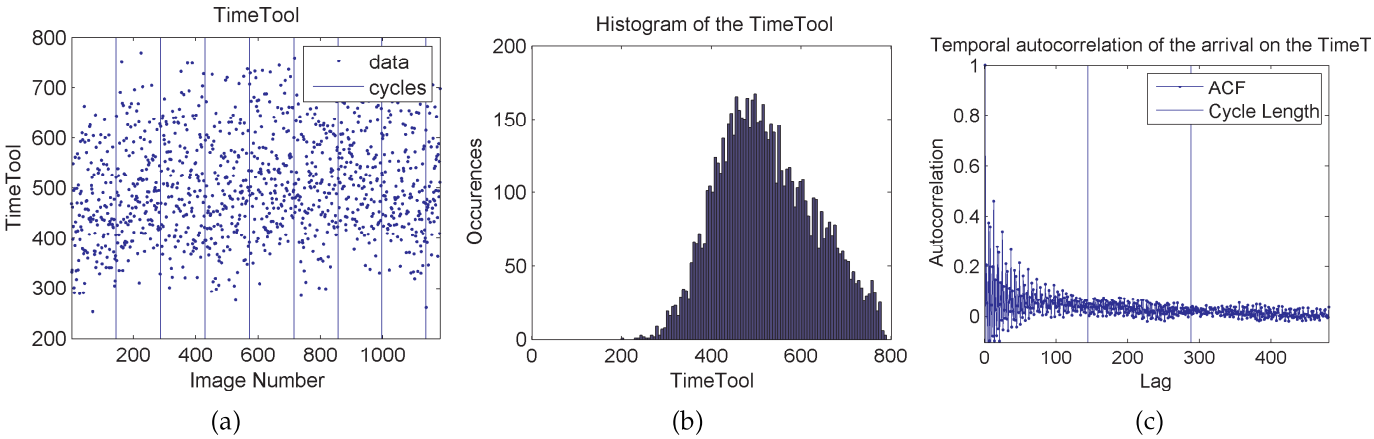

Figure 5.8: The TimeTool monitoring the arival time of the X-ray pulses (a) TimeTool value over time (b) A histogram of the TimeTool (c) The temporal autocorrelation of the TimeTool readout

can be directly translated into an arrival time. The quality of the fit was later compared with values from the XPP software showing good agreement in figure 5.7 (b).

The timing tool is calibrated by moving the nominal time a fixed value and fitting the distribution of timing values. This allows for a linear fit of the centre of the distribution vs. nominal time. For the $Ir_2(dimen)_4^{2+}$experiments at the XFEL the timing tool was calibrated to -3.0804fs per pixel.

Having extracted the timing tool values they can be added to the long list of diagnostics available for each scan and used for filtering and time-sorting the data to achieve the best possible time-resolution.

For determining time-zero (t_0) a diode can be used down to $\sim$ 10ps and fine timing can be redone once the timing tool has been calibrated. For absolute t_0 determination it is necessary to use a prompt signal. For many of the conducted experiments including X-ray spectroscopy a prompt signal is available. Otherwise a timing sample needs to be used. Based on the beautiful oscillations easily measured in bismuth [71] this sample is often used if t_0 needs to be determined or timing verified [70][67].

When the timing tool is used during an experiment the temporal jitter can also be used deliberately to probe a window in time. measuring at exactly 0 delay will probe at least 150 fs in either direction with good statistics. With the timing tool engaged, there is therefore no reason to take smaller delay steps as the data can be binned arbitrarily at a later time. Fewer scan steps results in a higher duty cycle essentially getting more data in a shorter time. It is also possible to loosen the mode-lock of the laser thereby deliberately increasing the jitter to $\sim$ 1ps as many interesting dynamics occur on the very earliest time steps it is possible to map out the first ps by standing at a single delay. In this case the duty cycle is close to 100 % and the jitter randomly probes the entire range minimising systematic fluctuations.

5.6.1 Crude timing - phase cavity

The phase cavity monitors the timing of the beam compared to the RF phase and can also be used to correct the X-ray timing [70].

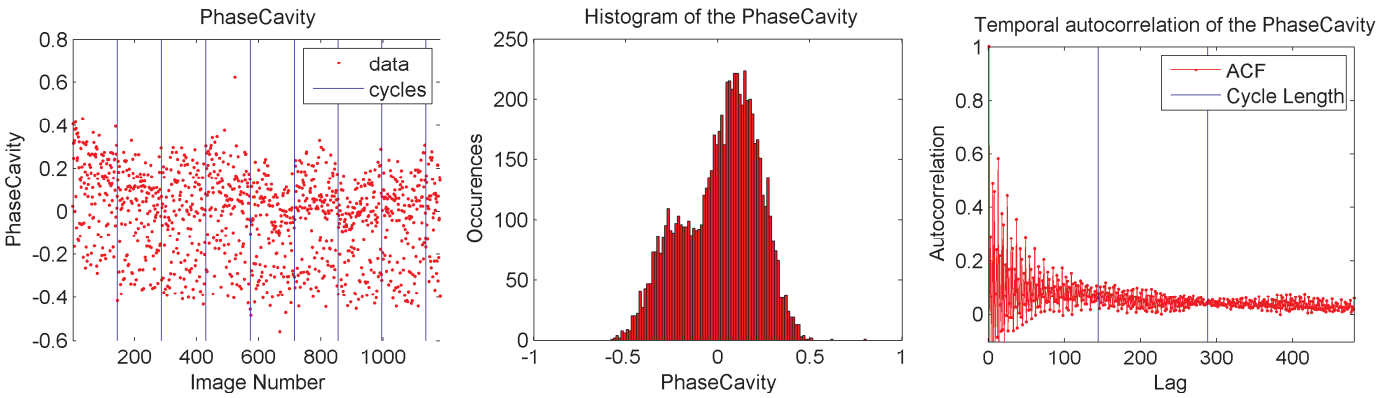

Figure 5.9: The phase cavity measures the difference between the phase of the electron beam and the reference frequency (a) phase cavity over time (b) Histogram of the phase cavity (c) The temporal autocorrelation of the phase cavity.

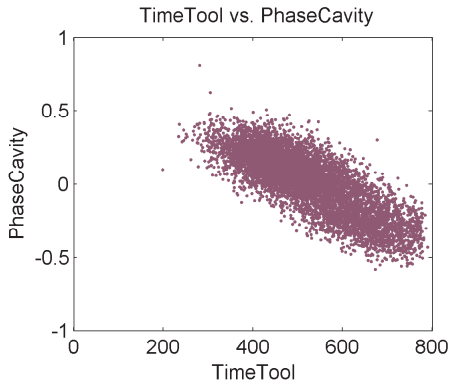

Figure 5.10: The phase cavity plotted against the TimeTool showing a definite correlation fitting the reported 300fs of the phase cavity

Plotting the phase cavity against the timing tool shows a linear correlation, allowing the timing to be determined with $\sim$ 300fs FWHM. This information is redundant in the presence of the timing tool but sometimes it is valuable to have redundancy in case something stops working.

5.7 Detectors

The commercial X-ray detectors in use at most synchrotron beamlines have been developed for a substantial amount of time and resources. These detectors are well understood and well behaved. In general a 2D X-ray detector needs to have a linear response in order to reliably convert the measured pixel Analog-to-Digital Units (ADU) into a corresponding number of photons.

For scattering experiments we are not usually interested in the absolute number of X-ray photons. The X-ray intensity on a normal detector can be described by:

$$I_{pixel} = Gain_{pixel} \cdot I_0 + Dark_{pixel} \tag{5.4}$$

Where I_0 is the incoming flux, and the dark and gain are calibrated corrections.

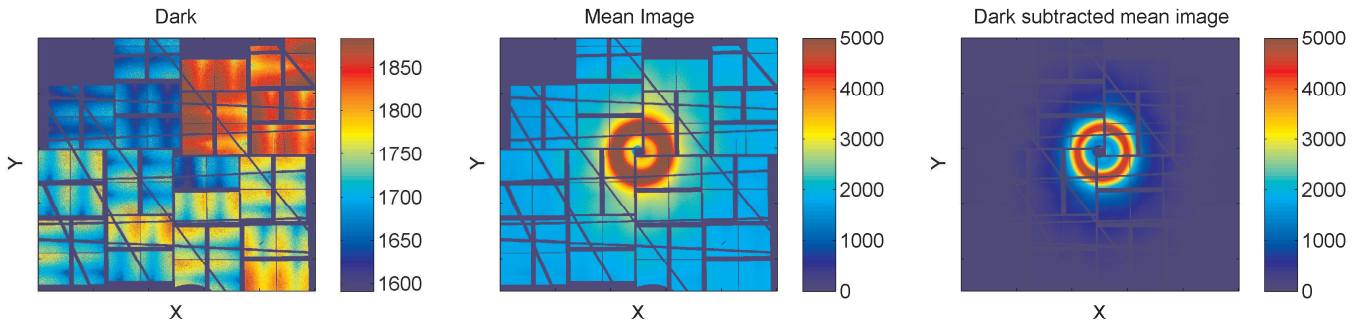

(a) Dark - zoom (b) Average (c) Dark subtracted image

Figure 5.11: 2D images from the CSPAD detector (a) dark image (b) Average image showing the solvent ring of acetonitrile scattering (c) a dark subtracted average image.

The commonly used detectors come in many different variants but have a few things in common. Either they are tailored toward single photon counting with a limit to the amount of photons/time or integrating detectors with long readout times.

For XFEL purposes fast, single-shot readout is neccesary. This puts a limit on the readout time at the repetiton-rate of the XFEL (120hz for LCLS and 20hz for SACLA) making traditional detectors unusable for XFEL's unless the conducted measurement has very low throughput eg. XES, RIXS.

This obstacle has been challenged individually at the current facilities ending at a similar result. constructing a larger area detector from an array of smaller units and tailoring the readout for speed.

5.7.1 The CSPAD

The Cornell-Slac Photo Array Detector (CSPAD) is a purpose built detector designed for the specific conditions at LCLS. Several smaller 2-tile detectors [72] and a few large CSPAD consisting of 32 tiles [73, 74]. Each tile consisting of 185*388 pixels. The detector can run in either a low or high gain mode with a 7x higher sensitivity. The two gain modes allows it to be used both as a few-photon counter able to distinguish single photons(as used for XES detection in [**VIII**]) or as an integrating detector that can measure the scattered signal from the intense X-ray shots at LCLS [**VII**]. In order to avoid saturation of the detector the X-ray beam or detector face is attenuated a factor of 3. Due to the complexity of the used setups at XPP, attenuation is often done with a thin absorber in front of the detector to maintain the full signal strength for XES and timing determination using the TimeTool 5.6.

Figure 5.11 shows the dark image and an avarage XDS image on acetonitrile. The dark subtracted image is close to saturation in the liquid peak and the high angles have very low counts due to the geometry of the detector (see chapter 3.1 on geometry correction). In order to get the needed high-Q information at XDS experiments the detector is placed very close to the sample (4.5cm). The direct beam passes through a hole in the centre of the detector.

The tiled detectors implemented at LCLS and SACLA have an interesting layout with a modular construction consisting of many tiles. As shown in figure

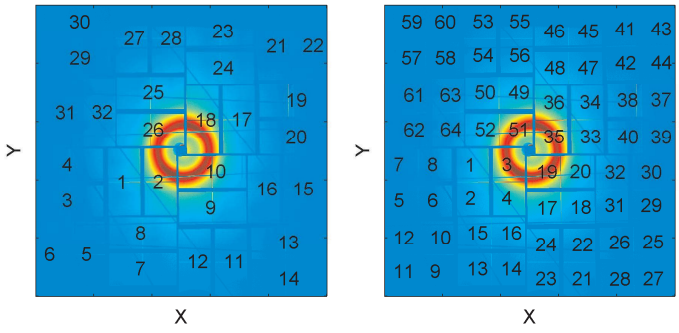

(a) (b)

Figure 5.12: The CSPAD is devided into 4 quadrants and a total of (a) 32 tiles (b) each consisting of 2 asics.

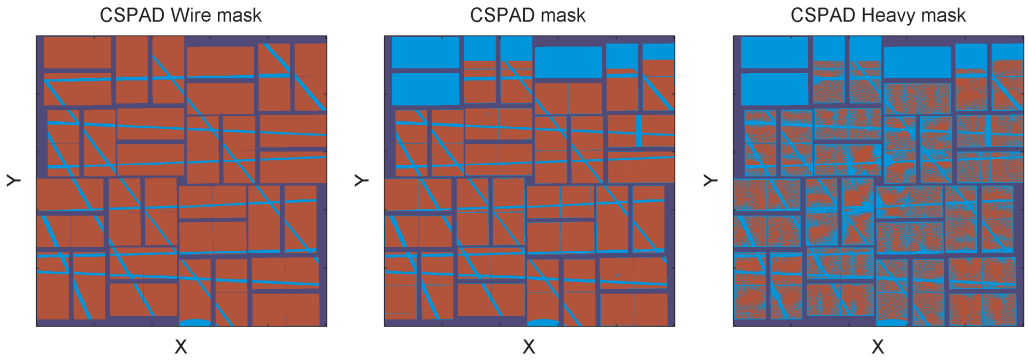

(a) (b) (c)

Figure 5.13: The CSPAD images where masked to remove outlier pixels (a) the wiremask removing the pixels covered by wires (b) a mask removing the shade of the nozzle and some bad pixels (c) A heavy mask masking all but the most reliable pixels.

5.12 the detector reads out data for the individual tiles. This is no problem once software has been adapted to take arbitrary pixel locations but the technical implications of a modular design can be challenging. Having separated the detector into many smaller independent units allows them to fluctuate independently of each other. When plotting consecutive shots it is possible to se quadrants and tiles fluctuating independently of each-other. This independent fluctuation of areas on the detector requires new thoughts on identification and correction of the detector output. The CSPAD detector was covered with metal wires in order to produce "dark" regions on the detector. It was believed that this would help correct for fluctuations. Many additional masks where made to mask out bad pixels and less reliable pixels as seen in figure 5.13.

Finally the avarage of the CSPAD is used as a beam diagnostic for the X-ray intensity as it is the only handle on the X-ray intensity after the liquid sheet. The properties of this diagnostic are plotted in figure 5.14 and show a nice symmetric intensity distribution as well as some drifts and an ACF lasting for ∼200 shots, similar to IPM3.

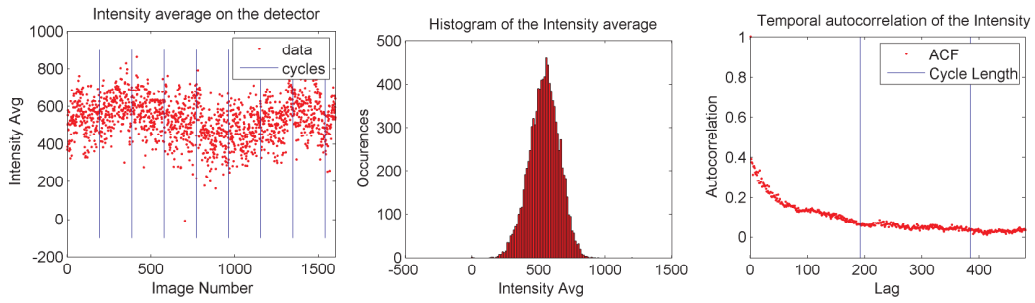

(a) (b) (c)

Figure 5.14: The Average Intensity measured on the CSPAD (a)Intensity average over time (b) A histogram of the Intensity (c) The temporal autocorrelation of the intensity average.

5.8 Dataflow

The data from LCLS experiments is initially saved as several XTC files and concatenated, translated and compressed into the HDF5 file format that can be accessed with commercial software and standard libraries in Matlab and Python.

For online analysis, simple software (ami_offline) is available at the beamline and is used in solution scattering experiments to extract T0 as fast as possible. This method relies on plotting the ratio of ΔS in different Q regions identified to change after heating of the solvent [**III**], a so called Figure-of-Merit scan (FOM) originally developed at ID09b. At the time of this experiment however this software was unavailable, resulting in at least 1h delay of any online analysis. The onlyne analysis relies on several steps before any XRD results can be extracted. The XTC files need to be saved to disk, HDF files need to be translated and the files need to be reduced and analysed. This results in long delay, purely due to transfer/read speeds before conclusions can be drawn, making feedback from the on-line analysis much slower. After each 12 hour shift it is possible to catch up with reduction and analysis, but re-alignment is necessary in the next shift and conclusions regarding overlap from previous shifts are outdated.

The specific data treatment from the CSPAD at LCLS is covered in the following chapter (6) where the data from a dedicated TR-XDS experiment are extracted and treated for analysis.

Chapter 6

XFEL experiments on $Ir_2dimen_4^{2+}$

This chapter covers a time-resolved X-ray Diffuse Scattering (TR-XDS) experiment at an X-ray Free Electron Laser (XFEL). The specific study was focused on measuring the sub-ps structural dynamics of a bimetallic Iridium compound in solution, carried out at the X-ray Pump-Probe (XPP) beamline at the Linac Coherent Light Source (LCLS) in March 2012

The introduction of XFEL sources facilitated the use of time-resolved X-ray techniques in the sub-ps time domain. Previously ps resolution was achieved with slicing experiments ([75, 76]), but photon hungry techniques such as TR-XDS and TR-XES have been unavailable at these time-scales.

The first TR-XDS experiments proposed at XFEL sources were naturally based on results from synchrotron experiments and optical studies. Since transient optical techniques predict the kinetics, energy and time-sales of a system and the synchrotron experiments show the sensitivity and applicability of a given X-ray technique.

The $Ir_2(dimen)_4^{2+}$experiment was proposed for the XPP beamline at LCLS in 2011, based on a new collaboration between Kelley Gaffneys group at Pulse, California and the Centre for Molecular Movies at DTU Denmark; bringing together the ultra-fast optical- and X-ray diffuse scattering-expertise necessary to study $Ir_2(dimen)_4^{2+}$at XPP. $Ir_2(dimen)_4^{2+}$has been studied in comparison with $Rh_2(dimen)_4^{2+}$and other d8-d8 metal complexes in the 1980s and '90s [52, 77, 49]. It was selected as a good XFEL candidate due to the clear coherent oscillations identified in transient optical spectroscopy by Hartsock et al. [78] as well as the structural sensitivity of TR-XDS shown by Haldrup et al. in [**I**]. It has also been suggested as a good XDS candidate by others[79].

The goal of the XFEL experiment was to:

- Study bond formation with sub-ps time-resolution.
- Measure ground- and excited-state atomic motions, emphasizing the Ir-Ir bond length.

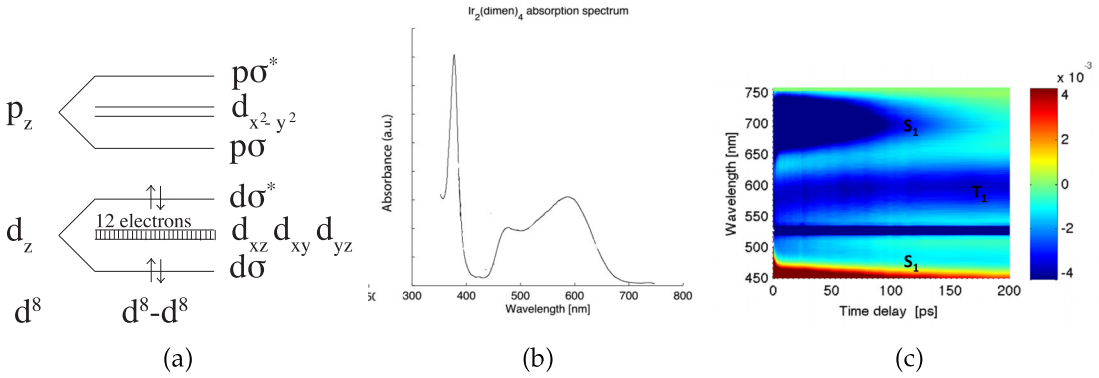

Figure 6.1: (a) Linear combination of atomic orbitals for d8-d8 metals adapted from [53] (b) The optical absorption spectrum of $Ir_2(dimen)_4^{2+}$in acetonitrile (c) Transient absorption spectrum of $Ir_2(dimen)_4^{2+}$pumped at 527 nm, with the corresponding excited states assigned to the spectral features.

- Correlate the dynamics observed with X-ray scattering to optical spectroscopy in order to decompose normal mode vibrations into the component changes in bond lengths and angles.
- Construct mechanistic understanding of the structure-function correlation in a photo-catalyst.

The proposal was granted beamtime in march 2012 and involved some preparation work regarding synthesis and experimental-setup.

However, the two biggest complications, previously encountered when measuring TR-XDS on $FeBPY_3$ [**VII**], where it was realised that the acquired images would require a much larger analysis effort than previous experiments at synchrotron sources, both with regards to data handling and sorting, as well as correcting for fluctuations. In addition, the 416fs time jitter [67] would make it difficult if not impossible to see rapidly dampened structural oscillations with a 500fs oscillation period [43]. The TimeTool for measuring the X-ray arrival time (see chapter 5.6) was tested and implemented before the beamtime, making it possible to correct for the temporal jitter.

This chapter shows the most recent status of the data extraction and analysis from this beamtime.

6.1 Excited state dynamics of $Ir_2dimen_4^{2+}$ in acetonitrile solution

$Ir_2(dimen)_4^{2+}$, (dimen = 1,8-diisocyanomenthane), is analogous to the $Rh_2(dimen)_4^{2+}$molecule presented in chapter 4. It consists of two Ir(I) metal centres bound in a 4 dimen ligand framework (see figure 6.4). Excitation of $Ir_2(dimen)_4^{2+}$promotes an electron from the anti-bonding $d\sigma^*$ to the $p\sigma$ orbital (see figure 6.1). This excitation changes the Ir-Ir bond order and causes a large contraction along this axis, as well as a significant twist in the dihedral angle of the ligands around the Ir-Ir axis [**I**].

The broad band in the optical absorption spectrum 430-700nm (figure 6.1) is due to the desired $d\sigma^* \rightarrow p\sigma$ transition and the width and splitting of the spectral feature is assigned to the presence of several different Ir-Ir distances in ground-state equilibrium[49, 78].

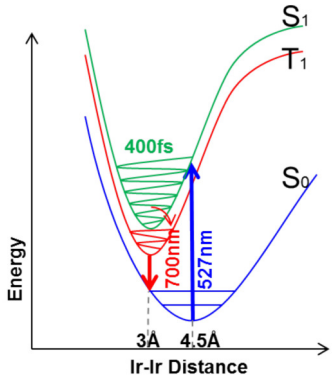

Figure 6.2: Franc-Condon Diagram showing a schematic of the Potential energy surfaces as a function of Ir-Ir Distance

The Franck-Condon diagram in figure 6.2 is useful when interpreting the wave-packet dynamics attributed to the sub-ps oscillations visible in the transient absorption [43], as well as the stimulated emission spectra by Hartsock et al. in figure 6.3

These coherent oscillations are the reason for the proposed XFEL experiment. The oscillation are due to a coherently excited wave-packet oscillating on the excited state potential surface of the Franck-Condon diagram in figure 6.2. The wave-packet is originally excited at ground state Ir-Ir distance 4.4Å and forces the molecule to contract as the wave-packet loses energy and settles in the excited state minimum 2.9Å Ir-Ir distance after a couple of oscillations in the potential. From optical studies combined with XRD studies [49] it has been possible to correlate the differences in the absorption spectrum with Ir-Ir distances attributing the oscillations to proportional structural changes. The availability of an XFEL allows us to probe the structure on sub-ps time-scales giving us the feasibility and motivation for this experiment.

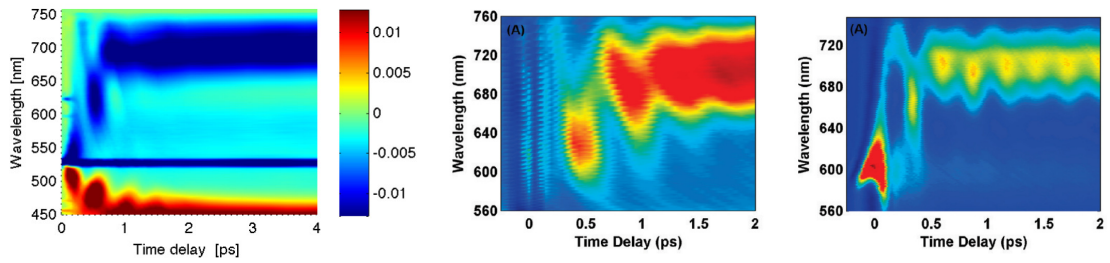

(a) (b) (c)

Figure 6.3: Ultra-fast transient optical measurements on $Ir_2(dimen)_4^{2+}$(a) Transient absorption spectrum pumped at 527nm from [43] (b-c) Stimulated emission spectra pumped at 477nm and 590nm respectively from [78]

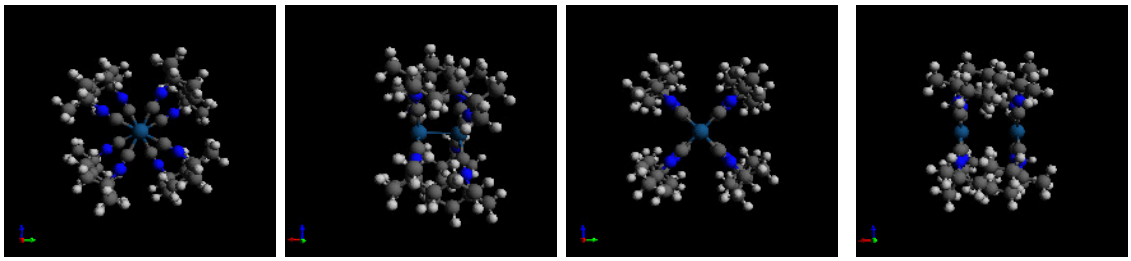

(a) (b) (c) (d)

Figure 6.4: Minimised molecular structures seen from the front and side for a+b) excited-state and c+d) the ground-state

6.2 Molecular modelling

In order to model the molecular structure, as well as simulate the energy landscape, a series of DFT calculations where carried out using ORCA ([54]).

The molecular structure of the 1:3 isomer was used due to the statistical abundance and a series of constrained calculations where carried out, varying the Ir-Ir distance and the dihedral twist in 0.5 Å and 5 degrees respectively. Some of these structures where used for the analysis in [**I**] and additional calculations where since carried out to give a better basis for interpretation and analysis of the sub-ps XFEL data. Compared with the model-system simulated by Hartsock et al. the energy landscape is somewhat similar (see figure 6.6). However, the population of two ground-states with different Ir-Ir distances at room temperature still elude the calculations (as seen in figure 6.5).

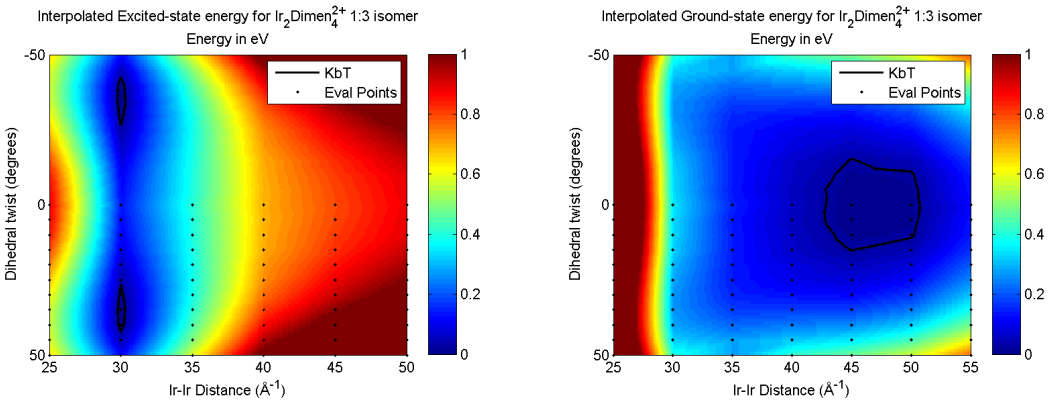

(a) Excited-state PES (b) Ground-state PES

Figure 6.5: (a) excited- and ground-state Potential Energy Surfaces (PES). Calculated using DFT for a constrained singlet and triplet geometry respectively. The structures were evaluated in the grid of points superimposed on the PES.

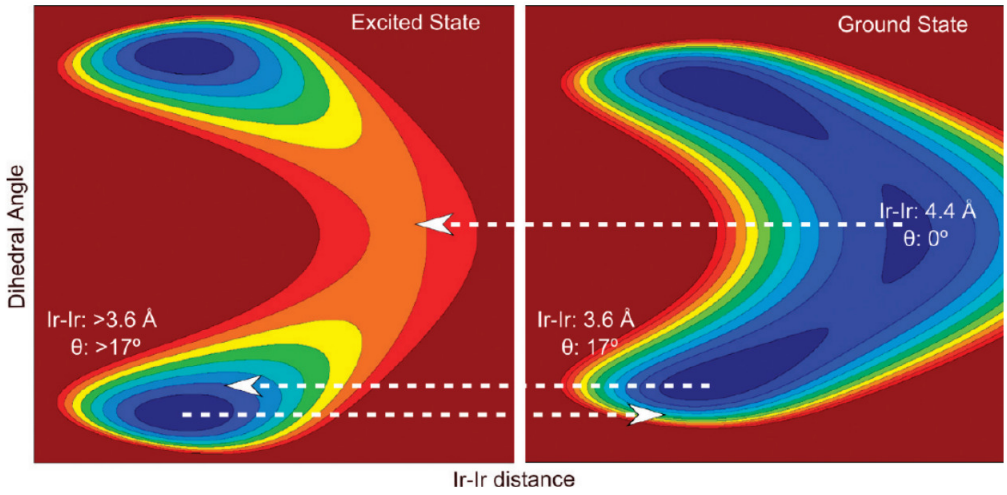

Figure 6.6: Potential energy diagram from Harsock et al. [78]

From these calculations, a set of 66x2 different molecular structures and the corresponding energies are available. The corresponding X-ray scattering can be calculated for each molecule. The minimum of the ground- and excited-state are localised at 4.5Å and 3.0Å respectively, with a dihedral twist of 0 and 35 degrees as seen on the structure in figure 6.5. These optimised structures correspond to the 4.4Å GS and 2.9Å ES fit to the TR-XDS measured at ESRF [**I**]. The second ground-state isomer was fit with a 3.4Å twisted $Ir_2(dimen)_4^{2+}$structure coinciding with the expanse of the low energy region on figure 6.5 (b) extending down to a preferentially twisted 3.5Å configuration.

In addition to the traditional DFT structure optimisations in ORCA, dynamical QM/MM calculations were carried out by Asmus Dohn in order to simulate the dynamics of the transition, including direct interactions with the solvent (see [**V**]). The dynamic QM/MM simulations will prove valuable in the final analysis of the $Ir_2(dimen)_4^{2+}$system, but will not be used in this dissertation as the structural analysis still remains to be done.

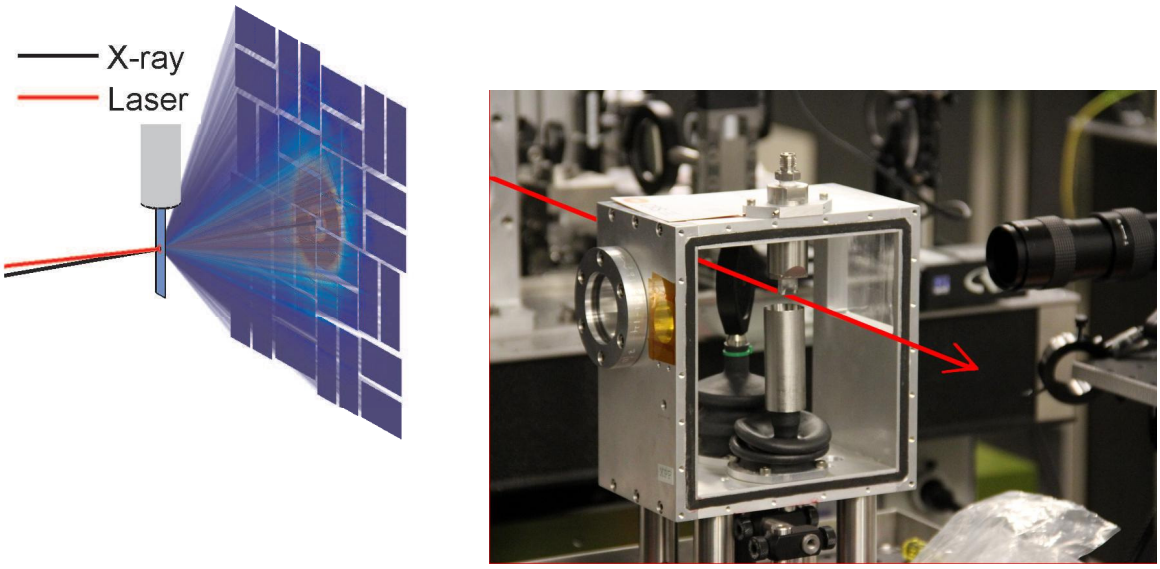

(a) Schematic representation

(b) Photo, (red line) is the X-ray/laser path

Figure 6.7: Experimental setup at XPP.

6.3 Experimental Setup

The setup used for solution experiments at XPP is constructed at the beamline based on sample chamber design by Henrik Lemke. It consists of a closed chamber with kapton exit windows; for XDS centred around the direct beam and windows for XES at 90 degress as seen in figure 6.7. The XDS window covers the entire back side of the chamber and the distance from sample to window is kept short to allow for detection of large exit angles. This allows measurement of scattering up to 5.5 $Å^{-1}$ at the available 9.5 keV. The sample flows from a thin 100μm Kyburz nozle mounted in the top of the chamber. The jet produces a thin free standing liquid sheet, that flows into a catcher returning the sample to a 100ml reservoir for circulation. The entire chamber is flooded with a slight over-pressure of He to minimise air scattering from the direct beam and protect the sample with an inert atmosphere.

In this particular experiment the sample reservoir was also flooded with He and the over-pressure was monitored through a small oil bubbler mounted on top of the sealed reservoir. From the reservoir, the intake of the sample pump was mounted as well as a secondary pump used to pump a small sample volume through a spectrometer to monitor the sample integrity. The $Ir_2(dimen)_4^{2+}$sample had previously shown instability in the proximity of air [**I**].

The CSPAD detector was placed against the kapton exit window, letting the direct beam pass through a hole in the centre of the detector. To mitigate scattering around the direct beam as it passes through kapton and air, a small copper tube was inserted into the central hole of the detector and pushed against the window to attenuate the kapton scattering.

The optical sample absorption spectra where monitored from a remotely

controlled laptop and showed a much higher degree of stability than previously experienced.

This setup was optimised for the measurement of TR-XDS. Compared to [**VII**] and [**VIII**] at LCLS and [**IV**] at SACLA the omitted XES measurements allowed for a perpendicular liquid-sheet, making the detector corrections simpler. Also, when only measureing XDS attenuation can be done on the X-ray beam making it easier to avoid detector saturation. However, doing XDS without the simultaneous X-ray spectroscopies removes the possibility of optimising and verifying overlaps on a diode. Additionally the analysis cannot benefit from the redundant information from overlapping information contents in the different techniques, such as the handle on the excitation fraction as in [**II**]. The Iridium L and K edges are above the 9.5 keV currently available at LCLS, also the lack of changes in spin and charge of Ir would question the usefulness of XES/XAS, which is why these techniques were not included in the $Ir_2(dimen)_4^{2+}$proposal.

6.4 Data workflow

For the first XDS experiments at XPP the software was developed, adapted and improved during the beamtime and therefore changed rapidly during the experiment. The measured data was mostly analysed locally on laptops, where future experiments rely increasingly on the localy available PSANA machines for data reduction. This increases the analysis speed and greatly decreases the data amount transferred to local computers. As seen in figure 6.8 the data reduction from 2D images to 1D difference scattering curves reduces an XDS scan size from 360Gb to 80 Mb.

The work flow at XPP is based on the flow of XDS experiments at synchrotrons as described in chapter 4.5. However, most steps have been improved for speed and robustness to effectively handle the much larger data amounts, as well as effectively remove the many outliers.

The data extracted from the CSPAD detector available at LCLS was known to have a messy signal from the beginning. Weather due to the setup, intensity distribution, detector crosstalk or readout was unknown even to the beamline staff and the detector group at LCLS. It was assumed that the fluctuations could easily be a mixture of all these effects, since the data was not limited by the counting statistics and showed very large shot-to-shot fluctuations. The measured signal was fluctuating enough to introduce artefacts much larger than the magnitude of the scattering signal ΔS we were trying to measure. The artefacts were initially approached by heavy filtering and masking of the detector.

6.4.1 Detector preparation

Due to the novelty of the experimental setup at XPP and the use of a newly updated detector and detector position, the experimental geometry needed to be quantified initially.

The corner coordinates of the 32 tiles is available in a metrology file, and a complete set of x, y, z coordinates to all pixels can be constructed from them.

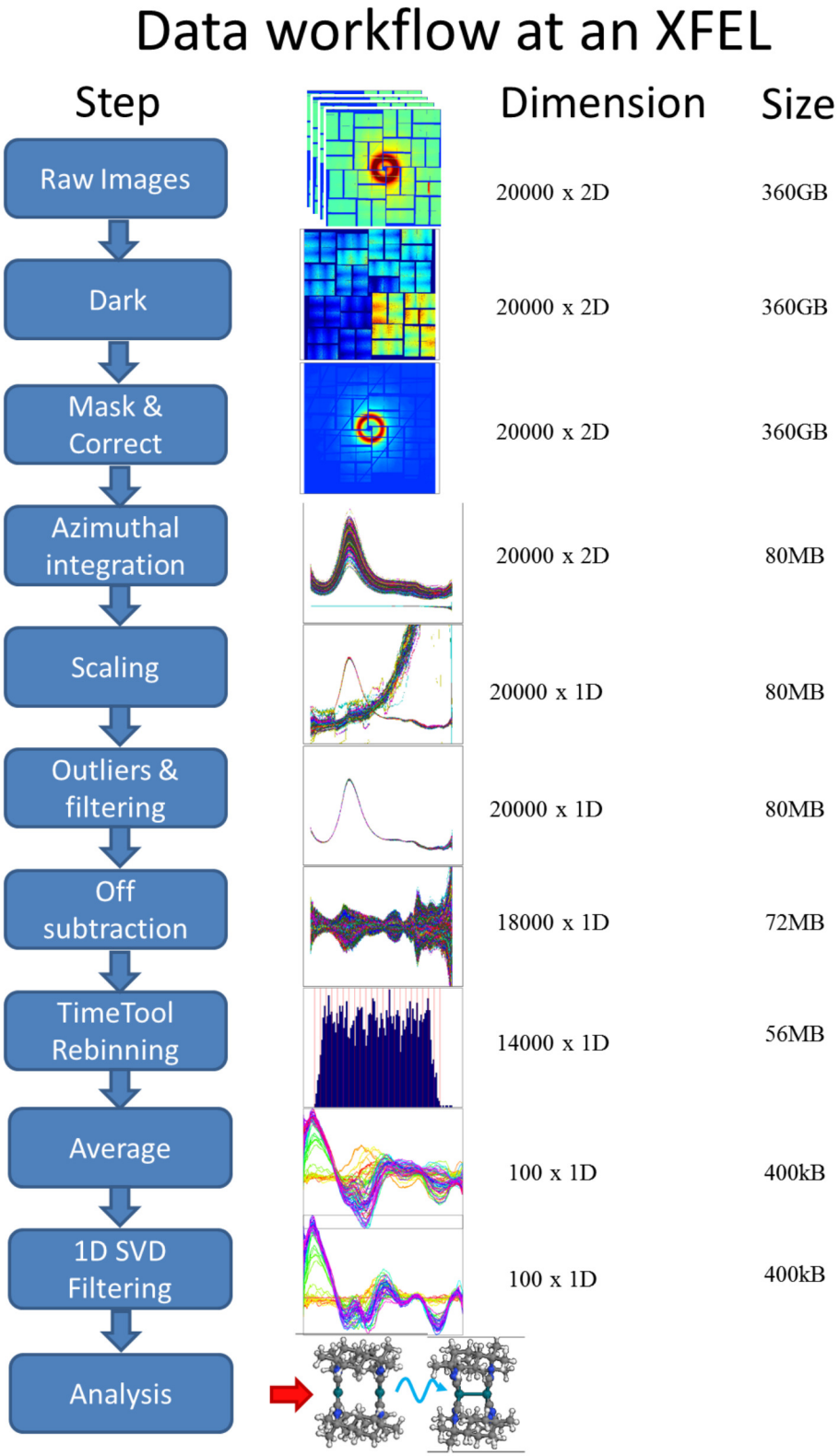

Figure 6.8: General workflow for TR-XDS experiments at XPP

For each set of experimental conditions a mask needs to be constructed. The mask removes untrustworthy areas on the detector (shaded, sample splatter, wiremasks) as well as bad pixels determined by the low signal-to-noise ratio.

From the xyz coordinates it is possible to calculate the corresponding 2θ angle and Q vector from:

$$Q = \frac{4pi \cdot sin(\frac{2\theta}{2}}{\lambda} \tag{6.1}$$

where θ is half the scattering angle 2θ and λ is the X-ray wavelength.

Based on the set of coordinates it is now possible to calculate the detector corrections for each pixel based on chapter 3.1, resulting in 3 different corrections: Polarisation, geometry and liquid sheet absorption. The product of these corrections yields a single final correction for each pixel.

The dark image is constructed as the average of a set of images taken without any incident X-ray or laser. This is done at least once every shift, but the dark shows good stability when measuring high intensities in low-gain mode. For single photon counting a common mode correction is applied to negate fluctuations of entire tiles as in [**VIII**]. However, a simple common mode correction require unexposed pixels on each tile and is not included here.

After constructing the needed vectors and corrections the data can be batch processed until changes in the experimental setup require a new set to be procured.

$$I_{pixel}^{Corrected} = \frac{I_{pixel}^{measured} - Dark_{pixel}}{Gain_{pixel}} \cdot Corrections_{pixel} \tag{3.1}$$

Raw Images

The raw images from the CSPAD are saved in the compressed HDF5 files. For each scan the raw images are read out in chunks, treated and reduced in order to clear up the memory for the next chunk. In addition to the images, all the relevant parameters are read out.

Dark

The newest dark image is subtracted from each image.

Mask and Correct

The corrections are applied to the image and the images are masked.

Azimuthal Integration

Since the pixels on each 2D image correspond to the same angular bins, the mapping for the radial integration is done once. All following images are merely re-binned speeding up this process significantly, bringing the time down to 30ms/image (∼33 Hz) compared to the 120Hz repetition rate of LCLS. Including the reading, decompression and correction it takes 100ms/image (∼10 Hz). Additionally changing the azimuthal integration from taking the mean of a bin to

taking the median to reduce the effect of outliers, the final result is 140 ms/image (∼7Hz) making the data reduction 17 times slower than taking them.

For online analysis this is a problem, especially combined with the slow translation and transfer speeds (XTC-> HDF5-> Storage).

However this process can be run on multiple cores/machines in parallel and is thereby limited by the transfer speeds.

Scaling

The radial curves are now scaled in a chosen area. Due to the lack of High Q data the curves are merely integrated to the entire peak and may be rescaled later on, depending on the identification of the difference signal in order to ensure that the scaling is done around a nodal point.

Outliers and filtering

Due to the large fluctuations identified at LCLS, a large set of the data needs to be discarded prior to analysis. Initially this was done by taking the central part of the distribution of each parameter (EBeam, IPM3, Intensity average on the detector) however a fast approach yielding better results was based on a 2D filtering approach. Each point of each curve was compared to the same points of the other curevs in a select region of interest. All curves with more than one MAD points deviating from this median were discarded. This approach discards a similar amount of data as the single parameter filtering, but is done fast and with a more homogeneous result.

This filtering approach is used instead of the Chauvenet criterion used at synchrotrons, due to the poor scaling with large datasets.

Off subtraction

Finally, in order to reach the difference scattering signal, each image was subtracted the mean of the two nearest off-images.

TimeTool Rebinning

The Timetool provided information on the true arrival time of each pulse making it possible to re-bin the data accordingly. Due to the +300fs FWHM of the time jitter, scans with many repetitions and small delay steps could be binned to any desired bin size. However, due to the velocity mismatch, a machine response function around 150fs is expected.

Average

Finally all difference scattering images present in each bin can be averaged. Again using a median instead of the mean reduces the outlier sensitivity producing a more robust result.

The final product of the data reduction and pre-analysis is a set of difference-scattering curves corresponding to the scanned time-delays.

Analysis

Each of these curves corresponds to the measured difference signal at the delay and needs to be analysed separately as in chapter 4, or by using a global fitting approach, applying a model to describe the kinetic changes of the different contributions to ΔS.

At this point in the data reduction, however, the data still contains fluctuations similar in magnitude to the underlying difference scattering signal. This realisation has prompted a large effort in different methods of filtering the data in such a way, that the pure difference signal could be extracted. At synchrotrons, the measured fluctuations, mainly noise, behave stochastically and are averaged out following many repetitions. This is not the case for XDS measured at XFELs.

The simple approaches of filtering and masking the images only showed small improvements and did not remove the fluctuations.

Therefore, other approaches were attempted, and some of them are presented in the following chapters.

6.4.2 1D SVD-filtering of TR-XDS

This filtering process (referred to as 1D SVD-filtering) is based on SVD (see chapter 5.4) and was implemented by Kristoffer Haldrup [65] while working on [**VII**].

The 1D SVD-filtering is used to identify independent fluctuations in the 1D azimuthally integrated difference scattering curves before t_0, where the signal should not be fluctuating. After identifying these components their contribution to each ΔS-curve is determined and subtracted. The 1D SVD-filtering method is very fast and effective, but has a number of problems. In particular, care has to be taken to avoid over-filtering the data, which can result in altering of the signal shape. In general, the kinetics of the difference signal can be trusted after 1D SVD-filtering. In order to conduct structural analysis of the difference scattering signal however, the subtracted SVD components have to be completely orthogonal to the difference signal measured, which is almost never the case.

To remedy this, an expected "placeholder" difference-signal can be estimated, either from large averages of the difference signal measured at late times, from calculations or from synchrotron measurements. Fitting these placeholder difference signals together with the fluctuation-components determined from the SVD, when determining the contribution of the fluctuation components subtracted from each difference curve preserves a signal similar to the provided placeholder. Using this approach will preferentially conserve a signal similar to the expectation, and will have problems mapping out structural dynamics where an evolution in the difference signal is expected. Using placeholders to extract structural dynamics would require a large series of placeholders to conserve the true dynamically changing difference scattering signals. This filtering approach will be described in detail in an upcoming article by Kristoffer Haldrup [65]. This approach has been used with great care to extract the difference scattering signal in [**IV**] and [**VII**].

With these cautions in mind, the 1D SVD-filtering can always be applied without placeholder signals in order to estimate signal strength and kinetics of measured data during experiments. An example of this is presented in figure 6.9.

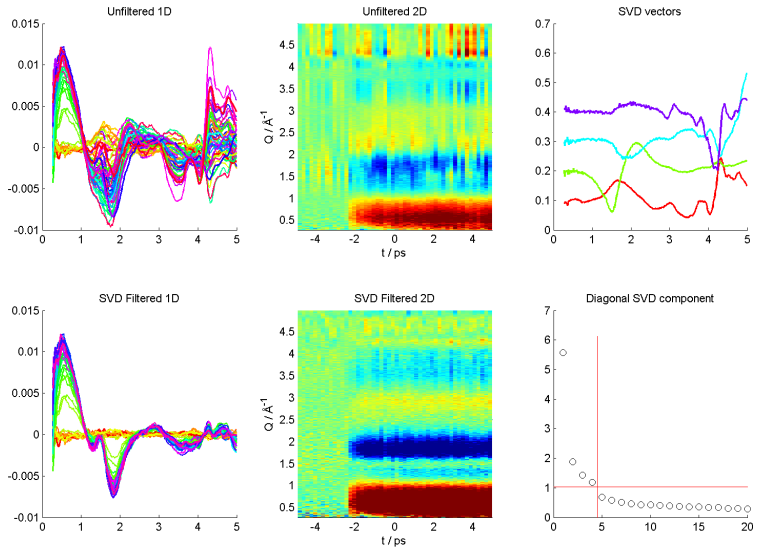

Figure 6.9: general use of the fast SVD filtering on a single scan of IrDimen

The 1D SVD-filtering without placeholder signals can be applied fast and robustly to the measured data and does not rely on any prior information or manual selections. By using images recorded with laser dropshots (see chapter 5.5.3) to determine the fluctuation components, the scheme is also independent of the absolute timing of the experiment. An example of this simple 1D SVD-filtering can be seen in figure where a comparison of 1(a-b) and 2(a-b) shows the effect of filtering out components 1(c) identified as the largest independently fluctuating 1D components in the difference scattering curves from the laser-off images. As seen on 2(a-b) the shape of the difference signal might have been altered as an effect of the filtering (seen by the separation of the dip at 1-2 Å^{-1}). Because of this inherent danger of altering the signal, significant efforts have been invested in identifying the cause of the fluctuations, and removing them from the signal at a much earlier point of the flow of data processing.

Chapter 7

XFEL experiments - 2D SVD-Corrections

This chapter describes the framework developed in order to directly apply corrections of the 2D detector images. Examples are shown of the results of this approach on the 1D data, and furthermore how this approach have allowed us to investigate the full 2D difference signal directly, such that the anisotropic dynamics can be identified. This method of treating CSPAD data is still under development, and is still being improved upon. It will be referred to as 2D SVD-correction to distinguish from the 1D SVD-filtering described in the previous chapter. It is noted that the 2D refers to the fact that each vector in the analysis is the full vectorised 2D image, unravelled into one long vector containing the pixels in the order they are read out of the detector.

The 2D SVD-correction approach is designed to clarify how the detector deviates from linear behaviour, and correct for it on a pixel to pixel level based on correlations with the beam diagnostics.

A normal linear detector would have the following behaviour:

$$I^{pixel}_{measured} = G^{pixel} \cdot I^{pixel}_{0} + Dark^{pixel} \tag{7.1}$$

where $I^{pixel}_{measured}$ is the measured pixel intensity, G^{pixel} is the pixel gain, I^{pixel}_{0} is the X-ray intensity incident on the pixel and $Dark^{pixel}$ is the measured intensity without any incoming X-rays. Following this description, the detector is linear in intensity with a constant (dark) offset. The gain and dark can be measured independently with dark and flat-field measurements. Within the dynamic range of the detector the measured intensity is linear.

This is not the case for the CSPAD, where a given pixel value does not behave entirely linearly as a function of incoming X-ray intensity I0.

An attempt to fit the individual linear gain response of the pixels based on the measurements at hand, was carried out to identify an effective gain and dark under working conditions, but did not account for the measured fluctuations.

Instead a full set of scattering images was studied with SVD and the individual independent components plotted in order to study their behaviour.

For the 2D SVD decomposition, a set of laser-off, dark subtracted, scattering images were used for decomposition as they represent experimental fluctuations without including pump-induced difference signal. The images were selected

using the event codes (see chapter 5.5.3). Additionally, a mask (figure 5.13 (a)) was used to select the ∼1.7 million best pixels (removing shadowed pixels, and pixels with high S/N), avoid outliers dominating the SVD components.

The full NxM U,S,V matrices cannot be computed using the normal SVD algorithm in MATLAB®, but since the collective images are heavily over-sampling and therefore of low rank, the less heavy low rank SVD can be used for the decomposition.

A scan on which the 2D SVD decomposition is carried out contains several thousand images. A low rank SVD decomposition makes it possible to SVD some images, but not all at once. A small subset of 100 images could be selected, but in order to cover the entire fluctuating parameter space, it is important that all available images are used. Based on work by M. Brand [80] on doing incremental SVD, and a MATLAB® implementation by D. Wingate [81] it is possible to include all the images of an experimental scan by iterating through the dataset in chunks and updating the U,S,V matrices accordingly.

In this fashion, low rank partial SVD takes comparably little time and results in the much smaller U,S,V matrices of size MxR, RxR and NxR respectively. R is the low rank chosen for the decomposition. With these crucial additions to the SVD, it is now possible to decompose the full detector images in reasonable time and also hold all the information in memory.

Figure 7.1 shows the first SVD component presented in 6 plots. Figure 7.1 (a) shows the real-space representation of the component, (b) the radially integrated component on top of the full radially integrated signal and (c) the amplitude of the component ($S_{i,i} \cdot V_i$) plotted against the incoming X-ray intensity. Similarly, (d) plots the amplitude against the incoming X-ray energy, (e) shows the fluctuations over time, monitoring drifts and (f) the autocorrelation of the component amplitude, showing if the component is completely random or fluctuating with some time-dependency.

These plots shows that the first SVD component as linear in intensity reflecting the linear behaviour in equation 7.1.

The full set of components identified by the SVD can be investigated by plotting them as described above. The correlation of each component with respect to different x-ray beam parameters (e.g. X-ray energy and X-ray intensity), can thus be investigated. Components that correlate systematically with the beam parameters can be removed from the data, by using the correlation between the component and the beam parameter with which it correlate. This approach circumvents the problem of fitting the amplitude fluctuating components to the data itself.

Thus, within this approach the fluctuations correlating with x-ray beam parameters can be corrected by subtracting the amplitude of each SVD component described as a function of beam parameters:

$$I_{Corrected} = I_{measured} - Dark - USV^T_{[2..n]} \tag{7.2}$$

$$I_{Corrected} = I_{measured} - Dark - U(I0, E0)_{[2..n]} \tag{7.3}$$

where the corrected intensity $I_{Corrected}$ is the remaining linearly intensity dependent detector response after subtracting the constant dark and a set of n-1 components, $U(I0, E0)_{[2..n]}$.

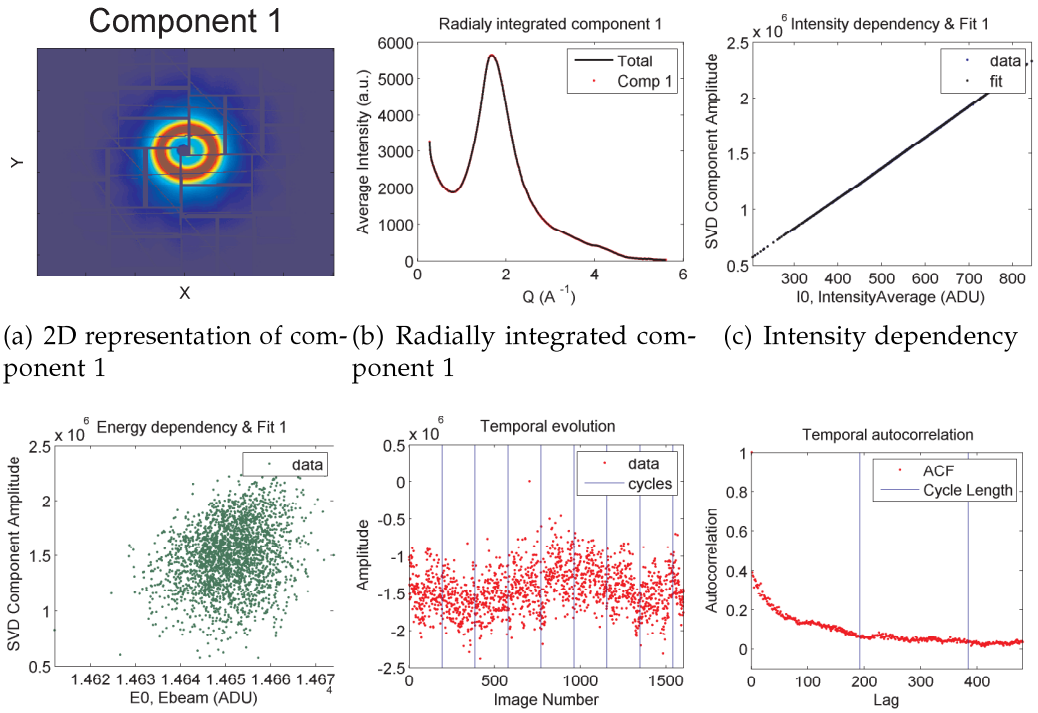

(a) 2D representation of component 1

(b) Radially integrated component 1

(c) Intensity dependency

(d) Energy dependency

(e) Temporal evolution

(f) autocorrelation

Figure 7.1: Component 1 from the 2D SVD

Using this approach, corrections can be made based on a selected number of SVD components, as long as they correlate with an external parameter. U_i is the correction and the correlation is fit with a 9th order polynomial. The fit should describe the correlation within the boundaries of the sampled data points and the 9th order polynomial is simply used for robustness, even though such a high order fit may introduce errors close to and outside the boundaries. Identifying the components and their correlations in a robust fashion is currently being developed, but no scheme has yet been tested thoroughly, and thus the approach described here still relies on manual inspection and selection of components used for correction.

For difference signals where the induced changes in the total scattering signal are, components used for correcting the data which were identified for unpumped images will work well for the pumped images. It should however be noted, that the detector response most definitely depends on the intensity distribution on the detector. This implies that the detector cannot be corrected once and for all, and also means that the identified corrections cannot be applied to images with a significantly different intensity distribution than the data used to generate them.

For TR-XDS experiments, the changes in total signal are very small (typically below a percent), and the reference images required to construct the set of corrections (exposures with laser drop shots) are already measured interleaved with the data in each scan. Due to the availability of these reference images, fresh correction terms can be constructed for each scan reflecting the exact experimental conditions of the images they are applied to.

The following section contains an example of the first 12 SVD components and their assignments.

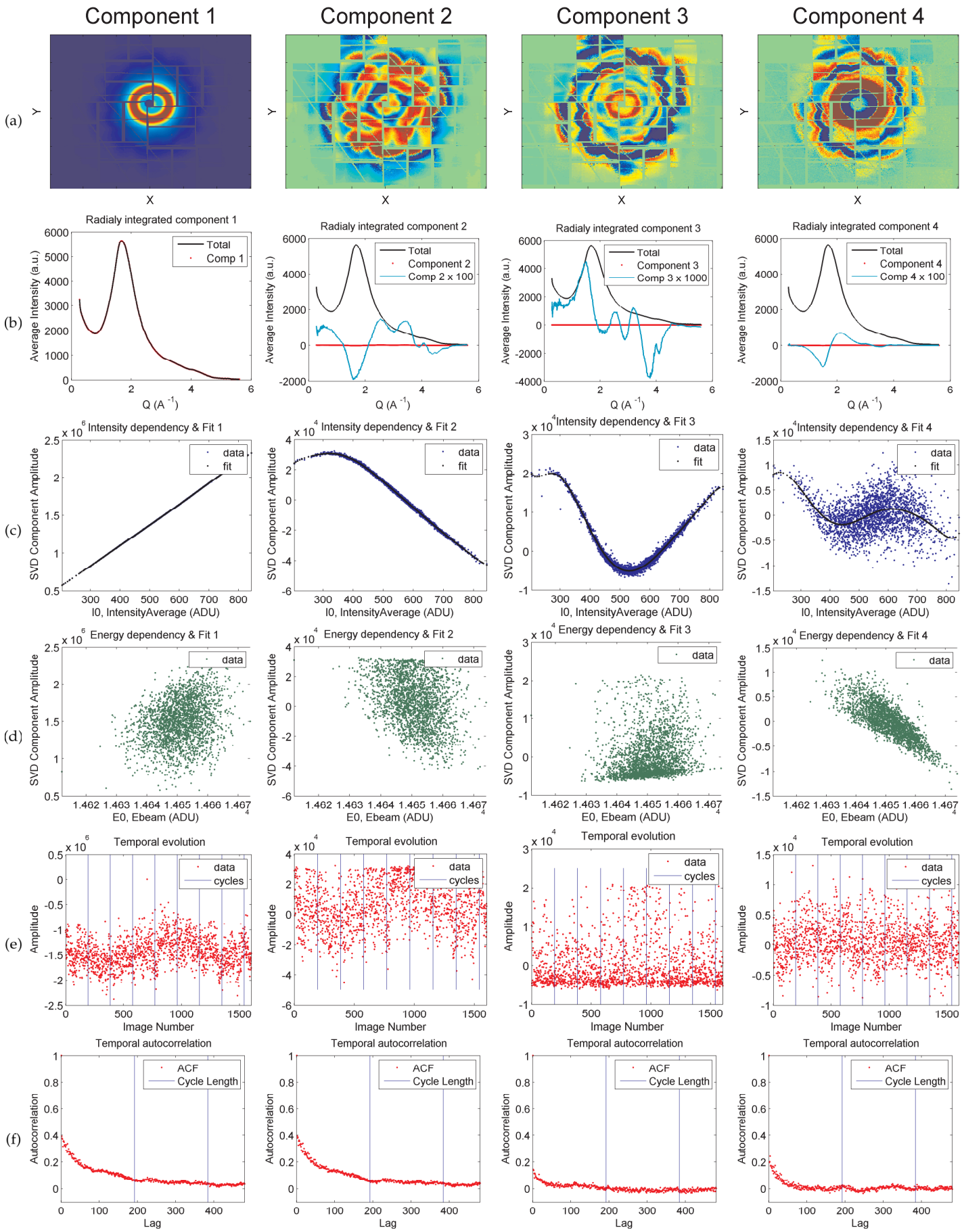

Figure 7.2: SVD components 1:4 (columns) visualised in different manners: a) 2D representation b) 1D representation c) Intensity dependency d) Energy depenedency e) Amplitude over time f) Temporal autocorrelation

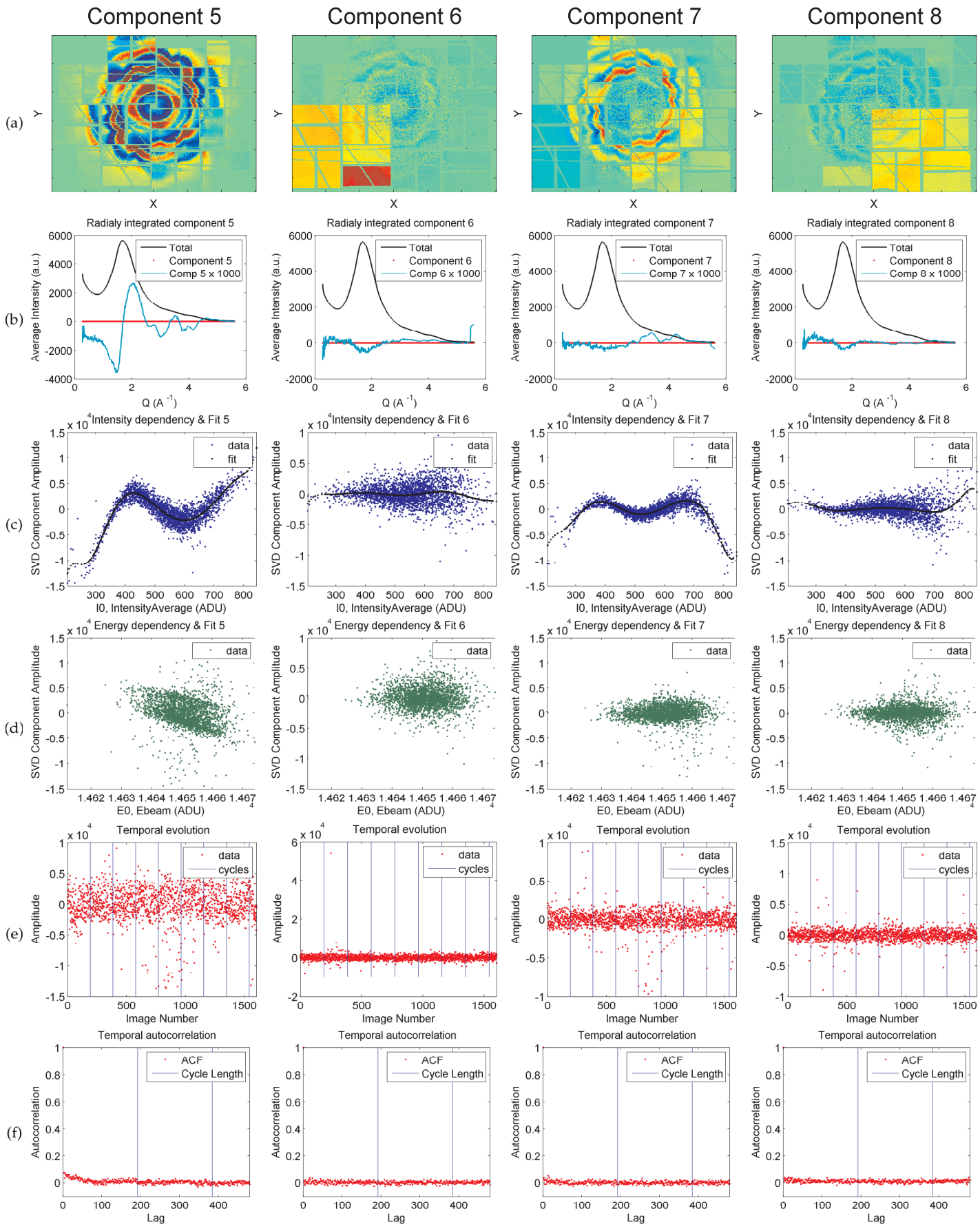

Figure 7.3: SVD components 5:8 (columns) visualised in different manners: a) 2D representation b) 1D representation c) Intensity dependency d) Energy dependency e) Amplitude over time f)Temporal autocorrelation

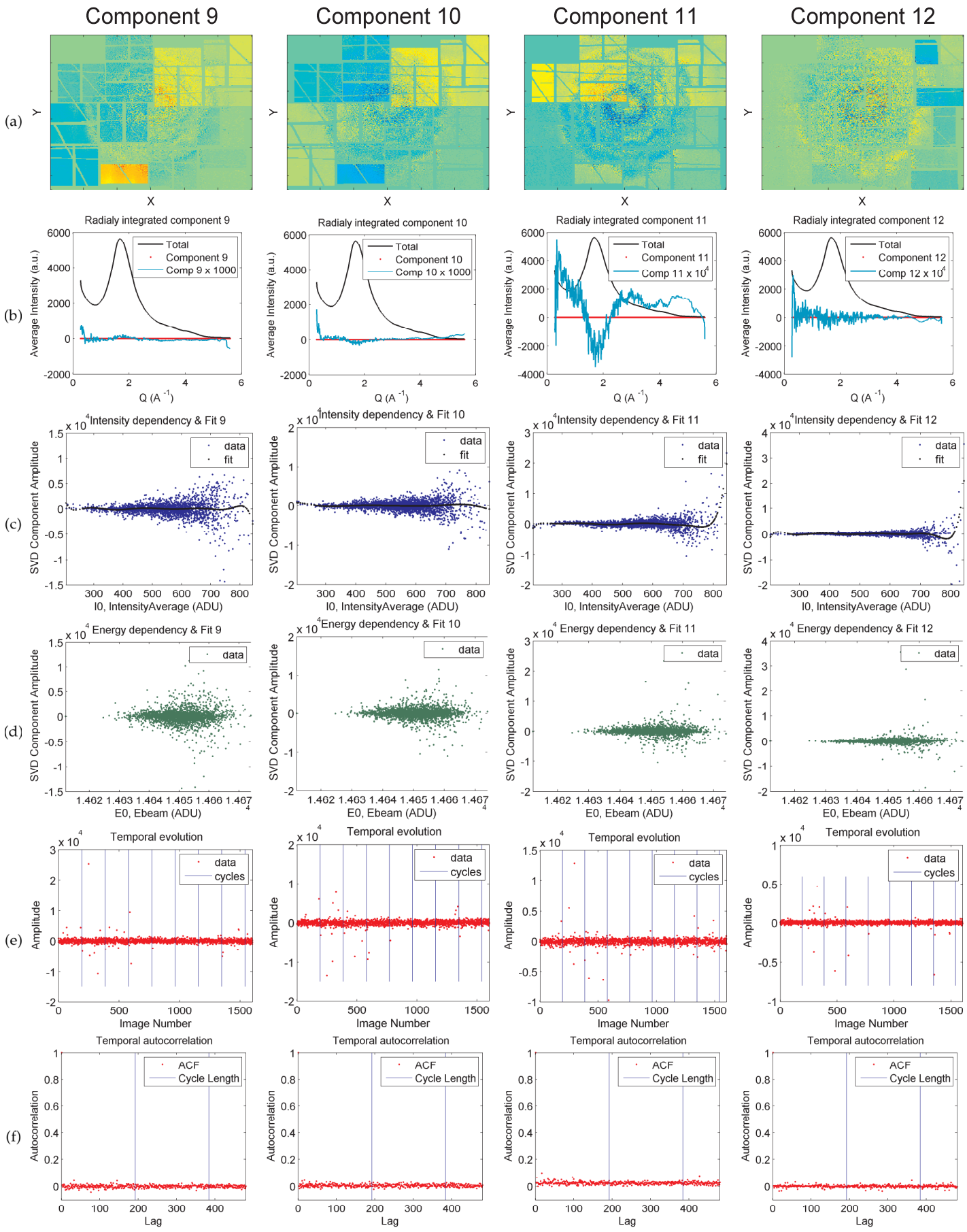

Figure 7.4: SVD components 9:12 (columns) visualised in different manners: a) 2D representation b) 1D representation c) Intensity dependency d) Energy depenedency e) Amplitude over time f)Temporal autocorrelation

7.1 The 2D SVD components

This section presents an overview of the SVD components identified for a specific scan and can be seen in figures(7.2, 7.3 and 7.4). The figures show the plots presented for component 1 in figure 7.1. A total of 12 components are shown here to illustrate the decreasing importance of the components and to give an overview of the information.

The fluctuations identified here can effectively be used to correct all measurements conducted on the same day, where the experimental setup remains largely unchanged. But as mentioned earlier, new corrections can in principle be generated for each scan.

A full set of 40 SVD components where calculated and the first 12 are shown here. Since the SVD components are identified in decreasing order, a reasonable cutt-off can be selected. As seen by comparing the 2D plots of the components, the components are increasingly dominated by quadrant and tile fluctuations and finally noise. These energy and intensity independent components can be studied in this fashion, but not corrected as these fluctuations are uncorrelated with an external parameter.

Once the correlated corrections have been applied, it would be possible to improve the detector additionally by developing a form of common mode correction to remove the tile and quadrant fluctuations.

Using the partial SVD described in chapter 7, 40 components are determined from all un-pumped shots from a selected scan. In itself, each SVD component is a 1.7 million element vector ordered according to pixel readout. Using the same tools used for reduction and visualisation of the data, it is possible to map the components onto the 2D detector. Furthermore, the data can be radially integrated to interpret the components as a function of Q and compare them with the components identified by the 1D SVD-filtering.

Linear intensity dependency

The first SVD component has a linear intensity dependency and is the largest component accounting for 99 % of the signal. Due to the intensity correlation, the autocorrelation is almost identical to the autocorrelation of the average intensity on the detector and IPM3, as seen in figure 5.1 and 5.14.

Non-linear intensity dependency

Component 2,3 and 7 show a clear intensity dependency and have the largest contributions in the liquid peak. These effects map out the non-linearity of the individual pixel gain and on average account for 0.5% 0.1% and 0.1 % of the total signal. Such small deviations would not matter much for non-difference signals, but for TR-XDS these fluctuations are translated directly to the difference scattering. They are not averaged out as they have significant autocorrelations spanning multiple scan cycles.

X-ray energy dependency

Component 4 and 5 also show some intensity correlation, but more importantly they show an energy correlation. Looking at the 1D components, it is clear that

they correspond to a liquid peak shift in either direction and could be explained by the ∼50ev X-ray energy fluctuations from the XFEL. These components are therefore primarily described as energy dependent. Since component 5 shows a bimodal correlation the data is filtered and an outlier insensitive theil sen estimator[82] is used to generate a robust linear fit. These two components are preferentially described as energy dependent since they can then easily be omitted in case an actual energy scaling is implemented (see figure 7.6).

Tile dependency

Component 6 shows little correlation and seems to be a quadrant fluctuation dominated by one single tile. Since it is uncorrelated, it cannot be corrected in the described fashion.

As all corrections are kept in the full detector frame describing all pixels, the corrections can be applied and the dataset can be studied anew in order to determine the effectiveness of the correction. The 2D SVD-correction is very effective and accounts for most of the fluctuations in a physically meaningful manner. There is, however, no reason for SVD components to have a physical meaning and future work on this method may include rotating components to maximise correlation with diagnostics and physical components.

The correction terms for this scan add up to 3 independent intensity corrections and 2 energy corrections. After applying these corrections the quadrant and tile fluctuations remain and introduce artefacts with an amplitude less than 0.1%. Further masking could be implemented if these fluctuations predominantly consist of asics, tiles or quadrants fluctuations, as seen from component 6, identifying tile seven as a dominating source of fluctuations.

7.2 Verification of the components

To test the physical significance of the components, several tests were carried out. SVD components were based on images from a narrow interval in Ebeam values, resulting in the disappearance of the energy dependent components and retaining the intensity dependent ones. Similarly, for SVD based on images from a narrow intensity interval an energy dependent becomes the most significant contribution. However, due to the images no longer probing the effect of the intensity distribution, the remaining components seem to be a mixture of all the components, no longer separated into physically meaningful ones.

Comparing the energy correlated components with the expected effect of energy shifts (figure 7.5) reveals a similarity in the shape of the components. The radially integrated SVD component 4 and 5 correspond to positive and negative energy shifts significantly smaller than the ±50eV shown in the plots. Based on the Ebeam calibration in figure 5.4 the actual energy fluctuations are in the order of 30 eV FWHM.

Finally, the realisation that the 30 eV energy fluctuations have a large contribution to the difference scattering makes it possible to take this into account in the reduction. As each scattering image is reduced individually, it is possible to reduce each image based on a different X-ray energy. The result of this can be seen in figure 7.6 (d) were only the intensity dependent components have been

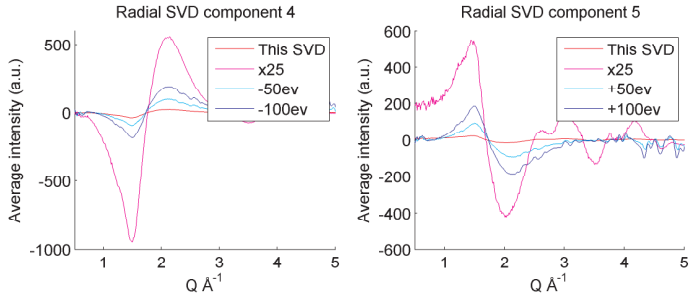

(a) Component 4 - positive energy shift

(b) Component 4 - negative energy shift

Figure 7.5: The energy dependent component 4 and 5 compared with shifts in energy.

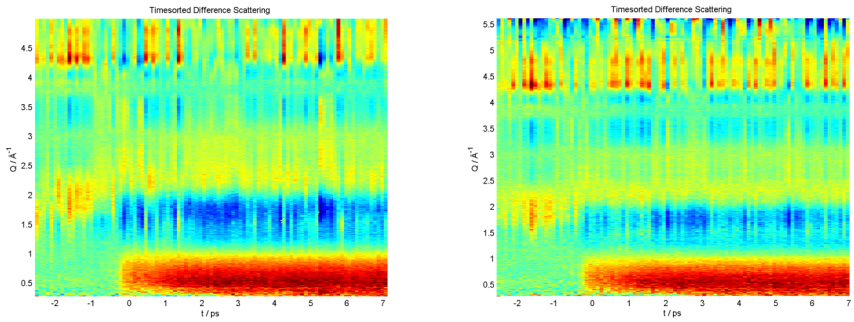

(a) no 2D SVD-Correction

(b) no 2D SVD-Correction, with energy scaling

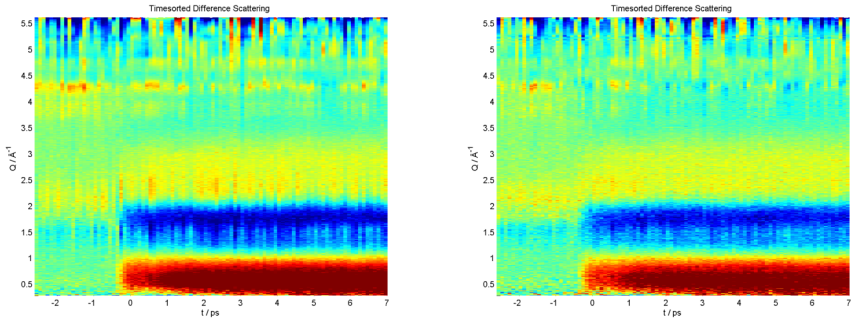

(c) 2D SVD-Correction, without energy scaling

(d) 2D SVD-Correction, with energy scaling

Figure 7.6: The reduced TR-XDS signal from $Ir_2(dimen)_4^{2+}$plotted against time using different corrections.

subtracted and the data has been properly scaled with the incident X-ray energy on a shot-to-shot basis. When comparing the 4 plots in figure 7.6 it can be seen that the 2D-SVD corrections (c-d) yield a much better result, especially when looking at the fluctuations before time 0.

The 2D SVD-correction scheme here has another advantage. The energy scaling mentioned, requires the data to be re-binned, since the Q of each pixel is different for each shot. The re-binning can take place as either reduction to 1D scattering curves or onto a new 2D detector grid. Using the 2D SVD-corrections to account for the energy shift as well, approximates the energy shift as one or

several linear contributions. This is of course an inaccurate description, but it has the advantage of retaining the 1-to-1 pixel correspondence allowing for full analysis on the 2D detector. This is important when implementing the anisotropic analysis, as it requires the full 2D data to extract the structural components (see chapter 8).

7.3 Characterising detector output using 2D SVD

The 2D SVD decomposition of entire detector images is a powerful tool for characterising both the detector and the setup. When applying SVD to a new dataset, it is important to identify a proper mask. If the mask chosen is insufficient, many of the first SVD components will have large contributions from a small region on the detector. However, once a proper mask is chosen no more than 10 components are necessary to give insight into the detector behaviour and setup.

The following sections gives a few examples of conclusions drawn from using 2D SVD.

7.3.1 Mask update

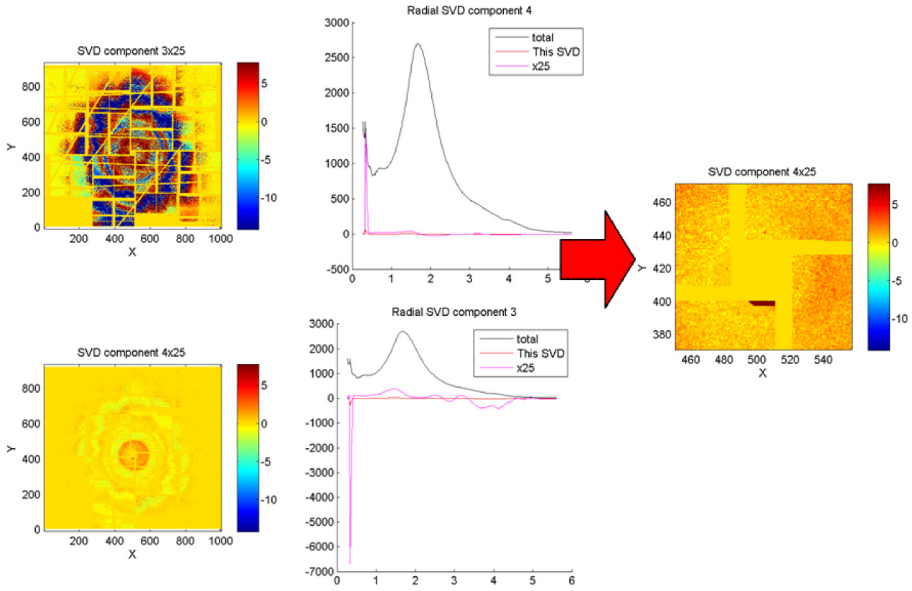

Figure 7.7: The corresponding pixels can easily be located and masked out.

Even though the detector has been masked to the very best of our capabilities, the first result from looking at the 2D SVD components is the large spike at low Q corresponding to fluctuations in the scattered intensity around the direct beam. The large peak may also be due to the beam position movements, known to be $\pm 20 \mu m$. The pixels can easily be masked out, letting us retain the remaining pixels in this Q region. If the pixels are not removed the 1D difference signal would be dominated by these fluctuations at low Q and would not be usable for analysis.

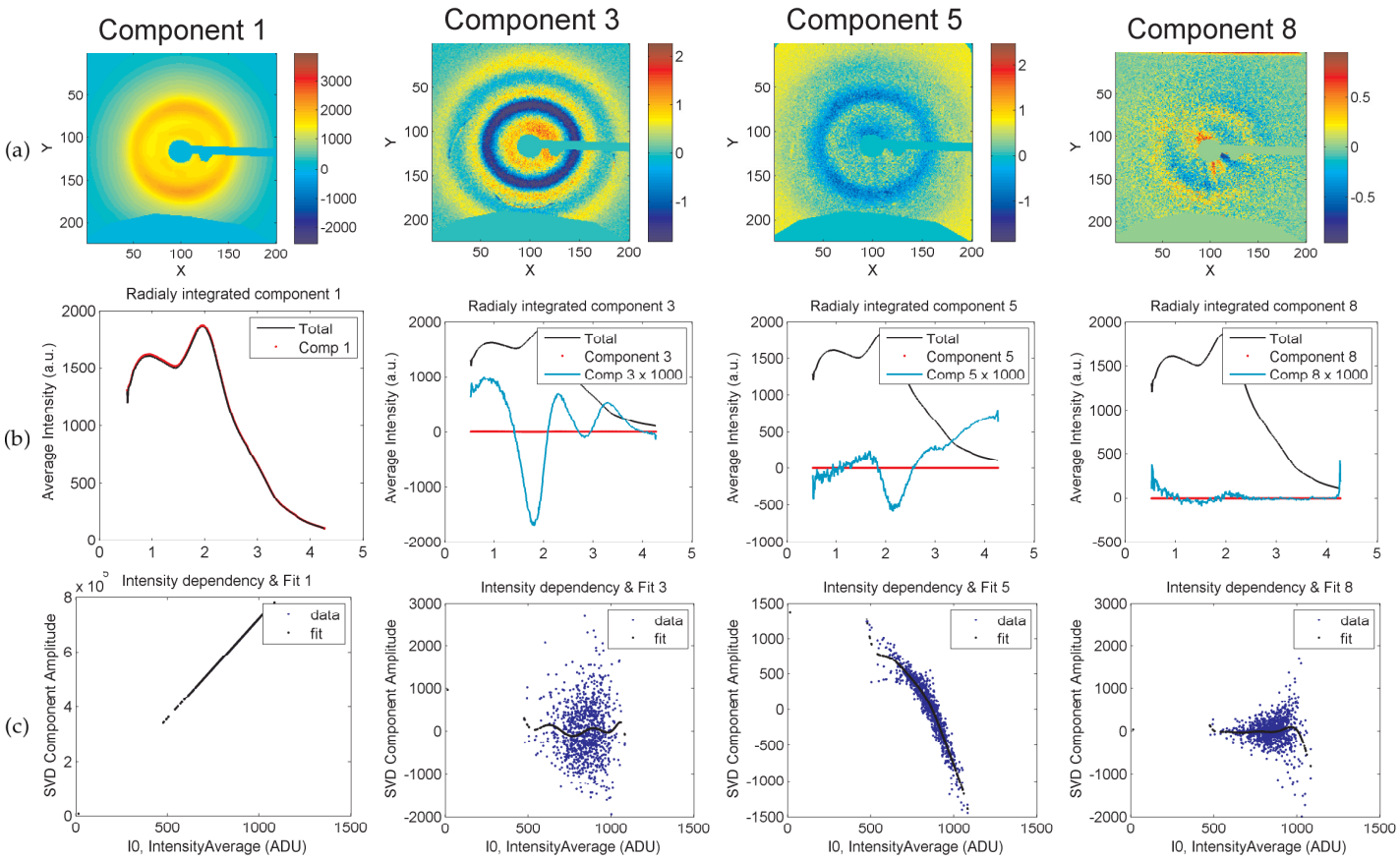

Figure 7.8: Select 2D SVD components for water scattering measured on the new Rayonix HS-170 detector at XPP

7.3.2 Other Detectors

Comparing different detectors is also a very useful approach. In this case, the new Rayonix HS-170 CCD at XPP was tested in order to decide if it was more suitable for TR-XDS measurements, than the CSPAD. The Ebeam values are not available, but component 3 is identified as X-ray energy dependent, due to the shape of the difference curve. Component 5 is an intensity dependent component and component 8 is X-ray scattered from the beamstop. In general, the fluctuations on the Rayonix were similar to those of the CSPAD, and due to the limited size of the detector and experience using it, we decided to use the CSPAD for the most recent experiment. Identifying these components during a beamtime would identify the beamstop as a source of fluctuations and make it possible to clean up the low Q part of the images.

7.3.3 Updated CSPAD

The newest update of the CSPAD shows great improvement (see figure 7.9). It is noted that the 2D images (a) are upside down. Selecting 4 interesting components the following can be seen. Component 3 shows the X-ray energy shift as before, and component 5 shows the first intensity dependent component. It is seen that the large non-linear intensity dependency has been greatly reduced over the 2 years of development, since $Ir_2(dimen)_4^{2+}$was measured in March 2012.

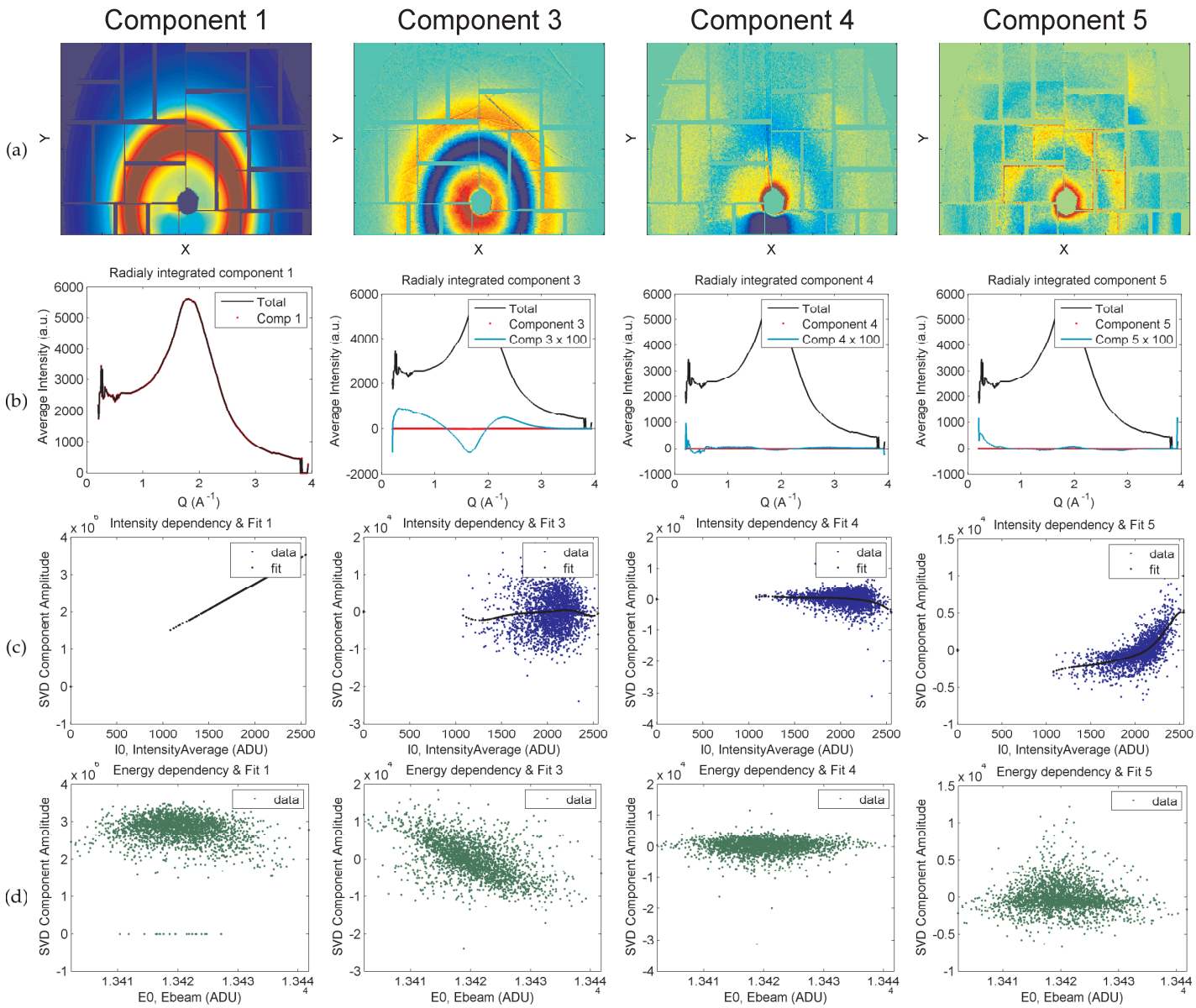

Figure 7.9: Select 2D SVD components for the newly updated version of the CSPAD detector at XPP (February 2014)

Component 4 contains clear scatter from upstream, as the shadow of the liquid jet can be seen. This component is assigned to scatter from the timing tool. As later informed by the staff, the X-ray clean-up slits had been removed explaining the additional scattering. Using 2D SVD on a dataset to identify unpredicted fluctuations in the detector images is a great tool for removing unwanted sources of errors in experiments.

Chapter 8

XFEL experiments - $Ir_2dimen_4^{2+}$ analysis

In this chapter the 2D SVD-Corrections are applied to the $Ir_2(dimen)_4^{2+}$ XFEL data in order to draw some preliminary conclussions from the experiment.

After going through the new 2D workflow (see figure 8.6) and applying 2D SVD-corrections to 20 consecutive scans it is now possible to access exceptional statistics in a scan range from -2 to 8 ps. Finally we can access the corrected data. After the corrections are applied it is not only as the reduced 1D difference scattering curves (as in [**VII**]), but as 200.000 full 2D corrected images.

The 2D images are re-binned into 10fs steps using the information from the timing tool, and the images are averaged in each bin to produce a set of 800 averaged difference scattering images, each containing the average of ∼250 shots. Each 2D image can now be azimuthally integrated as usual but also separated into the 2 components, S_0 and S_2 as described in chapter 5.3 and shown in figure 8.1.

For each time-step the 2D image is separated into the 2 components by taking a given Q bin and plotting the difference scattering ΔS as a function of $P_2(cos(\theta Q))$ where P2 is the second order Legendre polynomial. Doing this for each Q bin produces the 2 difference scattering terms S_0 and S_2 as a function of Q as seen in figure 8.1 and can be repeated for all time-steps producing two difference scattering curves for each time-delay.

Looking at the evolution of the different components, the radially integrated curve and S_0 look similar. But looking at the anisotropic signal S_2 it seems that there are several things happening on the ultra fast time-scales. Initially there is a huge dip just after t_0 followed by a dynamic peak shift for the first 2 ps.
Taking a 2D difference scattering image and comparing it with an anisotropic signal simulated from DFT structures, we find a similar shape and anisotropy (see figure 8.3). The signal from the relaxed excited state is shown in figure 8.3 (b) in some agreement with the 2D difference scattering at later times than 2 ps.

From the calculated anisotropy a much weaker low Q intensity can be seen, when the ligand framework remains static during the Ir-Ir motion. This could help explain the observed anisotropy. This Ir-Ir driven motion is also observed in time-resolved simulations [**V**].

The radially integrated images do not seem to show clear structural dynamics

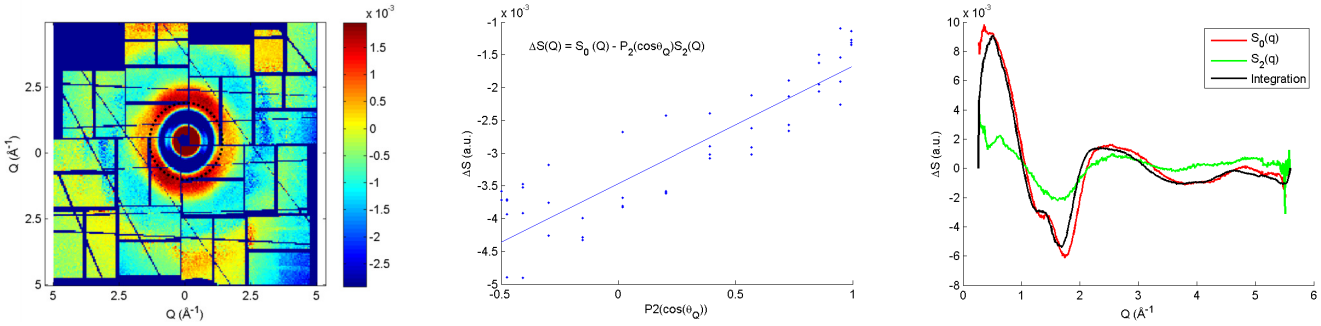

(a) 2D ΔS (b) $\Delta S(Q,\tau) = S_0(Q,\tau) - P_2(cos\theta)S_2(Q,\tau)$ (c) $\Delta S(\tau)$

Figure 8.1: (a) 2D scattering image (b) seperation of the S_0 and S_2 at Q=1.5 (c) The individual components; normal integration, S0 and S2

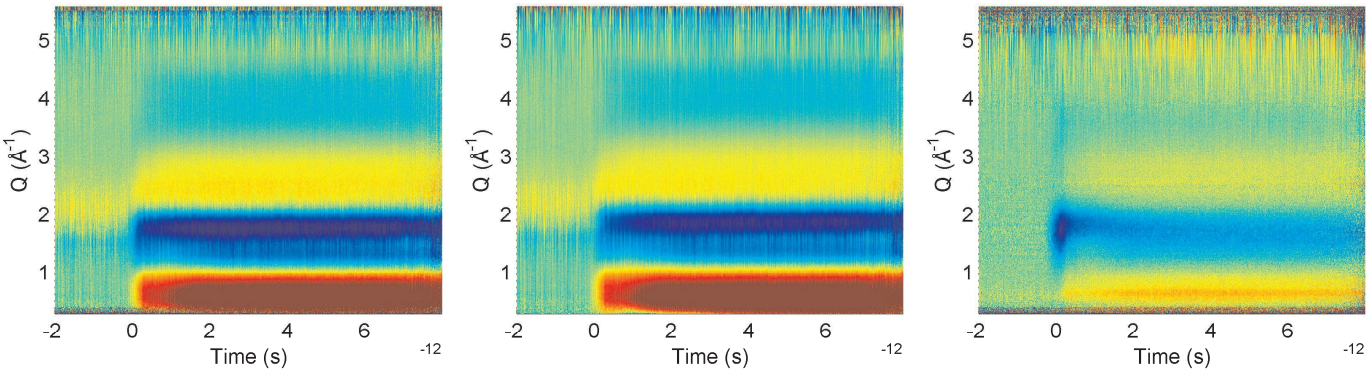

(a) Radially integrated (b) S0 (c) S2

Figure 8.2: Difference scattering over time. (a) Normal radial integration (b) S_0 , the isotropic term (c) S_2 , th anisotropic component of the scattering

in the first ps, except for a grow-in of the main structural signals that persists to synchrotron time-scales.

A quick SVD analysis of S_0 and S_2 yields the following components and dynamics and may hint at what we can expect from the further analysis of the data. The SVD can be seen in figure 8.5.

The SVD of S_0 shows a very clear 1st component very similar to the structural signal measured in [**I**]. Apart from the first component, component 3,5 and 6 have some evolution around t_0 and especially component 3 could be weak structural dynamics.

The same SVD of S_2 shows interesting dynamics in the first 3 components. The kinetics of the components have the same starting point but the evolution differs between them. A dynamically changing signal, would necessitate several linear SVD components mixing to approximate dynamics.

Finally the rotation time of $Ir_2(dimen)_4^{2+}$can be estimated to $\sim 30ps$ based on [83] in which case the slope of component 1 should match this decay time.

The $Ir_2(dimen)_4^{2+}$experiment included optical pumping at two different wavelengths. The data presented here was pumped with 480nm. Currently none of the 580nm data has been corrected. The comparison of the anisotropic signals,

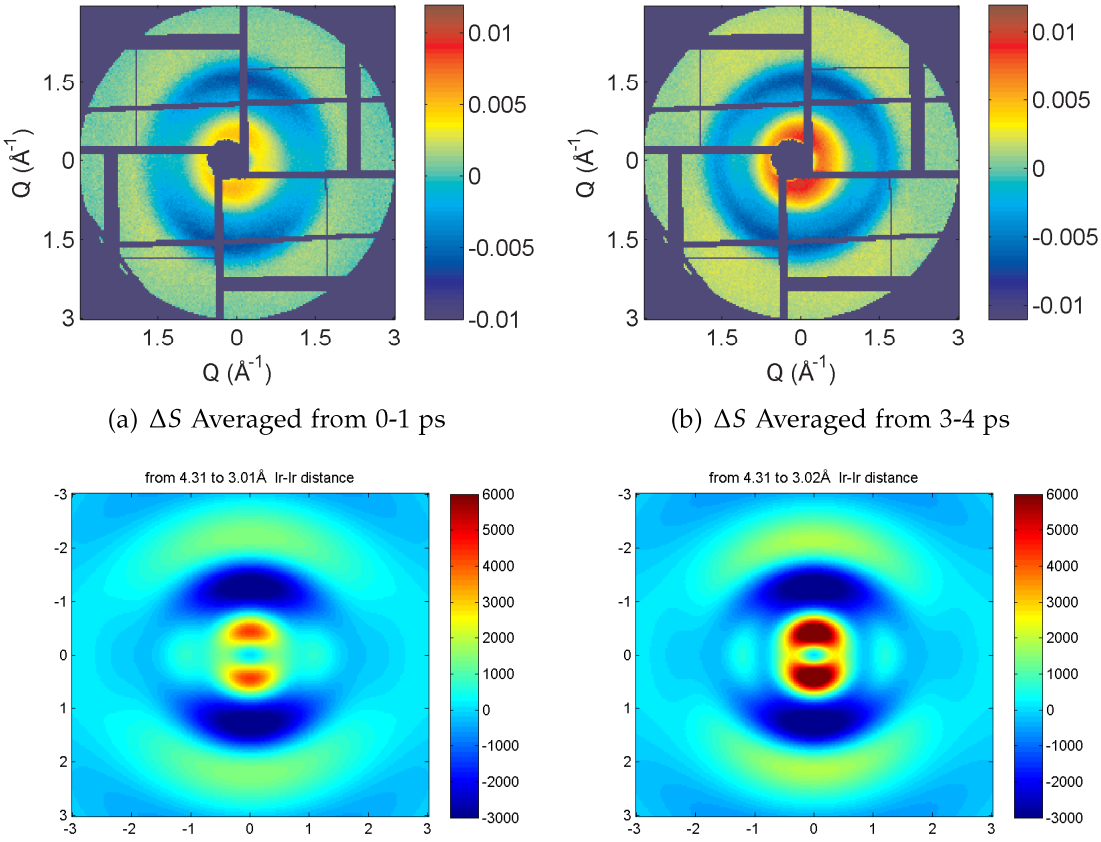

(a) ΔS Averaged from 0-1 ps

(b) ΔS Averaged from 3-4 ps

(c) Simulates scattering from only Ir contracting in $Ir_2(dimen)_4^{2+}$

(d) Simulates scattering from DFT structures of $Ir_2(dimen)_4^{2+}$

Figure 8.3: 2D difference scattering measured on $Ir_2(dimen)_4^{2+}$at early time delays (top). The anisotropic nature of the signal can be seen and shares features with simulated anisotropic scattering images(bottom). (a) Highly anisotropic 2D scattering right at the excitation moment (b) Anisotropic signal stabilises after 2ps (c) Simulated scattering from $Ir_2(dimen)_4^{2+}$where only Ir has moved (b) Simulated scattering from two optimised $Ir_2(dimen)_4^{2+}$structures

as well as the isotropic signals, when pumping at the two different wavelengths, will help disentangle the photo-induced dynamics occurring in this system. It will also help identify the different structures as well as their potential energy surfaces and interplay.

If no coherent structural oscillations are to be found, there will still be interesting information in the comparison and structural analysis of the two excitation wavelengths, as well as the disappearance of anisotropy due to rotational decoherence.

8.1 Further Analysis and conclusions

After two years of work on the $Ir_2(dimen)_4^{2+}$dataset, the 2D SVD-Corrections allows us to remove fluctuations and start analysing the data. Figure 8.6 shows a new updated workflow for XFEL experiments. The 2D SVD correction scheme is significantly more cumbersome than the initial workflow in figure 6.8 as most of

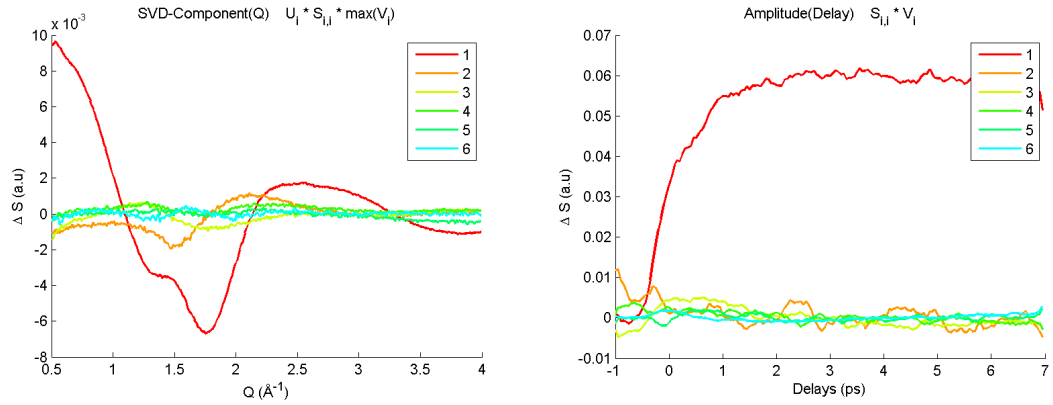

(a) First 6 components

(b) Kinetics of first 6 components

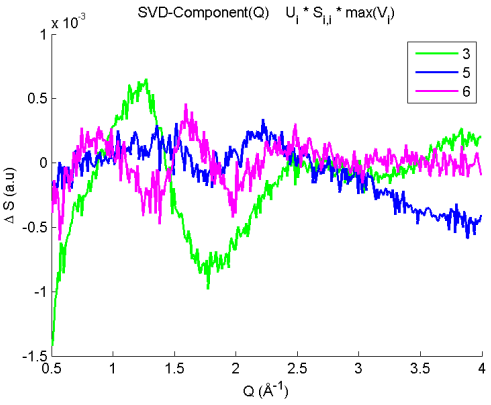

(c) Comp. 3,5,6

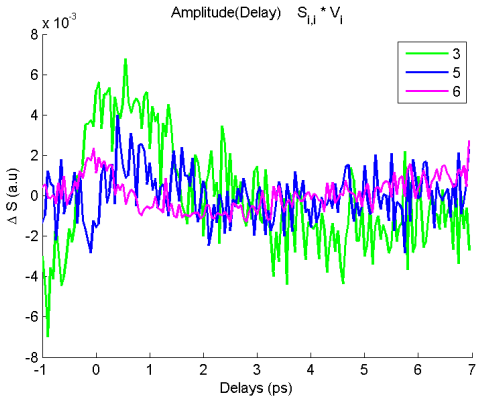

(d) Kinetics Comp. 3,5,6

Figure 8.4: Singular value decomposition of S_0 (top) first 6 components (bottom) components with evolution around t_0 apart from component 1.

the analysis has to remain 2 dimensional. The full 2D dataset cannot be stored in memory so in order to run this reduction, data has to be saved and loaded from disc continuously slowing down the process and taking up a lot of space. Once the data is reduced it will be possible to only store the 1d curves as well as 1 average image from each bin. If this path is chosen the reduction will probably take 10 times what it does now and require machines with ample (TB) temporary storage, but only require additional Silicon time. The cumbersome part is in the manual identification of components until a robust approach is identified.

The systematic approach to the treatment of 2D difference scattering data, allows for the proper anisotropic decomposition of the signal. This is opening a way to systematically enhance the signal from certain parts of the structural dynamics as discussed in section 5.3 within the field of ultra-fast TR-XDS. The $Ir_2(dimen)_4^{2+}$data, in conjunction with the time-resolved computations from A. Dohn et al. [**V**] combined with the work on anisotropy by U. Lorenz et al. [62] will test the waters for what can be measured, simulated and concluded with TR-XDS on the sub-ps time-scale.

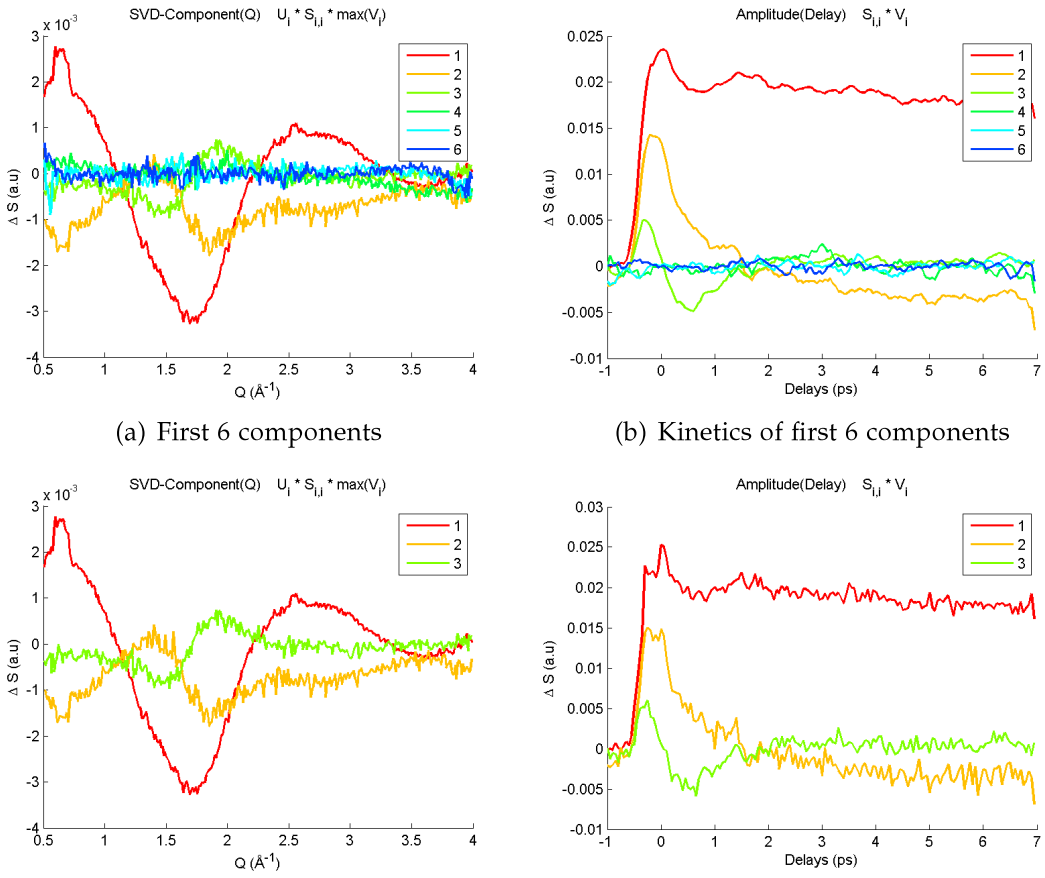

(a) First 6 components

(b) Kinetics of first 6 components

(c) Comp. 1,2,3

(d) Kinetics Comp. 1,2,3

Figure 8.5: Singular value decomposition of S_2 (top) first 6 components (bottom) components with evolution around t_0.

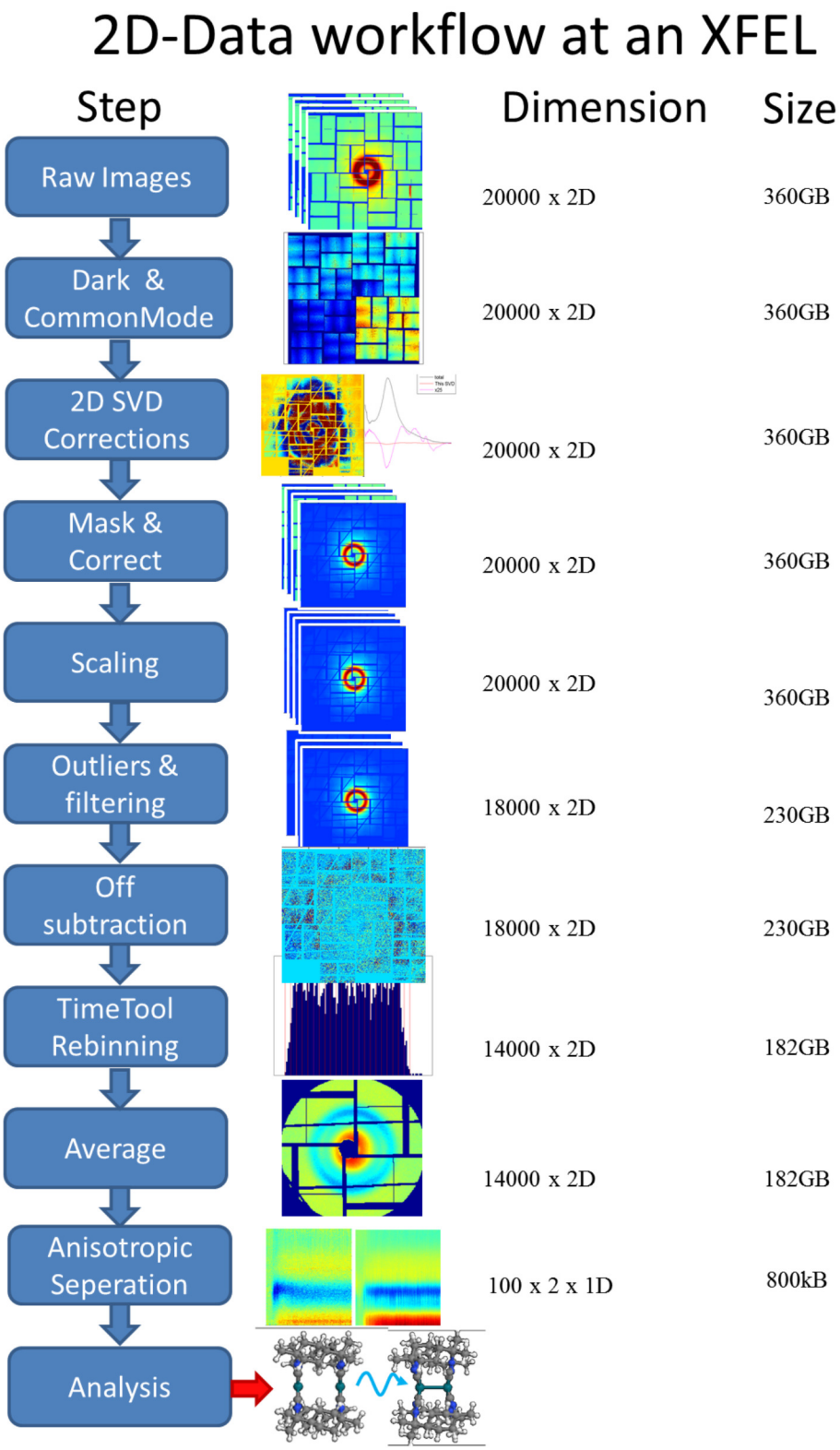

Figure 8.6: Updated workflow for XDS experiments at an XFEL (XPP@LCLS) correcting for energy fluctuations and detector behavior as well as taking anisotropy into account.

Chapter 9

Discussion and Conclusion

This dissertation presents the use of time resolved X-ray Diffuse Scattering at both synchrotron and XFEL X-ray facilities.

TR-XDS measurements on $Rh_2(dimen)_4^{2+}$ show a time-resolved signal corresponding to a large contraction along the Rh-Rh axis as expected from published literature. The measured excitation fraction turned out to be lower than expected but the structural analysis yields results comparable to expectations.

DFT calculations on $Rh_2(dimen)_4^{2+}$ shows good agreement with the result from the TR-XDS. The full 2D Potential Energy Surfaces (PES) for Rh are the result of a years worth of silicon time and provide a good insight and basis for analysis. However, full PES calculations are probably not necessary for all TR-XDS measurements unless they are needed in order to answer specific questions.

The DFT calculations for $Ir_2(dimen)_4^{2+}$ provide a basis for discussing the exited state dynamics, but similar results can be obtained by modelling internal strain by simple spring constants as in [42, 78]. The DFT calculations do not predict the two different ground-state structures measured in [78] and [**I**]. Never the less, the structures resulting from the DFT calculations were a good basis for the TR-XDS analysis, supplying the initial structural guesses used to fit the data. Constraining the structures in the DFT optimisations allows the construction of valid input structures for TR-XDS analysis. The many molecular structures are sufficient to describe the structures in a traditional TR-XDS experiment where the experiment tracks population dynamics of vibrationally cold exited states. For the dynamically changing structures on the atomic-timescale measured at XFELs the wave-packet dynamics as well as the population distributions have to be simulated. The work presented in [**V**] shows the the type of calculations necessary for investigation of molecular dynamics.

The $Ir_2(dimen)_4^{2+}$ experiments at XPP were the first TR-XDS experiment, with access to the atomic time-scale necessary to measure the structural dynamics upon excitation. The timing tool was implemented right before the beamtime as the temporal jitter would smear the time-resolution sufficiently to remove all hope of seeing the structural dynamics predicted with transient optical techniques.

The structural analysis of $Ir_2(dimen)_4^{2+}$ still remains to be done and requires some new approaches compared to TR-XDS at synchtrotrons.

Given the newly developed 2D SVD-Correction approach to identify and

correct the 2D detector images, to account for non-linear intensity dependence as well as X-ray energy fluctuation, the signal-to-noise and stability of the measured data is comparable to data from synchrotrons.

Improving this methodology and applying it to the large amounts of data already taken will reveal the true quality of the underlying difference signals.

Having extracted the $Ir_2(dimen)_4^{2+}$data, it has to be analysed dynamically allowing the structures and distributions of structures to change rapidly on the fs time-scale. A scheme for conducting full structural analysis with the anisotropic components has to be implemented to use the added information and sensitivity of the anisotropic signal S_2 to extract the molecular dynamics.

The lack of clear structural oscillations is still puzzling, from the large changes in the optical measurements as well as the coupling between structure and optical properties identified in the literature. Initially structural oscillations where expected to be hidden under the fluctuations and detector artefacts. Since the 2D SVD corrections extract high quality 2D scattering images and the time-resolution after use of the timing tool is 150fs we should have the resolution to see structural oscillations with a 500fs period as measured for $Ir_2(dimen)_4^{2+}$[43].

However, the information in the TR-XDS signal is different in nature than the transient optical spectra. Therefore, the dynamic structural signal from the entire population distribution may not integrate to well defined regions in Q as they do in energy for optical spectra.

The preliminary anisotropic analysis shows dynamics within the first 2 ps, the dynamic structural analysis of the full anisotropic signal will be of great interest. The continued efforts on the analysis of the data presented here, will start to elucidate the questions that can be answered using TR-XDS on the femtosecond time-scale.

In summary, this work has presented the shift of TR-XDS from synchrotron sources and time-scales to XFELs. Many of the encountered challenges can be specified and solved based on the extremely large amounts data read out at such a facility. New approaches and solutions have to be developed and implemented in a robust fashion before experiments at XFELs will be available to a broader audience. However, The future of XFEL research is bright and with it many interesting questions will be answered over the years to come.

Chapter 10

Future work

The work presented in this dissertation highlights some of the problems arising when moving experiments from one setup to another, where the experimental parameters differ a lot. In this case the increase in time-resolution and X-ray flux brings forth a completely new time-scale on which to apply existing techniques. In addition to all the new possibilities, a comparable amount of challenges also arise.

On the one side, more X-rays greatly increase the things that can be seen in a given amount of time. On the other side, more X-rays also means more to detect accurately within the same time-frame. The sample, optics and detectors are exposed to more photons, setting new requirements for the sample integrity, hardening of electronics as well as the purity and manufacture or replacement of elements in the beam path.

Though many of the challenges faced and solved at LCLS can be applied to all XFELs, other facilities will encounter new problems. The European XFEL will drastically increase the repetition-rate of the X-ray pulses. Once again this will give new technical challenges for the entire XFEL, in addition to the experimental challenges to the users.

During the timespan of the work presented here a large number of improvements have been implemented at LCLS. The general stability of the machine has increased and the beamline staff has improved their skills. The data management, software and computer power has improved, removing bottlenecks and implementing many of the tools necessary for quick feedback and online analysis.

Based on the amount of time put into studying fluctuations of the CSPAD, it is now clear how much the detector staff has improved the CSPAD during the last two years.

Given the XFEL development since the first came online in 2010, many interesting areas can, and will, be improved over the next several years.

10.1 The Sources:

Stability

Running an XFEL requires good technical staff, and as they improve, so will the stability and output of the machine. Allready now Klystron replacement is fast and downtime much less than before.

X-ray energy range

Currently the XFELs are usable up to 10keV, the 3rd harmonic is available but with very low X-ray flux. Increasing the range of the available Hard X-rays will give access to higher resolution in XDS and expand the elemental range for X-ray spectroscopic techniques.

Multiplexing

As shown in [**XII**][**XIII**] beam-splitting using a thin diamond monochromator has been shown, allowing two simultaneous experiments. This results in more available beamtime (corresponding to lower beamtime cost). Currently simultaneous experiments constrain each other a lot, but experiments can be chosen to minimise this problem, along with the ongoing technical improvements. Similarly the European XFEL is working on distributing consecutive pulses and/or pulse-trains to be able to utilise the 27000 pulses/s to their full potential.

Self-Seeding

Self seeding has been shown to greatly decrease the energy bandwidth [59],and as this technique is improved it will increase in popularity. Stability, flux, tune-up time and scanning-ability need to be improved for general use in XDS/XES/XAS experiments.

Availability

As more facilities are constructed and improved to allow multiple experiments at once, XFEL beamtime will be more readily available.

10.2 The Experimental setup:

Thinner jet

A thinner sample jet will increase the time resolution for liquid experiments. Many coherent structural and electronic dynamics occur with vibrational timescales. Therefore, better time-resolution will increase the dynamics that can be studied and make dynamics easier to separate.

Better detectors and detection schemes

As the CSPAD has improved, several other detectors are being developed both for use at LCLS and other facilities. This is exemplified with the LPD developed for European XFEL [84] and the MPCCD development at SACLA [85]. The

collaborative effort will make fast repetition-rate integrating detectors more readily available. Additionally, new detection schemes will appear, such as the energy dispersive von Hamos spectrometer [86], the single shot transmissive X-ray spectrometer [66] or a zone-plate for specific partial fluorescence yield detection [87].

Fast sample changes

The experimental setup will improve to minimise the necessary sample volume, as well as identify the best components and decrease the time needed for sample changes.

Sample delivery systems

Other sample delivery systems are under development. XFEL protein crystallography has had great success with new injection systems. The high repetition rate at new XFEL sources will also require faster flow speeds if the pumped sample volume needs to be replenished between consecutive shots.

10.3 The Techniques and Tools:

New interesting and relevant samples

Several of the first experiments at XFELs where based on model systems in order to show the applicability of the techniques at fs time-scales, and identify the possibilities. As the facility and experiments become more established, more relevant samples will be studied. For recent TR-XDS proposals there has been a general shift toward more relevant samples, such as charge transfer molecules and solvent interactions as well as dyes for use in solar-cells.

New techniques and applications

With the increased performance of XFELs, new techniques are sure to develop, niche techniques evolve as well as novel applications appear. Exemplified with TR-XDS, Anomalous TR-XDS will benefit from the increased flux and tuneability of the XFEL. This will also improve the interplay between XDS, XAS and RIXS as the incoming X-ray energy will be scanned.

Multiple simultaneous techniques

As shown with the recent work on combined techniques, simultaneous combination of different tecniques holds great prommise. As the interest and implementations of these improve, more experiments will utilise the combined setups to extract as much information as possible [12]. As shown in [**VII**],[**IV**],[**XVIII**],[**II**],[**VI**], as well as more recent experiments simultaneous XDS/XES requires little more time during the beamtime, as the requirements for the two techniques are very similar. Additional use of XAS/RIXS requires shifting to monochromatic X-ray beam, but the full interplay of techniques allows for excellent separation of the many degrees of freedom in the molecular ensemble.

10.4 The computer software and hardware:

Converge to standard packages

As the technical needs become more clear and defined, the applied methods and software implementations will converge toward something more stable, robust as well as partially integrated at the facilities.

Speed

Better utilisation of hardware and better algorithms will increase the reduction and analysis speed.

Increased hardware performance: Parralel, GPU, transfer speeds, fast storage media

Hardware development, as well as identification of the bottlenecks will also improve the overall time.

10.5 Final perspective

Because the facilities are also improving, there will be a constant necessary development and ballance between the XFEL output and data processing. Increased data acquisition also increases the data amount, as well as the strain on all the previously identified bottlenecks.

Currently a typical scan at XPP is a 100GB file taken in 5 minutes at 120Hz, containing 36000 shots. The XFE beamline at European XFEL will accumulate 500 images at 10 Hz repetition rate on a 1000x1000 LPD detector. This proposed repetition rate will produce 20 times the data resulting in 400GB/minute. Even at a 30% duty cycle, as was run at the most recent XPP beamtime, the entire European XFEL storage of 10 PB will be full in 50 days from the XFE beamline alone.

The challenges, as well as possibilities arriving with such an additional increase in everything, will probably keep us all occupied for some time.

Bibliography

1. nobleprize.org, *Nobel prize in chemistry*, web (1999), URL http://www.nobelprize.org/nobel_prizes/chemistry/laureates/1999/press.html.

2. M. Wulff, S. Bratos, A. Plech, R. Vuilleumier, F. Mirloup, M. Lorenc, Q. Kong, and H. Ihee, The Journal of chemical physics **124**, 034501 (2006), ISSN 0021-9606, URL http://www.ncbi.nlm.nih.gov/pubmed/16438591.

3. T. K. Kim, J. H. Lee, M. Wulff, Q. Y. Kong, and H. Ihee, Chemphyschem **10**, 1958 (2009).

4. H. Ihee, M. Wulff, J. Kim, and S.-i. Adachi, INTERNATIONAL REVIEWS IN PHYSICAL CHEMISTRY **29**, 453 (2010), ISSN 0144235X, 1366591X, 1366591x, 0144-235X, 0144235x.

5. H. Jaffe and A. Miller, Journal of Chemical Education **43**, 469 (1966), URL http://pubs.acs.org/doi/abs/10.1021/ed043p469.

6. G. Salvato-Vallverdu, *The perrin - jablonski diagram* (2009), URL http://www.texample.net/tikz/examples/.

7. B. Valeur, *Molecular Fluorescence. Principles and Applications.* (Wiley, Weinheim, Germany, 2002), 1st ed.

8. J. Als-Nielsen and D. McMorrow, *Elements of Modern X-Ray Physics* (Wiley, West Sussex, England, 2001), 1st ed.

9. W. Commons, *A diagram of the em spectrum* (2007), file: EmSpectrum.png, URL http://en.wikipedia.org/wiki/File:EM_Spectrum_Properties_edit.svg.

10. H. Winick, Journal of synchrotron radiation pp. 1–12 (1998), URL http://scripts.iucr.org/cgi-bin/paper?S0909049597018761.

11. H. N. Chapman, P. Fromme, A. Barty, T. a. White, R. a. Kirian, A. Aquila, M. S. Hunter, J. Schulz, D. P. DePonte, U. Weierstall, et al., Nature **470**, 73 (2011), ISSN 1476-4687, URL http://www.pubmedcentral.nih.gov/articlerender.fcgi?artid=3429598&tool=pmcentrez&rendertype=abstract.

12. J. Kern, R. Alonso-Mori, R. Tran, J. Hattne, R. J. Gildea, N. Echols, C. Glöckner, J. Hellmich, H. Laksmono, R. G. Sierra, et al., Science (New York, N.Y.) **340**, 491 (2013), ISSN 1095-9203, URL http://www.ncbi.nlm.nih.gov/pubmed/23413188.

13. L. Young, E. P. Kanter, B. Krässig, Y. Li, a. M. March, S. T. Pratt, R. Santra, S. H. Southworth, N. Rohringer, L. F. Dimauro, et al., Nature **466**, 56 (2010), ISSN 1476-4687, URL http://www.ncbi.nlm.nih.gov/pubmed/20596013.

14. M. M. Seibert, T. Ekeberg, F. R. N. C. Maia, M. Svenda, J. Andreasson, O. Joensson, D. Odic, B. Iwan, A. Rocker, D. Westphal, et al., NATURE **470**, 78 (2011), ISSN 00280836, 14764687, 0028-0836.

15. J. N. Clark, L. Beitra, G. Xiong, A. Higginbotham, D. M. Fritz, H. T. Lemke, D. Zhu, M. Chollet, G. J. Williams, M. Messerschmidt, et al., Science (New York, N.Y.) (2013), ISSN 00368075, 10959203.

16. P. Emma, R. Akre, J. Arthur, R. Bionta, C. Bostedt, J. Bozek, A. Brachmann, P. Bucksbaum, R. Coffee, F. Decker, et al., Nature Photonics **4**, 641 (2010).

17. G. R. Jr., *A growth spurt for x-ray lasers* (2013), URL https://news.slac.stanford.edu/features/growth-spurt-x-ray-lasers.

18. F. Hajdu, Acta Crystallographica Section a-Crystal Physics Diffraction Theoretical and General Crystallography **28**, 250 (1972).

19. G. Palinkas, Acta Crystallographica Section A **29**, 10 (1973).

20. M. Newville, University of Chicago (USA)[http://xafs.org (2004), URL http://franklin.chem.colostate.edu/nel/XASTutorials.pdf.

21. P. Glatzel and U. Bergmann, Coordination Chemistry Reviews **249**, 65 (2005), ISSN 00108545, URL http://linkinghub.elsevier.com/retrieve/pii/S0010854504001146.

22. G. Hura, J. M. Sorenson, R. M. Glaeser, and T. Head-Gordon, The Journal of Chemical Physics **113**, 9140 (2000), ISSN 00219606, URL http://link.aip.org/link/JCPSA6/v113/i20/p9140/s1&Agg=doi.

23. P. Bösecke and O. Diat, Journal of Applied Crystallography **30**, 867 (1997), ISSN 00218898, URL http://scripts.iucr.org/cgi-bin/paper?S0021889897001647.

24. B. R. Pauw, Journal of physics. Condensed matter : an Institute of Physics journal **25**, 383201 (2013), ISSN 1361-648X, URL http://www.ncbi.nlm.nih.gov/pubmed/23988669.

25. L. B. Skinner, C. Huang, D. Schlesinger, L. G. M. Pettersson, A. Nilsson, and C. J. Benmore, The Journal of chemical physics **138**, 074506 (2013), ISSN 1089-7690, URL http://www.ncbi.nlm.nih.gov/pubmed/23445023.

26. M. Christensen, K. Haldrup, K. Bechgaard, R. Feidenhans'l, Q. Y. Kong, M. Cammarata, M. Lo Russo, M. Wulff, N. Harrit, and M. M. Nielsen, Journal of the American Chemical Society **131**, 502 (2009).

27. P. Anfinrud and F. Schotte, SCIENCE -NEW YORK THEN WASHINGTON- **309**, 1192 (2005), ISSN 0036-8075.

28. Q. Kong, M. Wulff, J. H. Lee, S. Bratos, and H. Ihee, JOURNAL OF THE AMERICAN CHEMICAL SOCIETY **129**, 13584 (2007), ISSN 00027863, 15205126.

29. Q. Kong, J. H. Lee, A. Plech, M. Wulff, H. Ihee, and M. H. J. Koch, Angewandte Chemie (International ed. in English) **47**, 5550 (2008), ISSN 1521-3773, URL http://www.ncbi.nlm.nih.gov/pubmed/18563771.

30. M. Cammarata, M. Levantino, F. Schotte, P. A. Anfinrud, F. Ewald, J. Choi, A. Cupane, M. Wulff, and H. Ihee, Nature Methods **5**, 881 (2008).

31. K. Haldrup, M. Christensen, and M. M. Nielsen, Acta Crystallographica Section A **66**, 261 (2010).

32. M. Cammarata, M. Lorenc, T. K. Kim, J. H. Lee, Q. Y. Kong, E. Pontecorvo, M. Lo Russo, G. Schiro, A. Cupane, M. Wulff, et al., Journal of Chemical Physics **124** (2006).

33. Finocchi, Fabio (2008).

34. L. M. Lawson Daku and A. Hauser, The Journal of Physical Chemistry Letters **1**, 1830 (2010), ISSN 1948-7185, URL http://pubs.acs.org/doi/abs/10.1021/jz100548m.

35. D. Jacquemin, B. Mennucci, and C. Adamo, PHYSICAL CHEMISTRY CHEMICAL PHYSICS -CAMBRIDGE- ROYAL SOCIETY OF CHEMISTRY **13**, 16987 (2011), ISSN 1463-9076.

36. C. Adamo and V. Barone, The Journal of Chemical Physics **110**, 6158 (1999).

37. C. Adamo and V. Barone, Theoretical Chemistry Accounts **105**, 169 (2000).

38. K. Haldrup, M. Christensen, M. Cammarata, Q. Y. Kong, M. Wulff, S. O. Mariager, K. Bechgaard, R. Feidenhans'l, N. Harrit, and M. M. Nielsen, Angewandte Chemie-International Edition **48**, 4180 (2009).

39. V. Pham, I. Tavernelli, C. Milne, R. van der Veen, P. D'Angelo, C. Bressler, and M. Chergui, Chemical Physics **371**, 24 (2010), ISSN 03010104, URL http://linkinghub.elsevier.com/retrieve/pii/S0301010410001163.

40. V.-T. Pham, T. J. Penfold, R. M. van der Veen, F. Lima, A. El Nahhas, S. L. Johnson, P. Beaud, R. Abela, C. Bressler, I. Tavernelli, et al., Journal of the American Chemical Society **133**, 12740 (2011), ISSN 1520-5126, URL http://www.ncbi.nlm.nih.gov/pubmed/21740023.

41. M. Christensen, K. Haldrup, K. S. Kjaer, M. Cammarata, M. Wulff, K. Bechgaard, H. Weihe, N. H. Harrit, and M. M. Nielsen, Physical Chemistry Chemical Physics **12**, 6921 (2010).

42. V. M. Miskowski, S. F. Rice, H. B. Gray, R. F. Dallinger, S. J. Milder, M. G. Hill, C. L. Exstrom, and K. R. Mann, Inorganic Chemistry **33**, 2799 (1994).

43. T. Harlang, Master's thesis, Uiversity of Copenhagen (2010).

44. P. Coppens, O. Gerlits, I. I. Vorontsov, A. Y. Kovalevsky, Y. S. Chen, T. Graber, M. Gembicky, and I. V. Novozhilova, Chemical Communications **19**, 2144 (2004).

45. S. F. Rice and H. B. Gray, Journal of the American Chemical Society **103**, 1593 (1981).

46. S. F. Rice, S. J. Milder, and H. B. Gray, Coordination Chemistry Reviews **43**, 349 (1982).

47. J. J. Stace, K. D. Lambert, J. A. Krause, and W. B. Connick, Inorganic Chemistry **45**, 9123 (2006).

48. M. R. Rhodes and K. R. Mann, Inorganic Chemistry **23**, 2053 (1984).

49. C. L. Exstrom, D. Britton, K. R. Mann, M. G. Hill, V. M. Miskowski, W. P. Schaefer, H. B. Gray, and W. M. Lamanna, Inorganic Chemistry **35**, 549 (1996).

50. K. R. Mann, N. S. Lewis, V. M. Miskowski, D. K. Erwin, G. S. Hammond, and H. B. Gray, Journal of the American Chemical Society **99**, 5525 (1977).

51. K. R. Mann, R. A. Bell, and H. B. Gray, Inorganic Chemistry **18**, 2671 (1979).

52. A. Sykes and K. R. Mann, Journal of the American Chemical Society **110**, 8252 (1988).

53. D. M. Roundhill, H. B. Gray, and C. M. Che, Accounts of Chemical Research **22**, 55 (1989).

54. F. Neese, Wiley Interdisciplinary Reviews: Computational Molecular Science **2**, 73 (2012), ISSN 1759-0884, URL http://dx.doi.org/10.1002/wcms.81.

55. T. B. van Driel, *Master Thesis* (Niels Bohr Institute, University of Copenhagen, 2010).

56. K. R. Mann, B. M. Hunter, C. L. Exstrom, R. M. Villahermosa, M. G. Hill, and H. B. Gray, Inorganic Chemistry **51**, 6898 (2012), ISSN 00201669, 1520510x.

57. J. R. Taylor, *An Introduction to Error Analysis: The Study of Uncertainties in Physical Measurements* (University Science Books, 1997).

58. P. R. Ribic and G. Margaritondo, Journal of Physics D: Applied Physics **45**, 213001 (2012), URL http://stacks.iop.org/0022-3727/45/i=21/a=213001.

59. J. Amann, W. Berg, V. Blank, F. J. Decker, Y. Ding, P. Emma, Y. Feng, J. Frisch, D. Fritz, J. Hastings, et al., NATURE PHOTONICS **6**, 693 (2012), ISSN 17494885, 17494893.

60. H. T. Lemke, C. Bressler, L. X. Chen, D. M. Fritz, K. J. Gaffney, A. Galler, W. Gawelda, K. Haldrup, R. W. Hartsock, H. Ihee, et al., The Journal of Physical Chemistry A **117**, 735 (2013), http://pubs.acs.org/doi/pdf/10.1021/jp312559h, URL http://pubs.acs.org/doi/abs/10.1021/jp312559h.

61. J. Kim, K. H. Kim, J. G. Kim, T. W. Kim, Y. Kim, and H. Ihee, J Phys Chem Lett. pp. 350–356 (2011).

62. U. Lorenz, K. B. Møller, and N. E. Henriksen, New Journal of Physics **12**, 113022 (2010), ISSN 1367-2630, URL http://stacks.iop.org/1367-2630/12/i=11/a=113022?key=crossref.0b33b3394cb64e18c7744ae893b8a31d.

63. N. E. Henriksen and K. B. Moller, Journal of Physical Chemistry B **112**, 558 (2008).

64. R. W. Hendler and R. I. Shrager, Journal of biochemical and biophysical methods **28**, 1 (1994), ISSN 0165-022X, URL http://www.ncbi.nlm.nih.gov/pubmed/8151067.

65. K. Haldrup, accepted in Philosophical Transactions B.

66. D. Zhu, M. Cammarata, J. Feldkamp, D. M. Fritz, J. Hastings, S. Lee, H. T. Lemke, A. Robert, J. Turner, and Y. Feng, Journal of Physics - Conference Series **425**, 052033 (2013), ISSN 17426588, 17426596.

67. M. Harmand, R. Coffee, M. R. Bionta, M. Chollet, D. French, D. Zhu, D. M. Fritz, H. T. Lemke, N. Medvedev, B. Ziaja, et al., Nature Photonics **7**, 215 (2013), URL http://dx.doi.org/10.1038/nphoton.2013.11.

68. O. Krupin, M. Trigo, W. F. Schlotter, M. Beye, F. Sorgenfrei, J. J. Turner, D. a. Reis, N. Gerken, S. Lee, W. S. Lee, et al., Optics express **20**, 11396 (2012), ISSN 1094-4087, URL http://www.ncbi.nlm.nih.gov/pubmed/22565760.

69. M. Beye, O. Krupin, G. Hays, a. H. Reid, D. Rupp, S. D. Jong, S. Lee, W.-S. Lee, Y.-D. Chuang, R. Coffee, et al., Applied Physics Letters **100**, 121108 (2012), ISSN 00036951.

70. H. T. Lemke, M. Weaver, M. Chollet, J. Robinson, J. M. Glownia, D. Zhu, M. R. Bionta, M. Cammarata, M. Harmand, R. N. Coffee, et al., Proc. SPIE **8778**, 87780S (2013), URL http://dx.doi.org/10.1117/12.2017603.

71. D. M. Fritz, D. a. Reis, B. Adams, R. a. Akre, J. Arthur, C. Blome, P. H. Bucksbaum, a. L. Cavalieri, S. Engemann, S. Fahy, et al., Science (New York, N.Y.) **315**, 633 (2007), ISSN 1095-9203, URL http://www.ncbi.nlm.nih.gov/pubmed/17272718.

72. S. Herrmann, S. Boutet, B. Duda, D. Fritz, G. Haller, P. Hart, R. Herbst, C. Kenney, H. Lemke, M. Messerschmidt, et al., Nuclear Instruments and Methods in Physics Research Section A: Accelerators, Spectrometers, Detectors and Associated Equipment **718**, 550 (2013), ISSN 01689002, URL http://linkinghub.elsevier.com/retrieve/pii/S0168900213001496.

73. P. Hart, S. Boutet, G. Carini, M. Dubrovin, B. Duda, D. Fritz, G. Haller, R. Herbst, S. Herrmann, C. Kenney, et al., Proc. SPIE **8504**, 85040C (2012), URL http://proceedings.spiedigitallibrary.org/proceeding.aspx?articleid=1381232.

74. P. Hart, G. Carini, A. Dragone, K. J. Morse, M. Nordb, J. P. N. V. Bakee, M. Weaverl, and G. I. Williams, IEEE Nuclear Science Symposium and Medical Imaging Conference Record pp. 538–541 (2012).

75. C. Bressler, C. Milne, V.-T. Pham, A. ElNahhas, R. M. van der Veen, W. Gawelda, S. Johnson, P. Beaud, D. Grolimund, M. Kaiser, et al., Science **323**, 489 (2009), http://www.sciencemag.org/content/323/5913/489.full.pdf, URL http://www.sciencemag.org/content/323/5913/489.abstract.

76. R. W. Schoenlein, Science **287**, 2237 (2000), ISSN 00368075, URL http://www.sciencemag.org/cgi/doi/10.1126/science.287.5461.2237.

77. A. G. Sykes and K. R. Mann, Journal of the American Chemical Society **112**, 7247 (1990).

78. R. W. Hartsock, W. Zhang, M. G. Hill, B. Sabat, and K. J. Gaffney, The journal of physical chemistry. A **115**, 2920 (2011), ISSN 1520-5215, URL http://www.ncbi.nlm.nih.gov/pubmed/21428426.

79. T. J. Penfold, I. Tavernelli, R. Abela, M. Chergui, and U. Rothlisberger, New Journal of Physics **14**, 113002 (2012), ISSN 1367-2630, URL http://stacks.iop.org/1367-2630/14/i=11/a=113002?key=crossref.f58d09ceb7b22095fd290a7ee87b6428.

80. M. Brand, LINEAR ALGEBRA AND ITS APPLICATIONS **415**, 20 (2006), ISSN 00243795, 18731856, 0024-3795.

81. D. Wingate, *Incremental svd updates*, web (2007), URL http://www.mit.edu/~wingated/resources.html.

82. R. R. Wilcox, Introduction To Robust Estimation and Hypothesis Testing pp. – (2012).

83. M. Horng, J. Gardecki, and M. Maroncelli, JOURNAL OF PHYSICAL CHEMISTRY a **101**, 1030 (1997), ISSN 10895639, 15205215, 1089-5639.

84. S. Hauf, T. Nicholls, D. Zhu, P. Fischer, M. Chollet, G. A. Carini, M. Turcato, S. Nelson, C. Angelsen, J. Coughlan, et al., Journal of Instrumentation **8**, (2013), ISSN 17480221.

85. xfel.riken.jp, *Instructions of mpccd detector specification and data format*, web (2012), URL http://xfel.riken.jp/users/mpccd_detector/instructions_ver1.0_revised.pdf.

86. R. Alonso-Mori, J. Kern, D. Sokaras, T.-C. Weng, D. Nordlund, R. Tran, P. Montanez, J. Delor, V. K. Yachandra, J. Yano, et al., REVIEW OF SCIENTIFIC INSTRUMENTS **83**, (2012), ISSN 00346748, 10897623.

87. R. Mitzner, J. Rehanek, J. Kern, S. Gul, J. Hattne, T. Taguchi, R. Alonso-Mori, R. Tran, C. Weniger, H. Schroeder, et al., JOURNAL OF PHYSICAL CHEMISTRY LETTERS **4**, 3641 (2013), ISSN 19487185.

Comments on the Papers

I **Bond shortening (1.4 Å) in the singlet and triplet excited states of [Ir2(dimen)4]2+ in solution determined by time-resolved X-ray scattering.**
I was involved in computational chemistry, experimental setup, data acquisition, data reduction and data analysis.

II **Guest-host interactions investigated by time-resolved X-ray spectroscopies and scattering at MHz rates solvation dynamics and photoinduced spin transition in aqueous Fe(bipy)32+.**
I was involved in experimental setup, data acquisition and data reduction.

III **Introducing a standard method for experimental determination of the solvent response in laser pump,X-ray probe time-resolved wide-angle X-ray scattering experiments on systems in solution**
I was involved in experimental setup, data acquisition, data reduction and data analysis.

IV **Probing the Nonequilibrium Dynamics of Photoinduced Electron Transfer with Femtosecond X-ray Pulses**
I was involved in experimental setup, data acquisition, data reduction and data analysis.

V **Direct dynamics studies of a binuclear metal complex in solution: The interplay between vibrational relaxation, coherence decay and solvation effects.**
I was involved in DFT Structure optimisations in ORCA and discussions

VI **Experimental and theoretical investigation of the photoinduced high-spin state of the [Fe(terpy)$_2$]$^{2+}$ complex.**
I was involved in experimental setup, data acquisition and data reduction.

VII **Fingerprinting and tracking sub-picosecond spin- and solvation dynamics of the spin-crossover complex [Fe(bpy)3]2+ by simultaneous ultrafast X-ray emission and X-ray scattering**
I was involved in experimental setup, data acquisition, data reduction and data analysis.

VIII **Ligand and Solvent Manipulation of Electronic Excited State Spin Dynamics in Iron Coordination Complexes**
I was involved in experimental setup, data acquisition and data reduction.

IX **Theoretical study of the triplet excited state of PtPOP and the exciplexes M-PtPOP (M=Tl, Ag) in solution and comparison with ultrafast X-ray scattering results**
I was involved in ADF calculations on PtPOP, X-PtPOP and X2-PtPOP.

X **Spin-state studies with XES and RIXS: From static to ultrafast**
I was involved in computational chemistry and experimental setup.

XI **Toward Highlighting the Ultrafast Electron Transfer Dynamics at the Optically Dark Sites of Photocatalysts**
I was involved in experimental setup, data acquisition, data reduction and data analysis.

XII **Recent development of thin diamond crystals for X-ray FEL beam-sharing**
I was involved in experimental setup and data acquisition.

XIII **Performance of a beam-multiplexing diamond crystal monochromator at the Linac Coherent Light Source Recent development of thin diamond crystals for X-ray FEL beam-sharing**
I was involved in experimental setup and data acquisition.

XIV **A protein quake through a photosynthetic reaction centre**
I was involved in discussions and interpretation of ultra-fast heating in water.

XV **Bond shortening of Rh_2dimen$_4^{2+}$ upon excitation studied with Time-Resolved X-ray Diffuse Scattering**
I was involved in computational chemistry, experimental setup, data acquisition, data reduction and data analysis.

XVI **Disentangling x-ray detector data at an XFEL**
I was involved in experimental setup, data acquisition, data reduction and data analysis.

XVII **Coherent Structural Dynamics in a Solution Phase Coordination Complex Studied with Time-Resolved X-ray Diffuse Scattering**
I was involved in computational chemistry, experimental setup, data acquisition, data reduction and data analysis.

XVIII **Structural Characterization of Photo Induced Electron Transfer in a Bimetallic Complex**
I was involved in experimental setup, data acquisition, data reduction and data analysis.

XIX **Watching a Capacitor at Work - Molecular Scale Structure and Dynamics at an Ionic Liquid/Electrode Interface**
I was involved in experimental setup, data acquisition, data reduction and data analysis.

XX **Origin of piezoelectricity in ferroelectric PVDF-TrFE capacitors**
I was involved in experimental setup, data acquisition, data reduction and data analysis.

Papers

Paper I

Bond shortening (1.4 Å) in the singlet and triplet excited states of [Ir2(dimen)4]2+ in solution determined by time-resolved X-ray scattering.

Kristoffer Haldrup, Tobias Harlang, Morten Christensen, Asmus Dohn, **Tim Brandt van Driel**, Kasper Skov Kjær, Niels Harrit, Johan Vibenholt, Laurent Guerin, Michael Wulff and Martin Meedom Nielsen.

Inorganic chemistry **50 (19)**, 9329-36(2011).

Inorganic Chemistry

ARTICLE

pubs.acs.org/IC

Bond Shortening (1.4 Å) in the Singlet and Triplet Excited States of $[Ir_2(dimen)_4]^{2+}$ in Solution Determined by Time-Resolved X-ray Scattering

Kristoffer Haldrup,*[,†] Tobias Harlang,[‡] Morten Christensen,[‡,§] Asmus Dohn,[‡] Tim Brandt van Driel,[‡] Kasper Skov Kjær,[‡] Niels Harrit,[‡,§] Johan Vibenholt,[§] Laurent Guerin,[∥] Michael Wulff,[∥] and Martin Meedom Nielsen[†]

[†]Centre for Molecular Movies, Technical University of Denmark, Risø National Laboratory, Materials Department, Roskilde, Denmark

[‡]Centre for Molecular Movies and [§]Chemistry Department, University of Copenhagen, Nano Science Centre, Copenhagen, Denmark

[∥]European Synchrotron Radiation Facility, Grenoble Cedex 38043, France

Supporting Information

ABSTRACT: Ground- and excited-state structures of the bimetallic, ligand-bridged compound $Ir_2(dimen)_4^{2+}$ are investigated in acetonitrile by means of time-resolved X-ray scattering. Following excitation by 2 ps laser pulses at 390 nm, analysis of difference scattering patterns obtained at eight different time delays from 250 ps to 300 ns yields a triplet excited-state distance between the two Ir atoms of 2.90(2) Å and a triplet excited-state lifetime of 410(70) ns. A model incorporating the presence of two ground-state structures differing in Ir−Ir separation is demonstrated to fit the obtained data very well, in agreement with previous spectroscopic investigations. Two ground-state isomers with Ir−Ir separations of 3.60(9) and 4.3(1) Å are found to contribute equally to the difference scattering signal at short time delays. Further studies demonstrate the feasibility of increasing the effective time resolution from the ∼100 ps probe width down to the 10 ps regime by positioning the laser pump pulse at selected points in the X-ray probe pulse. This approach is used to investigate the structures of both the singlet and the triplet excited states of $Ir_2(dimen)_4^{2+}$.

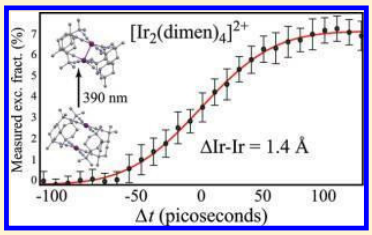

INTRODUCTION

Since their first synthesis in 1976,[1] the binuclear ligand-bridged "windmill" complexes of the general form $M_2(bridge)_4^{2+}$ (M = Ir, Rh) (Figure 1A) have received significant attention due to their redox activity and ability to facilitate photoinduced hydrogen evolution.[2] The high reactivity of the triplet excited state of these and related compounds prompted much subsequent research on determining the structure−function relationship of the excited state, leading to the highly detailed spectroscopic characterization presented for $Rh_2(dimen)_4^{2+}$ (dimen =1,8-diisocyano-*p*-menthane) by Miskowski et al. in 1994.[3] Through these and related studies (cf. the review by P. Harvey[4] and the later theoretical investigation of Rh_2(1,3-diisocyanopropane)$_4^{2+}$[5]), it was concluded that the excited state of $M_2(bridge)_4^{2+}$ complexes exhibits pronounced conformational changes compared to the ground state, including a significant shortening of the metal−metal distance. This conclusion was confirmed by low-temperature time-resolved crystallographic measurements in 2004 when Coppens et al. succeeded in directly measuring a very large (0.86 Å) shortening of the Rh−Rh distance from 4.50 to 3.64 Å in PF_6 crystals of $Rh_2(dimen)_4^{2+}$[6] following electronic excitation. This shortening is only slightly less than the value derived from spectroscopic data by Miskowski et al.[3] However, no direct determination of the excited-state structure has been undertaken under the less constraining conditions in liquid solution, and no information regarding the excited-state structure has been reported for the iridium analogue $Ir_2(dimen)_4^{2+}$. The present study addresses both of these issues to shed light on solution-state structures in

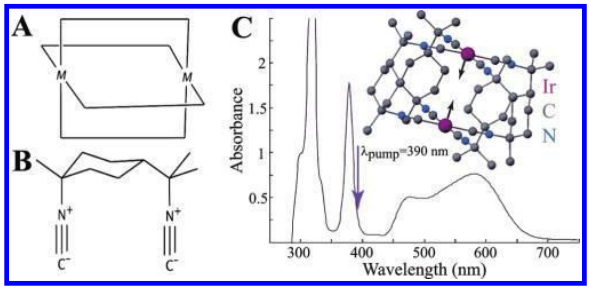

Figure 1. (A) Schematic depiction of the $M_2(bridge)_4^{2+}$ complexes. In the present work, the metal centers are Ir atoms and bridging ligands are the asymmetric dimen units for which the molecular structure is shown in B. (C) Absorption spectrum of $Ir_2(dimen)_4^{2+}$ in acetonitrile. Excitation is expected to be associated with a contraction of the two Ir atoms along their connecting vector, as depicted in the insert. For the experiments reported here, the excitation wavelength was 390 nm.

Received: April 5, 2011
Published: August 08, 2011

general and in particular on the excited-state structures of this class of bimetallic transition-metal compounds.

The structure of $Ir_2(dimen)_4^{2+}$ in its ground state is shown schematically in Figure 1. The two metal atoms are connected by four dimen units, giving rise to a ligand framework with a square-planar isocyanide configuration in the end groups (Figure 1A and 1B). In the crystalline state, the distance between the two Ir atoms is known to be strongly dependent on the crystal packing forces, with the distance varying from 3.60 Å in the $B(C_6H_5)_4$ salt to 4.41 Å in the PF_6 salt. Shortening of the Ir−Ir distance is associated with a ligand twist of 16° in the $B(C_6H_5)_4$ salt.[7] The significant flexibility of the ligand framework and corresponding variation in M−M distances is further established in crystallographic studies utilizing end-on adducts and Ag^+ encapsulation for which the Ir−Ir distances were reported as 2.986[8] and 5.28 Å,[9] respectively. Again, the shortest distance is associated with a significant ligand twist of 39°. Such large variation in the metal distance is in good agreement with the spectroscopy-based calculations,[3] where the ground-state distance between the metal atoms in the $M_2(dimen)_4^{2+}$ compounds was found to be determined by a very shallow potential governed primarily by the dimen ligands.

Figure 1C shows the absorption spectrum of $Ir_2(dimen)_4^{2+}$ in acetonitrile solution at room temperature. It differs from the spectrum obtained in the crystalline state[7] in displaying two overlapping transitions in the region of the metal-centered $d\sigma^* \rightarrow p\sigma$ transition at 450−650 nm. This observation was made by Exstrom et al. and interpreted as being due to different metal−metal separations among the $Ir_2(dimen)_4^{2+}$ molecules.[7] Specifically, the absorption spectrum in solution was interpreted as arising from two coexisting populations of $Ir_2(dimen)_4^{2+}$ with Ir−Ir distances close to 3.6 and 4.4 Å, respectively. The single-maximum emission spectrum (not shown) was interpreted as arising from only one excited-state population in terms of Ir−Ir distance. This was very recently supported by ultrafast transient absorption spectroscopy,[10] but further information on the photophysical properties of $Ir_2(dimen)_4^{2+}$ is scarce, as the emission quantum yields are low, and no information regarding the lifetime of the excited state appears to have been published.

For the experiments reported here, excitation of $Ir_2(dimen)_4^{2+}$ was at 390 nm, which is on the long-wavelength side of the ~375 nm peak associated with the $d_{xz,yz} \rightarrow p\sigma$ transition. Assuming direct analogy with the $Rh_2(TMB)_4^{2+}$ complex (TMB = 2,5-diisocyano-2,5-dimethylhexane), this excitation is followed by a very efficient intersystem crossing to the $^3A_{2u}$ triplet state.[11] As in the analogous and very well-studied Pt complex PtPOP,[12−16] population of the bonding orbital located between the two metal centers is expected to lead to a contraction along the metal−metal axis as also directly observed in $Rh_2(dimen)_4^{2+}$.[6]

The present work reports time-resolved X-ray scattering measurements of the structural changes due to electronic excitation of $Ir_2(dimen)_4^{2+}$ in acetonitrile solution. As demonstrated in previous work,[17,18] structural modeling and analysis of difference scattering signals can give detailed insight into the photoinduced structural changes and kinetics. In addition, special emphasis will be given to determining the ground-state structure of $Ir_2(dimen)_4^{2+}$ in solution from the X-ray scattering data.

EXPERIMENTAL SECTION

Methods. The experiments reported in this work were all carried out at beamline ID09B at the European Synchrotron Radiation Facility (ESRF, Grenoble, France) using the well-established 986.3 Hz laser pump/X-ray probe protocol with 2 ps 390 nm laser pulses and pink-beam X-ray energy spectrum with an intensity maximum at 18.25 keV.[17,18] A solution of $Ir_2(dimen)_4^{2+}$ (6 mM) in acetonitrile was constantly circulated through a fast-flowing liquid-jet setup, ensuring complete sample replacement between each pump−probe cycle. Data were analyzed using the structural fitting approach previously used for this class of experiments and previously described in detail,[15,19,20] in this work using DFT-derived structures as the starting point for analysis.

Synthesis. $Ir_2(dimen)_4^{2+}$ was synthesized onsite by direct mixing of 1,8-diisocyano-paramenthane (dimen) and $Ir_2Cl_2(COD)_2$ (COD = 1,5-cyclooctadiene) in a 4:1 ratio in acetontrile rigorously purged with argon. The 6 mM solution displayed an intense dark purple color. The typical solution volume for one experiment was 150 mL. Under deoxygenized conditions the $Ir_2(dimen)_4^{2+}$ solution was observed to be very robust under laser and X-ray irradiation with only minor sample decay over long periods (12 h) of near-constant exposure to laser and X-ray pulses. The sample volume was constantly monitored for loss due to evaporation (~10 mL/4 h) and kept constant by topping up with Ar-purged acetonitrile.

Experimental Setup. Details of the experimental setup at ESRF beamline ID09B for time-resolved studies are given elsewhere[17] but are briefly reviewed here. Individual ~100 ps long X-ray pulses from the u17 undulator were selected by means of a high-speed mechanical chopper with a 265 ns opening time, sufficient to isolate X-ray bursts from the individual electron bunches in several of the ESRF filling modes.[21] Thereby the frequency of X-ray pulses arriving at the sample was reduced to 986.3 Hz (360th subharmonic of the synchrotron orbit frequency). A Ti:sapphire amplified femtosecond laser with a 780 nm fundamental wavelength was phase locked to the same 986.3 Hz frequency. For the experiments reported here, the 780 nm pulses were frequency doubled to 390 nm in a BBO crystal and stretched to 2 ps by passing through two fused silica prisms, the latter in order to reduce two-photon excitation events. Spatial overlap between the laser and X-ray beams at the sample position was attained using a pinhole, with the laser beam incident at a 10° angle to the X-ray beam and focused to a 120 μm diameter spot size. A corresponding X-ray focus of 100 μm × 60 μm ($w \times h$) was obtained with a Pt-coated toroidal mirror, also used for rejecting higher harmonics of the undulator spectrum. This renders the X-ray energy spectrum quasi-monochromatic with a triangular energy profile peaking at 18.25 keV (9 mm gap) and 4.5% bandwidth. Absolute timing of the laser and X-ray pulses was measured with a fast GaAs photodiode. Subnanosecond changes in the arrival time of the laser pulses at the sample position were controlled by shifting the phase of the laser oscillator feedback loop. Timing jitter was better than 5 ps.

The sample solution was continuously circulated through a sapphire nozzle, producing a stable liquid film with 300 μm thickness at the laser/X-ray overlap position and a flow speed of ~4 m/s, ensuring complete sample replacement between each pump−probe cycle. An Ar-filled chamber protected the liquid jet from exposure to atmospheric oxygen, and the sample reservoir was likewise protected by continuous purging by Ar saturated with acetonitrile vapor.

Scattered X-rays were collected on a 2048 × 2048 FReLoN CCD detector, integrating 2000 X-ray pulses for each image, corresponding to ~2 s exposure time. Scattering images were subsequently corrected for polarization of the X-ray beam, solid angle coverage, and the angle-dependent absorption efficiency of the detector before being azimuthally integrated to give 1-dimensional scattering curves $S(2\theta)$. For clarity of presentation but not used in the analysis, all scattering angles were converted to scattering vectors $Q = (4\pi \sin(2\theta/2))/\lambda$, with λ being the X-ray wavelength and using a weighted average corresponding to the undulator spectrum $I(\lambda)$. For the experiments reported here, scattering

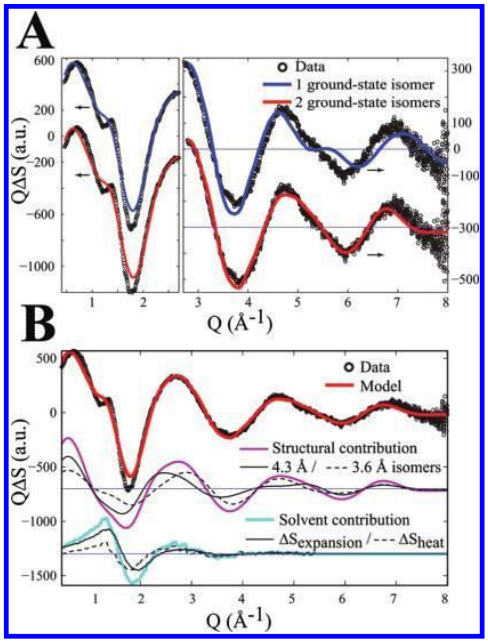

Figure 2. (A) Results of fitting structural models incorporating one (blue line) and two (red line) ground-state structures in the simulated difference scattering signal fit to the acquired difference signal $\Delta S(Q)$ at $\Delta t = 30$ ns. A very significant improvement in the quality of the fit at $Q > 3$ Å^{-1} is observed when two possible ground-state structures are used. (B) Partitioning of the best-fit model simulation into the contribution from structural changes in the solute (magenta) and solvent (blue). These are further partitioned into contributions from the structural changes in the long (full) and short (dashed) isomers as well as contributions due to expansion (full line) and heating (dashed line) of the solvent.

patterns were acquired in sequences of 4−5 images with the laser pulse arriving at predetermined time intervals $\Delta t \equiv t_{probe} - t_{pump}$ before the center of the X-ray pulse (positive delay, "Laser-on"), with such sequences separated by individual reference images (also 2 s integration time) where the laser pulse arrived after the X-ray pulse (negative delay, "Laser-off"). For each time delay, 100−200 images were acquired.

Difference scattering signals were constructed by first scaling the high-Q part of the individual scattering curves to the calculated coherent + incoherent molecular scattering from a "liquid unit cell" representing the stoichiometry of the solution. From each scattering curve with a positive delay Δt, the average of the two nearest laser-off curves was then subtracted to form the difference signal, $\Delta S(Q)$. For each time delay Δt, the 100−200 individual $\Delta S(Q)$ curves were subsequently analyzed and statistically significant outliers removed by successive point-by-point and ensemble application of the Chauvenet Criterion.[18,22] The outliers constituted on the order of 1% of the curves. The final step in the preanalysis was construction of averaged $\Delta S(Q)$ curves for each time delay, Figure 2A showing one such curve. The noise level $\sigma(Q)$ for each curve was estimated from the residual of local (20 points) fit to low-order (second) polynomials.[18,23]

DFT Calculation of Starting-Point Structures. To provide starting structures for the structural analysis described in detail below, several DFT calculations were performed. All calculations were carried out in the ORCA framework[24] with the one-parameter hybrid version of the Perdew−Burke−Erzerhoff functional with 25% HF exchange (PBE0). In earlier work Adamo et al. demonstrated successful use of the PBE0 hybrid functional for transition-metal complexes.[25] The Gaussian-type Ahlrichs double-ζ basis set (DZ) was used in all calculations, and COSMO was used to include electrostatic interactions with the acetonitrile solvent. Def2-triple-ζ Stuttgart−Dresden effective core potentials (ECP[Ir=def2-TZVP])[26,27] were used for the Ir atoms to reduce the computation time. Ground-state calculations were done using restricted Kohn−Sham (RKS) method, and the excited-state calculations were done for the triplet by setting the spin multiplicity to 3 and doing unrestricted Kohn−Sham (UKS) calculations. For all four structural isomers, DFT calculations uniformly favor a ground state with d_{IrIr} = 4.6−4.9 Å located in a very shallow Ir−Ir potential when no structural or symmetry restrictions are imposed.

Data Analysis. Analysis of the difference scattering signals shown in Figure 2A followed the general methodology described in detail in our previous work[18] except for treatment of the solvent response and determination of the solution ground-state structure of $Ir_2(dimen)_4^{2+}$. Turning first to the solvent response, the laser pump leads to impulse heating and subsequent expansion of the solvent due to ultrafast release of excess vibrational energy from the excited solute molecules.[28] The contribution from these effects to the difference scattering signal can be included through the use of previously determined solvent differentials[15,28] or through molecular dynamics simulations.[17] However, such data were not available for the present study, and instead, the immediate (<100 ps, heating $\Delta S_{\Delta T}$) and long-term (>10 ns, expansion-dominated $\Delta S_{\Delta\rho}$) response of the solvent were determined in another set of experiments using a chemically inert chromophore as in the recent work reported by Salassa et al.[29] and detailed in the Supporting Information. Figure 2B, lower part, shows these two solvent contributions to the difference scattering signal.

Turning next to determination of the solution ground-state structure, the spectroscopic evidence presented by Exstrom et al.[7] indicates the presence of not one but two distinct solution-state structures characterized by different Ir−Ir distances. To provide a basis for structural analysis, DFT calculations of the electronic and geometric structure of $Ir_2(dimen)_4^{2+}$ were carried out within the ORCA framework as described above.

Structural information was obtained by fitting[18] a simulated difference signal ΔS_{Sim} to the acquired difference signal ΔS_{Data} for a given time delay Δt while varying the excitation fraction α and a set of n structural parameters P_n. The scattering is calculated through the (orientation-averaged) Debye expression for the molecular form factor

$$S(Q) \propto F_{mol}^2(Q) = \sum_{\substack{i,j,k \\ i<j}}^{N} f_i f_j \frac{\sin(Qr_{ij})}{Qr_{ij}} + |f_{kk}|^2 \qquad (1)$$

Here, f_i is the atomic form factor for atom i and r_{ij} is the distance between atoms i and j. Introducing the excitation fraction α, the structural part of the simulated difference signal is given by $\alpha\Delta S_{Sim,struct} = \alpha(S_{On} - S_{Off}) = (\alpha S^n_{Exc} + (1 - \alpha)S_{Ground}) - S_{Ground}$, with the superscript n denoting the nth set of structural parameters. To accurately fit the experimental data, the solvent contribution is included such that the full time-dependent simulated signal is given by

$$\begin{aligned} \Delta S(Q)_{Sim} &= \alpha\Delta S(Q)_{Sim,struct} + \Delta S(Q)_{Solv} \\ &= \alpha\Delta S(Q)_{Sim,struct} + \alpha_{\Delta T}\Delta S(Q)_{\Delta T} \\ &\quad + \alpha_{\Delta\rho}\Delta S(Q)_{\Delta\rho} \end{aligned} \qquad (2)$$

In this expression, $\Delta S(Q)_{\Delta T}$ and $\Delta S(Q)_{\Delta\rho}$ are the difference signal responses to, respectively, solvent heating and subsequent expansion, as described above. $\alpha_{\Delta T}$ and $\alpha_{\Delta\rho}$ are the corresponding scaling factors.

dx.doi.org/10.1021/ic2006875 |Inorg. Chem. 2011, 50, 9329–9336

Inorganic Chemistry ARTICLE

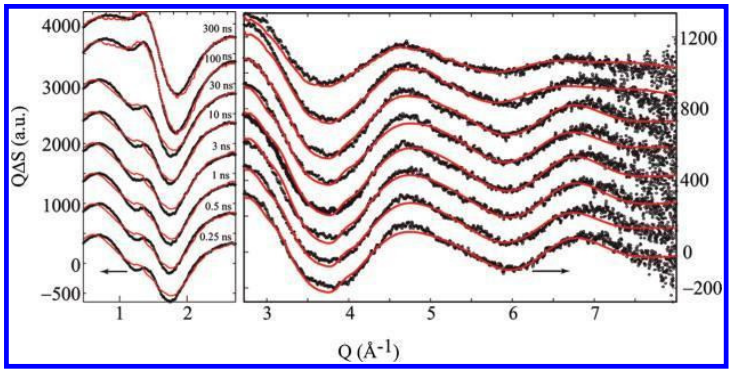

Figure 3. Data (black points) and best-fit models (red lines) for the eight investigated time steps from 250 ps to 300 ns after excitation. Good agreement between data and simulations is observed for all time delays, in particular for $Q > 3$ Å^{-1}. The comparatively poor fit around $Q = 1.5$ Å^{-1} is most pronounced at short time delays, where the difference signal in this region is dominated by the change in scattering due to solvent heating, cf. Figure 4. The noise level $\sigma(Q)$ is reflected by the local scatter in the data points.

The fit is evaluated through minimizing a χ^2 estimator[30]

$$\chi^2 = \sum_N \frac{(\Delta S_{\mathrm{Sim}} - \Delta S_{\mathrm{Data}})^2}{\sigma^2} / (N - P - 1) \quad (3)$$

where N is the number of data points, σ the experimental uncertainty at each point, and P the number of free parameters in the model. The χ^2 value for each possible set of parameters can be associated with a relative likelihood L defined as $L_{p_n} \propto \exp(-\chi^2/2)$.

Figure 2A shows in blue the result of such a fit, taking as starting points DFT-derived structures for the triplet excited state and ground state, with minimum energy Ir−Ir separations of 2.88 Å and 4.68 Å, respectively. To allow for differences between the calculated and the actual molecular structures, the Ir−Ir separation was further varied from 2.5 to 3.5 Å for the excited state and from 3 to 5.5 Å for the ground-state structure, keeping all other structural parameters constant. As is evident from Figure 2A, the resultant fit (blue line) to the data is not satisfactory.

A better fit was obtained assuming two coexisting ground-state structures as deduced from spectroscopy by Exstrom et al.[7] Figure 2A shows in red the result of fitting a model accommodating two ground-state structures that differ in the Ir−Ir distance. The structural part of the expanded model is quantitatively given by $\Delta S_{\mathrm{Sim,struct}} = \beta \Delta S_{\mathrm{short}} + (1 - \beta)\Delta S_{\mathrm{long}}$, where both the long and the short Ir−Ir distances are allowed to vary independently as is the partitioning β among the two contributions. Thus, the goodness-of-fit measure χ^2 and the likelihood L are functions of the three Ir−Ir distances $d_{\mathrm{IrIr}}^{\mathrm{GS1}}$, $d_{\mathrm{IrIr}}^{\mathrm{GS2}}$, and $d_{\mathrm{IrIr}}^{\mathrm{ES}}$, the partitioning β, and the three α parameters introduced above

$$\chi^2 = \chi^2(d_{\mathrm{IrIr}}^{\mathrm{GS1}}, d_{\mathrm{IrIr}}^{\mathrm{GS2}}, d_{\mathrm{IrIr}}^{\mathrm{ES}}, \beta, \alpha_{\mathrm{exc}}, \alpha_{\Delta T}, \alpha_{\Delta \rho}) \quad (4)$$

From the seven-dimensional likelihood space, the most-likely set of parameter values, their uncertainties, and their correlations can be determined.[18]

DFT-optimized structures with Ir−Ir distances of 2.9 Å in the excited state and 3.5 and 4.3 Å in the two ground-state isomers were used as starting points for the fitting procedure (see Supporting Information for details). When fitting to the scattering data, the Ir−Ir distances were allowed to vary freely around the initial guess while the ligand structure was kept rigid. It is noted that while this structural variation gives a good estimate of the scattering signal, it does not accurately capture the overall structure of the molecules in question, as the Ir−Ir distance is known to be strongly coupled to both pyramidal deformation of the square-planar isocyanide end groups and the dihedral C−Ir−Ir−C ligand twist angle.[7] As Figure 2A shows, application of the "two-isomer" model results in a significantly better fit.

RESULTS

The analysis strongly indicates that the difference scattering signal acquired 30 ns after laser excitation of $Ir_2(dimen)_4^{2+}$ in acetonitrile can be interpreted through a structural analysis incorporating one population of excited-state $Ir_2(dimen)_4^{2+}$ with a single well-defined Ir−Ir bond length and two ground-state populations with significantly longer Ir−Ir distances. From the maximum likelihood analysis we arrive at an excited-state Ir−Ir distance of 2.90(2) Å and ground-state distances of 3.60(9) and 4.3(1) Å. The excitation fraction α is determined as 9.7(5)% and the ground-state partitioning parameter β as 0.54(7). The cited 1-σ confidence intervals are conservative and incorporate all correlations between the fit parameters.

To further investigate the excited-state structure and related dynamics of the photoexcited $Ir_2(dimen)_4^{2+}$ system, Figure 3 shows difference signals and best fits for the eight time delays from 250 ps to 300 ns. Very good agreement between data and simulations is observed in the high-Q part of the signal for all time delays, although an inability of the simulations to capture the sharp features at $Q = 1-2$ Å^{-1} is noticed. We attribute this to a necessary smoothing of the temperature-related solvent contribution (see Supporting Information) and the choice not to include the ligand twist as a fit parameter, two features of our model expected to be most consequential in the low-Q part of the difference scattering signal.

Figure 4A shows the temporal evolution of the excitation fraction (black circles) and an exponential fit to this time series. A best-fit lifetime of 410(70) ns is obtained. Also shown in this figure are the scaling factors $\alpha_{\Delta T}$ (red) and $\alpha_{\Delta \rho}$ (blue) for the two solvent contributions. The initial temperature increase within the first 100 ps is followed by cooling on the 10−100 ns time scale concomitant with solvent expansion (density decrease, $-\alpha_{\Delta \rho}$), in accordance with the expected hydrodynamics.[28] Figure 4B illustrates the obtained best-fit values of the four parameters related to structure. Essentially no time dependence up to 100 ns is observed, at which point there is a decrease in the partitioning fraction β, suggesting faster relaxation to the short-distance isomer. This change in partitioning is associated with a slight increase in the best-fit values for the ground-state Ir−Ir distances, suggesting a more elaborate model is needed to fully describe the structural dynamics at long time delays as discussed further below.

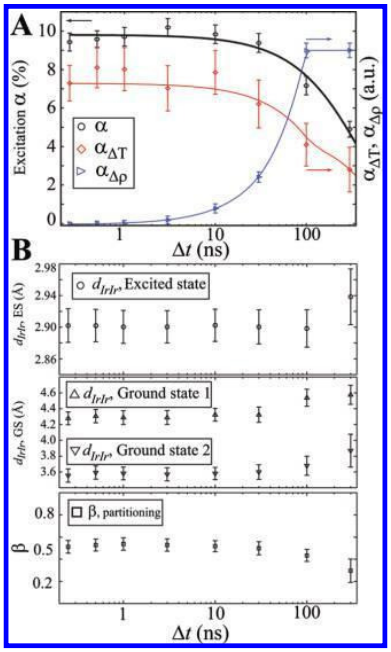

Figure 4. (A) Excitation fraction (black circles) for the best-fit models as a function of time delay Δt. The observed excitation fraction is well fitted by a single-exponential decay with lifetime τ = 410 ns (black line). Red and blue points show the hydrodynamic scaling factors $\alpha_{\Delta T}$ and $\alpha_{\Delta\rho}$. A fast initial increase $\alpha_{\Delta T}$ due to impulse heating is followed by cooling and expansion on the 10−100 ns time scale. The red and blue lines are interpolations of the data points to illustrate the temporal evolution. (B) Structural parameters for the best-fit models as a function of time delay. These appear essentially independent of the time delay, with an excited-state Ir−Ir distance of 2.90 Å. The best-fit ground-state structures have d_{IrIr} = 3.6 and 4.3 Å for the short- and long-distance isomer, respectively. The lower panel illustrates the ground-state partition fraction, with the two isomers present in equal amounts for all but the longest time delays.

Figure 5 presents a 10-ps time-slicing study aimed at investigating the excited-state structure at shorter time scales. The arrival time of the 2 ps laser pulse on the sample was gradually moved through the ∼100 ps long X-ray pulse with temporal envelope $I(t)$. On the 10 ps time scale, the structural change due to the excitation pulse can be considered instantaneous. In the limit of infinitely short pump and probe pulses (omitting the Q dependence to simplify the notation), the expected signal can thus be represented as the signal due to the instantaneous structural change, ΔS_{Inst}, multiplied by a heaviside step function $H(t)$ centered at t = 0, $\Delta S(t) = H(t)_{\Delta t=0}\Delta S_{Inst}$. Representing the finite length of the probe pulse as a Gaussian intensity profile of width σ_p, the experimental scheme is depicted in the top panel of Figure 5. The time delay is calculated from the arrival time of the midpoint of the pulses and referenced to the arrival time of the pump pulse. In the present case the arrival time of the laser pump pulse at the sample position is defined to be t_{pump} = 0. Considering all possible values of the time delay $\Delta t \equiv t_{probe} - t_{pump}$, the measured difference signal can now be written as the

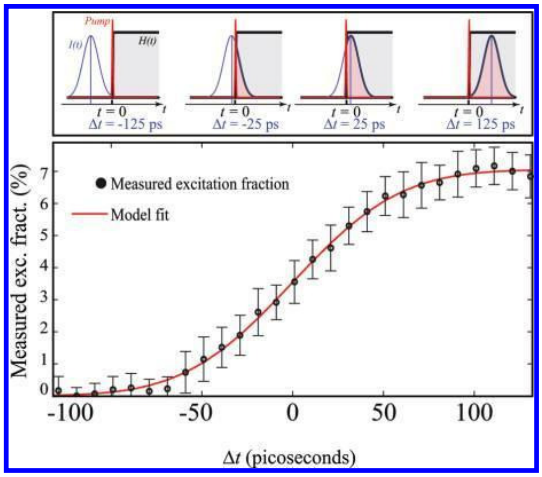

Figure 5. Schematic depiction of the slicing methodology and measured excitation fraction as a function of time delay Δt (black circles). Assuming instantaneous formation of the excited state on the 10 ps time scale, the red line is a fit of a broadened step function, eq 6, to the excitation fraction. The quality of the fit supports the model assumptions of instantaneous formation and no excited-state depopulation at the investigated time scale.

convolution of the step function and the intensity profile

$$\Delta S(\Delta t) \propto \int_{-\infty}^{\infty} dt \Delta S_{Inst} H(t)_{\Delta t=0} I(t) \quad (5)$$

Introducing $I(t) = (1/(2\pi\sigma_p)^{1/2})\exp(-((t - \Delta t)^2)/(2\sigma_p{}^2))$ and substituting $t' = t - \Delta t$ this integral can be solved to give

$$\Delta S(\Delta t) \propto 1 + \mathrm{erf}\left(\frac{\Delta t}{\sqrt{2}\sigma_p}\right) \quad (6)$$

Comparing with the top part of Figure 5, this expression is recognized as the integral of the probe pulse from the point of intersection with the pump pulse to infinity. Referring to eq 2, the signal from the structural change ΔS_{Struct} is linear in the excitation fraction α, and from the expressions above, the measured excitation fraction from the structural analysis of the difference scattering signal at each time delay would be expected to follow the form of eq 6. Figure 5 shows the excitation fraction α (black circles) as a function of the nominal time delay Δt. In this analysis, only the excitation fraction, the temperature increase, and the excited-state Ir−Ir bond length (α_{exc}, $\alpha_{\Delta T}$, and d^{ES}_{IrIr} in eq 3) were allowed to vary in the structural fitting. The red line in Figure 5 is a fit of eq 6 to the data points, and excellent agreement between data and fit is observed. From the analysis we recover a probe pulse length $l_p = 2.35\sigma_p$ of 110(10) ps, in good agreement with published ESRF values for the 4-bunch filling mode. Carrying out the same analysis for the prefactor of the heating contribution to the scattering signal, $\alpha_{\Delta T}$, we obtain essentially the same result for the probe pulse length, l_p = 100(30) ps.

The lifetime of the singlet excited state has been determined from transient spectroscopy (see Supporting Information) to be ∼65 ps, shorter than the probe pulse duration but longer than the effective time resolution of the time-slicing method. The demonstrated slicing scheme thus offers an opportunity to investigate

dx.doi.org/10.1021/ic2006875 |Inorg. Chem. 2011, 50, 9329–9336

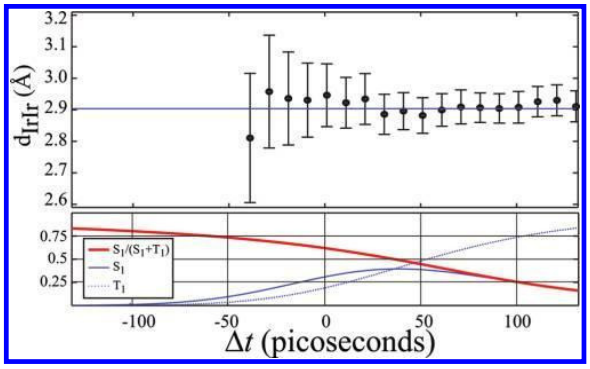

Figure 6. (Top) Ir−Ir distance measured as a function of time delay Δt. For $\Delta t < -40$ ps ($\alpha_{Eff} < 1\%$) no reliable estimate of the distance could be obtained. The blue line represents the result of the longer time scales study. (Bottom) Relative fractions of the singlet (full) and triplet (dashed) excited state probed by the 100 ps long X-ray pulse as a function of time delay. (Red line) Relative strength of the singlet contribution to the difference signal, which dominates until $\Delta t = 0$ ps. Any change in the Ir−Ir separation related to the singlet−triplet transition is at the limit of detection, but a slight shortening of the Ir−Ir bond is suggested.

any structural change accompanying the singlet−triplet electronic transition. If the singlet state is assumed to undergo intersystem crossing to the triplet state with unity efficiency we can write

$$\Delta S_{S_1}(\Delta t) \propto \int_{-\infty}^{\infty} dt \Delta S_{inst} H(t) \exp\left(\frac{-t}{\tau}\right) I(t) \quad (7)$$

$$\Delta S_{T_1}(\Delta t) \propto \int_{-\infty}^{\infty} dt \Delta S_{inst} H(t) \left[1 - \exp\left(\frac{-t}{\tau}\right)\right] I(t) \quad (8)$$

where the dependence on Δt is contained in $I(t)$ as above. These convolution integrals can again be solved analytically to give

$$\Delta S_{S_1}(\Delta t) \propto -\exp\left(\frac{\sigma^2 - 2\Delta t\tau}{2\tau^2}\right) \times \left(1 - \mathrm{erf}\left(\frac{\sigma^2 - \Delta t\tau}{\sqrt{2}\sigma\tau}\right)\right) \quad (9)$$

$$\Delta S_{T_1}(\Delta t) \propto \left(1 + \mathrm{erf}\left(\frac{\Delta t}{\sqrt{2}\sigma}\right)\right) - \exp\left(\frac{\sigma^2 - 2\Delta t\tau}{2\tau^2}\right) \times \left(1 - \mathrm{erf}\left(\frac{\sigma^2 - \Delta t\tau}{\sqrt{2}\sigma\tau}\right)\right) \quad (10)$$

To relate this to the relative signal strengths from the singlet and triplet excited-state populations of $Ir_2(dimen)_4^{2+}$, the bottom panel in Figure 6 shows in blue eqs 9 and 10 as calculated for τ_{S1} = 63 ps and l_p = 110 ps. The red line illustrates the contribution to the difference signal ΔS from the singlet population relative to the triplet population as a function of time delay. From this it is clear that at nominal time delays Δt earlier than $\Delta t = 0$ the measured difference signal is dominated by the singlet excited state. The top part of Figure 6 shows the result of fitting the excited-state Ir−Ir separation for each time delay beyond $\Delta t = -40$ ps, corresponding to an "effective" probed excitation fraction exceeding ~1%. At $\Delta t = -10$ ps the signal strength allows determination of d_{IrIr} with reasonable accuracy. Taking a five-point uncertainty-weighted average around this time delay, where the singlet still dominates the signal, leads to d_{IrIr} = 2.93(2) Å. This can be compared with a similar five-point average for the five points at Δt = 90−140 ps, where d_{IrIr} = 2.91(1) Å is obtained. Thus, from these data no significant shift in Ir−Ir separation is observed as the signal gradually becomes dominated by the triplet excited-state population. However, it is evident that even in this experiment with comparatively few repetitions (108 exposures/time delay) and thus a relatively poor S/N ratio for each time step kinetics and structural changes can be followed with a time resolution significantly better than the ~100 ps given by the probe pulse. Thus, this methodology is paving the way for new classes of experiments.

DISCUSSION

Determination of the excited-state structure of $Ir_2(dimen)_4^{2+}$ with a 2.9 Å separation between the two Ir atoms in the triplet excited state represents an exceptionally large structural rearrangement due to photoexcitation. We interpret our observations in the framework derived by Miskowski et al.,[3] where the metal atoms in the ground state exist on a very shallow ligand-dominated potential surface along the M−M coordinate. Upon excitation, the bonding orbital between the two Ir atoms becomes populated, effectively enhancing the attractive interaction between the two metal atoms, which changes the potential to a steeper and more metal-dominated configuration with a significantly shorter metal−metal equilibrium distance. From steady-state crystallographic data for both $Ir_2(dimen)_4^{2+}$ and $Rh_2(dimen)_4^{2+}$, short M−M distances in these compounds are accompanied by both a torsional twist of the ligand system and pyramidal distortion of the isocyanide conformation around the metal centers. We ascribe the observed difference between the present results and earlier diffraction work[6] on the excited-state structure of the analogue $Rh_2(dimen)_4^{2+}$ system to hindering of these secondary deformation mechanisms due to crystal packing forces. However, the effect of these appears significantly less pronounced in the excited state than for the ground-state structures, in accordance with the much shallower metal−metal potential in the ground state.

While already suggested by Exstrom et al. in 1996, the possible coexistence of at least two different structural isomers of $Ir_2(dimen)_4^{2+}$ in acetonitrile solution has led to very little discussion in the literature and was never confirmed until very recent ultrafast transient absorption experiments.[10] Exstrom et al. discussed the solution-state spectra in terms of bond-stretch isomerism and associated the spectroscopic features in the solution state data to ground-state populations with Ir separations of 4.4 and 3.6 Å, respectively. Although not supported by our DFT calculations, this part of our interpretation is in good agreement with the hypothesis of more than one ground-state structure. The almost exact 50/50 partitioning between the long and short distance populations also determined in the present study suggests an explanation. As discussed in the 1990 work by A. Sykes et al.,[8] the asymmetric geometry of the dimen ligand allows for the possible coexistence of four structural isomers being present both in solution and in crystals. In the latter case, this leads to ligand disorder in structural refinements from

crystallographic data. From statistical arguments, one of these isomers, the 1:3 isomer with one ligand having the ring near one Ir atom and the other three ligands having the ring oriented toward the second Ir atom, should have an abundance of 1/2, whereas the other isomers have abundances of 1/4 (2:2-*cis*) and 1/8 (both 2:2-*trans* and 4:0 isomer). The optical excitation pulse at 390 nm addresses a position in the absorption spectra where the absorption is equal for all isomers. On the basis of the statistical abundances of the four isomers and our result of $\beta = 0.5$, we tentatively assign either the long (4.3 Å) or the short (3.6 Å) Ir−Ir distance to the 1:3 isomer. This suggestion of a direct connection between head/tail ligand arrangements and Ir−Ir distance does not disagree with analysis of the ultrafast spectroscopy data presented by Hartsock et al.[10] However, further work incorporating, e.g., the temperature dependence of the spectroscopic features or X-ray investigations of the ground-state solution scattering at different temperatures will be needed to distinguish between the models proposed. This work is under way.

While the 10 ps time resolution results presented above do not imply any significant structural change related to the electronic singlet−triplet transition in $Ir_2(dimen)_4^{2+}$, the data shown demonstrate the feasibility of this type of study. Further studies along this line of inquiry would benefit from data obtained with lower bunch-charge filling patterns in the synchrotron, where X-ray intensity is sacrificed for shorter pulse lengths, as this would effectively sharpen the probed population distributions depicted in blue in Figure 4A.

CONCLUSIONS

In the present study, time-resolved liquid-state X-ray scattering has been utilized to demonstrate remarkable bond shortening in $Ir_2(dimen)_4^{2+}$ in acetonitrile following photoexcitation by short laser pulses at 390 nm. From an analysis incorporating two ground-state structures differing significantly in the Ir−Ir separation, the difference scattering signals were found to be very well described by a contraction in Ir−Ir distance from 3.60(9)/4.3(1) to 2.90(2) Å upon population of the pσ orbital. This corresponds to 1.4 Å contraction of the Ir−Ir distance in the case of the long-distance isomer. Such a dramatic reduction in Ir−Ir distance is significantly greater than the contraction observed in crystal studies of the analogous Rh compound $Rh_2(dimen)_4^{2+}$.[6] We ascribe this difference to the absence of crystal packing forces in the present solution-state study. From the analysis of eight time delays in the range from 250 ps to 300 ns, the lifetime of the triplet excited state has been determined to be 410(70) ns, with the possibility of differing lifetimes between the two structural isomers included in the model description noted.

A second study demonstrated a 5−10-fold improvement of the effective time resolution of the chopper-based setup at ESRF beamline ID09B beyond the intrinsic ~100 ps width of the probe pulse. Gradually shifting the temporal position of the laser pump pulse within the X-ray probe pulse in 10 ps steps allowed the fraction of excited-state solute molecules probed by the X-ray pulse to be monitored with good accuracy as a function of sub-100 ps time delay. From analysis of this "effective excitation fraction" as a function of pump−probe delay, the reported fwhm X-ray pulse width of the ESRF in 4-bunch mode was recovered. Independent analysis of the solvent heating signal confirmed the feasibility of the method. Analysis of the Ir−Ir bond length as a function of time delay on the sub-100 ps time scale was inconclusive but suggested a slight shortening of the bond upon intersystem crossing from the singlet to the $^3A_{2u}$ triplet state. Ten picosecond time resolution appears feasible, paving the way for studying new classes of phenomena.

In summary, the present study has determined the excited-state Ir−Ir distance of $Ir_2(dimen)_4^{2+}$ in acetonitrile to be 2.90(2) Å and confirmed the existence of at least two structural isomers present in the ground state. Further investigations of this system will utilize different excitation wavelengths and temperature-dependence studies to elucidate the structural isomerism in this system.

ASSOCIATED CONTENT

Supporting Information. The supplementary online information includes information on the difference-signal contributions from impulsive solvent heating, details of the data analysis approach, transient absorption data and further details of the 10 ps time slicing experiment. This material is available free of charge via the Internet at http://pubs.acs.org.

AUTHOR INFORMATION

Corresponding Author
*E-mail: hald@risoe.dtu.dk.

ACKNOWLEDGMENT

The authors are grateful for computer resource allocation and discussion of the DFT results with Stephan Sauer and Casper Steinmann, both Chemistry Department, University of Copenhagen. The assistance of K. Bechgaard, P. Hammershøj, and T. Just (Chemistry Department, University of Copenhagen) with the synthesis work is very much appreciated. The assistance of S. Canton (Maxlab, Sweden) with the transient optical measurements performed at CNM, Argonne National Laboratory, is gratefully acknowledged. This work was supported by the Danish National Research Foundation's Centre for Molecular Movies and DANSCATT

REFERENCES

(1) Lewis, N. S.; Mann, K. R.; Gordon(II), J.; Gray, H. B. *J. Am. Chem. Soc.* **1976**, *98:23*, 7461–7463.
(2) Lewis, N. S.; Mann, K. R.; Gordon(II), J.; Gray, H. B. *J. Am. Chem. Soc.* **1977**, *99:16*, 5525–5526.
(3) Miskowski, V. M.; Rice, S. F.; Gray, H. B.; Dallinger, R. F.; Milder, S. J.; Hill, M. G.; Exstrom, C. L.; Mann, K. R. *Inorg. Chem.* **1994**, *33*, 2799–2807.
(4) Harvey, P. D. *Coord. Chem. Rev.* **2001**, *219−221*, 17–52.
(5) Novozhilova, I. V.; Volkov, A. V.; Coppens, P. *Inorg. Chem.* **2004**, *43*, 2299–2307.
(6) Coppens, P.; Gerlits, O.; Vorontsov, I.; Kovalevsky, A.; Chen, Y.; Graber, T.; Gembicky, M.; Novozhilova, I. *Chem. Commun.* **2004**, *19*, 2144–2145.
(7) Exstrom, C. L.; Britton, D.; Mann, K. R.; Hill, M. G.; Miskowski, V. M.; Schaefer, W. P.; Gray, H. B.; Lammana, W. M. *Inorg. Chem.* **1996**, *35*, 549–550.
(8) Sykes, A. G.; Mann, K. R. *J. Am. Chem. Soc.* **1990**, *112*, 7247–7254.
(9) Sykes, A. G.; Mann, K. R. *Inorg. Chem.* **1990**, *29*, 4449–4453.
(10) Hartsock, R. W.; Zhang, W.; Hill, M. G.; Sabat, B.; Gaffney, K. J. *J. Phys. Chem. A* **2011**, *115*, 2920–2926.
(11) Miskowski, V. M.; Rice, S. F.; Gray, H. B.; Milder, S. J. *J. Phys. Chem.* **1993**, *97*, 4277–4283.

(12) Rice, S. F.; Gray, H. B. *J. Am. Chem. Soc.* **1983**, *105*, 4571–4575.
(13) Kim, C. D.; Pillet, S.; Wu, G.; Fullagar, W.; Coppens, P. *Acta Crystallogr., Sect. A* **2001**, *A58*, 133–137.
(14) Novozhilova, I.; Volkov, A.; Coppens, P. *J. Am. Chem. Soc.* **2002**, *125*, 1079–1087.
(15) Christensen, M.; Haldrup, K.; Bechgaard, K.; Feidenhans'l, R.; Kong, Q.; Cammarata, M.; Russo, M. L.; Wulff, M.; Harrit, N.; Nielsen, M. M. *J. Am. Chem. Soc.* **2009**, *131*, 502–508.
(16) van der Veen, R. M.; Milne, C. J.; Nahhas, A. E.; Lima, F. A.; Pham, V.-T.; Best, J.; Weinstein, J. A.; Borca, C. N.; Abela, R.; Bressler, C.; Chergui, M. *Angew. Chem., Int. Ed.* **2009**, *48*, 2711–2714.
(17) Kim, T. K.; Lee, J. H.; Wulff, M.; Kong, Q.; Ihee, H. *ChemPhysChem* **2009**, *10*, 1958–1980.
(18) Haldrup, K.; Christensen, M.; Nielsen, M. M. *Acta Crystallogr., Sect. A* **2010**, *A66*, 261–260.
(19) Haldrup, K.; Christensen, M.; Cammarata, M.; Kong, Q.; Wulff, M.; Mariager, S. O.; Bechgaard, K.; Feidenhans'l, R.; Harrit, N.; Nielsen, M. M. *Angew. Chem., Int. Ed.* **2009**, *48*, 4180–4184.
(20) Christensen, M.; Haldrup, K.; Kjær, K. S.; Cammarata, M.; Wulff, M.; Bechgaard, K.; Weihe, H.; Harrit, N. H.; Nielsen, M. M. *Phys. Chem. Chem. Phys.* **2010**, *12*, 6921–6923.
(21) Cammarata, M.; Eybert, L.; Ewald, F.; Reichenbach, W.; Wulff, M.; Anfinrud, P.; Schotte, F.; Plech, A.; Kong, Q.; Lorenc, M.; Lindenau, B.; Raebiger, J.; Polachowski, S. *Rev. Sci. Instrum.* **2009**, *80*, 124505-1–124504-9.
(22) Taylor, J. R. *Introduction to Error Analysis*; University Science Books, 1997.
(23) Dent, A.; Stephenson, P.; Greaves, G. *Rev. Sci. Instrum.* **1991**, *63*, 856–852.
(24) http://www.thch.uni-bonn.de/tc/orca/.
(25) Adamo, C.; Barone, V. *Theor. Chem. Acc.* **2000**, *105*, 169–172.
(26) Andrae, D.; Haussermann, U.; Dolg, M.; Stoll, H.; Preuss, H. *Theor. Chim. Acta* **1991**, *78*, 247–266.
(27) Weigend, F.; Ahlrichs, R. *Phys. Chem. Chem. Phys.* **2005**, *7*, 3297–3305.
(28) Cammarata, M.; Lorenc, M.; Kim, T.; Lee, J. H.; Kong, Q. Y.; Pontecorvo, E.; Russo, M. L.; Schiro, G.; Cupane, A.; Wulff, M.; Ihee, H. *J. Chem. Phys.* **2006**, *124* (124504), 1–9.
(29) Salassa, L.; Borfecchia, E.; Ruiu, T.; Garino, C.; Gianolio, D.; Gobetto, R.; Sadler, P. J.; Cammarata, M.; Wulff, M.; Lamberti, C. *Inorg. Chem.* **2010**, *49*, 11240–11248.
(30) Press, W. H.; Flannery, B. P.; Teukolsky, T. A.; Vetterling, W. T. *Numerical Recipes-The Art of Scientific Computing*; Cambridge University Press: Cambridge, UK, 1986.

Paper II

Guest-host interactions investigated by time-resolved X-ray spectroscopies and scattering at MHz rates solvation dynamics and photoinduced spin transition in aqueous Fe(bipy)32+.

K. Haldrup, G. Vankó, W. Gawelda, A. Galler, G. Doumy, A.M. March, E.P. Kanter, A. Bordage, A. Dohn, **T.B. van Driel**, K.S. Kjær, H.T. Lemke, S.E. Canton, J. Uhlig, V. Sundstrom, L. Young, S.H. Southworth, M. M. Nielsen and C. Bressler.

The journal of physical chemistry. A **116(40)**, 9878-87(2012).

THE JOURNAL OF PHYSICAL CHEMISTRY A

Article

pubs.acs.org/JPCA

Guest–Host Interactions Investigated by Time-Resolved X-ray Spectroscopies and Scattering at MHz Rates: Solvation Dynamics and Photoinduced Spin Transition in Aqueous $Fe(bipy)_3^{2+}$

K. Haldrup,*[,†] G. Vankó,*[,‡] W. Gawelda,[¶] A. Galler,[¶] G. Doumy,[§] A. M. March,[§] E. P. Kanter,[§] A. Bordage,[‡] A. Dohn,[∥] T. B. van Driel,[†] K. S. Kjær,[⊥] H. T. Lemke,[#] S. E. Canton,[▽] J. Uhlig, V. Sundström,[△] L. Young,[§] S. H. Southworth,[§] M. M. Nielsen,[†] and C. Bressler[¶]

[†]Centre for Molecular Movies, Department of Physics, Technical University of Denmark, DK-2800 Lyngby, Denmark

[‡]Wigner Research Centre for Physics, Hungarian Academy Sciences, H-1525 Budapest, POB 49, Hungary

[¶]European XFEL, Albert-Einstein Ring 19, D-22 761 Hamburg, Germany

[§]Argonne National Laboratory, 9700 South Cass Avenue, Argonne, Illinois 60439, United States

[∥]Chemistry Department, Danish Technical University, DK-2800 Lyngby, Denmark

[⊥]Centre for Molecular Movies, Niels Bohr Institute, University of Copenhagen, DK-2100 Copenhagen, Denmark

[#]Linac Coherent Light Source, SLAC National Accelerator Laboratory, Menlo Park, California 94025, United States

[▽]Department of Synchrotron Instrumentation and [△]Department of Chemical Physics, Lund University, Box 124, 22100 Lund, Sweden

ABSTRACT: We have studied the photoinduced low spin (LS) to high spin (HS) conversion of $[Fe(bipy)_3]^{2+}$ in aqueous solution. In a laser pump/X-ray probe synchrotron setup permitting simultaneous, time-resolved X-ray diffuse scattering (XDS) and X-ray spectroscopic measurements at a 3.26 MHz repetition rate, we observed the interplay between intramolecular dynamics and the intermolecular caging solvent response with better than 100 ps time resolution. On this time scale, the initial ultrafast spin transition and the associated intramolecular geometric structure changes are long completed, as is the solvent heating due to the initial energy dissipation from the excited HS molecule. Combining information from X-ray emission spectroscopy and scattering, the excitation fraction as well as the temperature and density changes of the solvent can be closely followed on the subnanosecond time scale of the HS lifetime, allowing the detection of an ultrafast change in bulk solvent density. An analysis approach directly utilizing the spectroscopic data in the XDS analysis effectively reduces the number of free parameters, and both combined permit extraction of information about the ultrafast structural dynamics of the caging solvent, in particular, a decrease in the number of water molecules in the first solvation shell is inferred, as predicted by recent theoretical work.

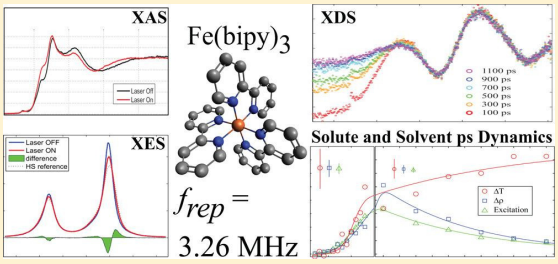

INTRODUCTION

Chemical reactivity in the solution phase manifests itself often via a complex interplay between intramolecular processes of the parent molecule and guest–host interactions with the caging solvation shell. As a consequence, the influence of the solvent on the reactivity of chemical and biological species has been the subject of intense research over the past decades. Dynamic guest–host interactions are responsible for Stokes shifts between the absorption and emission spectra of excited molecules, which have been extensively studied by static and ultrafast optical studies.[1−3] Most studies for this purpose have focused on small molecules, where the close proximity to the solvent bath allowed extraction of substantial signals.[1,4] However, although, for example, ultrafast optical studies clearly show how fast the dynamics occur, the details of the structural rearrangement processes remained largely in the dark. Extending these studies to potentially functional systems, thus to larger molecules, has so far appeared unfeasible due to the expected small interaction between the central atom and the solvent host.

$[Fe(bipy)_3]^{2+}$ is a model compound for such functional systems as it can dynamically switch between a low spin (LS) ground to a high spin (HS) excited state upon illumination, starting via a metal to ligand charge transfer (MLCT) process, followed by an ultrafast back transfer within 130 fs, eventually undergoing a spin–flip to the HS state as well as a 0.2 Å

Received: July 12, 2012
Revised: September 11, 2012
Published: September 12, 2012

lengthening of the Fe−N bonds.[5,6] The bpy ligands are expected to effectively shield the central metal atom from the solvation shell, so that it appears impossible to extract any spectroscopic information on the solvation dynamics following the ultrafast LS−HS conversion. In order to investigate these dynamics, we have designed an ultrafast laser pump/X-ray probe experiment, where the probe exploits complementary structural tools to simultaneously reveal different details of the ongoing processes.

Time-resolved X-ray science on the ultrafast time scales is a young field aiming to deliver direct structural information with atomic-scale resolution about reaction intermediates during a light-triggered reaction. For such investigations, a UV−vis optical laser pulse serves as the pump source, and a time-delayed X-ray pulse serves as the probe. Most of the experimental methodology has been developed to an advanced state at synchrotron radiation sources over the past decade,[7−20] with the time resolution usually limited to ∼50−100 ps due to the intrinsic X-ray pulse width at synchrotrons, although the effective time resolution can be somewhat improved by a dense sampling of time points.[21,22] In nearly all cases, such studies on molecular systems have only employed X-ray absorption spectroscopy (XAS)[8,12,13,15−17,20,23−28] or X-ray scattering[7,9,11,14,18,19,21] techniques and have been, with few exceptions,[29] limited to rather low (1−2 kHz) pump/probe repetition rates, mainly due to the availability and constraints provided by chirped pulse amplifier (CPA) laser systems. In these experiments, a sufficient number of optical photons to match the number of ground-state molecules in the sample volume probed by the X-ray beam is available. In this way, photoexcitation of a large fraction of the sample (10−50%) can be obtained. However, due to the mismatch between the intrinsic (multi) MHz repetition rate of synchrotron sources and the kHz repetition rate of the CPA laser systems, the effective number of X-ray photons available for time-resolved measurements has remained several orders of magnitude lower than that actually delivered by conventional synchrotron sources. Experiments requiring significant X-ray flux such as nonresonant and resonant X-ray emission spectroscopies (XES) thus become very difficult to perform, although a recent breakthrough showed the first time-resolved XES experiment with picosecond time resolution using such a kHz laser system.[30] The results of that experiment demonstrated that the integrated number of X-ray probe photons is the bottleneck for using XES as a time-resolved X-ray technique, and consequently, it is highly desirable to increase the number of X-ray probe photons by better matching the repetition rates of the laser source to that of a synchrotron. The corresponding 10^3 increase in effective X-ray flux would further allow many new applications within photochemical and photobiological dynamics,[31] where the low S/N for achievable and/or physiological concentrations has so far been a very significant limitation.

Only very recently and with the advent of high-power MHz laser systems have such photon-hungry experiments become feasible. So far, MHz laser pump/X-ray probe experiments have mainly been used in X-ray spectroscopy experiments,[32−34] and an extension to other X-ray tools is highly desired. In this paper, we report a study of the light-induced switching of the prototypical spin-crossover Fe(II) complex $[Fe(bipy)_3]^{2+}$ (see, e.g., ref 6 and references therein) at 3.26 MHz pump repetition rates with highly efficient use of the hard X-ray probe on the 10−100 ps time scale. The setup combines an emission spectrometer with absorption spectroscopy and includes a gateable area detector for collecting X-ray scattering data. This setup allows simultaneous acquisition of XES, XAS, and X-ray diffuse scattering (XDS) patterns. These complementary spectroscopic and scattering techniques are sensitive to, respectively, the spin state and configuration of the electron system and to the local and molecular structure and, in the case of XDS, include information about the solvent surrounding the complex. The complete setup thus allows full characterization of both electronic and geometric degrees of freedom simultaneously, as well as utilization of the full intensity of a third-generation synchrotron X-ray source in a time-resolved experiment. These advances in turn allow us to directly describe details of the solvent−solute dynamics previously only suggested by theory.

EXPERIMENTAL METHODS

The X-ray microprobe capabilities[35] of beamline 7ID at Argonne National Laboratory's Advanced Photon Source (APS) and the experimental setup for ultrafast measurements at MHz repetition rates have previously been described in detail.[32] In the following sections, a brief overview will be presented, with particular focus on the experimental techniques and acquisition strategies employed in the present study.

X-ray Spectroscopy. X-ray absorption near-edge structure (XANES) spectroscopy relies on detecting modulations of the absorption cross section as a function of photon energy near an absorption edge. The absorption is dependent on both the local atomic configuration as well as the electronic configuration and the oxidation state of the absorber and thus provides information on the unoccupied electronic states, as well as the local molecular structure around the absorption center. Hence, the combination of electronic and structural changes can complicate interpretation, but the signal can be very intense, and the measurement is straightforward and employs either transmission detection or, as in the present setup, fluorescence detection.

By using, for example, a Bragg crystal spectrometer, the fine structure of the emitted X-ray fluorescence (individual emission lines) can be resolved. Such an XES spectrum stems from X-rays emitted when electrons fill in core holes; thus, this technique brings information about the occupied electronic states, information which is further enriched by the signatures of several key interactions (spin−orbit, multiplet, exchange) in the final state. The final states of XES are identical to those of photoemission spectroscopy; therefore, similar chemical sensitivity is observed.[36,37] The $K\alpha$ (1s2p) and $K\beta$ (1s3p) spectra of 3d transition-metal ions clearly reflect the 2p−3d and 3p−3d exchange interactions, respectively, which make the line shapes highly sensitive to the spin state.[38,39] (For the notations on X-ray transitions, see, for example, ref 40.) Owing to this, XES is more and more often used in spin state studies, particularly when there are advantages of working with penetrating hard X-rays, such as in high-pressure experiments.[41−43] When a transition involves two spin states, their distribution (the HS fraction, γ) can be readily and precisely calculated from the line shape variations.[39]

Diffuse Scattering. While the spectroscopic methods described above give accurate information on the electronic structure of the investigated systems, they are sensitive at best to the local structure around the absorber atom only, and they do not provide precise information about the full structural configuration of the other nuclei in the molecule under

investigation. This information is readily available from scattering studies, which probe the relative positions of the atomic nuclei by elastic scattering off (primarily) the associated core electrons in the entire sample.

In time-resolved studies utilizing X-ray Diffuse Scattering (XDS) from liquid samples, it is often beneficial to analyze the difference scattering signal $\Delta S \equiv S_{\mathrm{LaserOn}} - S_{\mathrm{LaserOff}}$, as this is a highly efficient way of suppressing the large static contribution to the scattering signal from the bulk solvent. By analyzing the difference signal, one studies the photoinduced changes triggered by the laser pump pulse only, typically a structural change in the solute coinciding with a (small) temperature increase of the solvent followed by subsequent bulk solvent expansion. These latter bulk solvent contributions to the difference signal can be readily determined in a separate experiment and can be robustly included in any structural analysis.[44]

As discussed in detail by Haldrup et al.,[45] the differenc scattering signal ΔS from solution state studies does not contain enough information to allow a direct structure determination. However, as has been established in previous time-resolved scattering studies, the information content is sufficient to allow quantitative model comparisons.[14,18,19,46−50] Within this approach, possible structural changes of an assumed initial structure are parametrized in terms of a few structural parameters, such as key bond lengths or angles. The best-fit or most-likely structure is then found by comparing simulated ΔS signals calculated from the putative structures of the solute molecules with the measured scattering signal. Such model comparisons are highly quantifiable[51] and can be implemented through both fast minimum searches[52] and full parameter-space mappings.[45] Both methods yield best-fit combinations of the model parameters, and the correlations between the parameters and parameter uncertainties can be estimated.

Beamline Layout and Laser Setup. Beamline 7ID is provided with X-ray photons from an APS type A undulator monochromatized by a double-crystal diamond monochromator. After focusing by Kirkpatrick−Baez mirrors, 2×10^{12} ph/s (3×10^5 ph/pulse in 24-bunch mode at a ring current of 102 mA) are delivered at a 10 keV energy to a sample spot size focused down to 5 μm (fwhm).[53]

The laser setup installed in the 7ID-D hutch is based on the high repetition rate Duetto system from Time-Bandwidth Products and is described in detail in the work by March et al.[32] This laser emits at a fundamental wavelength of 1064 nm with a repetition rate up to 6.52 MHz. The pulse width was chosen to be 10 ps. Focusing optics and an attenuator setup allow the fluence on the sample to be accurately controlled and can provide a 25 μm (fwhm) spot at the sample position. The spatial overlap between X-ray and laser pulses at the sample position is obtained by means of a motorized pinhole setup, and temporal overlap is achieved using a removable MSM (metal−semiconductor−metal) photodetector with a 30 ps rise time at the sample position. The spatial and temporal stability are 5 μm and 10 ps over several hours.[32] For all experiments reported in this work, the second harmonic at 532 nm was used to excite the sample, the pulse energy was 1.8 μJ focused onto a 100×80 μm^2 fwhm spot, and the repetition rate of the laser was 3.26 MHz. For the XES/XDS measurements, a 7.5 keV monochromatic X-ray beam was focused to 7 μm × 8 μm and centered on the laser spot. The data shown in this work were acquired in two runs separated by only a few minutes. First, data from a laser/X-ray time delay of $\Delta t = -100$ to +1100 ps with 200 ps between time points were acquired; then, data from $\Delta t = -80$ to +30 ps with 10 ps between time points were acquired. Negative Δt corresponds to the X-ray probe preceding the laser excitation pulse, and the total acquisition time was ∼12 h.

Figure 1 shows a schematic layout of the experimental setup. The laser and X-ray beams are almost collinear (5° crossing angle) and overlap on a fast-flowing 100 μm thick liquid jet mounted at 45$^{\mathrm{circ}}$ to the X-ray beam propagation direction. Lead foil with pinholes for the two beams is installed to limit air scattering, which is very significant at energies below 10 keV. In the horizontal plane and at right angles to the X-ray beam, X-ray emission detectors are installed, both a scintillator and a crystal spectrometer, and behind the sample, a Pilatus 100K area detector collects the forward-scattered X-rays. These detector systems for spectroscopy and scattering are described in further detail below.

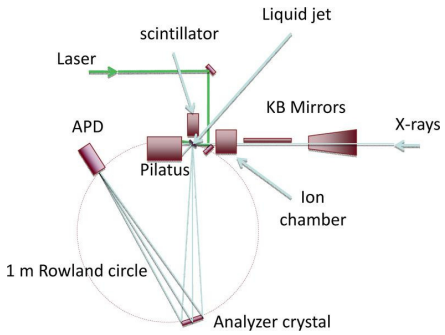

Figure 1. Experimental setup for the experiments reported here, seen from above. Laser and X-ray beams are focused and overlapped on a fast-flowing 100 μm thick sample sheet, and scattered X-rays are collected by a Pilatus 100K detector. The emitted X-ray photons are collected either directly by a scintillation detector for XANES using fluorescence detection or by an APD mounted in a 1 m Rowland circle dispersive setup within a He bag for XES measurements.

XES Data Acquisition. A wavelength-dispersive crystal spectrometer was constructed to measure the XES signal, with a spherically bent analyzer crystal of 10 cm diameter positioned at a 90° scattering angle and an avalanche photodiode (APD) detector at its focus, such that the sample−analyzer−detector setup constituted a 1 m Rowland circle. A thin plastic bag filled with He was installed around the spectrometer to minimize absorption losses. The spectra of the emitted X-rays were taken by scanning the Ge(440) and Si(531) spherically bent analyzer crystals through the appropriate Bragg angle range to collect the Fe Kα and Kβ spectra, respectively, and the APD was moved accordingly. For a particular time delay, two spectra were collected alternately, following the laser on/off pumping pattern. The total energy resolution measured through the spectrometer was 1.0 eV (fwhm) at 6404 eV, a resolution composed of 0.5 and 0.9 eV contributions from the beamline monochromator and the spectrometer, respectively.

XDS Data Collection. As described in detail by Ejdrup et al.,[54] the gated mode of the Pilatus detector is sufficiently fast to isolate single X-ray pulses from individual electron bunches with 153 ns spacing in the APS storage ring in 24-bunch mode. Combined with a synchronized laser system, this allows pump−probe studies with a time resolution determined by the width of the probe pulse, typically close to 80 ps in this mode.

dx.doi.org/10.1021/jp306917x | J. Phys. Chem. A 2012, 116, 9878−9887

To collect scattering data, a Pilatus 100K detector was placed 55 mm behind the sample. The detector plane was perpendicular to the X-ray beam direction and mounted with a horizontal offset to allow collection of scattered X-rays up to an angle of 53°. As the first step in the analysis, the direct beam and areas of the detector significantly affected by air scattering and by shadowing from the nozzle and beam stop mounts were masked out. Each image was then azimuthally integrated after applying appropriate geometric corrections.

The scattering data were collected in a sequential acquisition mode to allow robust construction of difference scattering signals ΔS. For a given time delay, the laser pulses were synchronized to arrive Δt before every other X-ray bunch from the synchrotron, giving an effective pump−probe repetition rate of 3.26 MHz. The gating signal to the Pilatus detector was then set to allow the scattering either from the laser-synchronized X-ray pulses or from the laser-off pulses to be detected and stored on the detector. The number of individual gating events per image acquisition was set to correspond to integration times of 5−10 s ($\sim 10^7$ gating events), leading to single-pixel photon counts of $\sim 10^5$ in the liquid peak. For each time delay, this sequence was then repeated until satisfying counting statistics for calculating ΔS with adequate signal-to-noise was reached, typically after 130 repetitions, corresponding to a total integration time of 40 min per time delay point for the best quality data. Choosing an energy of 7.5 keV, nearly 400 eV above the iron K-edge, this choice of integration time also allowed simultaneous collection of high-quality X-ray emission data.

A particular complication of the high-repetition-rate experiments in this and similar studies is that the sample volume investigated by a single pair of pump−probe pulses has already been previously subjected to a laser pump pulse. For setups conceptually similar to the one used here, this can be avoided up to repetition rates of ∼1 MHz using high-speed pump/jet systems (30 m/s) and small laser focus (<25 μm), but in the present case, the repetition frequency was significantly higher than the refresh rate of $f_{\text{refresh}} \approx 100$ kHz. For the X-ray spectroscopy data, this is not an issue as the lifetime of the photoexcited compound (τ = 665 ps[55]) is much less than the time between laser pulses (153 ns), effectively preventing multiphoton excitations from adjacent pump pulses. However, for the X-ray scattering studies, the changes in scattering due to the hydrodynamic evolution (heating followed by expansion) of the solvent need to be taken into account. For the experiments reported here, the contribution to the individual difference signals from previous pump events is common for all of the investigated time delays as the hydrodynamic evolution of the solvent is negligible on the single-nanosecond time scale after the first 100 ns following the impulsive heating event.[44] This contribution can therefore be readily determined by including a set of measurements where the laser pulse arrives shortly after the trailing edge of the X-ray pulse (e.g., Δt = −100 ps). This "background" difference signal can then be directly subtracted from the positive time delays to yield the difference scattering signal due only to the most-recent laser pulse, $\Delta S(\Delta t) = [S_{\text{On}}(\Delta t) - S_{\text{Off}}] - \Delta S_{\Delta t=-100\text{ ps}}$. All difference signals shown below have had the contribution from previous pump pulses removed by this background-subtraction method. This method is generally applicable for short-lived sample systems where the energy release to the solvent is fast compared to the 153 ns bunch spacing and where the solvent hydrodynamics evolve slowly after the first 100 ns. In cases where these requirements are not fully met, the determination of excitation fractions and quantitative discussions of the solvent response (e.g., a temperature increase) must adequately include the contributions from previous pump pulses.

RESULTS AND DISCUSSION

Spectroscopic Characterization of the HS State of $[Fe(bipy)_3]^{2+}$. Figure 2 shows the XANES of $[Fe(bipy)_3]^{2+}$

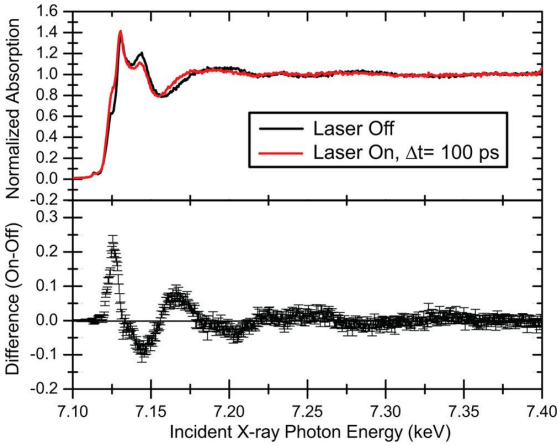

Figure 2. XANES spectra of a 20 mM aqueous solution of $[Fe(bipy)_3]^{2+}$, with and without laser excitation. The change from the LS to HS configuration is highly evident, and the S/N is observed to be excellent. XANES data were acquired in fluorescence-detection mode with a repetition frequency of 135.8 kHz.

before and 100 ps after the laser excitation, and the spectra are fully consistent with previous studies, indicating the light-induced formation of the HS state.[5,56] The S/N for both laser-on and laser-off measurements for this 135.8 kHz data acquisition are fully comparable to equivalent steady-state studies, highlighting the significant advantages of the high-repetition-rate schemes for time-resolved studies.

As described above, XES is a new probe in ultrafast experiments, and with a kHz repetition rate laser, it is at the limit of feasibility at synchrotron beamlines even at the most intense Kα_1 emission line.[30] However, MHz repetition rates make it possible to obtain count rates as high as those in conventional static experiments. In Figure 3, we present the first full Kα and Kβ spectra of photoexcited $[Fe(bipy)_3]^{2+}$, taken with a 3.26 MHz repetition rate at a delay of Δt = 100 ps. The spectra are in good agreement with the static HS/LS spectra taken on a closely related spin-crossover compound ($[Fe(phen)_2(NCS)_2]$),[39] and they allow us to determine the average spin momentum of Fe or directly determine the HS fraction γ using line shape analysis. In this paper, we use the approach called integrated absolute difference (IAD), which is performed by taking the absolute values of the difference between a sample and a reference spectrum and integrating them to obtain the IAD value. The IAD determined for the HS and LS spectra of appropriate reference materials can be referred to as IAD_{HL}, and the scaling factor between this and the IAD of a sample is the HS fraction, $IAD = \gamma IAD_{HL}$. The uncertainty of the IAD values can be readily calculated from the counting statistics using error propagation. This approach is explained in detail in ref 39 and has been used with success to

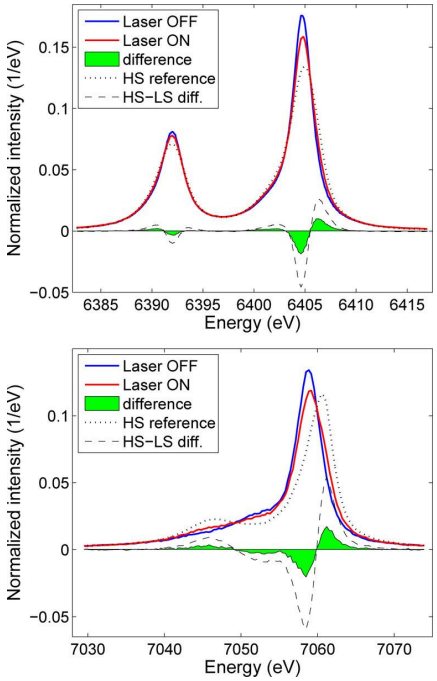

Figure 3. Kα (top) and Kβ (bottom) spectra of $[Fe(bipy)_3]^{2+}$ with Δt = 100 ps for the laser-on data. The change from the LS state at laser excitation is evident, and by direct comparison with HS/LS reference spectra, accurate determination of the HS fraction γ (close to 40% for this data set) can be determined from these spectra with very good S/N.

relate the spectral variations to spin state changes in many studies.[57−61] In the present work for the LS, we use an internal reference, the spectrum of the $[Fe(bipy)_3]^{2+}$ solution without laser excitation. The HS reference spectra were measured on a powder sample of $[Fe(phen)_2(NCS)_2]$ at room temperature. Figure 3 displays also the difference of the HS and LS reference spectra; the calculations behind the IAD method can be taken as finding the scaling factor between the sample difference spectrum and the HS−LS difference (displayed in Figure 3 as the green filled curve and dashed line, respectively). The IAD approach is very compatible with our data acquisition strategy of taking shot-by-shot alternating ground-state (laser-off, i.e., LS reference) and laser-on data at chosen delays. Typical values for the maximum HS fraction, here referred to as γ_0, were between 30 and 40%, depending on particular experimental parameters, such as spatial overlap of the X-ray and laser beams.

Difference Scattering Signatures of the Excited-State Structures. Figure 4 shows the acquired difference scattering signals for the six investigated time delays with $\Delta t \geq 100$ ps. The difference signals are each constructed from 134 on/off pairs of images with a 10 s integration time, azimuthally integrated and scaled to a known standard (water[62]). It is worth noting that for all time delays, the $\Delta S/S$ ratio is less than 10^{-3}, highlighting the need for the high repetition rate. The time delays were chosen to fully cover the lifetime of the excited HS state of $[Fe(bipy)_3]^{2+}$ (τ = 665 ps[55]).

Qualitative inspection of this set of difference curves reveals a negative feature at low Q that decays on a time scale of several hundred picoseconds and an oscillatory feature from Q = 1.5 to

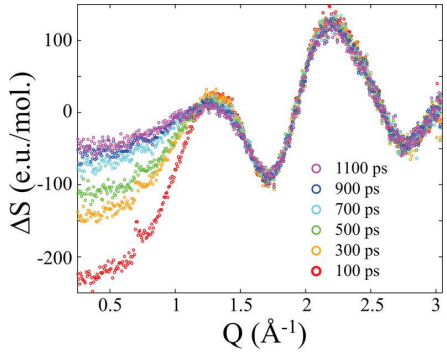

Figure 4. Averaged difference signals for 134 on/off repetitions at six time delays following the photoexcitation event at Δt = 0 ps. The signal is dominated by a negative feature at low Q related to the expansion of the solute molecule and an oscillatory feature arising from the changes in the bulk structure of the solvent (water).

3 Å^{-1}, which appears to be essentially constant for all of the investigated time delays. The negative feature in the low-Q region can be directly associated with the well-established[56,63] 0.2 Å elongation of the Fe−N bond in excited-state $[Fe(bipy)_3]^{2+}$. This feature and its observed dynamic time scale constitute an unambiguous scattering signature from the light-triggered formation of HS $[Fe(bipy)_3]^{2+}$ molecules with the excited-state structure. The oscillatory feature at around Q = 2 Å^{-1} arises from changes in the intermolecular structure of the bulk solvent, as discussed in detail below.

Comparison of XAS/XES/XDS-Measured Kinetics. The strong and prompt XAS response to photoexcitation was utilized to optimize the experimental conditions (notably, the overlap of the two beams in space and time), so that they were appropriate for studying the structural and electronic dynamics of the $[Fe(bipy)_3]^{2+}$. In the XANES spectrum, the 7125 eV feature shows the largest change following the spin transition. Figure 5a displays the time evolution of the intensity of this signal feature, which corresponds to the formation and decay of the HS state. The width of the rise centered at Δt = 0 corresponds to the X-ray probe pulse width, while the later exponential decay is governed by the lifetime of the HS state. This time evolution is fitted by an expression of the form

$$I(\Delta t) = I(t - t_0) = \gamma_0 \int_{-\infty}^{\infty} \frac{1}{\sigma\sqrt{2\pi}} e^{-y^2/2\sigma^2} H(t - t_0 - y)\, e^{-(t-t_0-y)/\tau}\, dy \quad (1)$$

derived from a Gaussian broadening (with width σ) of an exponential decay starting at t_0 with starting value γ_0, here interpreted as the photoexcitation (HS) fraction just after laser excitation. The τ stands for the lifetime of the HS state and H is the heaviside step function. Key parameters for each data set are listed in Table 1, and we note that for all three methods, the lifetime of the HS state is found to be in reasonable agreement with the lifetimes found in previous studies.[6] Also, the expected ~80 ps X-ray probe pulse width for APS in the 24-bunch mode is well reproduced between methods.

The simultaneous utilization of scattering and spectroscopy techniques allows us to follow the dynamics on both the local and a more extended range. XES is practically sensitive to the

dx.doi.org/10.1021/jp306917x | J. Phys. Chem. A 2012, 116, 9878−9887

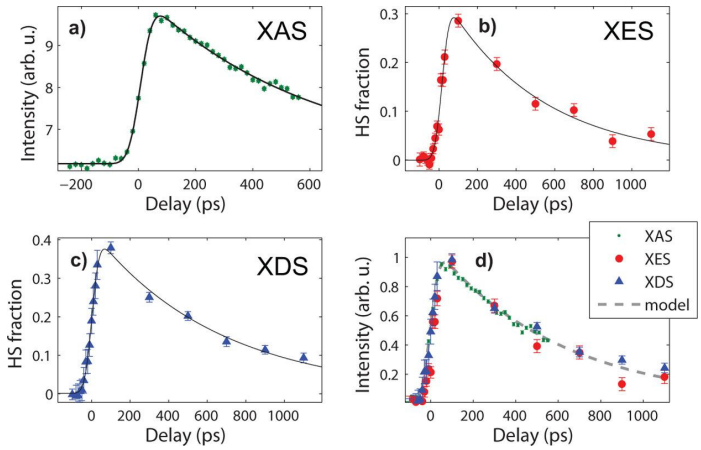

Figure 5. Time evolution of the HS fraction from (a) XAS, (b) XES, and (c) XDS, independently fitted with eq 1. The data in (a) were taken in a separate measurement, while the data in (b) and (c) were taken simultaneously. A unified plot of the results from the three techniques is seen in (d), highlighting how the observed dynamics are fully consistent between techniques as well as individual experiments.

Table 1. Parameter Estimates Obtained by Fitting Equation 1 to the XAS, XES, and XDS Data Sets, With 95% Confidence Limits[a]

technique	lifetime (τ) (ps)	fwhm pulse width (ps)	t_0 (ps)	γ_0
XAS	594 ± 30	78 ± 6	9.2 ± 2	n.a.
XES	503 ± 100	71 ± 18	17.6 ± 6	0.34 ± 0.04
XDS	657 ± 75	71 ± 16	4.2 ± 5	0.43 ± 0.03

[a]In general, good agreement between the three measurements is observed but with a tendency for the XES results to exhibit a slightly shorter lifetime.

changes on the Fe^{2+} ion only. From such measurements, the relative amount of excited complexes in the probed volume, the HS fraction, can be obtained from the laser-on/laser-off XES difference spectra at different delays. The HS fraction plotted against the delay reveals the spin state dynamics; see Figure 5b. The continuous line is a fitted model curve that corresponds to the above equation, and the fit parameters are listed in Table 1. Note that γ_0 also becomes relevant here as XES quantitatively determines the HS fraction. Therefore, this fit parameter is the HS conversion yield (initial HS population); the best-fit results correspond to an initial HS fraction of 0.34 ± 0.04. The lifetime of the HS state compares moderately well with that obtained from XAS.

To quantify the dynamics of the set of the difference scattering signals, each individual difference signal $\Delta S(Q,\Delta t)$ was considered to be a combination of contributions from changes in the structure of the solute and from changes in bulk solvent scattering due to changes in solvent temperature T and density ρ[19,44]

$$\Delta S(Q)_{\Delta t} = \gamma_{\Delta t}\Delta S(Q)_{\text{Solute}} + \Delta T_{\Delta t}\left.\frac{\partial(\Delta S(Q))}{\partial T}\right|_{\rho} + \Delta\rho_{\Delta t}\left.\frac{\partial(\Delta S(Q))}{\partial \rho}\right|_{T} \quad (2)$$

where the subscript Δt denotes dependence on the time delay. The simulated solute contribution $\Delta S(Q)_{\text{Solute}}$ was calculated by a combined approach utilizing both DFT-derived structures and molecular dynamics (MD) simulations. We used the molecular structures for the LS and the HS states calculated by Daku and Hauser using an ab initio molecular dynamics (AIMD) approach with water as the solvent.[63] The structures determined in their study were then introduced into classical MD simulations with 4171 water molecules (OPLS2005 force field with the TIP4P water model), which were then allowed to evolve at constant T and ρ for 2000 ps with a 2 fs step size and with the structure of the solute held rigid by imposing constraints on all $[Fe(bipy)_3]^{2+}$ bonds. From two ensembles (with either HS or LS solute molecules) of such simulations, the average scattering was calculated for both model structures (including the surrounding solvent) using the Debye equation to finally yield $\Delta S(Q)_{\text{Solute}} = \Delta S(Q)^{\text{model}}_{\text{HS}} - \Delta S(Q)^{\text{model}}_{\text{LS}}$. This combined approach allowed direct incorporation of local changes in scattering due to changes in solvation and excluded volume effects following the photoinduced change in the solute structure and improved the quality of the fits very significantly compared to only incorporating the structural changes in the solute.

Fitting eq 2 to the measured $[Fe(bipy)_3]^{2+}$ ΔS signals, Figure 5c shows the fitted excitation fraction $\gamma_{\Delta t}$ as a function of time delay. The good agreement observed between the three methods is illustrated in Figure 5d, and Table 1 reports key experimental parameters obtained by fitting eq 1 to each data set. The same kinetics are observed with all methods, and the small discrepancy in excitation fractions observed with XDS and XES is attributed to uncertainties in accurate scaling of the XDS data set due to the significant air scattering. In the fit process, strong correlation between $\Delta\rho$ and ΔT was observed and led to unstable fits for some time delays. This was handled by the reasonable assumption of a monotonically increasing transient temperature change (within the error bars).

Figure 6(left) shows the good agreement between the measured ΔS and the best-fit simulated signals; for clarity of presentation, only data points with $\Delta t \geq 0$ ps are shown. The right panel of Figure 6 shows the relative contributions from each of the three signals included in the model calculations. An immediate grow-in of all three components is observed, followed by a decrease in the contributions from structural changes in the solute and from changes in the density of the

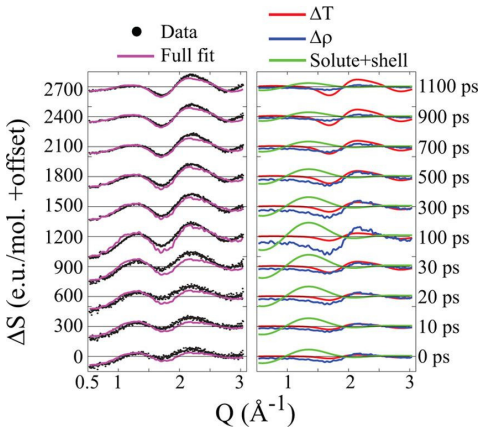

Figure 6. (Left) Data (black points) and fits (purple lines) for all time delays with $\Delta t \geq 0$ ps. Noise on the fit traces is due to the noise in the experimentally determined differential $[\partial(\Delta S)/\partial\rho]|_T$. (Right) The three contributions to the best-fit difference signals for each time delay. Green traces arise from changes in structure and solvation of $[Fe(bipy)_3]^{2+}$, red traces are from heating of the solvent, and blue traces arise from changes in the bulk density of the solvent.

solvent. The time scale for this decrease matches the 665 ps lifetime of the HS state of $[Fe(bipy)_3]^{2+}$ and is accompanied by a further increase in the temperature of the solvent.

Quantifying these general observations, Figure 7 shows the magnitude of each of the three components of the fits

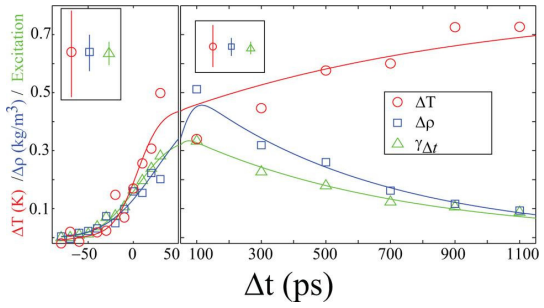

Figure 7. Time evolution of the magnitude of each of the three contributions to the total difference signal. A fast grow-in is observed for Δt < 100 ps for all three parameters. On time scales longer than Δt = 100 ps, the temperature is observed to rise further, whereas the density and excitation contributions are observed to decay on the time scale of the HS state of $[Fe(bipy)_3]^{2+}$, in full agreement with the model discussed in the text. The top-left insets illustrate the error bars (95% C.L.) for the fit parameters in the two regions.

presented in Figure 6 as a function of Δt. The behavior of these three contributions, which together describe the structural evolution of the investigated sample volume following photoexcitation, is essentially the same on the Δt < 50 ps time scale for all three but diverges for Δt > 50 ps.

Turning first to the fastest time scales, the common response is fully explained by a stepwise change due to the (short) excitation laser pulse, broadened by the finite width of the X-ray probe pulse, as described in detail above. On the longer time scales, the density change of the bulk solvent (Δ_ρ) is observed to follow the same exponential decay as the HS fraction $\gamma_{\Delta t}$ and with a similar time constant, $\tau_{\Delta\rho}$ = 500 ± 150 ps and τ_γ = 660 ± 90 ps. The observed increase in temperature is well captured by the same broadened step function followed by an increase taking the form of an exponential grow-in but with a poorly determined time constant, $\tau_{\Delta T}$ = 910 ± 600 ps. These functional forms have been independently fitted to the three data series shown in Figure 7 and are shown as solid lines.

The temperature response of the solvent can be understood immediately from the decay processes previously described for $[Fe(bipy)_3]^{2+}$ as the majority of the absorbed photon energy is released very fast ($\tau \approx 1$ ps) as vibrational energy to the solvent after the ~130 fs intersystem crossing.[55] This is then followed by a slower release of energy as the HS state decays nonradiatively ($\tau \approx 665$ ps). On the time scales accessible to the present experiment, this results in a (broadened) step-like increase in temperature followed by the observed further increase on the time scale of the HS lifetime. The average ~0.5° temperature increase over the probed sample volume is in good agreement but somewhat larger than the corresponding values obtained in previous studies using kHz repetition schemes with higher pump pulse fluences.[19] The larger temperature increase is expected as the concentration of excited molecules is more than 10 times higher in the present experiment and the decay modes of $[Fe(bipy)_3]^{2+}$ are almost completely nonradiative, but it is still significantly less than the temperature increase observed to drive LS−HS conversion in the low-temperature crystal studies of Cailleau et al.[64] No such temperature-driven processes are expected for $[Fe(bipy)_3]^{2+}$ due to the large LS−HS energy difference, 0.74 eV.[55]

To understand the prompt increase in density on the 100 ps time scale, we turn to a key finding of the computational study of Daku and Hauser,[63] namely, the change in solvation of $[Fe(bipy)_3]^{2+}$ following conversion to the HS state. From their theoretical investigations, a consequence of the excitation and the structural change is the expulsion of ~2 water molecules from the solvation shell to the bulk solvent. With the characteristic time scale for mass transport out of the probed volume given by the Longaker−Litvak time $\tau_L = L/c$, with as the L the pump pulse size and c as the the speed of sound,[44] there is no time for mass transport out of the investigated volume on the 100 ps time scale. Thus, the proposed solvation change would be expected to lead to an increase in the density of the bulk solvent. For a 20 mM solution (2750 solvent molecules per solute) with 40% photoexcitation, a lower limit on the associated change in density can be very roughly estimated to be 0.4 × 2/2750 = 0.03%, excluding all other changes such as, for example, the increased volume of the solute and the reported reorientation of the first solvent shell. This lower limit of a 0.03% fractional change corresponds to a change in density of 0.3 kg/m^3 and agrees reasonably well with the value estimated from our data analysis, ~0.5 kg/m^3. However, to fully establish and quantify the proposed direct connection between the observed macroscopic change in density and the microscopic phenomenon of solvent shell reorganization, further studies are needed.

Whereas this analysis fully accounts for the qualitative features of the observed evolution of the measured difference signals, a few minor discrepancies in the quantitative results are present. First, the decay time determined for ΔT and $\Delta\rho$ are similar but not identical, and the increase in density measured is somewhat larger than would be expected from the simplest interpretation of the computational result. To address these issues, a second analysis was performed, where advantage was

dx.doi.org/10.1021/jp306917x | J. Phys. Chem. A 2012, 116, 9878−9887

taken of the independent measurement of the excitation fraction offered by the XES data. This allowed us to lock in the excitation fraction in the analysis, and through the significant correlations between this parameter and $\Delta\rho$, the uncertainty in determining the numeric value of $\Delta\rho$ for each time step was reduced by ∼15%. The Δ_ρ value determined for each Δt was lowered by ∼10%, improving the agreement with the model prediction. Carrying these results over to the kinetic analysis, we find $\tau_{\Delta\rho} = 620 \pm 90$ ps, in much better agreement with both the present and previous results for τ_γ

A second issue to address in the qualitative analysis is the (small) discrepancy between the rise time of the three components of the fit. Within the physical model established here, one would expect these to be identical and to be given by the width of the X-ray probe pulse. However, the temperature appears to rise slightly faster than the excitation fraction, and the change in density appears to rise slightly slower. Although $[Fe(bipy)_3]^{2+}$ in solution is known to be exceptionally robust to even prolonged and intense X-ray exposure, we tentatively suggest that during the ∼12 h of exposure to the focused X-ray beam, a very small amount of degradation product capable of absorbing light at 532 nm and releasing the absorbed energy as heat is formed. This would lead to increased heat deposition by each pump pulse over the course of the experiment. In particular, the contribution from previous pump pulses would not be compensated for by the subtraction of only one background signal, and over the course of hours, the observed (transient) temperature increase would go up, and the observed (transient) density increase would diminish, as observed. Had the increased heating been due to changes in excitation fractions due to evaporative losses of solvent, we would expect to observe concomitant changes in the measured excitation fractions as the deposited energy from the laser-excited molecules and thus the solvent heating are linear functions of the excitation fraction. This is not observed.

The tentative suggestion of increased heat deposition due to a very small amount of decay product is further supported by a second analysis of the difference signals, where instead of one early ($\Delta t < -50$ ps) time delay being used as the background contribution, incremental difference patterns are calculated from successive time delays. Applying this analysis, the rise times are more in agreement, and we also obtain better fits to the $\Delta t < 100$ ps difference curves. However, due to the order in which the data for each time delay were acquired, this method cannot be applied to the entire data set.

A full investigation of the local solvation dynamics of photoexcited $[Fe(bipy)_3]^{2+}$ is beyond the scope of the present paper. However, the finding that such dynamics can be directly investigated by time-resolved XDS underscores the new possibilities opened up by increasing the available X-ray flux by 2−3 orders of magnitude, as well as the benefits of using a "tickle and probe" approach, where smaller laser fluences are used for the pump pulse, thus not drowning out small signals by large thermal effects.

■ CONCLUSIONS

In the present study, we have utilized the recently developed MHz laser pump/X-ray probe capability[32] of the 7ID beamline at the Advanced Photon Source to combine the complementary and photon-hungry techniques of X-ray emission spectroscopy and X-ray diffuse scattering in a single experiment. Even though the single-pulse energy of the laser pump pulses is limited to the <10 μJ regime for MHz repetition rates, tight focusing (<100 μm) of both beams allowed us to obtain high excitation fractions (30−40% HS $[Fe(bipy)_3]^{2+}$) in the probed sample volume. The 3.26 MHz repetition rate of the experiment is the highest reported yet and led to an increase in usable X-ray flux on the sample by 3 orders of magnitude compared to the usual kHz synchrotron-based time-resolved experiments. This rendered both techniques fully feasible and gave XES data quality comparable to that of steady-state experiments. The increase in flux and the experimental design also allowed simultaneous collection of high-quality scattering data for this comparatively light compound in only a few hours. By combining the XES data with XDS results, the presence of the high-spin configuration of the Fe^{II} ion could be unambiguously tied to the global structural changes in molecular structure observed directly in the ΔS signals. The direct and simultaneous measurement of the excited-state fraction was used to significantly reduce the uncertainties, directly addressing complications with strongly correlated fit parameters, as suggested in previous work.[45] The combined experiment thus offers benefits beyond that of simply combining information from two separate experiments, in addition to the highly efficient use of the X-ray beam.

The superior quality of the scattering data combined with the comparatively gentle laser excitation further allowed us to tentatively confirm a key prediction of recent theoretical work on $[Fe(bipy)_3]^{2+}$.[63] By quantitative analysis of the subnanosecond response of the bulk solvent structure, the consequences of the solvation dynamics of the HS $[Fe(bipy)_3]^{2+}$ were detected by monitoring the increase in solvent density due to expulsion of water molecules from the first solvation shell following photoexcitation.

Even as $[Fe(bipy)_3]^{2+}$ is a thoroughly studied model compound in time-resolved science, this experimental detection of a process involving only the disordered rearrangement of light elements highlights how the much increased X-ray flux will allow future time-resolved experiments to move from molecular systems tailored or chosen to match the usually low X-ray intensity and to move on to more general classes of systems that have so far only been studied with steady-state methods.

■ AUTHOR INFORMATION

Corresponding Author

*E-mail: hald@fysik.dtu.dk (K.H.); vanko@rmki.kfki.hu (G.V.).

Notes

The authors declare no competing financial interest.

■ ACKNOWLEDGMENTS

This project was supported by the European Research Council via Contract ERC-StG-259709, by the Danish National Research Foundation's Centre for Molecular Movies, by the European XFEL, and DANSCATT. A.M.M., G.D., S.H.S., E.P.K., and L.Y. acknowledge support from the U.S. Department of Energy (DOE) Office of Science, Division of Chemical, Geological and Biological Sciences, under Contract No. DE-AC02-06CH11357. K.H. gratefully acknowledges support from the Carlsberg and Villum Foundations. G.V. acknowledges support from the Bolyai János Fellowship of the Hungarian Academy of Sciences. V.S. acknowledges support from the European Research Council, Advanced Investigator Grant, VISCHEM-226136. S.E.C. gratefully acknowledges funding from the Swedish Research Council. C.B., A.G. and W.G. acknowledge funding from the German Research Association

DFG via SFB925 (project A4). Use of the Advanced Photon Source, an Office of Science User Facility operated for DOE Office of Science by Argonne National Laboratory, was supported by the U.S. DOE under Contract No. DE-AC02-06CH11357.

REFERENCES

(1) Fleming, G. R.; Cho, M. *Annu. Rev. Phys. Chem.* **1996**, *47*, 109−134.
(2) Ball, P. *Chem. Rev.* **2008**, *108*, 74−108.
(3) Zhong, D.; Pal, S. K.; Zewail, A. H. *Chem. Phys. Lett.* **2011**, *503*, 1−11.
(4) Cramer, C.; Truhlar, D. *Chem. Rev.* **1999**, *99*, 2161−2200.
(5) Bressler, C.; Milne, C.; Pham, V.-T.; ElNahhas, A.; van der Veen, R. M.; Gawelda, W.; Johnson, S.; Beaud, P.; Grolimund, D.; Kaiser, M.; Borca, C. N.; Ingold, G.; Abela, R.; Chergui, M. *Science* **2009**, *323*, 489−492.
(6) Cannizzo, A.; Milne, C.; Consani, C.; Gawelda, W.; Bressler, C.; van Mourik, F.; Chergui, M. *Coord. Chem. Rev.* **2010**, *254*, 2677−2686 ; 18th International Symposium on the Photochemistry and Photophysics of Coordination Compounds Sapporo, 2009..
(7) Lindenberg, A.; Kang, I.; Johnson, S.; Missalla, T.; Heimann, P.; Chang, Z.; Larsson, J.; Bucksbaum, P.; Kapteyn, H.; Padmore, H.; Lee, R.; Wark, J.; Falcone, R. *Phys. Rev. Lett.* **2000**, *84*, 111−114.
(8) Chen, L.; Jager, W.; Jennings, G.; Gosztola, D.; Munkholm, A.; Hessler, J. *Science* **2001**, *292*, 262−264.
(9) Techert, S.; Schotte, F.; Wulff, M. *Phys. Rev. Lett.* **2001**, *86*, 2030−2033.
(10) Schotte, F.; Lim, M.; Jackson, T.; Smirnov, A.; Soman, J.; Olson, J.; Phillips, G.; Wulff, M.; Anfinrud, P. *Science* **2003**, *300*, 1944−1947.
(11) Collet, E.; Lemee-Cailleau, M.; Buron-Le Cointe, M.; Cailleau, H.; Wulff, M.; Luty, T.; Koshihara, S.; Meyer, M.; Toupet, L.; Rabiller, P.; Techert, S. *Science* **2003**, *300*, 612−615.
(12) Johnson, S.; Heimann, P.; Lindenberg, A.; Jeschke, H.; Garcia, M.; Chang, Z.; Lee, R.; Rehr, J.; Falcone, R. *Phys. Rev. Lett.* **2003**, *91*, 157403.
(13) Saes, M.; Bressler, C.; Abela, R.; Grolimund, D.; Johnson, S.; Heimann, P.; Chergui, M. *Phys. Rev. Lett.* **2003**, *90*, 047403.
(14) Ihee, H.; Lorenc, M.; Kim, T.; Kong, Q.; Cammarata, M.; Lee, J.; Bratos, S.; Wulff, M. *Science* **2005**, *309*, 1223−1227.
(15) Gawelda, W.; Bressler, C.; Saes, M.; Kaiser, M.; Tarnovsky, A. N.; Grolimund, D.; Johnson, S. L.; Abela, R.; Chergui, M. *Phys. Scr.* **2005**, *T115*, 102−106.
(16) Gawelda, W.; Johnson, M.; de Groot, F.; Abela, R.; Bressler, C.; Chergui, M. *J. Am Chem. Soc.* **2006**, *128*, 5001−5009.
(17) Hertlein, M.; Adaniya, H.; Amini, J.; Bressler, C.; Feinberg, B.; Kaiser, M.; Neumann, N.; Prior, M.; Belkacem, A. *Phys. Rev. A* **2006**, *73*, 062715.
(18) Cammarata, M.; Levantino, M.; Schotte, F.; Anfinrud, P. A.; Ewald, F.; Choi, J.; Cupane, A.; Wulff, M.; Ihee, H. *Nat. Methods* **2008**, *5*, 881−886.
(19) Christensen, M.; Haldrup, K.; Bechgaard, K.; Feidenhans'l, R.; Kong, Q.; Cammarata, M.; Russo, M. L.; Wulff, M.; Harrit, N.; Nielsen, M. M. *J. Am. Chem. Soc.* **2009**, *131*, 502−508.
(20) van der Veen, R. M.; Milne, C. J.; El Nahhas, A.; Lima, F. A.; Pham, V.-T.; Best, J.; Weinstein, J. A.; Borca, C. N.; Abela, R.; Bressler, C.; Chergui, M. *Angew. Chem., Int. Ed.* **2009**, *48*, 2711−2714.
(21) Haldrup, K.; Harlang, T.; Christensen, M.; Dohn, A.; van Driel, T. B.; Kjær, K. S.; Harrit, N.; Vibenholt, J.; Guerin, L.; Wulff, M.; Nielsen, M. M. *Inorg. Chem.* **2011**, *50*, 9329−9336.
(22) Fornuier, B.; Coppens, P. *J. Synchrotron Radiat.* **2012**, *19*, 497−502.
(23) Khalil, M.; Marcus, M. A.; Smeigh, A. L.; McCusker, J. K.; Chong, H. H. W.; Schoenlein, R. W. *J. Phys. Chem. A* **2006**, *110*, 38−44.
(24) Elles, C. G.; Shkrob, I. A.; Crowell, R. A.; Arms, D. A.; Landahl, E. C. *J. Chem. Phys.* **2008**, *128*, 061102.
(25) Huse, N.; Kim, T. K.; Jamula, L.; McCusker, J. K.; de Groot, F. M. F.; Schoenlein, R. W. *J. Am. Chem. Soc.* **2010**, *132*, 6809−6816.
(26) Huse, N.; Cho, H.; Hong, K.; Jamula, L.; de Groot, F. M. F.; Kim, T. K.; McCusker, J. K.; Schoenlein, R. W. *J. Phys. Chem. Lett.* **2011**, *2*, 880−884.
(27) Van Kuiken, B. E.; Huse, N.; Cho, H.; Strader, M. L.; Lynch, M. S.; Schoenlein, R. W.; Khalil, M. *J. Phys. Chem. Lett.* **2012**, *3*, 1695−1700.
(28) Harpham, M. R.; et al. *Angew. Chem., Int. Ed.* **2012**, *51*, 7692−7696.
(29) Stern, E. A.; Brewe, D. L.; Beck, K. M.; Heald, S. M.; Feng, Y. *Phys. Scr.* **2005**, *T115*, 1044−1046.
(30) Vankó, G.; Glatzel, P.; Pham, V.-T.; Abela, R.; Grolimund, D.; Borca, C. N.; Johnson, S. L.; Milne, C. J.; Bressler, C. *Angew. Chem., Int. Ed.* **2010**, *49*, 5910−5912.
(31) Bressler, C.; Chergui, M. *Chem. Rev.* **2004**, *104*, 1781−1812.
(32) March, A. M.; Stickrath, A.; Doumy, G.; Kanter, E. P.; Krässig, B.; Southworth, S. H.; Attenkofer, K.; Kurtz, C. A.; Chen, L. X.; Young, L. *Rev. Sci. Instrum.* **2011**, *82*, 073110.
(33) Lima, F. A.; et al. *Rev. Sci. Instrum.* **2011**, *82*, 063111.
(34) Vanko, G.; et al. *J. Electron Spectrosc. Relat. Phenom.* **2012**, Accepted.
(35) Young, L.; Arms, D. A.; Dufresne, E. M.; Dunford, R. W.; Ederer, D. L.; Hohr, C.; Kanter, E. P.; Krassig, B.; Landahl, E. C.; Peterson, E. R.; Rudati, J.; Santra, R.; Southworth, S. H. *Phys. Rev. Lett.* **2006**, *97*, 083601.
(36) Glatzel, P.; Bergmann, U. *Coord. Chem. Rev.* **2005**, *249*, 65−95.
(37) Lee, N.; Petrenko, T.; Bergmann, U.; Neese, F.; DeBeer, S. *J. Am. Chem. Soc.* **2010**, *132*, 9715−9727.
(38) Wang, X.; de Groot, F. M. F.; Cramer, S. P. *Phys. Rev. B* **1997**, *56*, 4553−4564.
(39) Vankó, G.; Neisius, T.; Molnár, G.; Renz, F.; Kárpáti, S.; Shukla, A.; de Groot, F. M. F. *J. Phys. Chem. B* **2006**, *110*, 11647−11653.
(40) de Groot, F. M. F. *Chem. Rev.* **2001**, *101*, 1779−1808.
(41) Rueff, J. P.; Shukla, A.; Kaprolat, A.; Krisch, M.; Lorenzen, M.; Sette, F.; Verbeni, R. *Phys. Rev. B* **2001**, *63*, 132409.
(42) Badro, J.; Fiquet, G.; Guyot, F.; Rueff, J.-P.; Struzhkin, V. V.; Vankó, G.; Monaco, G. *Science* **2003**, *300*, 789−791.
(43) Lin, J.-F.; Vankó, G.; Jacobsen, S. D.; Iota, V.; Struzhkin, V. V.; Prakapenka, V. B.; Kuznetsov, A.; Yoo, C.-S. *Science* **2007**, *317*, 1740−1743.
(44) Cammarata, M.; Lorenc, M.; Kim, T.; Lee, J. H.; Kong, Q. Y.; Pontecorvo, E.; Russo, M. L.; Schiro, G.; Cupane, A.; Wulff, M.; Ihee, H. *J. Chem. Phys.* **2006**, *124*, 1245041−9.
(45) Haldrup, K.; Christensen, M.; Nielsen, M. M. *Acta Crystallogr., Sect. A* **2010**, *A66*, 261−260.
(46) Haldrup, K.; Christensen, M.; Cammarata, M.; Kong, Q.; Wulff, M.; Mariager, S. O.; Bechgaard, K.; Feidenhans'l, R.; Harrit, N.; Nielsen, M. M. *Angew. Chem., Int. Ed.* **2009**, *48*, 4180−4184.
(47) Kim, T. K.; Lee, J. H.; Wulff, M.; Kong, Q.; Ihee, H. *ChemPhysChem* **2009**, *10*, 1958−1980.
(48) Salassa, L.; Borfecchia, E.; Ruiu, T.; Garino, C.; Gianolio, D.; Gobetto, R.; Sadler, P. J.; Cammarata, M.; Wulff, M.; Lamberti, C. *Inorg. Chem.* **2010**, *49*, 11240−11248.
(49) Haldrup, K.; Harlang, T.; Christensen, M.; Dohn, A.; van Driel, T. B.; Kjaer, K. S.; Harrit, N.; Vibenholt, J.; Guerin, L.; Wulff, M.; Nielsen, M. M. *Inorg. Chem.* **2011**, *50*, 9329−9336.
(50) Kong, Q.; Kjaer, K. S.; Haldrup, K.; Sauer, S. P. A.; van Driel, T. B.; Christensen, M.; Nielsen, M. M.; Wulff, M. *Chem. Phys.* **2012**, *393*, 117−122.
(51) Press, W. H.; Flannery, B. P.; Teukolsky, T. A.; Vetterling, W. T. *Numerical Recipes — The Art of Scientific Computing*; Cambridge University Press: New York, 1986.
(52) Jun, S.; Lee, J. H.; Kim, J.; Kim, J.; Kim, K. H.; Kong, Q.; Kim, T. K.; Lo Russo, M.; Wulff, M.; Ihee, H. *Phys. Chem. Chem. Phys.* **2010**, *12*, 11536−11547.
(53) Dufresne, E. M.; Adams, B.; Arms, D. A.; Chollet, M.; Landahl, E. C.; Li, Y.; Walko, D. A.; Wang, J. *AIP Conf. Proc.* **2010**, *1234*, 181−184.

(54) Ejdrup, T.; Lemke, H. T.; Haldrup, K.; Nielsen, T. N.; Arms, D. A.; Walko, D. A.; Miceli, A.; Landahl, E. C.; Dufresne, E. M.; Nielsen, M. M. *J. Synchrotron Radiat.* **2009**, *16*, 387−390.
(55) Gawelda, W.; Cannizzo, A.; Pham, V.-T.; vanMourik, F.; Bressler, C.; Chergui, M. *J. Am. Chem. Soc.* **2007**, *129*, 8199−8206.
(56) Gawelda, W.; Pham, V.-T.; Benfatto, M.; Zaushitsyn, Y.; Kaiser, M.; Grolimund, D.; Johnson, S. L.; Abela, R.; Hauser, A.; Bressler, C.; Chergui, M. *Phys. Rev. Lett.* **2007**, *98*, 057401.
(57) Vankó, G.; de Groot, F. M. F. *Phys. Rev. B* **2007**, *75*, 177101.
(58) Sikora, M.; Knizek, K.; Kapusta, C.; Glatzel, P. *J. Appl. Phys.* **2008**, *103*, 07C907.
(59) Yamaoka, H.; Tsujii, N.; Oohashi, H.; Nomoto, D.; Jarrige, I.; Takahiro, K.; Ozaki, K.; Kawatsura, K.; Takahashi, Y. *Phys. Rev. B* **2008**, *77*, 115201.
(60) Herrero-Martin, J.; Mirone, A.; Fernandez-Rodriguez, J.; Glatzel, P.; Garcia, J.; Blasco, J.; Geck, J. *Phys. Rev. B* **2010**, *82*, 075112.
(61) Mao, Z.; Lin, J. F.; Jacobs, C.; Watson, H. C.; Xiao, Y.; Chow, P.; Alp, E. E.; Prakapenka, V. B. *Geophys. Res. Lett.* **2010**, *37*, L22304.
(62) Hura, G.; Sorenson, J.; Glaeser, R.; Head-Gordon, T. *J. Chem. Phys.* **2000**, *113*, 9140−9148.
(63) Daku, L. M. L.; Hauser, A. *J. Phys. Chem. Lett.* **2010**, *1*, 1830−1835.
(64) Cailleau, H.; Lorenc, M.; Guérin, L.; Servol, M.; Collet, E.; Buron-Le Cointe, M. *Acta Crystallogr., Sect. A* **2010**, *66*, 189−197.

Paper III

Introducing a standard method for experimental determination of the solvent response in laser pump,X-ray probe time-resolved wide-angle X-ray scattering experiments on systems in solution

Kasper Skov Kjær, **Tim Brandt van Driel**, Jan Kehres, Kristoffer Haldrup, Dmitry Khakhulin, Klaus Bechgaard, Marco Cammarata, Michael Wulff, Thomas Just Sørensen and Martin M. Nielsen.

Physical chemistry chemical physics **15(36)**, 15003-16(2013).

PCCP

RSC Publishing

PAPER

Introducing a standard method for experimental determination of the solvent response in laser pump, X-ray probe time-resolved wide-angle X-ray scattering experiments on systems in solution†

Cite this: *Phys. Chem. Chem. Phys.*, 2013, **15**, 15003

Kasper Skov Kjær,[ab] Tim B. van Driel,[b] Jan Kehres,[b] Kristoffer Haldrup,[b] Dmitry Khakhulin,[c] Klaus Bechgaard,[d] Marco Cammarata,[e] Michael Wulff,*[c] Thomas Just Sørensen*[d] and Martin M. Nielsen*[b]

Received 19th February 2013,
Accepted 20th June 2013

DOI: 10.1039/c3cp50751c

www.rsc.org/pccp

In time-resolved laser pump, X-ray probe wide-angle X-ray scattering experiments on systems in solution the structural response of the system is accompanied by a solvent response. The solvent response is caused by reorganization of the bulk solvent following the laser pump event, and in order to extract the structural information of the solute, the solvent response has to be treated. Methodologies capable of doing so include both theoretical modelling and experimental determination of the solvent response. In the work presented here, we have investigated how to obtain a reproducible solvent response—the solvent term—experimentally when applying laser pump, X-ray probe time-resolved wide-angle X-ray scattering. The solvent term describes difference scattering arising from the structural response of the solvent to changes in the hydrodynamic parameters: pressure, temperature and density. We present results based on NIR and dye mediated solvent heating, and demonstrate that the solvent response is independent of the heating method. The NIR heating is shown to be rendered unusable by higher order effects under certain experimental conditions, while the dye mediated solvent heating is demonstrated to exhibit first order behaviour with respect to the amount of energy deposited in the solution. We introduce a standardized method for recording solvent responses in laser pump, X-ray probe time-resolved X-ray wide-angle scattering experiments by using dye mediated solvent heating. Furthermore, we have generated a library of solvent terms, which can be used to describe the solvent term in any TRWAXS experiment, and made it available online.

1 Introduction

Laser pump, X-ray probe time-resolved wide-angle X-ray scattering (TRWAXS) experiments are one of the few techniques that allow for the direct study of transient structural changes of species in solution. In the earliest TRWAXS experiments, systems showing structural changes on the nanosecond timescale were investigated using synchrotron radiation.[1,2] The timescale has since been expanded to the picosecond regime,[3–9] and with the availability of the X-ray free electron lasers the femtosecond timescale has recently become accessible.[10–15] TRWAXS on systems in solution is an established technique,[16–34] which has been used to directly show structural changes occurring during photoinitiated uni- and bi-molecular chemical reactions in solution; as well as the temporal evolution of these reactions (references relating to X-ray absorption have been included for completeness).[35–46] The data obtained in a TRWAXS experiment—difference scattering images generated by subtracting an image recorded before the pump has arrived at the sample from an image recorded in a given time after the pump has arrived at the sample—arise from structural changes, which can be divided into three terms:[35,47,48]

(i) structural changes of the solute (*solute term*),

(ii) structural changes of the bulk solvent (*solvent term*),

[a] *Centre for Molecular Movies, Niels Bohr Institute, University of Copenhagen, Universitetsparken 5, DK-2100 København Ø, Denmark*
[b] *Centre for Molecular Movies, Department of Physics, Technical University of Denmark, Fysikvej 307, DK-2800 Kongens Lyngby, Denmark. E-mail: mmee@fysik.dtu.dk*
[c] *European Synchrotron Radiation Facility, 6 rue Jules Horowitz, BP220, Grenoble Cedex 38043, France. E-mail: wulff@esrf.fr*
[d] *Nano-Science Center and Department of Chemistry, University of Copenhagen, Universitetsparken 5, DK-2100 København Ø, Denmark. E-mail: TJS@chem.ku.dk*
[e] *Institut de Physique de Rennes, UMR UR1-CNRS 6251, Université de Rennes 1, F35042, Rennes, France*

† Electronic supplementary information (ESI) available: Absorption spectra of dyes and neat solvents. See DOI: 10.1039/c3cp50751c

(iii) structural changes of the solvent-shell surrounding the solute (*solute–solvent cross-term*).

In order to obtain information on the structural changes of the solute, the other terms have to be determined before the solute term can be reliably extracted from the data. At present, the solute–solvent cross-term can only be determined experimentally when convoluted with the solute term and the solvent term, while computational chemistry can reproduce the solute–solvent cross-term independently.[26,49] The solvent term can also be evaluated theoretically, in particular by Molecular Dynamics (MD) simulations,[27–30,33–35,48,50–53] or it can be determined experimentally.[30–35,48,50,52] In the single study where both experimental and theoretical solvent terms have been used to extract structural information from TRWAXS data, the experimentally determined solvent terms were shown to give a more accurate description of the data.[48]

Taking a step back from the context of TRWAXS, the solvent responses determined here are direct structural fingerprints of the changes in molecular structure of the solvent occurring with changes in temperature, pressure and density. As they are recorded using pseudo-monochromatic X-rays, the data we make available can be used to describe the transient scattering of a solution at any X-ray source (*e.g.* at free electron X-ray lasers, where experiment time is highly limited). Futhermore, they may also be used to benchmark MD-simulations. A good correlation between MD-simulations and TRWAXS data may show which structural changes correspond to the observed fingerprint. Here, we do a direct interpretation relating the fingerprint to inter-molecular distances. While the solvent term has been used extensively in data processing to obtain the solute term,[30–35,48,50,52] a unified investigation of the solvent term for several solvents had not been performed.

The experimental determination of the solvent response relies on point heating of the solvent. We define point heating as an event where individual sites (molecules) in a solution are promoted to a high-energy state, from which they release the energy to the surrounding solvent, resulting in an overall heating of the solution (point heating is explained in detail in the ESI†). Point heating of the solvent can be achieved by three methods: direct near-infrared (NIR) heating of the solvent through exciting vibrational overtones of individual solvent molecules,[30,47,48] UV photolysis of individual solvent molecules resulting in bulk heating,[52,54] and dye mediated heating of the solvent.[31–35] Depositing hard UV radiation in the sample volume is not considered further in this work, as it leads to undesired chemical reactions.[55] We have used NIR and dye mediated solvent heating to obtain the data needed to determine the solvent term in eight different solvents. We demonstrate that the results of dye mediated and NIR heating are identical in methanol at low laser fluencies, and that dye mediated solvent heating can be achieved using a large range of dye concentrations, wavelengths and laser fluencies. We have employed dye mediated solvent heating in a series of TRWAXS experiments in order to generate a library with parameters describing the solvent term for these solvents. The library is freely accessible online,[56] and the dyes used to generate the library can be acquired by contacting the authors.[57]

2 Experimental

2.1 Dye synthesis and characterization

The dyes (see Fig. 2, below) were chosen based on their spectral range and solubility. For water, a yellow dye, Fast Yellow, was chosen. Fast Yellow (**1**, sodium 4-aminoazobenzene-3,4′-disulphonate, CAS 2706-28-7) is commercially available with suitable purity. For the organic solvents a yellow and a red azobenzene were selected, 4-bromo-4′-(*N*,*N*-diethylamino)-azobenzene[58] (**2**, CAS 22700-62-5) and 4-(*N*,*N*-diethylamino)-2-methoxy-4′-nitro-azobenzene[59] (**3**, CAS 6373-95-1) were synthesized using an adapted method based on a large scale synthesis of methyl red from organic synthesis.[60] The purity of the dyes **2** and **3** was determined by NMR, GC-MS and elementary analysis and was found to be higher than 99%.

The absorption coefficients were determined by three independent measurements, by dissolving three different weighed quantities of a sample in an appropriate volume of solvent. The error is estimated to be $<10\%$. The solubility of the dyes was determined by making a saturated solution in each of the selected solvents, which were then left to equilibrate overnight. 50 μl of each solution was diluted to 200 ml and the absorption spectrum measured. The absorption coefficients, determined as described above, were then used to determine the solubility for each dye–solvent combination.

2.2 Experimental set-up – ESRF ID09B

Time-resolved scattering measurements were performed at the dedicated time-resolved laser pump, X-ray probe beamline ID09B at the ESRF (details of the setup are given in Appendix B).

The sample was placed in a temperature controlled water-reservoir kept at 25 °C for the pump–probe measurements. The sample was cycled in a fast-flowing liquid jet setup with a sapphire nozzle producing a 300 μm jet flowing at 2 m s^{-1}, ensuring total replenishment of the sample volume between each pump–probe event. An external temperature controller ensured that the sample temperature was kept within 0.1 °C of the reservoir temperature.

The sizes of the laser and X-ray focus were measured using a pinhole and determined to be 350 μm (h) × 340 μm (v) for the laser spot and 120 μm (h) × 80 μm (v) for the X-rays (horizontal and vertical dimensions respectively). The laser pulse length was 1.2 ps, and unless otherwise noted, the excitation energy was 200 μJ per pulse.

The pump–probe scattering images were accumulated in sequences of 2–5 images with a time delay between the laser pump and X-ray probe given by $\Delta t = t_{probe} - t_{pump}$. The sequences were spaced with a negative time delay (that is the X-rays arriving before the laser pump), which were used as references. Each image was integrated for 5 seconds, corresponding to 5000 individual pump–probe events. At each time delay 50–200 images were acquired.

Additionally, steady-state measurements were conducted for all solvents at different temperatures. The reservoir temperature was changed, and the samples were allowed to reach the equilibrium temperature before the measurement was started. The high speed chopper (see Appendix B for details) was moved slightly out

of the X-ray beam increasing the opening time from 260 ns to 2 μs, letting a pulse-train of 11 X-ray pulses through at a time reducing the exposure times to ~1 second.

2.3 X-ray data reduction

The 2D scattering patterns from the CCD detector were corrected for geometry and polarization (see ESI† for details). This was followed by azimuthal integration yielding 1D curves of the scattering intensity $S(2\theta)$ *versus* the scattering angle. The $S(2\theta)$ curves were scaled to the sum of the coherent and incoherent scattering of a single solvent molecule at high scattering angles. Scattering at high angles is dominated by the incoherent scattering and therefore relatively insensitive to structural changes as described elsewhere.[31,48]

Difference scattering intensities $\Delta S(2\theta)$ were generated from the scattering curves recorded at a positive time delay by subtracting the average of the two nearest scattering curves recorded at a negative time delay. Difference curves from the same pump–probe time-delay (Δt) were summed after an outlier rejection based on a point-by-point implementation of Chauvenet's criterion. The noise level was estimated from a second-order polynomial fit to a running 20 point interval in the data set as described previously.[35] The difference scattering curves presented in this work are plotted against the wave vector transfer $\Delta S(Q)$, $Q = 4\pi/\lambda \times \sin(2\theta)$. In order to generate these plots, the X-ray energy has been approximated by a monochromatic 18 keV spectrum.[61]

3 Theory

3.1 Energy dissipation from excited molecular states

The transient evolution of the energy deposited by the pump-laser in a single pump–probe cycle is described by:

$$S_0 \xrightarrow{h\nu} S_n^* \xrightarrow{\text{IC+IVR}} S_1^* \xrightarrow{\text{VR}} S_1 \xrightarrow{\text{IC}} S_0^* \xrightarrow{\text{VR}} S_0$$

The pump-laser excites the solute from its ground state (S_0), the initial electronically excited (S_n^*) state relaxes *via* a combination of intra-molecular vibrational redistribution[62–64] (IVR) and internal conversion (IC) to a vibrationally excited state of the lowest electronically excited state (S_1^*), which subsequently relaxes through vibrational relaxation (VR) to the vibrational ground state of the lowest electronically excited state (S_1); these processes occur within the first picoseconds after excitation.[65] The electronically excited state decays to a vibrationally excited electronic ground state (S_0^*). The last step in the energy transfer cascade is the VR step back to the vibronic ground state of the solute (S_0).[66] Note that energy is only transferred out of the solute through vibrational relaxation.

The timescales of the processes dictate that energy will be deposited into the solvent in two separate steps. The first step deposits energy corresponding to the difference between S_n^* and S_1 on a ~1–100 ps timescale. The second energy transfer occurs on a timescale directly linked to the lifetime of the lowest electronically excited state of the solute, which can be anything from picoseconds to seconds.

Vibrational relaxation deposits vibrational energy directly as heat into the solvent shell, which then dissipates to the bulk solvent giving rise to the structural changes seen in the TRWAXS data; this is the solvent term defined in the introduction.

3.2 Energy dissipation pathways in azo-benzene

Azobenzene can exist as a *cis* (*Z*-) and *trans* (*E*-) isomer, where the latter is the most stable. The two isomers can interconvert upon irradiation, a process that has been intensely studied.[62,67–73] The *trans* isomer is the more stable of the two. Donor and acceptor substituents increase the energy difference between the two isomers, and decrease the barrier of inter-conversion.[74] Thus, donor–acceptor substituted azobenzenes are isolated as the pure *trans* form. The *cis*/*trans* isomerization is associated with a potential loss of energy that otherwise would have been deposited in the solvent, as the formation energy of the *cis* form is higher than for the *trans* form. A cautious estimate based on numbers for azobenzene gives an energy-loss of <5% for excitation by light with wavelengths lower than 500 nm if only ground state absorption is considered.

Ultrafast dynamics govern the processes occurring in azobenzene upon photo-excitation.[75] The IC from the electronically exited state to the electronic ground state is very fast (~200 fs), and proceeds *via* the *cis*/*trans* isomerization process.[69–73] The time it takes for full VR to occur in azobenzene is solvent dependent and has been measured in hexane (16 ps), acetonitrile (17 ps) and DMSO-d_6 (20 ps).[62,68,76] We can conclude that at experiment times ≥100 ps no molecular signature can be present as the azo-benzene molecule will have returned to the ground state, and consequently must have transferred all absorbed energy to the solvent.

As volume changes following an isomerisation event will increase the local density, this change has to be evaluated. A combination of transient grating and photoacoustic experiments, computational methods and structural considerations have been done for azo-benzene.[77,78] The results yield values of the volume change caused by isomerisaton slightly above and below $\Delta V = 0$ Å^3 per molecule, and the two experimentally determined volume differences are of opposite sign. As the volume change represents less than a change of 5% of the total molecular volume we can ignore volume changes due to isomerisation in this study.

3.3 Thermodynamics of pump–probe experiments

The hydrodynamics of the pump–probe experiment has been discussed in detail by Cammarata *et al.*[48] A brief summary will be presented here.

The speed of a thermal redistribution after a point heating event is given by eqn (1).[79]

$$T(r,t) \propto \frac{1}{8(\pi\chi t)^{\frac{3}{2}}} \exp\left(-r^2/4\chi t\right), \quad (1)$$

$$\chi = \frac{\kappa}{\rho C_P} \quad (2)$$

where r is the distance from the source of the point heating, t is the time since the heating event, χ is the thermometric conductivity and κ is the thermal conductivity (eqn (2)).

Table 1 Physical properties of the solvents required for the calculation of the solvent term at ambient temperature and pressure. The listed properties are from ref. 83 unless otherwise noted

Solvent	C_V[a]/J mol^{-1} K^{-1}	C_P[b]/J mol^{-1} K^{-1}	ρ[c]/g cm^{-3}	κ[d]/W m^{-1} K^{-1}	v[e]/m s^{-1}	α_V[f] × 10^3/K^{-1}
H_2O	74.54[g]	75.33[g]	0.998	0.607[g]	1497[g]	0.214
MeCN	63.53[h]	90.0[h]	0.779	0.188	1278[h]	1.37
MeOH	67.53[g]	81.21[g]	0.789	0.202	1100[g]	1.49
EtOH	90.03[l]	112.3	0.787	0.167	1162	1.40
Cyclohexane	106.0[g]	149.3[g]	0.773	0.130	1292[g]	1.15
CH_2Cl_2	77.7[i]	101.2	1.318	0.140	1051[j]	1.39
$CHCl_3$	76.8[k]	114.2	1.483	0.117	987	1.21
CCl_4	91.0[k]	130.7	1.583	0.103	930	1.14

[a] Specific heat capacity at constant volume. [b] Specific heat capacity at constant pressure. [c] Density. [d] Thermal conductivity. [e] Speed of sound. [f] Cubic expansion coefficient. [g] Ref. 84. [h] Ref. 85. [i] Ref. 86. [j] Ref. 87. [k] Ref. 88. [l] Ref. 89.

The distance from the point of origin to the half maximum of the heat distribution is then given by:

$$d_{50\%} = 2\sqrt{\chi t \ln 2} \tag{3}$$

The relevant material constants for all solvents included in this study are compiled in Table 1. For an excitation fraction of 30% of a 1 mM solution of a dye molecule, the average distance between centres of heat deposition is 22 nm. It follows that the FWHM of the expanding thermal distributions from neighbouring centres of heat deposition will meet after an average of ~200 ps establishing homogeneity of the sample temperature distribution.

It can be shown that the thermal expansion of a volume heated by a Gaussian laser pulse sets in around times $t = L/v$, where L is the radius of the laser spot and v is the speed of sound in the solvent.[80–82] For a laser spot size of 170 μm and speeds of sound of 900 to 1500 m s^{-1}, the thermal expansion sets in 110–180 ns after the excitation. After thermal expansion, the solvent is in hydrodynamic equilibrium with elevated temperature at ambient pressure.

A hydrodynamic system can be completely described by two of its three hydrodynamic variables (pressure, temperature and density). Therefore, the difference scattering contribution associated with a change in any hydrodynamic variable can be described by a linear combination of the difference scattering signal resulting from a change in two of these.[48] Typically, the changes in temperature (ΔT) and density ($\Delta\rho$) are chosen, giving the following expression for the difference scattering (ΔS):

$$\Delta S(Q,t) = \left.\frac{\partial S(Q)}{\partial T}\right|_{\rho} \Delta T(t) + \left.\frac{\partial S(Q)}{\partial \rho}\right|_{T} \Delta\rho(t) \tag{4}$$

where $\partial S(Q)/\partial T|_\rho$ is the difference scattering signal resulting from a change in temperature at constant density and $\partial S(Q)/\partial\rho|_T$ is the difference scattering signal resulting from a change in density at constant temperature.

The difference scattering curve described by eqn (4) is the time-dependent solvent term, and describes any changes in the difference scattering signal caused by changes in the hydrodynamic variables of the sample. If the two differentials in eqn (4) have been experimentally determined, the absolute changes in temperature and density associated with a TRWAXS experiment, *i.e.* the solvent term, can be fully described. On short time scales with no thermal expansion, $t \ll L/v$ (*e.g.* ΔS (100 ps)), eqn (4) reduces to

$$\left.\frac{\partial S}{\partial T}\right|_{\rho} \Delta T(100\text{ ps}) = \Delta S(100\text{ ps}) \tag{5}$$

On much longer time scales, hundreds of nanoseconds, the thermal expansion of the irradiated volume is complete.[48] The sample will have returned to ambient pressure, and the temperature has dropped by C_V/C_P due to expansion (where C_V and C_P is the heat capacity at constant volume and pressure respectively). The difference scattering signal caused by density changes at constant temperature can be determined from a late time point ($t \gg L/v$, *e.g.* $\Delta S(1\ \mu s)$) by subtracting the difference scattering due to the still-elevated temperature following the thermal expansion, from the full difference scattering signal:

$$\left.\frac{\partial S}{\partial \rho}\right|_{T} \Delta\rho(1\ \mu s) = \Delta S(1\ \mu s) - \frac{C_V}{C_P}\Delta S(100\text{ ps}) \tag{6}$$

At $t \gg L/v$ the system will reach the same hydrodynamic change as associated with an increase in ambient (reservoir) temperature. Hence, a series of difference scattering signals calculated from static measurements at different temperatures can be compared directly to $\Delta S(1\ \mu s)$, and used to determine the temperature change after 1 μs, $\Delta T(1\ \mu s)$. The temperature increase after 100 ps, $\Delta T(100\text{ ps})$, and the density decrease at 1 μs, $\Delta\rho(1\ \mu s)$, can be determined directly from $\Delta T(1\ \mu s)$:

$$\Delta T(100\text{ ps}) = \frac{C_P}{C_V}\Delta T(1\ \mu s) \tag{7}$$

$$\Delta\rho(1\ \mu s) = \alpha_V \rho \Delta T(1\ \mu s) \tag{8}$$

where α_V is the volumetric isobaric expansion coefficient. Thus, in order to determine the absolute scale of the two contributions to the difference scattering as described by eqn (5) and (6) the following thermodynamic parameters need to be known: C_P, C_C and α_V. This allows for quantitative determination of the temperature and the density change from a difference scattering signal through eqn (4).

3.4 ΔT from optical density and temperature based measurements

The changes in temperature and density giving rise to the difference scattering curves of the late time-points ($t \gg L/v$) can be found by scaling the difference scattering curves measured, to the difference between steady-state measurements recorded at different temperatures as described in the previous section. However, the high degree of control of light absorption in the experiment using the dye molecules allows for direct estimates of the deposited energy from the experimental parameters. The expected temperature increase can be directly calculated from the amount of energy absorbed

by the dye molecules in the irradiated volume as described in the ESI.†

For acetonitrile the calculation predicts a temperature rise of ΔT = 0.6 °C. The largest error in calculating ΔT will result from the determination of the optical density of the sample; for the experiments presented here the error is below 10%.

4 Results and discussion

4.1 Dye and solvent properties

To deposit heat in a solvent with NIR radiation, the absorbing vibrational overtones have to be known. The absorption spectrum of acetonitrile is shown in Fig. 1 and relevant spectroscopic data on all the solvents investigated in the present study are summarized in Table 2 (absorption spectra of the other solvents are given in ESI†). From these experiments we estimate that an optical density exceeding 0.4 cm^{-1} is needed to obtain a solvent response using NIR heating.[90]

The wavelength ranges where this optical density can be achieved are included in Table 2; note that some solvents require NIR excitation at >1500 nm and solvents not containing hydrogen cannot be readily heated by NIR excitation.

If NIR excitation of solvent vibrational modes is used to deposit heat in the solvent, it is essential that the VR of the excited vibration occur much faster than the timescales of interest in experiments where solute dynamics are being studied. Characteristic lifetimes of the most long-lived vibrational modes are included in Table 2. Each vibrational mode in a given solvent has a different lifetime and as a consequence the solvent dynamics will depend on the wavelength of excitation.[63,91–94] The full VR process has been measured in a very limited number of solvents and only at selected excitation wavelengths.[64,95] In Table 2 the longest reported time required for full VR is given. In the present context, it is sufficient to note that in order to determine the solvent term, the ΔS(100 ps) curve can be measured using NIR excitation for all solvents in Table 2. This is most likely also true for experiments involving a solute, for instance: iodomethane deposits vibrational energy into CCl_4, $CDCl_3$ and acetone-d_6 in 50 ps, 44 ps and 16 ps respectively.[96] To develop a standardized method for determining the solvent term by using dye mediated solvent heating, a dye meeting the following requirements is needed; the dye has to:

(i) be stable under the relevant experiment condition,
(ii) absorb light across most of the visible spectrum,
(iii) be soluble in the most common solvents,
(iv) efficiently deposit energy into the solvent upon photo-excitation on a sub 100 ps timescale,
(v) have a negligible solute term and solute–solvent cross-term,
(vi) be readily available.

These requirements are all met by the tailor-made azo-dyes shown in Fig. 2. To meet the requirement of solubility three different dyes have to be used: the water soluble Fast Yellow (**1**), 4-bromo-4′-(*N*,*N*-diethylamino)-azobenzene (**2**) and 4-(*N*,*N*-diethylamino)-2-methoxy-4′-nitro-azobenzene (**3**). The absorption spectra of all three dyes in methanol are shown in Fig. 3.

As the dyes show a significant degree of solvatochromism, the absorption spectra of the dyes in all the investigated solvents are included in the ESI.† The solubility and molar absorptivity of **1** in water, methanol and ethanol are compiled in Table 3. **1** is completely insoluble in acetonitrile and all the less polar organic solvents. In water, concentrations of **1** sufficient to record a solvent response can be reached over the spectral range from 250 nm to 525 nm. In methanol and ethanol the achievable optical densities are only sufficient to deposit enough heat into the solution around λ_{max} in the 370–420 nm range to obtain a usable difference scattering curve in a reasonable experimental timeframe.

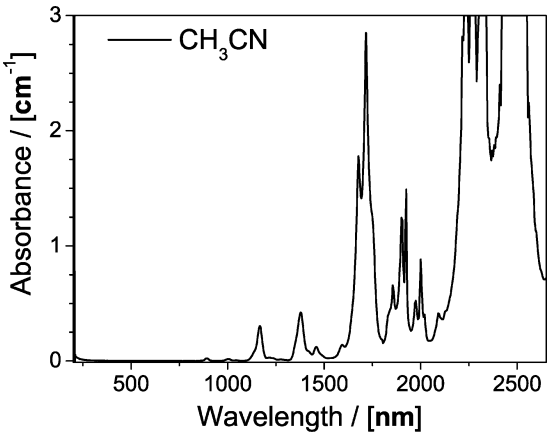

Fig. 1 The absorption spectrum of acetonitrile.

Table 2 The three lowest wavelength NIR absorption of solvents, with an absorbance higher than 0.4; the characteristic lifetime of the intramolecular vibrational redistribution (IVR) is given where it can be found in the literature

Solvent	λ/nm	A_{max}/cm^{-1}	λ/nm	A_{max}/cm^{-1}	λ/nm	A_{max}/cm^{-1}	VR[a]/ps
Cyclohexane	1180–1230	1.1	1386–1424	0.43	1688–1865	>4.0	—
Decalin	1180–1230	1.1	1386–1424	0.43	1688–1875	>4.0	—
CH_2Cl_2	1634–1732	3.4	2180–2295	2.4	2295–2455	2.4	—
$CHCl_3$[a]	1670–1710	2.1	1840–1875	0.9	2295–2420	2.3	23[92,94]
CCl_4	—	—	—	—	—	—	—
MeCN[a]	1374–1384	0.42	1642–1772	1.78, 2.88	1830–2020	1.49	~80[63]
EtOH	1174–1210	0.53	1356–1658	2.7	1658–1865	3.5	—
MeOH[a]	1176–1210	0.52	1348–1658	>4.0	1658–1890	3.9	10[93,97]
H_2O[a]	1150–1264	0.54	1264–1682	>4.0	1682–	>4.0	~1[98,99]

[a] In all cases only the major short component lifetime of the complex vibrational relaxation behaviour is given.

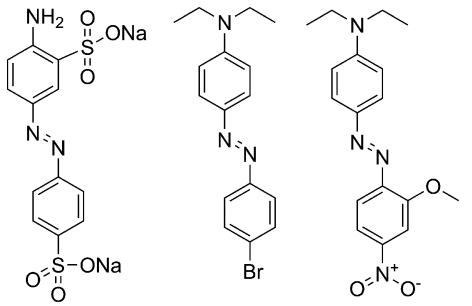

Fig. 2 Molecular structure of sodium 4-aminoazobenzene-3,4′-disulphonate (**1**), 4-bromo-4′-(*N*,*N*-diethylamino)-azobenzene (**2**) and 4-(*N*,*N*-diethylamino)-2-methoxy-4′-nitro-azobenzene (**3**).

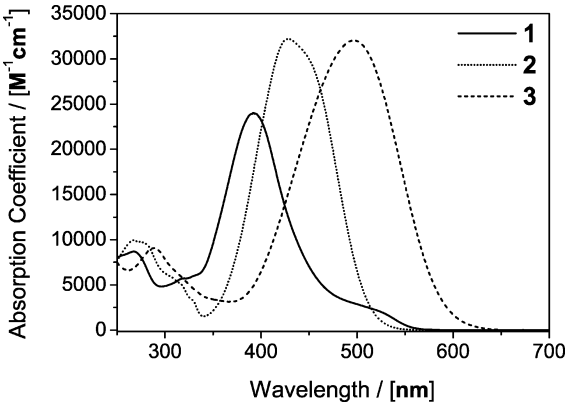

Fig. 3 Absorption spectra of sodium 4-aminoazobenzene-3,4′-disulphonate (**1**), 4-bromo-4′-(*N*,*N*-diethylamino)-azobenzene (**2**) and 4-(*N*,*N*-diethylamino)-2-methoxy-4′-nitro-azobenzene (**3**) in methanol.

Dyes **2** and **3** are sufficiently soluble in all commonly used organic solvents and they cover the optical spectrum in the wavelength range from 250 nm to 575 nm. Two dyes need to be used, as compound **2** shows only limited solubility in cyclohexane and **3** is poorly soluble in methanol and ethanol. Solubility, absorption maxima, and the molar absorptivity at selected wavelengths are compiled in Table 3 for dyes **1**, **2** and **3**.

4.2 Time-resolved X-ray scattering

A time resolved X-ray scattering experiment is initiated when a laser pulse hits the sample, exciting a fraction of the azo-dyes. The deactivation of the dyes releases the absorbed energy to the surrounding solvent. This results in a temperature and pressure increase at unchanged density. The process described above takes less than 100 ps. The solvent can now be treated as a solution that has been heated by several point sources. The solution will have gone through thermal expansion at ~150 ns, in a process where the volume increases and the pressure returns to ambient. That is, the temperature and the density decrease.

By choosing a time point prior to thermal expansion (t = 100 ps ≪ 150 ns) and a time point after thermal expansion (t = 1 μs ≫ 150 ns), we can obtain one difference scattering curve containing only a contribution from the temperature solvent differential and one difference scattering curve dominated by the density solvent differential. The full theoretical treatment is given in Section 3, note that the critical time constant (150 ns) arises from L/v, where L is the size of the laser spot and v is the speed of sound in the liquid. The temperature increase and the density decrease for each solvent are shown in Table 4.

Table 3 The molar absorptivity and solubility properties of **1**, **2** and **3** in the investigated solvents, and the molar absorptivity at common laser lines

Compound solvent	λ_{max}/nm	ε_{max}/M^{-1} cm^{-1}	ε_{532}/M^{-1} cm^{-1}	ε_{396}/M^{-1} cm^{-1}	ε_{265}/M^{-1} cm^{-1}	Solubility M	Solubility g l^{-1}
1							
H_2O	386	19 200	100	18 000	7500	0.12	55
MeOH	391	24 000	600	23 800	8600	0.0038	1.7
EtOH	395	19 200	700	19 000	6700	0.026	12
2							
Cyclohexane	419	24 700	500	19 500	11 700	0.057	19
Decalin[a]	422	19 300[b]	700	14 600	12 700	0.6	199
CH_2Cl_2	433	33 400	3300	16 200	10 300	0.97	323
$CHCl_3$	429	23 700	900	21 500	10 700	0.66	222
CCl_4[a]	422.5	28 800	500	20 200	11 700	0.25	83
MeCN[a]	442	15 900	1300	11 300	12 100	0.3	100
EtOH	426	32 100	500	20 300	9700	0.18	60
MeOH[a]	429.5	32 000	500	19 900	9900	0.151	49.8
3							
Cyclohexane	464	27 200	9000	4800	7800	0.0180	5.9
Decalin	469	26 500	6700	7700	8000	0.38	120
CH_2Cl_2	506	34 800	24 900	5500	10 400	0.17	56
$CHCl_3$	504	29 500	29 500	5600	8300	0.25	82
CCl_4	473.5	27 200	10 700	6500	8200	0.035	11
MeCN	498	31 900	24 800	5600	7100	0.245	80.5
EtOH	494	31 300	22 700	5500	9300	0.024	7.9
MeOH	495.5	32 000	24 000	5600	6700	0.0271	8.9

[a] The compound forms aggregates at high concentrations, with higher absorption coefficients per molecule than the isolated molecule. [b] Single molecule absorption coefficient at high dilution.

4.2.1 Solvent terms from dye mediated point heating. The difference scattering curves obtained after excitation with a 400 nm pulse of dyes **2** and **3** in acetonitrile are shown in Fig. 4. The dye mediated solvent heating is almost indistinguishable between the two experiments.

Dye **2** was used to determine the solvent term for acetonitrile, cyclohexane, methanol, ethanol, dichloromethane,

Table 4 The density and temperature changes obtained for the data constituting the solvent differentials of Fig. 5[a]

Solvent	ΔT(100 ps)/K	ΔT(1 μs)/K	$\Delta\rho$(1 μs)/kg m^{-3}
MeCN	1.01	0.71	−0.77
Cyclohexane	0.99	0.70	−0.63
MeOH	0.67	0.56	−0.66
EtOH	0.71	0.57	−0.63
CH_2Cl_2	1.11	0.71	−1.28
$CHCl_3$	0.86	0.66	−1.22
CCl_4	1.10	0.76	−1.40

[a] Parameters were determined as decribed in Section 3.

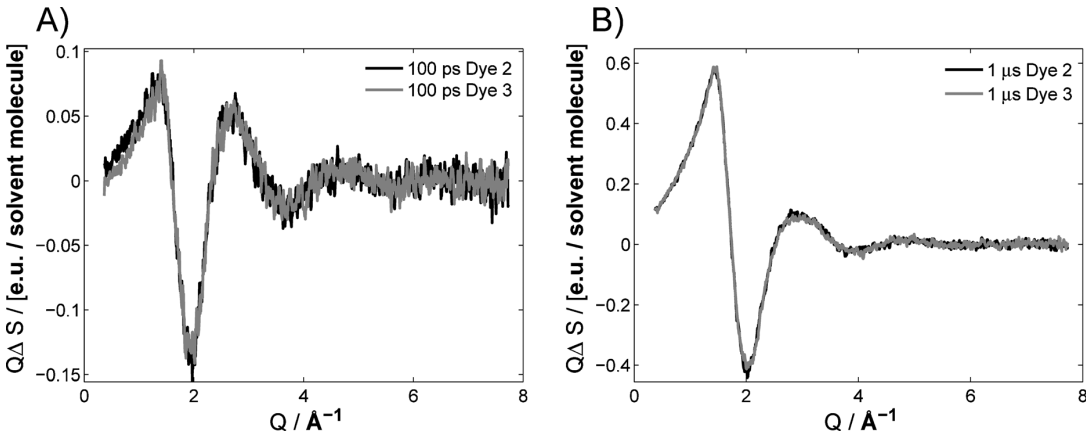

Fig. 4 Difference scattering curves at 100 ps (A) and 1 μs (B) for 1.5 mM 4-bromo-4′-(*N*,*N*-diethylamino)-azobenzene (**2**, black) in acetonitrile and 2 mM 4-(*N*,*N*-diethylamino)-2-methoxy-4′-nitro-azobenzene (**3**, gray) in acetonitrile excited at 400 nm, 200 μJ per pulse.

chloroform and carbontetrachloride. The solvent differentials extracted from the difference scattering are shown in Fig. 5 (see ESI† for a detailed description of the transformation of raw data to solvent differentials). The parameters needed to derive the solvent differentials from the difference scattering curves of the seven solvents can be found in Table 1.

4.2.2 Preliminary interpretation of solvent terms. The solvent term (eqn (4)) of each solvent comprises the two solvent differentials shown in Fig. 5. This term can describe the difference scattering induced by the structural changes in the solvent at any point in time following a point heating event. That is, no information regarding the molecules in solution or the mechanism of interaction between the solutes and the solvent is found in the solvent term. This information lies in the solute term and the solute–solvent cross term. The experiments described here are designed in a way that the signature from solute and solute–solvent interactions will have disappeared prior to data collection *i.e.* within the first 100 ps, see above.

The solvent differentials are normalised to one SI unit of change and scattering intensity corresponding to one solvent molecule. Thus, Fig. 5 shows the changes in scattering of a solvent, normalised to a single solvent molecule, when it is heated by one degree (1 K) at constant density, or when the density is decreased by one mg ml^{-1} (1 kg m^{-3}) at constant temperature.

A steady-state scattering curve shows the fingerprint of the structure of a solvent, the steady-state scattering is included as ESI.† For all solvents, a dominant peak is observed in the interval Q = 1.4–2 Å^{-1}. This peak, the solvent peak, arises from the most common nearest-neighbour distance ($r_{n\text{-}n}$) of the most strongly scattering atoms of the solvent (C, N, and O, where Cl is not present; otherwise Cl). $Q = 2\pi/r_{n\text{-}n}$ describes the solvent peak, where $r_{n\text{-}n}$ can take a range of solvent specific values.[100] A full interpretation of the steady-state scattering will be possible through extensive computational chemistry, which is outside the scope of the work presented here. However, qualitative conclusion can be made by cursory inspection of the solvent differentials.

The structural changes following a decrease in density at constant temperature can be interpreted as an increase in volume per molecule. This will induce an increase of the average nearest-neighbour distance, moving the solvent peak to lower Q. This is observed in all solvent density differentials as an increase in the scattering intensity at Q below the solvent peak position, and a decrease at Q above the solvent peak position.

The structural changes following an increase in temperature are less readily recognised. However, the difference scattering curves and solvent differential for acetonitrile (panel A, Fig. 5) show a decrease of scattering intensity at the maximum of the solvent peak, and an increase in scattering on the edges of the solvent peak. This corresponds to a lowering and widening of the solvent peak, which is identical to a broader range of nearest-neighbour distances of the most strongly scattering atoms of the solvent *i.e.* a widening of the Boltzmann-distribution describing $r_{n\text{-}n}$.

Cyclohexane and the chlorinated solvents show a different behaviour where the solvent peak moves to lower Q with increases in temperature. The protic solvents have another type of behaviour, where the solvent peak moves to higher Q. The former can be explained by a higher level of molecular vibration resulting in a longer average distance between nearest neighbours. The latter can be assigned to breaking of hydrogen bonds, which will decrease the average distance between the strongly scattering oxygen atoms. An effect that is diminished as the length of the alkane chain grows, resulting in the smaller difference scattering intensity change observed for ethanol when compared to methanol.

The solvent differentials shown in Fig. 5 can be used directly to describe the structural behaviour of the investigated solvent. Any change in the hydrodynamic parameters, starting from ambient experimental conditions, can be rationalised using these solvent differentials.

4.2.3 Factors influencing the determination of solvent terms. Having demonstrated that the selected dyes can be used to determine the solvent term of different commonly used solvents in TRWAXS experiments, we investigated the dependence

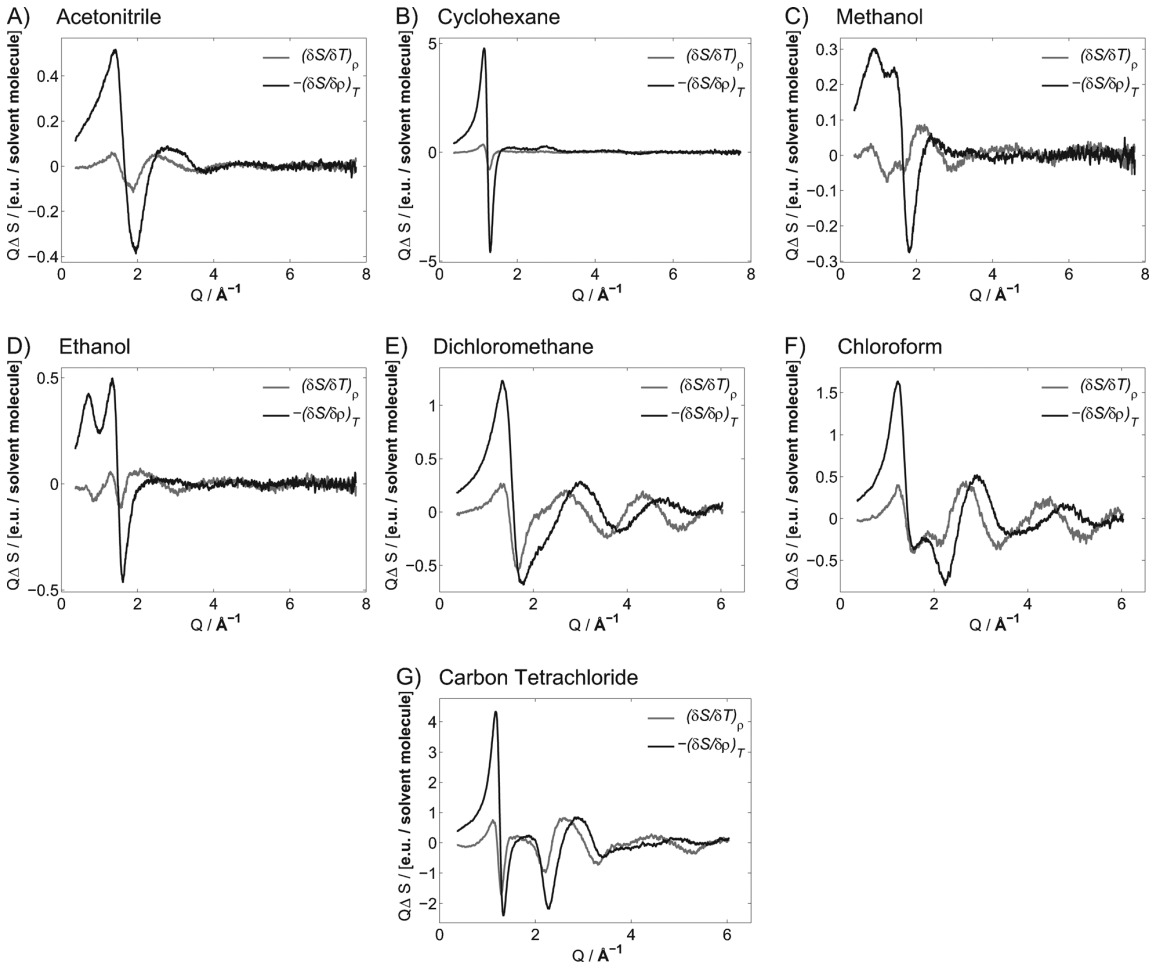

Fig. 5 Scattering response identical to the principal solvent differentials (density and temperature) for point heated acetonitrile (A), cyclohexane (B), methanol (C), ethanol (D), dichloromethane (E), chloroform (F) and carbon tetrachloride (G) from data obtained by exciting a solution of 4-bromo-4′-(*N*,*N*-diethylamino)-azobenzene (**2**) with an optical density of 0.15 at 400 nm with 200 μJ (0.15 J cm^{-2}) pulses (for an estimate of the error see ESI†).

of the difference scattering signal on dye concentration, laser power and excitation wavelength.

The data in Fig. 6 show that the difference scattering signal scales linearly with both dye concentration and laser power up to a limiting value of both parameters. The total difference scattering intensity was observed to increase linearly with the absorptivity *i.e.* with the expected energy deposited in the solute, to an absorbance/optical density of 0.8, for **2** this occurs at concentration of c = 5 mM at 400 nm. The laser power, and the resulting amount of energy deposited in the solution, was found to be linear up to around 0.2 J cm^{-2} (150 GW cm^{-2}), after which the difference scattering signal does not increase further. A possible explanation for the latter could be onset of intensity dependent multiphoton processes in the surface of the liquid sheet. This would explain why the onset of the nonlinearities is independent of dye concentration. It is worth noting that the changes in the signal monitored in these experiments are in the 10^{-3}-range of the total signal intensity measured. To see these signals relatively high laser powers are required. The probed volume is quite large and the detected signal is apparently not influenced by effects in the first few layers of molecules at the surface of the film (which in any case is different in structure than the bulk of the film). Only when the higher order effect disrupts the bulk of the solvent film, or sufficient amounts of energy are lost at the film surface, will the higher order effects be registered in the scattering signal.

Changing the excitation wavelength results in difference scattering curves of different amplitude, however, when scaled by the amount of energy deposited in the sample the signals become indistinguishable (Fig. 7). The amount of energy deposited in the sample can be calculated from both steady-state variable temperature data, and directly by using the optical density of the dye solution together with the laser fluency as described in Section 3.4. The energy deposition calculated using an optical density of 0.15 is compared to the results of scaling the data to steady-state measurements in Fig. 8. The amount of deposited

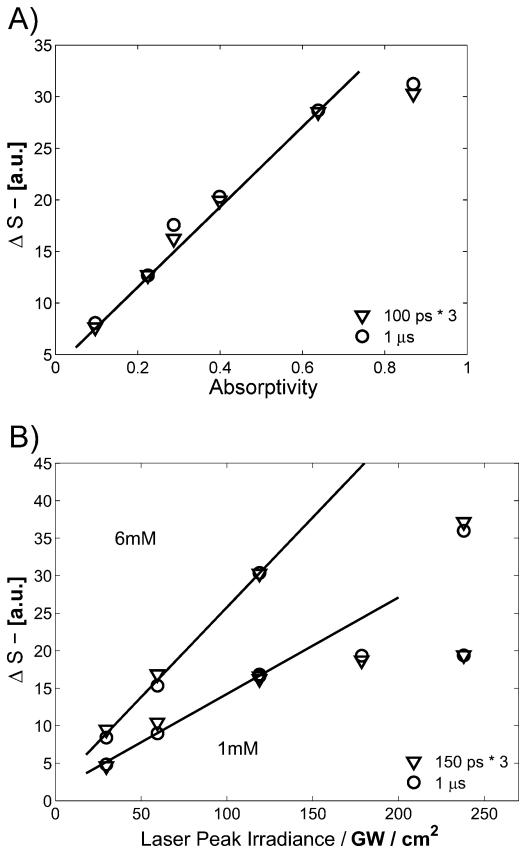

Fig. 6 Integrated signal strength of the total difference-scattering curve as a function of the concentration of 4-bromo-4′-(*N*,*N*-diethylamino)-azobenzene (**2**) (A) and laser power (B) excited at 400 nm; in A, laser power was 200 μJ (0.15 J cm^{-2}) per pulse, in B two concentrations are shown. Points at low concentration/laser power are fitted to a line.

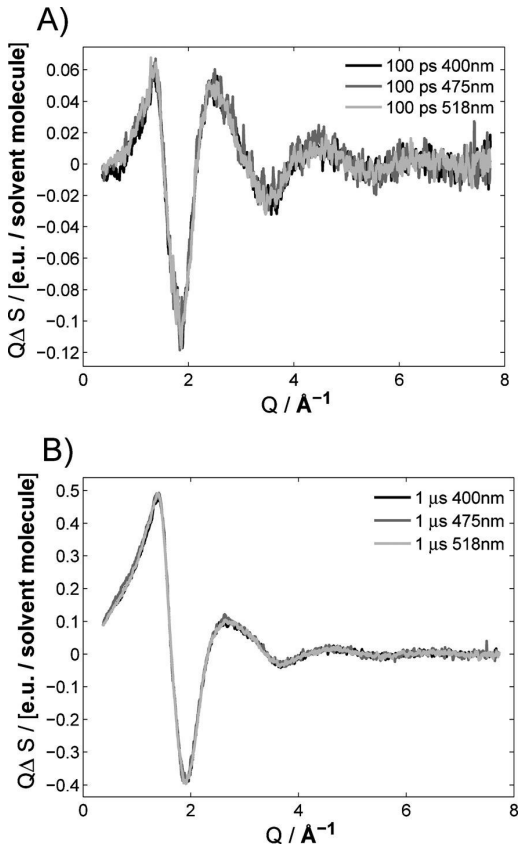

Fig. 7 100 ps (A) and 1 μs (B) difference scattering curves scaled to the 400 nm signal obtained for dye mediated solvent heating using 1 mM 4-bromo-4′-(*N*,*N*-diethylamino)-azobenzene (**2**) in acetonitrile and exciting at 400 nm, 475 nm and 518 nm. The recorded difference scattering curves are identical within the noise. All data have been recorded with 200 μJ (0.15 J cm^{-2}) per pulse.

energy estimated from the two methods is within 5% of each other for all solvents studied.[101] This shows that, when staying within the linear regime of the laser power, the absolute temperature change can be calculated directly from the spectroscopic parameters of the setup. Thus, the steady-state measurements at different temperatures become redundant. By using one of the azo-dyes, the solvent term described by eqn (4) can be determined on an absolute scale in a single TRWAXS experiment using only two time delays, 100 ps and 1 μs.

4.2.4 Heating method. To confirm that the solvent response is independent of the heating method, the difference scattering responses resulting from dye mediated solvent heating and NIR heating of acetonitrile and methanol were compared. The normalized difference scattering curves are shown in Fig. 9. It has previously been shown that NIR excitation of methanol, at intermediate laser powers, gives a better description of solute mediated heat deposition than MD simulations.[48] Panel A in Fig. 9 shows that for methanol, NIR and dye-mediated solvent heating results in identical difference scattering curves. This demonstrates that the solvent response can be recorded with

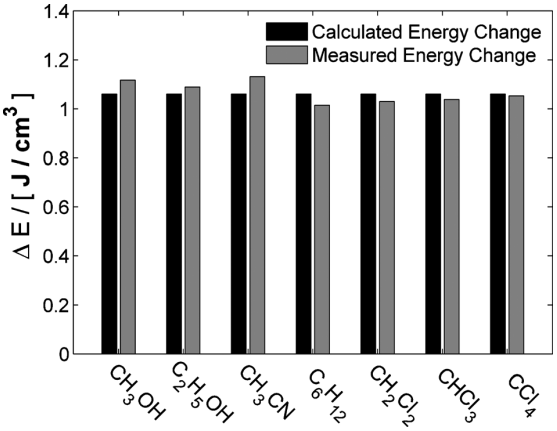

Fig. 8 Energy deposited in the solvent per unit volume in a laser pump, X-ray probe TRWAXS dye mediated solvent heating experiment calculated from the molar absorptivity and concentration of the dye (black) and determined from comparison with steady-state variable temperature experiments (grey).

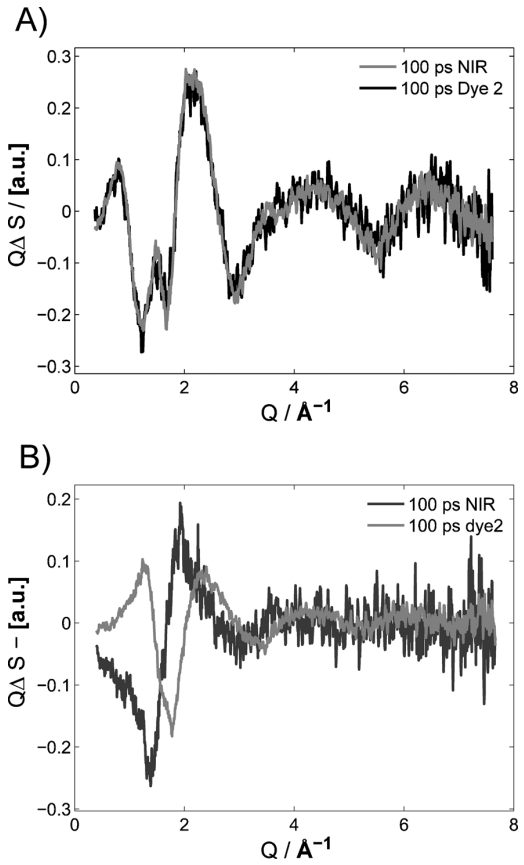

Fig. 9 Normalized difference scattering curves of methanol (A) and acetonitrile (B) recorded with Δt = 100 ps following direct vibrational NIR excitation at 1718 nm (black) and dye-mediated heating with 4-bromo-4′-(*N*,*N*-diethylamino)-azobenzene (**2**, black). Laser power was 400 μJ (0.30 J cm^{-2}) per pulse at 1718 nm, and 200 μJ (0.15 J cm^{-2}) per pulse at 400 nm.

both mechanisms of energy deposition, and that the structural dynamics of the dye molecules does not contribute to the difference signal. For NIR mediated energy deposition in methanol, a fluency threshold of ~1 J cm^{-2} (~800 GW cm^{-2}) has been identified, above which a signature corresponding to a density increase contributes to the difference scattering signal from $t < 50$ ps to $t = 2$ ns.[102] This short-lived density increase has been assigned to micro-cavitation (formation of micro-bubbles) in the liquid caused by extreme local heat deposition by higher-order absorption processes.

Panel B in Fig. 9 shows that a similar behaviour is observed for acetonitrile, with a significantly lower fluency threshold. As for methanol, the NIR mediated solvent heating results in difference scattering curves with a significant contribution of positive density change at the times up to $t = 1$ ns. The process of identifying the contribution as a result of a density increase is described in the ESI.† A cursory inspection shows that the NIR generated trace in panel B of Fig. 9 appears like a negative version of density differential in panel A of Fig. 5. Unlike methanol, the contribution from the density increase could be seen after NIR excitation of acetonitrile for all fluencies, where difference scattering signals could be detected. The minimum fluency where a difference scattering signal could be identified with NIR excitation of vibrational overtones of acetonitrile was 0.15 J cm^{-2} (120 GW cm^{-2}). We tentatively assign the lower fluency threshold for acetonitrile to an increased excited state absorption. This shows that NIR mediated energy deposition cannot be used to obtain the temperature component of the solvent differential for acetonitrile.

As the dependency on fluency and the fluency threshold is different from solvent to solvent, a scan of laser power has to be performed, when using NIR mediated solvent heating. This has to be done in order to verify that the solvent response is recorded at a laser power below the onset of any high-fluency effects. With the set-up used in these experiements, the transient signal recorded using NIR excitation of acetonitrile was monitored as the laser power was decreased to the point where no difference signal could be identified, even the least intense signal was dominated by high-fluency effects.

5 Conclusions

A set of three azo-dyes (**1**, **2** and **3**) has been investigated in order to introduce a standardised method for experimental determination of the solvent response in laser-pump, X-ray probe time-resolved wide-angle X-ray scattering experiments on molecular systems in solution. The photophysics of the parent azobenzene compound were reviewed and we can conclude that on current synchrotron time scales (t > 50 ps) all energy from excitation of the dyes **1–3** will have been deposited into the solvent as heat, and no other effects will be contributed to the difference scattering signal. The energy deposited in the solvent by dye-mediated solvent heating was shown to depend linearly on laser power and dye concentration. The magnitude of the difference scattering signal can be forced into a non-linear regime, but the shape of the measured difference scattering curve corresponding to a specific Δt remains unchanged. We must conclude that a difference scattering curve corresponding to point heating of the solvent can be obtained under a very wide range of experimental conditions; that is, dyes **1–3** are ideal dye candidates to be used in a standardized method for experimental determination of the solvent term using dye mediated solvent heating. Complications inherent to NIR heating of the solvent, as observed in both methanol and acetonitrile, suggest that although NIR heating can be used to determine the solvent term, a standardized method has to use dye-mediated solvent heating. Furthermore, dye-mediated solvent heating allows for direct calculation of the amount of energy deposited in the solvent, thus removing the need for steady-state measurements. We have used the method proposed here to generate a library of the hydrodynamic constants and solvent differentials that constitute the solvent term in laser-pump, X-ray probe time-resolved wide-angle X-ray scattering experiments on systems in solution.[56]

We conclude that the currently superior method for determining the solvent terms in a TRWAXS experiment is to use one of the dyes introduced here. The dyes are soluble in all solvents,

they cover most of the visible spectrum, they give reproducible results on multiple beamlines,[103] they exhibit linear behaviour in a large concentration and laser power range, and they are readily available in pure form.[57] If a solution of one of these azo standards with a concentration corresponding to an optical density of 0.3 and a laser power lower than 200 μJ per pulse is used, then a pure solvent signal will be obtained in all laser pump X-ray probe TRWAXS experiments. A detailed description of how to obtain the solvent differentials is given in Appendix A and expanded in the ESI.†

Appendix

Appendix A: how to measure a solvent response

A solution of one of the three selected dyes should be prepared such that the optical density of the solution at the wavelength of the pump laser is 0.15–0.5. The laser peak fluency should be in the high end of the linear regime at around 0.2 J cm^{-2}. For a typical 300 μm liquid sheet, the energy-deposition should thus amount to around 5 J cm^{-3}, and around 15 J cm^{-3} for a 100 μm liquid sheet. These are 'typical' experimental values and should give standard signal to noise ratios. Typically, only two time-delays are needed. One delay before the onset of the thermal expansion and one after the thermal expansion has run to completion ($t \ll L/v$ and $t \gg L/v$, as described in the main text). Usually, a delay in the 100–500 ps range and a delay in the 1–3 μs range are used.

The early time point will contain the signal from the temperature change caused by the energy deposition at constant volume ($\Delta T = \Delta E/C_V$). While the late time-point will contain the signal from the temperature and density change experienced by the probe pulse after the thermal expansion has run its course ($\Delta T = \Delta E/C_P$, $\Delta\rho = \alpha_V \Delta E/C_P$). Thus, a linear combination of these two difference scattering curves can be used to describe any change in hydrodynamic parameters of the bulk solvent, and will be able to describe the solvent at any time-point during an experiment. The absolute value of heat and density change can be obtained, either through a steady-state experiment or by evaluating the deposited energy experienced by the X-ray probe pulse (both methods are described in the main text).

If NIR excitation is preferred, a wavelength should be chosen where the optical density of the sample is greater than 0.1 and the laser fluency should be adjusted to the optical density such that the initial temperature increase is no larger than 1.5 K. This will in most cases ensure that the data are recorded at a laser power lower than the breakdown of the linear response, although this might not be possible for all solvents (*e.g.* acetonitrile as shown in the main text). For an expanded description and a summarized experimental log see the ESI.†

Appendix B: description of the ID09B setup

Optical pump pulses were generated by frequency conversion of the fundamental radiation from the Legend Elite Ti:sapphire amplified system (Coherent Inc.) configured to produce picosecond near-IR pulses (802 nm, ~1.2 ps FWHM), with the amplifier synchronized to the 360th subharmonic of the synchrotron RF clock (986.3 Hz). Frequency conversion was performed either by optical parametric amplification (TOPAS-800, LightConversion) or second harmonic generation. After frequency conversion the laser pulses were guided to the sample, arriving at a 10° inclination angle with respect to the incoming X-ray beam.

Single X-ray pulses (~100 ps FWHM) generated from the U17 undulator were selected using a mechanical chopper, which – like the laser amplifier – was synchronized to the 360th subharmonic of the synchrotron orbit clock (986.3 Hz). For the measurements of the signal strength as a function of dye concentration and laser power, the raw pink-beam energy spectrum of the U17 undulator was used. For the rest of the measurements the X-ray energy-range was selected using a Ru-multilayer. For these measurements the energy spectrum of the X-ray pulses arriving at the sample is nearly perfectly Gaussian centered at 18.0 keV with a bandwidth of 2.5%. The sizes of the laser and X-ray focus were measured using a pinhole and determined to be 350 μm (h) × 340 μm (v) for the laser spot and 120 μm (h) × 80 μm (v) for the X-rays (horizontal and vertical dimensions respectively).

Before starting the experiment, a coarse timing (~70 ps) of the laser/X-ray delay was determined by a GaAs diode placed just behind the sample system. During the experiment, the actual pump–probe delay on the sample was monitored non-invasively (~10 ps precision) using a GaAs photo-diode capturing the laser scattering from one of the guiding mirrors and a fast diamond X-ray detector set in the direct beam transmitting about 90% of the radiation. The timing jitter was determined to be <2 ps (rms). The scattered X-rays were detected by a FreLON CCD detector with 2048 × 2048 pixels placed 45 mm from the liquid sheet sample produced by a high pressure nozzle.

Acknowledgements

The authors thank the Danish National Research Foundation's Centre for Molecular Movies, ESRF and DANSCATT for financial support, and Carlsbergfondet and the Villum Foundation for support for KH.

Notes and references

1 V. Srajer, T. Y. Teng, T. Ursby, C. Pradervand, Z. Ren, S. Adachi, W. Schildkamp, D. Bourgeois, M. Wulff and K. Moffat, *Science*, 1996, **274**, 1726–1729.
2 B. Perman, V. Srajer, Z. Ren, T. Y. Teng, C. Pradervand, T. Ursby, D. Bourgeois, F. Schotte, M. Wulff, R. Kort, K. Hellingwerf and K. Moffat, *Science*, 1998, **279**, 1946–1950.
3 C. Rischel, A. Rousse, I. Uschmann, P. A. Albouy, J. P. Geindre, P. Audebert, J. C. Gauthier, E. Forster, J. L. Martin and A. Antonetti, *Nature*, 1997, **390**, 490–492.
4 D. A. Reis, M. F. DeCamp, P. H. Bucksbaum, R. Clarke, E. Dufresne, M. Hertlein, R. Merlin, R. Falcone, H. Kapteyn, M. M. Murnane, J. Larsson, T. Missalla and J. S. Wark, *Phys. Rev. Lett.*, 2001, **86**, 3072–3075.
5 A. Rousse, C. Rischel, S. Fourmaux, I. Uschmann, S. Sebban, G. Grillon, P. Balcou, E. Foster, J. P. Geindre, P. Audebert, J. C. Gauthier and D. Hulin, *Nature*, 2001, **410**, 65–68.

6 S. Techert, F. Schotte and M. Wulff, *Phys. Rev. Lett.*, 2001, **86**, 2030–2033.
7 F. Schotte, M. H. Lim, T. A. Jackson, A. V. Smirnov, J. Soman, J. S. Olson, G. N. Phillips, M. Wulff and P. A. Anfinrud, *Science*, 2003, **300**, 1944–1947.
8 M. Lorenc, J. Hebert, N. Moisan, E. Trzop, M. Servol, M. Buron-Le Cointe, H. Cailleau, M. L. Boillot, E. Pontecorvo, M. Wulff, S. Koshihara and E. Collet, *Phys. Rev. Lett.*, 2009, **103**, 028301.
9 S. O. Mariager, D. Khakhulin, H. T. Lemke, K. S. Kjaer, L. Guerin, L. Nuccio, C. B. Sorensen, M. M. Nielsen and R. Feidenhans'l, *Nano Lett.*, 2010, **10**, 2461–2465.
10 G. Dixit, O. Vendrell and R. Santra, *Proc. Natl. Acad. Sci. U. S. A.*, 2012, **109**, 11636–11640.
11 T. J. Penfold, I. Tavernelli, R. Abela, M. Chergui and U. Rothlisberger, *New J. Phys.*, 2012, **14**, 113002.
12 G. Dixit and R. Santra, *J. Chem. Phys.*, 2013, **138**, 134311–134319.
13 A. Aquila, M. S. Hunter, R. B. Doak, R. A. Kirian, P. Fromme, T. A. White, J. Andreasson, D. Arnlund, S. A. Bajt, T. R. M. Barends, M. Barthelmess, M. J. Bogan, C. Bostedt, H. Bottin, J. D. Bozek, C. Caleman, N. Coppola, J. Davidsson, D. P. DePonte, V. Elser, S. W. Epp, B. Erk, H. Fleckenstein, L. Foucar, M. Frank, R. Fromme, H. Graafsma, I. Grotjohann, L. Gumprecht, J. Hajdu, C. Y. Hampton, A. Hartmann, R. Hartmann, S. Hau-Riege, G. Hauser, H. Hirsemann, P. Holl, J. M. Holton, A. Hömke, L. Johansson, N. Kimmel, S. Kassemeyer, F. Krasniqi, K.-U. Kühnel, M. Liang, L. Lomb, E. Malmerberg, S. Marchesini, A. V. Martin, F. R. N. C. Maia, M. Messerschmidt, K. Nass, C. Reich, R. Neutze, D. Rolles, B. Rudek, A. Rudenko, I. Schlichting, C. Schmidt, K. E. Schmidt, J. Schulz, M. M. Seibert, R. L. Shoeman, R. Sierra, H. Soltau, D. Starodub, F. Stellato, S. Stern, L. Strüder, N. Timneanu, J. Ullrich, X. Wang, G. J. Williams, G. Weidenspointner, U. Weierstall, C. Wunderer, A. Barty, J. C. H. Spence and H. N. Chapman, *Opt. Express*, 2012, **20**, 2706–2716.
14 S. P. Hau-Riege, A. Graf, T. Döppner, R. A. London, J. Krzywinski, C. Fortmann, S. H. Glenzer, M. Frank, K. Sokolowski-Tinten, M. Messerschmidt, C. Bostedt, S. Schorb, J. A. Bradley, A. Lutman, D. Rolles, A. Rudenko and B. Rudek, *Phys. Rev. Lett.*, 2012, **108**, 217402.
15 B. Rudek, S.-K. Son, L. Foucar, S. W. Epp, B. Erk, R. Hartmann, M. Adolph, R. Andritschke, A. Aquila, N. Berrah, C. Bostedt, J. Bozek, N. Coppola, F. Filsinger, H. Gorke, T. Gorkhover, H. Graafsma, L. Gumprecht, A. Hartmann, G. Hauser, S. Herrmann, H. Hirsemann, P. Holl, A. Homke, L. Journel, C. Kaiser, N. Kimmel, F. Krasniqi, K.-U. Kuhnel, M. Matysek, M. Messerschmidt, D. Miesner, T. Moller, R. Moshammer, K. Nagaya, B. Nilsson, G. Potdevin, D. Pietschner, C. Reich, D. Rupp, G. Schaller, I. Schlichting, C. Schmidt, F. Schopper, S. Schorb, C.-D. Schroter, J. Schulz, M. Simon, H. Soltau, L. Struder, K. Ueda, G. Weidenspointner, R. Santra, J. Ullrich, A. Rudenko and D. Rolles, *Nat. Photonics*, 2012, **6**, 858–865.
16 L. X. Chen, W. J. H. Jager, G. Jennings, D. J. Gosztola, A. Munkholm and J. P. Hessler, *Science*, 2001, **292**, 262–264.
17 R. Neutze, R. Wouts, S. Techert, J. Davidsson, M. Kocsis, A. Kirrander, F. Schotte and N. Wulff, *Phys. Rev. Lett.*, 2001, **87**, 195508.
18 C. Bressler, M. Saes, M. Chergui, D. Grolimund, R. Abela and P. Pattison, *J. Chem. Phys.*, 2002, **116**, 2955–2966.
19 M. Saes, C. Bressler, R. Abela, D. Grolimund, S. L. Johnson, P. A. Heimann and M. Chergui, *Phys. Rev. Lett.*, 2003, **90**, 047403.
20 C. Bressler and M. Chergui, *Chem. Rev.*, 2004, **104**, 1781–1812.
21 H. Ihee, M. Lorenc, T. K. Kim, Q. Y. Kong, M. Cammarata, J. H. Lee, S. Bratos and M. Wulff, *Science*, 2005, **309**, 1223–1227.
22 M. Cammarata, M. Levantino, F. Schotte, P. A. Anfinrud, F. Ewald, J. Choi, A. Cupane, M. Wulff and H. Ihee, *Nat. Methods*, 2008, **5**, 881–886.
23 A. Plech, M. Wulff, S. Bratos, F. Mirloup, R. Vuilleumier, F. Schotte and P. A. Anfinrud, *Phys. Rev. Lett.*, 2004, **92**, 125505.
24 S. Bratos, F. Mirloup, R. Vuilleumier, M. Wulff and A. Plech, *Chem. Phys.*, 2004, **304**, 245–251.
25 C. Bressler, C. Milne, V. T. Pham, A. El Nahhas, R. M. van der Veen, W. Gawelda, S. Johnson, P. Beaud, D. Grolimund, M. Kaiser, C. N. Borca, G. Ingold, R. Abela and M. Chergui, *Science*, 2009, **323**, 489–492.
26 H. Ihee, *Acc. Chem. Res.*, 2009, **42**, 356–366.
27 S. Bratos, F. Mirloup, R. Vuilleumier and M. Wulff, *J. Chem. Phys.*, 2002, **116**, 10615–10625.
28 Q. Kong, M. Wulff, J. H. Lee, S. Bratos and H. Ihee, *J. Am. Chem. Soc.*, 2007, **129**, 13584–13591.
29 J. Vincent, M. Andersson, M. Eklund, A. B. Wohri, M. Odelius, E. Malmerberg, Q. Kong, M. Wulff, R. Neutze and J. Davidsson, *J. Chem. Phys.*, 2009, **130**, 154502.
30 S. Bratos and M. Wulff, in *Advances in Chemical Physics*, ed. S. A. Rice, 2008, vol. 137, pp. 1–29.
31 M. Christensen, K. Haldrup, K. Bechgaard, R. Feidenhans'l, Q. Kong, M. Cammarata, M. Lo Russo, M. Wulff, N. Harrit and M. M. Nielsen, *J. Am. Chem. Soc.*, 2009, **131**, 502–508.
32 K. Haldrup, T. Harlang, M. Christensen, A. Dohn, T. B. van Driel, K. S. Kjaer, N. Harrit, J. Vibenholt, L. Guerin, M. Wulff and M. M. Nielsen, *Inorg. Chem.*, 2011, **50**, 9329–9336.
33 K. Haldrup, M. Christensen, M. Cammarata, Q. Kong, M. Wulff, S. O. Mariager, K. Bechgaard, R. Feidenhans'l, N. Harrit and M. M. Nielsen, *Angew. Chem., Int. Ed.*, 2009, **48**, 4180–4184.
34 M. Christensen, K. Haldrup, K. S. Kjaer, M. Cammarata, M. Wulff, K. Bechgaard, H. Weihe, N. H. Harrit and M. M. Nielsen, *Phys. Chem. Chem. Phys.*, 2010, **12**, 6921–6923.
35 K. Haldrup, M. Christensen and M. M. Nielsen, *Acta Crystallogr., Sect. A: Found. Crystallogr.*, 2010, **66**, 261–269.
36 H. Cailleau, M. Lorenc, L. Guerin, M. Servol, E. Collet and M. Buron-Le Cointe, *Acta Crystallogr., Sect. A: Found. Crystallogr.*, 2010, **66**, 189–197.
37 L. X. Chen, X. Zhang, J. V. Lockard, A. B. Stickrath, K. Attenkofer, G. Jennings and D.-J. Liu, *Acta Crystallogr., Sect. A: Found. Crystallogr.*, 2010, **66**, 240–251.

38 M. Chergui, *Acta Crystallogr., Sect. A: Found. Crystallogr.*, 2010, **66**, 229–239.
39 P. Coppens, J. Benedict, M. Messerschmidt, I. Novozhilova, T. Graber, Y.-S. Chen, I. Vorontsov, S. Scheins and S.-L. Zheng, *Acta Crystallogr., Sect. A: Found. Crystallogr.*, 2010, **66**, 179–188.
40 T. Elsaesser and M. Woerner, *Acta Crystallogr., Sect. A: Found. Crystallogr.*, 2010, **66**, 168–178.
41 S. L. Johnson, P. Beaud, E. Vorobeva, C. J. Milne, E. D. Murray, S. Fahy and G. Ingold, *Acta Crystallogr., Sect. A: Found. Crystallogr.*, 2010, **66**, 157–167.
42 J. Kim, K. H. Kim, J. H. Lee and H. Ihee, *Acta Crystallogr., Sect. A: Found. Crystallogr.*, 2010, **66**, 270–280.
43 Q. Kong, J. H. Lee, M. Lo Russo, T. K. Kim, M. Lorenc, M. Cammarata, S. Bratos, T. Buslaps, V. Honkimaki, H. Ihee and M. Wulff, *Acta Crystallogr., Sect. A: Found. Crystallogr.*, 2010, **66**, 252–260.
44 R. J. D. Miller, R. Ernstorfer, M. Harb, M. Gao, C. T. Hebeisen, H. Jean-Ruel, C. Lu, G. Moriena and G. Sciaini, *Acta Crystallogr., Sect. A: Found. Crystallogr.*, 2010, **66**, 137–156.
45 M. Schmidt, T. Graber, R. Henning and V. Srajer, *Acta Crystallogr., Sect. A: Found. Crystallogr.*, 2010, **66**, 198–206.
46 S. Westenhoff, E. Nazarenko, E. Malmerberg, J. Davidsson, G. Katona and R. Neutze, *Acta Crystallogr., Sect. A: Found. Crystallogr.*, 2010, **66**, 207–219.
47 Q. Kong, J. H. Lee, K. H. Kim, J. Kim, M. Wulff, H. Ihee and M. H. J. Koch, *J. Am. Chem. Soc.*, 2010, **132**, 2600–2607.
48 M. Cammarata, M. Lorenc, T. K. Kim, J. H. Lee, Q. Y. Kong, E. Pontecorvo, M. Lo Russo, G. Schiro, A. Cupane, M. Wulff and H. Ihee, *J. Chem. Phys.*, 2006, **124**, 124504.
49 K. Haldrup, G. Vankó, W. Gawelda, A. Galler, G. Doumy, A. M. March, E. P. Kanter, A. Bordage, A. Dohn, T. B. v. Driel, K. S. Kjær, H. T. Lemke, S. E. Canton, J. Uhlig, V. Sundstrom, L. Young, S. H. Southworth, M. M. Nielsen and C. Bressler, *J. Phys. Chem. A*, 2012, **116**, 9878–9887.
50 G. Hura, J. M. Sorenson, R. M. Glaeser and T. Head-Gordon, *J. Chem. Phys.*, 2000, **113**, 9140–9148.
51 A. M. Lindenberg, Y. Acremann, D. P. Lowney, P. A. Heimann, T. K. Allison, T. Matthews and R. W. Falcone, *J. Chem. Phys.*, 2005, **122**, 204507.
52 P. Georgiou, J. Vincent, M. Andersson, A. B. Wohri, P. Gourdon, J. Poulsen, J. Davidsson and R. Neutze, *J. Chem. Phys.*, 2006, **124**, 234507.
53 Q. Kong, M. Wulff, S. Bratos, R. Vuilleumier, J. Kim and H. Ihee, *J. Phys. Chem. A*, 2006, **110**, 11178–11187.
54 S. Ibrahimkutty, J. Kim, M. Cammarata, F. Ewald, J. Choi, H. Ihee and A. Plech, *ACS Nano*, 2011, **5**, 3788–3794.
55 A. Plech, V. Kotaidis, M. Lorenc and J. Boneberg, *Nat. Phys.*, 2006, **2**, 44–47.
56 https://sites.google.com/site/trwaxs/.
57 contact: TJS@chem.ku.dk.
58 S. Yin, H. Xu, W. Shi, Y. Gao, Y. Song and B. Z. Tang, *Dyes Pigm.*, 2006, **71**, 138–144.
59 J. Griffiths and K.-C. Feng, *J. Mater. Chem.*, 1999, **9**, 2333–2338.
60 H. T. Clarke and W. R. Kirner, *Org. Synth.*, 1922, **2**, 47.
61 Even though the ML-spectrum is a Gaussian with a 2.5% bandwidth, the difference in the resulting scattering signal are quite similar to a monochromatic spectrum as the smearing from the 'tail' of the undulator spectrum has been filtered out.
62 P. Hamm, S. M. Ohline and W. Zinth, *J. Chem. Phys.*, 1997, **106**, 519–529.
63 J. C. Deak, L. K. Iwaki and D. D. Dlott, *J. Phys. Chem. A*, 1998, **102**, 8193–8201.
64 J. C. Deak, S. T. Rhea, L. K. Iwaki and D. D. Dlott, *J. Phys. Chem. A*, 2000, **104**, 4866–4875.
65 B. Valeur, *Molecular Fluorescence: Principles and Applications*, Wiley-VCH, Weinheim, 2002.
66 The decay from the lowest electronically excited state to the ground state can occur *via* radiative (luminescence) or non-radiative processes (IC). In the case of a non-radiative decay, the process releases more energy into the solvent.
67 P. Bortolus and S. Monti, *J. Phys. Chem.*, 1979, **83**, 648–652.
68 T. Fujino and T. Tahara, *J. Phys. Chem. A*, 2000, **104**, 4203–4210.
69 T. Fujino, S. Y. Arzhantsev and T. Tahara, *J. Phys. Chem. A*, 2001, **105**, 8123–8129.
70 H. Satzger, S. Sporlein, C. Root, J. Wachtveitl, W. Zinth and P. Gilch, *Chem. Phys. Lett.*, 2003, **372**, 216–223.
71 C. W. Chang, Y. C. Lu, T. T. Wang and E. W. G. Diau, *J. Am. Chem. Soc.*, 2004, **126**, 10109–10118.
72 Y. C. Lu, E. W. G. Diau and H. Rau, *J. Phys. Chem. A*, 2005, **109**, 2090–2099.
73 T. Cusati, G. Granucci and M. Persico, *J. Am. Chem. Soc.*, 2011, **133**, 5109–5123.
74 H. Zollinger, *Color Chemistry*, Wiley VCH, New York, 3rd edn, 2001.
75 C. Roldan-Carmona, A. M. Gonzalez-Delgado, A. Guerrero-Martinez, L. D. Cola, J. J. Giner-Casares, M. Perez-Morales, M. T. Martin-Romero and L. Camacho, *Phys. Chem. Chem. Phys.*, 2011, **13**, 2834–2841.
76 M. Terazima, M. Takezaki, S. Yamaguchi and N. Hirota, *J. Chem. Phys.*, 1998, **109**, 603–609.
77 K. Takeshita, N. Hirota and M. Terazima, *J. Photochem. Photobiol., A*, 2000, **134**, 103–109.
78 C. Ridley, A. C. Stern, T. Green, R. DeVane, B. Space, J. Miksosvska and R. W. Larsen, *Chem. Phys. Lett.*, 2006, **418**, 137–141.
79 L. D. Landau and E. M. Lifshitz, *Fluid Mechanics*, Pergamon Press, Oxford, 2nd edn, 1987.
80 P. R. Longaker and M. M. Litvak, *J. Appl. Phys.*, 1969, **40**, 4033.
81 F. Mirloup, R. Vuilleumier, S. Bratos, M. Wulff and A. Plech, *Femtochemistry and Femtobiology: Ultrafast Events in Molecular Sciences*, Elsevier, New York, 2004.
82 S. Bratos and M. Wulff, in *Advances in Chemical Physics*, ed. S. A. Rice, 2008, vol. 136.
83 http://www.hbcpnetbase.com/.
84 http://webbook.nist.gov/chemistry/fluid/.
85 M. Nakamura, K. Chubachi, K. Tamura and S. Murakami, *J. Chem. Thermodyn.*, 1993, **25**, 1311–1318.

86 P. Georgiou, J. Vincent, M. Andersson, A. B. Wöhri, P. Gourdon, J. Poulsen, J. Davidsson and R. Neutze, *J. Chem. Phys.*, 2006, **124**, 234507.
87 J. Nath, *J. Chem. Thermodyn.*, 1996, **28**, 481–490.
88 D. Harrison and E. A. Moelwyn-Hughes, *Proc. R. Soc. London, Ser. A*, 1957, **239**, 230–246.
89 G. V. Stepanov, K. A. Shakhbanov, I. M. Abdurakhmanov and L. V. Malysheva, *Russ. J. Phys. Chem.*, 1992, **12**, 1493–1494.
90 In order to obtain a usable signal-to-noise ratio within a reasonable amount of time, at least 3% of the laser pump pulse should be deposited in the sample. This amounts to a decrease in signal strength by an order of magnitude compared to these experiments, where 200 repetitions were needed to obtain a good statistics S/N ratio. 3% absorptivity of a 300 μm liquid sheet corresponds to an optical density of 0.4 cm^{-1}.
91 R. Rey and J. T. Hynes, *J. Chem. Phys.*, 1996, **104**, 2356–2368.
92 H. Graener, R. Zurl and M. Hofmann, *J. Phys. Chem. B*, 1997, **101**, 1745–1749.
93 O. V. Boyarkin, T. R. Rizzo and D. S. Perry, *J. Chem. Phys.*, 1999, **110**, 11346–11358.
94 E. L. Sibert and R. Rey, *J. Chem. Phys.*, 2002, **116**, 237–257.
95 L. K. Iwaki and D. D. Dlott, *J. Phys. Chem. A*, 2000, **104**, 9101–9112.
96 C. G. Elles, D. Bingemann, M. M. Heckscher and F. F. Crim, *J. Chem. Phys.*, 2003, **118**, 5587–5595.
97 O. V. Boyarkin, L. Lubich, R. D. F. Settle, D. S. Perry and T. R. Rizzo, *J. Chem. Phys.*, 1997, **107**, 8409–8422.
98 S. Ashihara, N. Huse, A. Espagne, E. T. J. Nibbering and T. Elsaesser, *Chem. Phys. Lett.*, 2006, **424**, 66–70.
99 J. Lindner, P. Vöhringer, M. S. Pshenichnikov, D. Cringus, D. A. Wiersma and M. Mostovoy, *Chem. Phys. Lett.*, 2006, **421**, 329–333.
100 H. E Fischer, A. C. Barnes and P. S. Salmon, *Rep. Prog. Phys.*, 2006, **69**, 233–299.
101 The energy-deposition in acetonitrile has been corrected for direct multi-photon excitation of the solvent. The energy-deposition from direct excitation of the solvent has been found by back-extrapolating the linear regression Fig. 6A to zero and subtracting the back-extrapolation of Fig. 6B at zero yielding an estimated energy deposition of 0.12 J cm^{-3}. No evidence of excessive energy deposition was found for the remaining solvents.
102 E. Pontecorvo, PhD thesis, Universitá degli Studi di Roma, 2006.
103 Unpublished results.

Paper IV

Probing the Nonequilibrium Dynamics of Photoinduced Electron Transfer with Femtosecond X-ray Pulses

Sophie E. Canton, Kasper S. Kjær, György Vankó, Shin-ichi Adachi, Christian Bressler, Morten Christensen, Asmus O. Dohn, **Tim B. van Driel**, Andreas Galler, Wojciech Gawelda, Kristoffer Haldrup, Tobias Harlang, Yizhu Liu, Klaus B. Møller, Zoltan Nemeth, Shunsuke Nozawa, Mátyás Pápai, Tokushi Sato, Takahiro Sato, Tadashi Togashi, Kensuke Tono, Jens Uhlig, Kenneth Wärnmark, Makina Yabashi, Jianxin Zhang, Villy Sundström and Martin M. Nielsen.

Advanced Draft.

Title: Probing the Nonequilibrium Dynamics of Photoinduced Electron Transfer with Femtosecond X-ray Pulses

Authors: Sophie E. Canton[1†*], Kasper S. Kjær[2,3†*], György Vankó[4*], Tim B. van Driel[3], Shin-ichi Adachi[5], Christian Bressler[6], Pavel Chabera[7], Morten Christensen[3], Asmus O. Dohn[8], Andreas Galler[6], Wojciech Gawelda[6], Kristoffer Haldrup[3], Tobias Harlang[7], Yizhu Liu[9], Klaus B. Møller[8], Zoltán Németh[4], Shunsuke Nozawa[5], Mátyás Pápai[4], Tokushi Sato[5], Takahiro Sato[10‡] Karina Suarez-Alcantara[1],Tadashi Togashi[11], Kensuke Tono[11], Jens Uhlig[7], Kenneth Wärnmark[9], Makina Yabashi[10], Jianxin Zhang[9], Villy Sundström[7*] and Martin M. Nielsen[3*]

Affiliations:

[1] Department of Synchrotron Radiation Instrumentation, PO Box 118, Lund University, 22100 Lund, Sweden

[2] Centre for Molecular Movies, Niels Bohr Institute, University of Copenhagen, DK-2100, Copenhagen, Denmark

[3] Centre for Molecular Movies, Department of Physics, Technical University of Denmark, DK-2800, Lyngby, Denmark

[4] Wigner Research Centre for Physics, Hungarian Academy Sciences, H-1525 Budapest, P.O.B. 49, Hungary

[5] High Energy Accelerator Research Organization, 1-1 Oho, Tsukuba, Ibaraki 305-0801, Japan.

[6] European XFEL, Albert-Einstein Ring 19, D-22761 Hamburg, Germany

[7] Chemical Physics Department, PO Box 124, Lund University, S-22100 Lund, Sweden

[8] Department of Chemistry, Technical University of Denmark, DK-2800, Kgs. Lyngby, Denmark

[9] Centre for Analysis and Synthesis, Department of Chemistry, PO Box 124, Lund University, S-22100 Lund, Sweden

[10] RIKEN SPring-8 Center, 1-1-1 Kouto, Sayo-cho, Sayo-gun, Hyogo 679-5148, Japan

[11] Japan Synchrotron Radiation Research Institute (JASRI), 1-1-1 Kouto, Sayo-cho, Sayo-gun, Hyogo 679-5198, Japan

*Correspondence to: sophie.canton@maxlab.lu.se, kaspersk@gmail.com, vanko.gyorgy@wigner.mta.hu, villy.sundstrom@chemphys.lu.se, mmee@fysik.dtu.dk

[†] These authors have contributed equally to the work.

[‡] Current address: Department of Chemistry, School of Science, The University of Tokyo, 7-3-1 Hongo, Bunkyo-ku, Tokyo 113-0033, Japan

Abstract: Photoinduced electron transfer preceding energy equilibration enables entirely new applications but still challenges theoretical modeling. Understanding this regime requires an improved atomistic description of the coupled electronic and nuclear dynamics on the ultrafast time scale. X-ray diffuse scattering and X-ray emission spectroscopy have been recently combined at the SACLA free-electron laser facility to benchmark such a process in a photoexcited bimetallic complex. These experiments have captured simultaneously the sub-picosecond charge migration, the triggered structural rearrangements and the rate of concurrent heat transfer to the surrounding solvent. Correlation with transient absorption spectroscopy measurements in the visible range illustrates the extensive potential of femtosecond X-ray techniques as diagnostics of non-equilibrated electron transfer processes.

Main Text: Electron transfer (ET) is one of the primary events that mediate photoinduced functionality in solution (1). Studies across scientific fields have been rationalizing how intra and intermolecular factors determine the rates and the yields of this fundamental process (2). The definite roles of structure and surrounding in shaping the free-energy landscape can usually be disentangled for ET involving equilibrated reactants (3). This is no longer the case on the ultrafast time scale, since neither the nuclear degrees of freedom, nor the first solvation shell have yet adapted to the excited electronic configuration (4,5). The photoinduced charge migration is thus proceeding out of equilibrium. The paramount importance of this regime has been recognized with the progress of femtosecond laser spectroscopy techniques (6). Numerous experiments focusing on intramolecular ET have shown that the branching between the possible reactive pathways frequently occurs during the relaxation from the Franck-Condon state to the lowest thermally excited state (7). Over the last decades, these investigations have been geared

intensively toward optimizing the excited-state properties of molecular complexes that perform efficient solar energy conversion and photocatalysis (8,9). Maximizing the yields of long-lived charge-separated species, while minimizing adverse heat dissipation are highly complementary goals pursued to increase selectivity and stability *in operando*. Ultimately, controlling ultrafast photoinduced ET as the system relaxes and thermalizes has become an integral aspect of harnessing hot transitions for practical applications (10,11).

Unraveling nonequilibrium effects in the dynamics of ET requires mapping the spatial and temporal redistribution of the energy deposited initially through photoabsorption. So far, this problem has been tackled with the spectroscopic tools developed for tracking solvation and vibronic cooling in large molecules (12). The salient challenge faced in the UV-visible and near infrared range is the low degree of atomic specificity displayed by the broad optical signals. In addition, the kinetics often exhibit pronounced excitation wavelength-dependencies and non-exponential behaviors, so that their interpretation has to be assisted by Molecular Dynamics simulations (5,13). Consequently, building descriptive and predictive models of non-equilibrated ET relies heavily on refining the current understanding of the process at the molecular level. The exploration of this conceptual frontier is anticipated to advance rapidly with the coming online of X-ray Free Electron Laser (XFEL) facilities. While X-ray diffuse scattering (XDS) allows retrieving information about structural changes from intensity profiles $S(Q)$ (where Q is the momentum transfer) (14,15), X-ray emission spectroscopy (XES) based on electronic transitions from deep core levels is inherently element- and spin-sensitive (16,17). Combining these two techniques into optical pump-X-ray probe detection schemes at XFELs is now providing unprecedented instrumentation that achieves the femtosecond and the atomic-scale resolutions

necessary for monitoring ET out of equilibrium. The present work reports the first measurements of the rates that characterize the photoinduced ET and the local thermalization in a benchmark bimetallic complex (18), using the bright ultra-short X-ray pulses delivered by the SACLA XFEL (19).

The bimetallic complex $[(bpy)_2Ru^{II}(tpphz)^1Co^{III}(bpy)_2]^{5+}$ (abbreviated as $Ru^{II}{=}^1Co^{III}$ (20)) and its optical absorption spectrum in acetonitrile (MeCN) are shown in Figure 1A. A pump-probe setup accommodating simultaneous XES and XDS measurements (21) was implemented at BL3 of the SACLA XFEL (Figure 1B). A 6 mM solution of $Ru^{II}{=}^1Co^{III}$ was circulated through a 100 μm planar jet. The molecules were photoexcited at 400 nm by the 60 fs frequency-doubled pulses from a Ti:Sapphire laser, and subsequently probed with 8 keV X-ray pulses of 10 fs duration (22) at a 10 Hz repetition rate. The Co Kα XES lines were resolved by a spherical analyzer crystal and recorded with a MultiPort Charged Coupled Device (MPCCD) detector positioned on a Rowland circle. The XDS signal was collected with a second MPCCD placed after the sample. The setup is illustrated in Figure 1B, with additional details given in the supplementary materials (SM1).

Figure 2A displays the Co $K\alpha_1$ XES difference signal (XES-DS) [$laser_{ON}$ – $laser_{OFF}$)] acquired at time delays Δt fixed to 2.5, 20 and 150 ps after the selective excitation of the ^{1}MLCT state in the Ru^{II} moiety (SM2). This emission line originates from the secondary 2p → 1s transition subsequent to 1s core ionization. Steady-state and time-resolved (23) experiments at storage ring facilities have established that for spin-state transitions (SST) in 3d transition metal ions, the full width at half maximum (FWHM) (hence the inverse maximum

intensity) of the Kα lines is directly proportional to the number of unpaired electrons. This spectral feature therefore carries information about the total spin momentum of the X-ray absorbing center. In order to assign the transient XES-DS, a reference trace is constructed by subtracting the normalized lineshape obtained for a $(\pi t_{2g})^6$ $^1Co^{III}$ mononuclear complex in the low-spin (LS) state from that of a $(\pi t_{2g})^5$ $(\sigma e_g)^2$ $^4Co^{II}$ in the high-spin (HS) state (SM3). The excellent agreement with the XES-DS at 150 ps demonstrates that ET from Ru^{II}* to $^1Co^{III}$ (LS) and a SST within the Co moiety have both taken place during this time interval. In addition, relative scaling readily delivers 65 ± 8% as the fraction of $^4Co^{II}$(HS) present at 150 ps, reflecting the yield of photoexcited Ru^{II}*=$^1Co^{III}$ and the overall ET/SST rate of Ru^{III}=$^4Co^{II}$ (HS) population. Assuming a *concerted* mechanism where the SST is concurrent with the ET, i.e. Ru^{II}= $^1Co^{III}$ (LS) + hν → Ru^{III} = $^4Co^{II}$ (HS), the XES-DS amplitude at 6.93 keV, $\gamma_{XES}(t)$, monitors the formation kinetics of this species (Figure 2B). A single-exponential fit gives a rise time of 1.7 ± 0.4 ps broadened by a 550 ± 230 fs Gaussian Machine Response Function (MRF) dominated by the temporal jitter between optical pump and X-ray probe (SM7). It should be noted that fits where the primary contribution to the time scales of the kinetics was the MRF could be unambiguously discarded through statistical analysis (SM7). Since the observed rate is not instrument-limited, the XES measurement is accessing the intrinsic time scale of the ET/SST process.

This result guides the interpretation of the XDS difference signal (XDS-DS) $\Delta S(Q,t)$ shown in Figure 3A, after data reduction (SM4). It contains contributions from the changes in solute structure $\Delta S_{solute}(Q,t)$, the bulk-solvent response $\Delta S_{solvent}(Q,t)$ and possibly, a solute-solvent 'caging' term that depends markedly upon the nature of their interactions. Within the *concerted* model suggested by XES, $\Delta S_{solute}(Q,t)$ can be expressed as $\gamma_{XDS}(t).\Delta S_{solute}(Q)$,

where $\gamma_{XDS}(t)$ is the time-dependent fraction of Ru^{III}=$^4Co^{II}$ (HS), while the profile $\Delta S_{solute}(Q)$ is calculated from the DFT-optimized geometries of the ground state and this charge-separated species. The distinctive negative dip at Q = 0.5 $Å^{-1}$ is associated to the Co-N bond length elongation by 0.2 Å in the HS state (18). The methodology for analyzing $\Delta S_{solvent}(Q,t)$ has been elaborated at third generation synchrotron facilities (24,25). Within the framework of classical hydrodynamics, $\Delta S_{solvent}(t)$ is well described by:

$$\Delta S_{solvent}(Q,t) = \Delta T(t) \cdot \left.\frac{\partial S(Q)}{\partial T}\right|_{\rho} + \Delta\rho(t) \cdot \left.\frac{\partial S(Q)}{\partial \rho}\right|_{T} \quad (1)$$

where ΔT and $\Delta\rho$ are small variations of the temperature T and the density ρ, while $\left.\frac{\partial S(Q)}{\partial T}\right|_{\rho}$ (resp. $\left.\frac{\partial S(Q)}{\partial \rho}\right|_{T}$) are the scattering profiles at constant ρ (resp. at constant T). For Δt << 10 ns, mass transfer has not yet set in ($\Delta\rho$ = 0), so that $\Delta S_{solvent}(Q,t)$ can be ascribed solely to impulsive heating at constant ρ. A global-fit analysis of the XDS-DS was performed (26) using ΔS_{solute} and the $\left.\frac{\partial S(Q)}{\partial T}\right|_{\rho}$ of MeCN (25) convoluted with the XFEL spectrum as principal components (Figure 3B and SM5). Figure 3C and 3D show the fitted $\gamma_{XDS}(t)$ and $\Delta T(t)$ after broadening by the 550 fs XFEL MRF. No 'caging' contribution could be isolated. The step-like increase of $\gamma_{XDS}(t)$ to 67 ± 4 % for t > 0 matches the 65 ± 8 % obtained for γ_{XES} at 150 ps.The evolution of $\Delta T(t)$ follows a single-exponential rise of 12 ± 3 ps and reaches a final value ΔT_f = 1.0 ± 0.1 K. The XDS measurements therefore capture the structural changes of the solute and the early dynamics of impulsive solvent heating until local thermalization. Comparing the time scales extracted independently from the transient XES and XDS signals provides the first X-ray based

visualization of a photoinduced ET event proceeding faster than the energy equilibration between the excited solute and its surrounding.

The strengths of the ultrafast X-ray techniques are further evidenced when attempting to relate these dynamics to the quenching of the Franck-Condon state $Ru^{II}*={}^{1}Co^{III}$ seen with transient optical absorption spectroscopy (TOAS) (18) (Figure 4A). Upon photoexcitation, the known signature of reduced pyrazine appears quasi-instantaneously (< 50 fs) as a strong signal at 625 nm (27). This bridge-localized state $Ru^{III}\doteq{}^{1}Co^{III}$ (LS) decays exponentially with a 240 ± 70 fs time constant (inset of Figure 4A), in stark contrast to the 1.7 ± 0.4 ps formation time constant of $^{4}Co^{II}$ (HS) tracked by XES. In other words, the time taken by the electron to leave the bridge cannot be identified with the time necessary for the $^{4}Co^{II}$ (HS) to appear. This clearly points to the participation of an additional step. Since no other spectral fingerprints from reduced ligands can be observed with TOAS, a *sequential* mechanism involving an optically-dark excited state of Co^{II} can be proposed: $Ru^{II}={}^{1}Co^{III}$ (LS) + hν → $Ru^{II}*={}^{1}Co^{III}$ → $Ru^{III}\doteq{}^{1}Co^{III}$ (LS) → $Ru^{III}={}^{2}Co^{II}$ (LS) → $Ru^{III}–{}^{4}Co^{II}$ (HS). Fixing the formation rate of this intermediate species to the $(240\ fs)^{-1}$ decay rate of reduced pyrazine, and the $^{2}Co^{II}$(LS)/$^{4}Co^{II}$(HS) amplitude ratio to 1/3 (from the FWHM of the respective XES lines), while leaving the $^{2}Co^{II}$(LS) → $^{4}Co^{II}$(HS) rate and the MRF as free parameters does produce the most-likely fit, with a time constant for the SST of 1.9 ± 0.6 ps (SM6). The various steps of this model are summarized in Figure 4B and 4C. Elucidating the precise role of $^{2}Co^{II}$(LS) in promoting the charge separation calls for further investigations with the higher selectivity and temporal resolution that will be enabled by the ongoing development of timing tools (28) and self-seeding schemes (29) at XFEL facilities (SM8).

In summary, the combination of XES and XDS at the SACLA XFEL facility has unveiled the fundamental time scales of non-equilibrated ET in a photoexcited bimetallic $Ru^{II}=^{1}Co^{III}$ complex, with element and spin sensitivity. While XES follows the reduction of the Co center and the accompanying SST, XDS catches the structural changes of the solute, as well as the onset of impulsive solvent heating. The stabilization of the charge-separated state in this dyad is evidently faster than the dissipation of excess energy to the surroundings. Correlation with TOAS results indicates the participation of at least one optically-dark intermediate tentatively assigned as a $^{2}Co^{II}$(LS) species. The present work illustrates the unique capabilities of complementary ultrafast X-ray techniques as diagnostic tools of ET out of equilibrium, since they can reliably unravel, within a single experiment, the time scales of intramolecular and intermolecular processes, even when highly coupled. Considering that the analysis of these XFEL-based measurements are entering previously uncharted territory, benchmarking simple systems is providing the guidelines required for extending the methodology to more advanced instances of electron driven reactivity, such as solvent-mediated ET (30,31) or conformationally-gated ET (32,33). Ascertaining the energetic pathways associated to this regime in the homogeneous phase is also paving the way to tailoring the process for optimized functionality of photoactive interfaces (34). Finally, manipulating hot ET is generally foreseen as a stepping stone for unlocking the untapped potential of photoinduced quantum coherence, which has been connected to the unrivaled efficiency of natural photosynthesis (35).

References and Notes:

1. N. Sutin, C. Creutz, *Pure Appl. Chem.* **52**, 2717 (1980).

2. R. A. Marcus, *Rev. Mod. Phys*. **65**, 599 (1993).

3. J. F. Endicott *et al., Prog. Inorg. Chem.* **30** , 141 (1983).

4. H. Heitele, *Angw. Chem. Int. Ed. Engl.* **32**, 359 (1993).

5. P. F. Barbara, G. C. Walker, T. P. Smith, *Science* **256**, 975 (1992).

6. M. J. Rosker, M. Dantus, A. H. Zewail, *Science* **241**, 1200 (1988).

7. A. Mokhtari, P. Cong, J. L. Herek, A. H. Zewail, *Nature* **348**, 225 (1990).

8. N. H. Damrauer *et al., Science* **275**, 54 (1997).

9. M. R. Wasielewski, *Chem. Rev*. 92, 435 (1992).

10. M. Z. Bazant, *Acc. Chem. Res.* **46**, 1144 (2013).

11. W. A. Tidsale *et al., Science* **328**, 1543 (2010).

12. T. Elsaesser, W. Kaiser, *Annu. Rev. Phys. Chem.* **42**, 83 (1991).

13. P. J. Rossky, J. D. Simon, *Nature* **370**, 263 (1994).

14. K. B. Møller and N. E. Henriksen, *Struct. Bond.* **142**, 185 (2012).

15. H. Ihee *et al., Int. Rev. Phys. Chem.* **12**, 453 (2010).

16. P. Glatzel, U. Bergmann*, Coord. Chem. Rev.* **249**, 65 (2005).

17. J. Kern *et al., Science* **340**, 491 (2013).

18. S. E. Canton *et al.*, *J. Phys. Chem. Lett.* **4**, 1972 (2013).

19. T. Ishikawa *et al*., *Nature Photon*. **6**, 540 (2012).

20. bpy and tpphz respectively stand for bipyridine and tetrapyrido[3,2-*a*:2',3'-*c*:3",2"-*h*:2"':2"'-3"'-*j*]phenazine.

21. K. Haldrup *et al*., *J. Phys. Chem. A,* **116**, 9878 (2012).

22. Y. Inubushi *et al.*, *Phys. Rev. Lett.* **109**, 144801 (2012).

23. G. Vanko *et al., Angew. Chem*. **46**, 5306 (2007).

24. M. Cammarata *et al.*, *J. Chem. Phys.* **124**, 124504 (2006).

25. K. S. Kjær *et al., Phys. Chem. Chem. Phys.,* DOI: 10.1039/C3CP50751C.

26. K. Haldrup, M. Christensen, M. M. Nielsen, *Acta Cryst. A* **66**, 261 (2010).

27. C. Chiorboli, M. A. J. Rodgers, F. Scandola, *J. Am. Chem. Soc.* **125**, 483 (2003).

28. M. Harmand *et al., Nature Photonics* **7**, 215 (2013).

29. J. Amann *et al.*, *Nature Photonics* **6**, 693 (2012).

30. A. Troisi, M. A. Ratner, M. B. Zimmt, *J. Am. Chem. Soc.* **126**, 2215 (2004).

31. L. Scheps *et al., Science* **328**, 220 (2010).

32. P. P. Laine, S. Campagna, F. Loiseau, *Coord. Chem. Rev*. **252**, 2552 (2008).

33. H. Wang *et al., Science* **316**, 747 (2007).

34. J. Chang, A. J. Fredo, M. van Veenendaal, *Chem. Phys*. 407, 65 (2012).

35. H. Lee, Y. C. Cheng, G. R. Fleming, *Science* **316**, 1462 (2007).

36. G. Vankó *et al., Angew. Chem. Int. Ed.* **49**, 5910 (2010).

37. J. P. Rueff *et al*., *Phys. Rev. B* **63**, 132409 (2001).

38. Sikora, K. Knizek, C. Kapusta, P. Glatzel, *J. Appl. Phys*. **103,** 07C907 (2008).

39. H. Yamaoka *et al., Phys. Rev. B*., **77**, 115201 (2008).

40. J. Herrero-Martín *et al., Phys. Rev. B* **82**, 075112 (2010).

41. G. Vanko *et al., J. Phys. Chem. B* **110**, 11647 (2006).

42. G. Vankó *et al., J. Electron Spectrosc. Relat. Phenom.* DOI: 10.1016/j.elspec.2012.09.012.

43. D. T. Cromer, J. B. Mann, *Acta Crystallogr. Sect. A*, **24**, 321–324 (1968).

44. F. Hajdu, *Acta Cryst. A* **28**, 250–252. (1972).

45. F. Neese, *ORCA, version 2.8*; (Max-Planck-Institut für Bioanorganische Chemie: Mülheim an der Ruhr, Germany, 2004).

46. A. D. Becke, *Phys. Rev. A* **38**, 3098−3100 (1988).

47. J. P. Perdew, *Phys. Rev. B* **33**, 8822−8824 (1986).

48. L. D. Landau, E. M. Lifshitz, *Fluid Mechanics* (Pergamon Press, Oxford, ed. 2, 1987).

49. K. P. Burnham, D. R. Anderson, *Model Selection and Multimodel Inference: A Practical Information-Theoretic Approach* (Springer-Verlag, New York, 2nd ed. 2002), ISBN 0-387-95364-7.

Acknowledgments:

This project was supported by the X-ray Free Electron Laser Priority Strategy Program of MEXT, Japan (to SA), the Swedish Research Council, the Knut and Alice Wallenberg Foundation, the Crafoord Foundation, the Swedish Energy Administration, the Science Faculty at Lund University (MAXIV and ESS initiative grant), the Danish National Research Foundation Center for Molecular Movies, DANSCATT, Carlsberg, the Lundbeck Foundation, the European Research Council (ERC-AdvG-VISCHEM-226136 to VS, and ERC-StG-259709 to GV). The XFEL experiments were performed at the BL3 of SACLA with the approval of JASRI (Proposal No. 2012A8049).

Fig. 1.

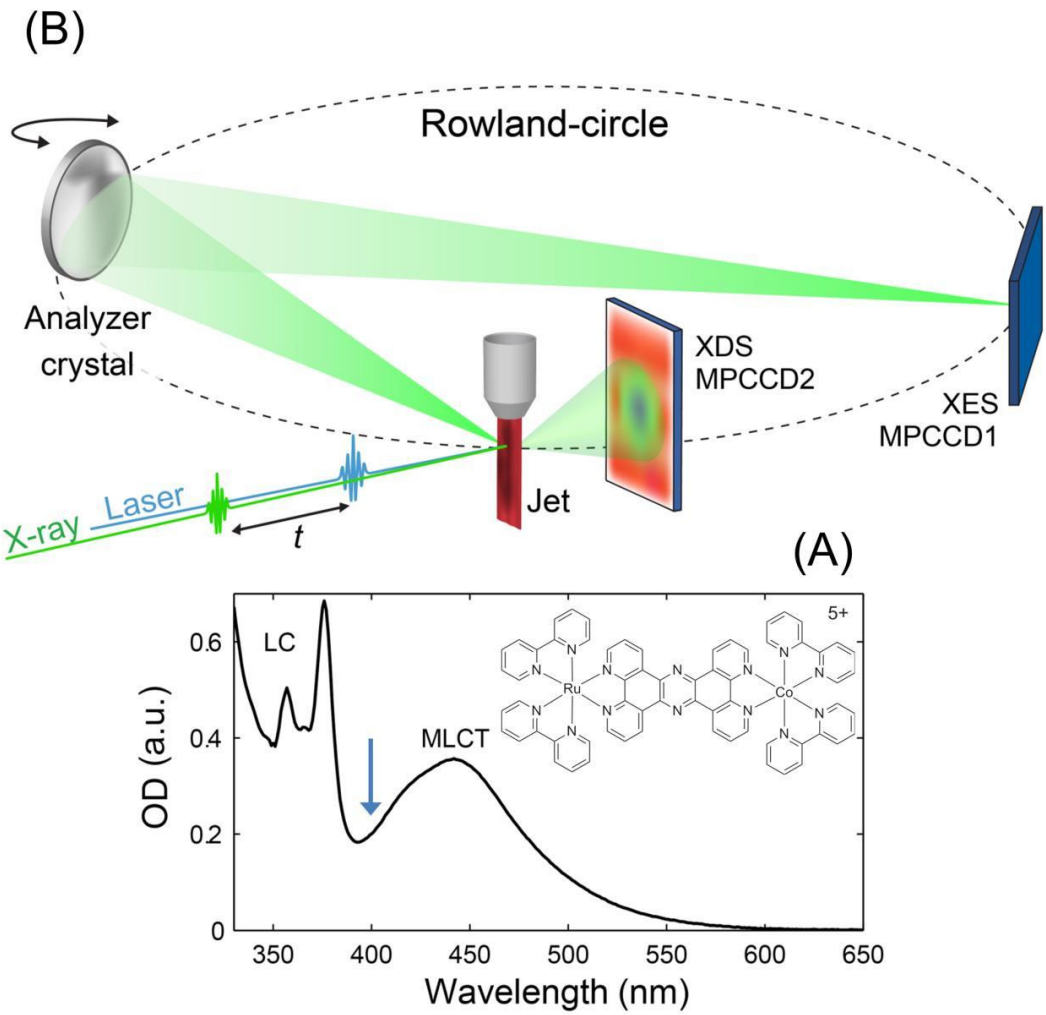

Figure 1: (A) Ru^{II}=$^{1}Co^{III}$ complex and its optical absorption spectrum in MeCN. The blue arrow shows the photoexcitation wavelength. (B) Experimental setup.

Fig. 2.

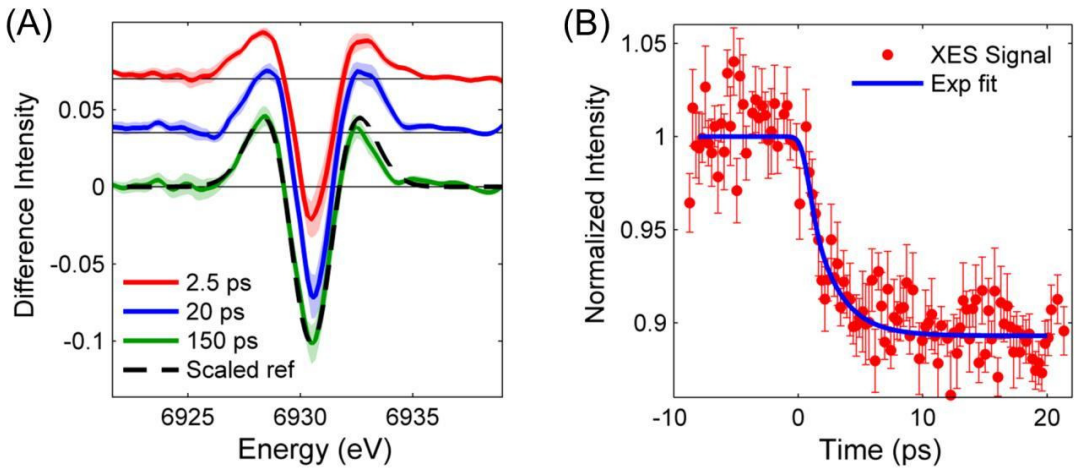

Figure 2: (A) Co $K\alpha_1$ XES-DS at 2.5 ps (red), 20 ps (blue) and 150 ps (green) pump-probe delay. The shaded areas indicate the uncertainty level. The dashed black curve is the reference for a $^{1}Co^{III}(LS) \rightarrow {}^{4}Co^{II}(HS)$ conversion, scaled to the 150 ps trace. (B) Kinetic trace at 6.93 keV (red dots) and single-exponential fit (blue line).

Fig. 3.

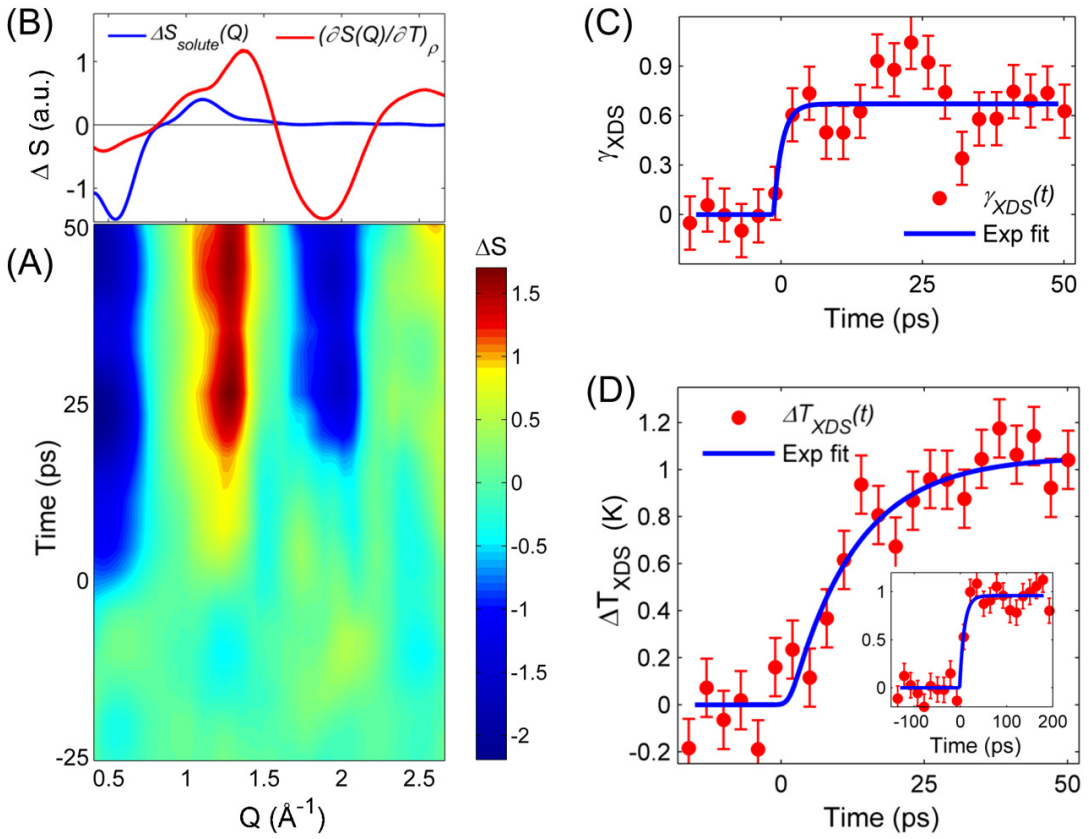

Figure 3: (A) Median filtered XDS-DS. (B) Reference XDS-DS for the solute (blue) and solvent (red) contributions. (C) $\gamma_{XDS}(t)$ and (D) $\Delta T(t)$ kinetics (red dots), with their single-exponential fits (blue line).

Fig. 4.

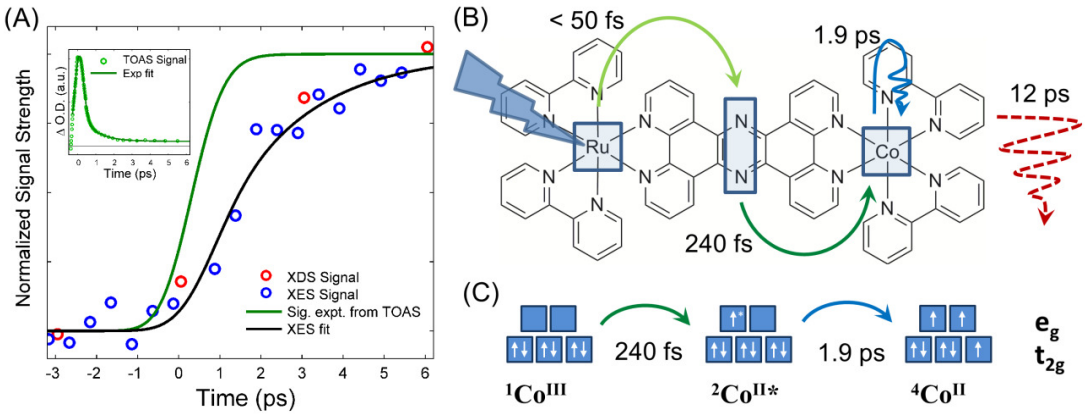

Figure 4: (A) Zoom on the early times of the kinetics: XDS (red circles), XES (blue circles) and fit to the sequential ET model (black line), TOAS at 625 nm broadened by the XFEL MRF (green line). The inset shows the original TOAS trace (green circles) at longer pump-probe delays, and its single-exponential fit (dark green line). (B) Schematic summarizing the various steps of the non-equilibrated charge separation: selective photoexcitation of Ru^{II}, quasi-instantaneous formation of a bridge-localized state (light green arrow), population of $^2Co^{II}$ (LS) (dark green arrow), which undergoes a SST to $^4Co^{II}$ (HS) with a ~ 1.9 ps time constant (dark blue arrow). Concurrently, the solvent is heated at an exponential rate of ~ $(12\ ps)^{-1}$. (C) Time-evolution of the charge and spin-state at the Co center.

Supplementary Materials:

Materials and Methods:

Supplementary Materials for:

Probing the Nonequilibrium Dynamics of Photoinduced Electron Transfer with Femtosecond X-ray Pulses

Sophie E. Canton[1†*], Kasper S. Kjær[2,3†*], György Vankó[4*], Tim B. van Driel[3], Shin-ichi Adachi[5], Christian Bressler[6], Pavel Chabera[7], Morten Christensen[3], Asmus O. Dohn[8], Andreas Galler[6], Wojciech Gawelda[6], Kristoffer Haldrup[3], Tobias Harlang[7], Yizhu Liu[9], Klaus B. Møller[8], Zoltán Németh[4], Shunsuke Nozawa[5], Mátyás Pápai[4], Tokushi Sato[5], Takahiro Sato[10‡] Karina Suarez-Alcantara[1],Tadashi Togashi[11], Kensuke Tono[11], Jens Uhlig[7], Kenneth Wärnmark[9], Makina Yabashi[10], Jianxin Zhang[9], Villy Sundström[7*] and Martin M. Nielsen[3*]

Contents

SM1 Experimental setup

The dinuclear complex studied in this work was $[(bpy)_2Ru^{II}(tpphz)^1Co^{III}(bpy)_2]^{5+}$ where "bpy" is 2,2'- bipyridine, and "tpphz" tetrapyrido[3,2-*a*:2',3'-*c*:3",2"-*h*:2"':2"'-3"'-*j*]phenazine. Its PF_6 salt was synthesized following the improved protocol given in (18). Its chemical structure is abbreviated as $Ru^{II}=^1Co^{III}$ hereafter.

An optical pump – X-ray probe setup combining X-ray Emission Spectroscopy (XES) and X-ray Diffuse Scattering (XDS) was implemented at beamline BL 3 of the SACLA XFEL facility, Japan (see Figure 1 in the main text). A 6 mM solution of $Ru^{II}=^1Co^{III}$ in acetonitrile (MeCN) was continuously circulated in a free flowing planar liquid sheet (100µm). The molecules were optically excited at 400 nm (60 fs pulse length, 500µm FWHM focus spot, 220 µJ/pulse). The probe consisted of 8 keV X-ray pulses (10 fs pulse length, 0.3% bw, 450 µm FWHM beam size, 10^{10} photons/pulse) generated by SACLA. Both laser and X-rays were operated at a 10 Hz repetition frequency. The two beams crossed under a 10 degree angle in the horizontal plane. Prior to introducing the liquid sheet, the spatial overlap at the sample position was established by scanning a pinhole. The temporal overlap was determined with 10 ps resolution using a photodiode. The effective time-resolution was given by the shot-to-shot jitter between the optical and FEL pulses. It was estimated to be 530 ±250 fs (as described in SM7).

A 4" diameter spherically bent Si(531) analyzer crystal (1010 mm bent radius) working in the Rowland circle geometry was placed at 105 degrees scattering angle, in order to resolve and focus the X-ray emission at a Bragg angle of 77 degrees in the horizontal plane, which corresponds to the Co $K\alpha_1$ emission maximum at 6.93 keV. This signal was detected using the MultiPort Charged Coupled Device (MPCCD) area detector. Rotation of the analyzer crystal with concurrent movement of the MPCCD allowed for energy (wavelength) selection. The X-ray

diffuse scattering (XDS) signal was recorded on a second MPCCD detector placed 3.5 cm behind the sample (with the direct beam blocked), allowing for detection in a *Q*-range spanning from 0.4 $Å^{-1}$ to 3.2 $Å^{-1}$. The XES and XDS detectors were read out after every X-ray pulse. The signal of interest is extracted from a differential measurement on the sample with and without laser irradiation, i.e. as a [$laser_{ON}$ – $laser_{OFF}$] trace. Two types of scans were acquired:

1) Kinetic-scans where the time delay Δt between the laser and the X-ray pulse was varied by steps of 0.3 ps, 3 ps or 10 ps. The signal was integrated for 20 s (corresponding to 200 X-ray pulses, with the detector signal read out for each individual pulse).

   For the scans with 0.3 ps step size, negative delays of -100 ps (corresponding to the X-rays arriving 100 ps *before* the laser pump) were interspaced such that every 4th delay was a $laser_{OFF}$ measurement allowing for correction of any long-term drifts in the signal during the measurements.
2) Energy-scans of the XES intensity at constant Δt. The signal was integrated for 4 s (corresponding to 40 X-ray pulses) at each energy point.

SM2: XES data extraction and reduction

The low readout noise of the MPCCD detector allowed explicit single-photon discrimination of the XES signal. A flow-chart of the data extraction-correction process is shown in Figure S1.

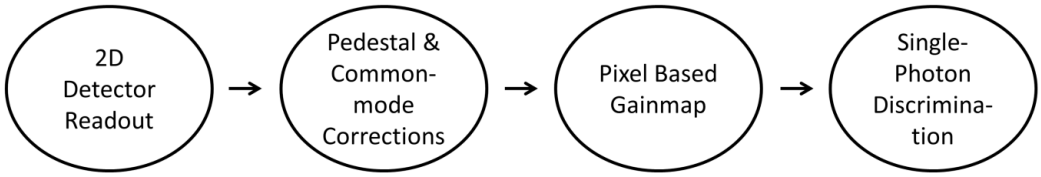

Figure S1: Flowchart of the XES data extraction-correction process.

Step 1: Readout

The MPCCD detector is read out as a 2D image containing the read-out value (ROV) of each pixel.

Step 2: Detector corrections

The so-called "pedestal" correction ensures that the zero-photon ROVs of all the pixels are close to 0 analogue-to-digital units (ADU). A set of 15000 dark-measurements (i.e. images with the X-rays shutter closed and no X-rays hitting the detector) was averaged, yielding the average 0-photon signal level for each pixel. This background was subtracted from all further images. Three sets of such dark-measurements were recorded in the course of the experimental run in order to confirm that this background did not change over time. Common-mode artefacts arising from amplifier/current supply electronics were negligible.

Step 3: Calibration/scaling

A pixel-specific gainmap constructed from single-pixel ROVs was applied. A typical histogram of the ROVs for a pixel seeing a high photon intensity is plotted in Figure S2 (blue line), the insert shows a zoom-in.

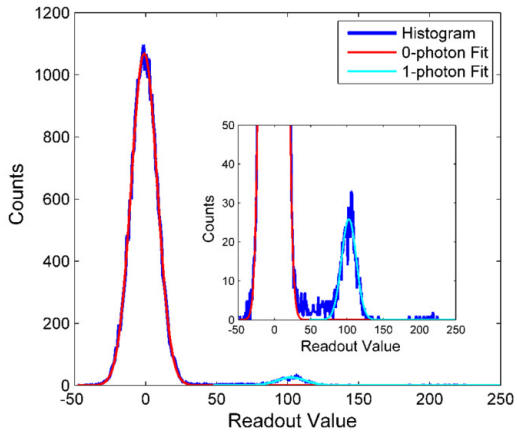

Figure S2: Single-pixel histogram of a strongly illuminated pixel after step 1 and 2. The peak at ROV = 0 corresponds to readout of the pixel after no photons were detected, the peak at ROV = 100 corresponds to 1-photon counting events, while the clustering of counts observed around ROV = 210 originates from 2-photon events.

The peaks centered at ROV= 0 ADU, at ROV= 100 ADU and the clustering of counts around 210 ADU correspond to 0, 1 and 2 photon counting events respectively. For each X-ray illuminated pixel, Gaussian functions of r.m.s σ were fitted to the 0-photon signal (red line), and the 1-photon signals (cyan line) individually. The single-pixel gainmap was constructed by defining the center peak positions of the two Gaussians to 0 and 1 respectively. As can be seen from the inset in Figure S2, many ROVs fall between the 0- and 1-photon peaks. This interval is assigned to fractional photon events. The most robust approach to account for them was to define the number of detected 1-photon and 2-photon events in an exposed image as the number of

pixels for which the single-pixel gain corrected ROVs were such that 0.5<ROV<1.5 and ROV>1.5 respectively. Since the maximum count rate of any pixel was ~0.025 ph/exposure, gain-corrected ROVs corresponding to 3 or more photons were not considered. A lower threshold of 9σ of the zero-photon readout was enforced in the single-photon discrimination to remove false counting events from the readout noise. Figure S3 follows a detector image across the 3 stages of the data extraction-correction procedure. Note that the high read-out noise of the third detector from the top made explicit single-photon counting in this element impossible, resulting in the partial lack of data in the corresponding panel of the final figure. Even though this approach discards all photons hitting 1/3 of active area of the detector, it resulted in the best signal to noise ratio, with the mean standard deviation of each data point typically being within 30% of that expected from a true Poisson distribution. The final signal strength obtained in the Co Kα emission peak is the sum of all the detector counts for a given pulse and was typically ~20 photons/pulse, while the background count was ~0.2 photons/pulse.

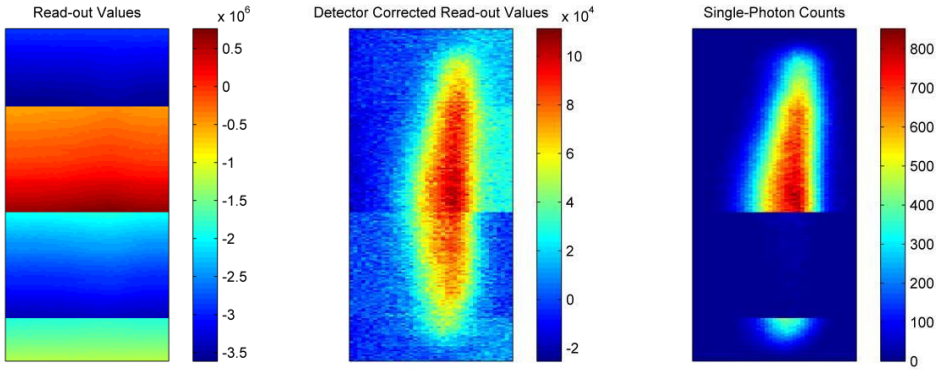

Figure S3: Processing of an XES kinetic-scan: (Left) Sum of the ROVs for each pixel after read-out (step 1), (Middle) Summed ROVs after detector corrections, (step 2), (Right) Summed photon counting events for each pixel after single-photon discrimination (step 3).

SM3: XES data analysis

The Kα spectra originate from multiplet and spin orbit interactions. In transition metal systems, it is highly sensitive to the oxidation state and to the number of unpaired electrons. Due to the large core-hole lifetime broadening, the lines seem rather unresolved. However, with careful lineshape analysis, the information content can be extracted. A frequent evaluation approach that is applicable to the interpretation of photoinduced transient Kα and Kβ spectra is based on constructing differences of steady-state spectra from suitable reference complexes. The integrals of the absolute values of the difference spectra are then proportional to the conversion yield. This approach is somewhat similar to the treatment of X-ray dichroism, although sum rules do not apply, and one needs to find acceptable reference complexes. Still, this approach can be quantitative for two-state transitions (36) as demonstrated in numerous studies (23,37,38,39,40). However, in the experiments reported in this work, the short effective data collection time did not permit to obtain a sufficiently large set of spectra with clear references and good statistics to fully exploit this approach. It was nevertheless indirectly applied to follow the spectral variations, since for the Kα spectra, the linewidth can also be exploited to calibrate the spin momentum on the cobalt center. Although the 2p-3d exchange interaction is rather small, its variation upon increase in spin-state appears as a clear broadening (41). For this experiment, the linewidth difference of the ground state and the photoexcited state is 0.6 eV. This value corresponds to a spin-state change of $\Delta S=1.5$. Since the initial spin momentum of the S $^{1}Co^{III}$ is $S=0$, this corresponds to $S=3/2$, a spin-state of HS $^{4}Co^{II}$. Given that the total Kα emission intensity does not depend upon the charge and spin-state (within 5 % (42)) the relative changes in the width of the emission line for the different Co species directly result in an inverse lowering of the maximum emission intensity, i.e. the peak height. This is the parameter measured and plotted in the kinetic traces presented in the main text.

SM4: XDS data extraction and reduction

Construction of the XDS difference signals

The 2D X-ray Diffuse Scattering (XDS) images extracted from the MPCCD detector were corrected to account for the effects of:

1) the X-ray beam polarization

2) the X-ray absorption of 8 keV photons throughout the liquid sheet

3) the solid angle subtended by each detector pixel

4) the X-ray absorption probability of an 8 keV photon within a pixel

The resulting images were then integrated azimuthally around the beam center (found by circle-fits to the liquid-peak in the 2D images) producing 1D curves of the scattering intensity *S(Q)*, where $Q = \frac{2\pi \sin(2\theta)}{\lambda}$ is the momentum transfer, 2θ is the scattering angle, and λ is the X-ray wavelength. The first step in the analysis of *S(Q)* was a simple filtering procedure. Any exposure where either I_0 (the incident intensity) or I (the integrated intensity on the MPCCD) fell outside one standard deviation from the mean of either of the two intensities was discarded. The remaining *S(Q,t)* were averaged for each time-delay and scaled to a simulated scattering curve $S_{Sim}(Q) = S_{Coh}(Q) + S_{Incoh}(Q)$, which is the sum of the coherent $S_{Coh}(Q)$ and incoherent $S_{Incoh}(Q)$ scattering arising from a "Liquid Unit Cell", L.U.C, i.e. an ensemble of molecules representing the stoichiometry of the sample. In the present case, the L.U.C consisted of a single Ru^{II}=$^{1}Co^{III}$ molecule, 5 PF_6^- ions and 19.15 M/6 mM = 3191 acetonitrile molecules. $S_{Coh}(Q)$ was calculated from the orientation-averaged Debye equation by using the isolated-atom formalism. The atomic form factors were described by the Cromer-Mann parameterization (43). $S_{Incoh}(Q)$ was obtained from the parameterization provided by Hajdu (44). Scaling *S(Q,t)* to the L.U.C. $S_{sim}(Q)$ was done

by minimizing $[S_{Sim}(Q) - \alpha \cdot S(Q,t)]$ for 1.5 $Å^{-1}$ <Q< 1.8 $Å^{-1}$ around a nodal point in the difference scattering signal (24). This step effectively put the *S(Q,t)* on an absolute scale of electron units/LUC (26). The XDS difference signals (XDS-DS) *ΔS(Q,t)* were finally calculated for each time point, by subtracting the signal from the unpumped sample $\Delta S(Q,t) = S(Q,t) - S(Q)_{Off}$, where S_{Off} was defined as the mean of the earliest 12 time delays for which the X-ray pulses arrived from 12 ps to 45 ps before the laser pulse, namely $S(Q)_{Off} = \sum_{i=1}^{12} S(Q,t_i) \Big/ 12$

SVD-based background contributions

The XDS-DS *ΔS(Q,t)* obtained for t<0 contain a considerable amount of noise. If the background contributions were constant during acquisition, these *ΔS(Q,t)* should in principle amount to statistical fluctuations. In order to identify and remove these contributions, Singular Value Decomposition (SVD) was applied to the set of *ΔS(Q,t)* curves calculated in the region used to construct S_{Off}. In general, SVD analysis decomposes any matrix X as the product $X = U*S*V^{\dagger}$, where U and V are unitary matrices, while S is a diagonal matrix. Taking X as the data matrix, the columns of U are the singular vectors representing the variation in the data matrix X along the time coordinate, and V contains the time-dependency of this variation. The elements of the diagonal matrix S denote the relative magnitudes of the singular vectors. Inspection of S indicates that five singular vectors are sufficient to accurately represent the variation in the S_{off} data matrix, as the singular values S_{ii} for i > 5 become very small. The residual signal $\Delta S_{res}(Q, t) = |\Delta S(Q,t) - \Sigma\alpha_i \cdot S_{ii} \cdot U_{ji}|$ for each t as a function of the 5 scaling parameters $\alpha_{1\text{-}5}$ is shown in Figure S4.

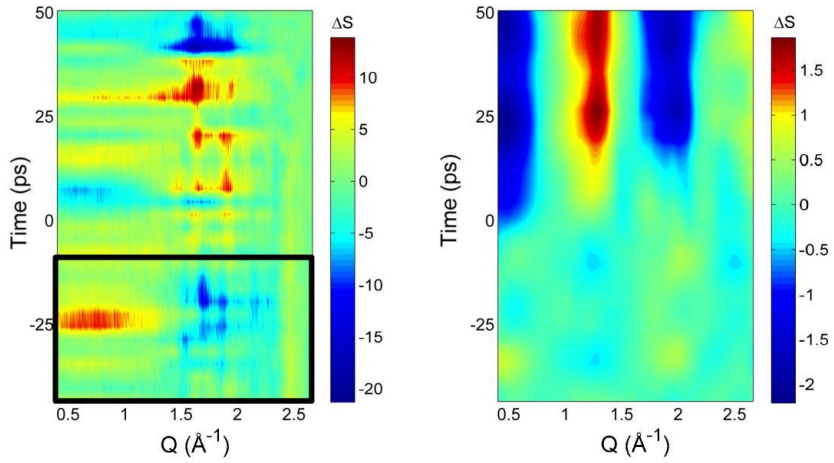

Figure S4: XDS data before (left) and after (right) the SVD-based background-removal procedure. The black box on the left figure shows the subset of data used to construct the SVD components.

For all time delays, the fluctuating background can therefore be accurately described by a sum of five singular vectors such that $\Delta S_{back}(Q,t) = \sum_{i=1-5} \alpha_i(t) \Delta S_i^{SVD}(Q)$, where $\Delta S_i{}^{SVD}(Q) = S_{ii} \cdot U_{ij}$. Observing that this background-removal procedure reduced the subset of data for t < 0 to counting noise validated the use of the SVD-determined descriptor vectors in an unconstrained fit of the $\Delta S(Q,t)$. The implementation of this methodology in the full global-fit analysis is described in the next section.

Sample contributions to XDS-DS

The XDS-DS contains contributions from all the structural changes that occur in the probed sample volume upon laser excitation. It is usually expressed as the sum of 3 terms:

i) The solute term $\Delta S_{solute}(Q,t)$, arising from structural changes in the solute

ii) The solvent term $\Delta S_{solvent}(Q,t)$, arising from structural changes of the bulk solvent

iii) The solute-solvent cross-term, arising from structural changes of the solvent-shell surrounding the solute.

The solute term

This term was estimated from the molecular geometries of the $Ru^{II}={}^{1}Co^{III}$(LS) and $Ru^{III}={}^{4}Co^{II}$(HS) optimized through DFT using the ORCA 2.8 program package (45) with the BP86 (46,47) gradient-corrected (GGA) exchange-correlation functional and Gaussian type TZVP basis set. The coherent scattering of these two structures was then simulated by employing the orientation-averaged Debye equation (the incoherent scattering was discarded since it does not depend on the molecular structure). Figure S5 shows the simulated XDS-DS obtained from subtracting the two patterns.

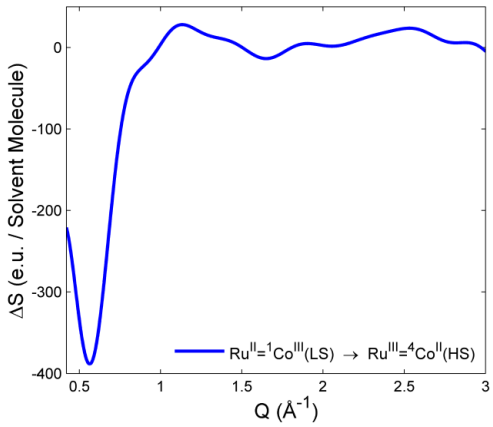

Figure S5: XDS-DS resulting from a $Ru^{II}={}^{1}Co^{III}$(LS) to $Ru^{III}={}^{4}Co^{II}$(HS) conversion.

From these considerations, the solute term was expressed as $\Delta S_{solute}(Q,t)=\gamma(t)\cdot\Delta S_{solute}(Q)$, where *γ(t)* is the time-dependent excitation fraction of $Ru^{III}={}^{4}Co^{II}$(HS).

The solvent term

Assuming the validity of a classical continuum description, the equilibrated state of the solvent can be expressed as a function of two independent hydrodynamical variables chosen as the temperature (T) and the density (ρ). The XDS-DS $\Delta S_{solvent}$ that originates from the bulk-solvent response can be described in terms of their elementary variations $\Delta T(t)$ and $\Delta\rho(t)$. Numerous investigations at synchrotron sources have demonstrated that a first order treatment is adequate to model the response on the hundreds of picoseconds to hundreds of milliseconds time scales. Within this framework the solvent term is quantified through the following linear combination:

$$\Delta S_{solvent}(Q,t) = \Delta T(t) \cdot \left.\frac{\partial S(Q,T)}{\partial T}\right|_{\rho} + \Delta\rho(t) \cdot \left.\frac{\partial S(Q,\rho)}{\partial \rho}\right|_{T}$$

where $\left.\frac{\partial S(Q,T)}{\partial T}\right|_{\rho}$ and $\left.\frac{\partial S(Q,\rho)}{\partial \rho}\right|_{T}$ are the XDS-DS arising from a change in T at constant ρ and from a change in ρ at constant T, respectively. These studies have also shown that $\left.\frac{\partial S(Q,T)}{\partial T}\right|_{\rho}$ and $\left.\frac{\partial S(Q,\rho)}{\partial \rho}\right|_{T}$ can be measured independently, making it possible to extract $\Delta T(t)$ and $\Delta\rho(t)$ directly from the transient $\Delta S_{solvent}$ signals. Simple arguments allow determining the time scales on which the various contributions play a role. Considering first $\Delta\rho(t)$, it has been shown (24) that for times t such that $t < d/v_s$, where d is the FWHM of the laser spot and v_s is the speed of sound in the liquid, no thermal expansion of the solvent has yet taken place. With the present experimental conditions (d =500 μm FWHM and v_s=1280 m/s for MeCN), thermal expansion is expected to happen on the 400 ns time scale, which is beyond the temporal window probed, so that $\Delta S_{solvent}$ reduces to the contribution from impulsive solvent heating :

$$\Delta S_{solvent}(Q,t) = \Delta T(t) \cdot \left.\frac{\partial S(Q)}{\partial T}\right|_{\rho} .$$

The reference XDS-DS $\left.\frac{\partial S(Q)}{\partial T}\right|_{\rho}$ (called the temperature solvent differential (TSD)) was acquired independently during a dedicated study at ID09b, ESRF (25). The data were measured using multilayer optics characterized by a 2.5% bandwidth (bw). Since this is broader than the intrinsic 0.3% bw of the XFEL beam, the influence of the X-ray source spectrum had to be investigated. As a first step, a TSD that would be obtained from a monochromatic beam was constructed from the measurement in (25) shown in Figure S6 (A) (black trace) after standard filtering (red trace). Figure S6 (B) shows the resulting curve after Gaussian deconvolution (blue trace). This "monochromatic" TSD (blue) was convoluted with the 2.5% bw of the multilayer (red) and the intrinsic 0.3% bw of an XFEL beam (green). The three curves are indistinguishable, proving that the ID09b reference can be introduced in the analysis of the XDS-DS from XFEL sources. The convolution of the simulated monochromatic TSD with the full spectrum of the U17 undulator at ID09b ('pink' beam) is included for comparison (black trace).

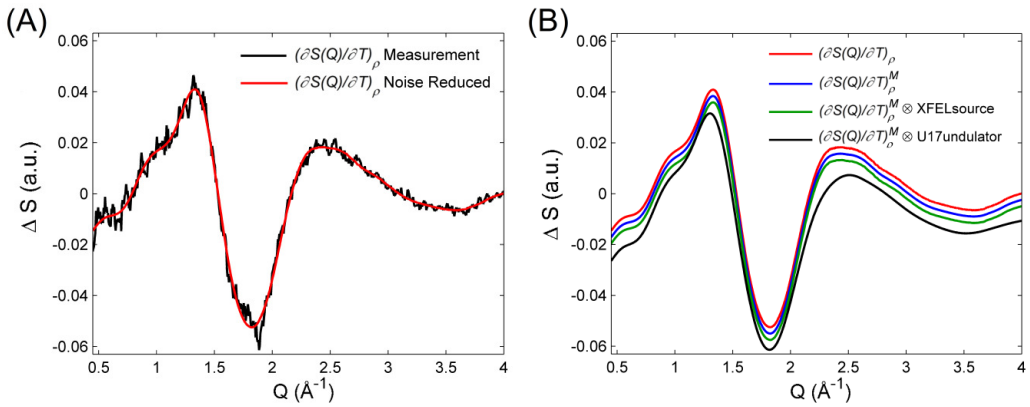

Figure S6: The effect of the X-ray source energy spectrum on the TSD. (A) Experimental TSD obtained at ID09b (black) and noise-reduced profile (red). (B) A "monochromatic" TSD (blue) was obtained by deconvoluting the noise-reduced profile (red) by the energy spectrum of the ID09 multilayer optics. This simulated "monochromatic" curve was then convoluted with the energy spectrum of the XFEL source (green) and with the U17 pink beam at ID09 (black) for comparion.

The XDS-DS from the sample

Summarizing the previous sections, ΔS_{sample} could be expressed as:

$$\Delta S_{sample}(Q,t) = \gamma(t) \cdot \Delta S_{solute}(Q) + \Delta T(t) \cdot \left.\frac{\partial S(Q)}{\partial T}\right|_{\rho},$$

where $\gamma(t)$ is the fraction of charge-separated molecules, $\Delta S_{solute}(Q)$ is the simulated XDS-DS between of Ru^{II}=$^{1}Co^{III}$(LS) and Ru^{III}=$^{4}Co^{II}$(HS), $\Delta T(t)$ is the change in temperature and $\left.\frac{\partial S(Q)}{\partial T}\right|_{\rho}$ is the XDS-DS signal caused by an increase of MeCN temperature at constant density.

Global-fit analysis of the XDS-DS

The XDS-DS $\Delta S(Q,t)$ were expressed as a sum of a background contribution ($\Delta S_{back}(Q,t) = \sum_{i=1-5} \alpha_i(t) \Delta S^i{}_{SVD}(Q)$) and a term $\Delta S_{sample}(Q,t)$ from sample structural changes, both introduced above. For each time delay, the residual function:

$$\Delta S_{res} = \frac{\left(\Delta S_{\cdot}(Q,t) - \Delta S_{sample}(Q,t) - \sum_{i=1-5} \alpha_i(t) \Delta S^i{}_{SVD}(Q) \right)^2}{\sigma^2_{XDS}(Q,t)/(N-p-1)}$$

was minimized. The denominator $\sigma^2_{XDS}(Q,t)/(N-p-1)$ incorporates the point-to-point difference signal noise $\sigma_{XDS}(Q,t)$ (26), as well as the number of data points N, and the number of free parameters p in the fit. As such, ΔS_{res} can be directly interpreted as a χ^2 estimator. This allowed extracting the absolute magnitude of every SVD scaling parameters $\alpha_i(t)$, for each time point. While the average value for two of the $\alpha_i(t)$ parameters changed gradually over the duration of the scan, no systematic evolution was observed around or after t = 0. Explicit inclusion of a

density term $\Delta S_{solvent}$ returned $\Delta\rho(t) \approx 0$ for all time delays recorded. In other words, any XDS-DS from the solute-solvent cross-term was below the detection threshold.

The heat response of the solvent on ultra-short timescales

The solvent term is derived within a classical hydrodynamic framework that assumes a homogeneous temperature distribution (24). Following photoabsorption, homogeneity is reached on a time scale that depends on the distance between excited centers. It ranges from ~ 15 ps to ~350 ps for excited state concentrations of 40 mM and 0.3 mM respectively (24,25). Given the 6 mM * 0.65 = 4 mM concentration of absorbing centers that act as point sources of heat, homogeneity should be restored within ~ 65 ps via thermal diffusion for the experiment presented in this work. On one hand, this shows that the signature of the homogenized temperature distribution has been recorded for the later time points of the covered temporal window. On the other hand, for the earlier times, the influence of these hot spots on $\Delta S_{solvent}(Q,t)$ has to be assessed, and this requires the XDS analysis to enter previously uncharted territory. A detailed treatment is awaiting for QM/MM simulations of heat dissipation in large molecular ensembles (~ 4800 molecules) that can be benchmarked against data exclusively obtainable at XFEL facilities. Such calculations are still challenging computing power since the XDS difference patterns have to be generated from the sampled history for a large number of individual trajectories. Moreover, the simplified model described below establishes that sizing the signature of inhomogeneous thermalization in $\Delta S_{solvent}(Q,t)$ would necessitate higher temporal resolution than the one that could be achieved in these very first experiments. The argument derives from inspection of XDS-DS simulated from a series of Molecular Dynamics (MD) calculations that exhibit the same changes in hydrodynamic parameters as those arising from

impulsive heating. These calculations allow extracting the radial pair distribution functions (RPDF) for acetonitrile shown in figure S7.

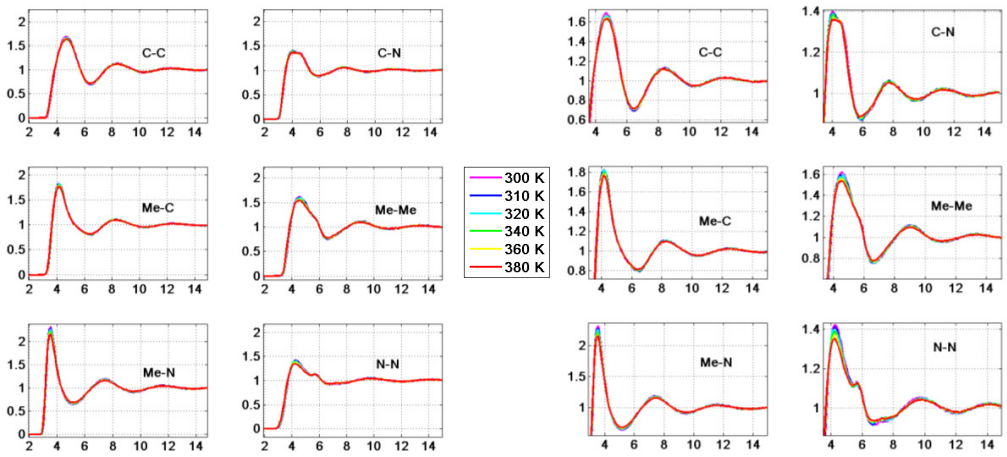

Figure S7: RPDF for the constituent components of acetonitrile.

During the calculation of the XDS-DS from the RPDF generated by the MD simulations (15), a cut-off value is defined. Beyond this distance the RPDF is damped towards to unity and ceases to contribute to the signal. It was found that the difference scattering arising from the calculated scattering curves reproduced the data measured in (25), and were insensitive to the choice of threshold as long as it was larger than 10 Å. This shows that the characteristic length-scale on which a solvent molecule contributes to the solvent XDS-DS is about 10 Å, corresponding to the first two solvation shells. This implies that this distance should be used when estimating the criterion for temperature homogeneity as measured by XDS. From Landau and Lifshitz (48) the time scale on which a volume reaches local homogeneity after an impulse temperature change is given by $\tau = l^2/\chi$ where l is the characteristic distance and χ is the thermometric conductivity of the solvent. A distance l = 10 Å leads a homogenization time of 3.1 ps for MeCN. In conclusion,

the perturbations to the signal caused by an inhomogeneous temperature distribution are negligible on all but the very shortest times.

SM6 Kinetic models for the XES data: concerted versus sequential mechanism

Three different kinetic models of charge and spin dynamics have been tested against the observed XES kinetics:

A) $^1Co^{III} \rightarrow {}^4Co^{II}(HS)$, concerted electron transfer (ET) and spin-state transition (SST) with an overall rate constant $1/\tau_0$, where τ_0 is the lifetime of the reduced bridge as measured with optical transient optical absorption spectroscopy (TOAS).

B) $^1Co^{III} \rightarrow {}^4Co^{II}(HS)$, concerted ET and SST with a free rate constant $1/\tau_1$

C) $^1Co^{III} \rightarrow {}^2Co^{II}(LS) \rightarrow {}^4Co^{II}(HS)$, sequential ET with optical rate constant $1/\tau_0$, matching the decay rate of reduced bridge from TOAS, followed by SST $^2Co^{II}(LS) \rightarrow {}^4Co^{II}(HS)$ with a free rate constant $1/\tau_2$. With an initial excitation fraction of γ_0, the time-dependent concentrations of the transient species for the three models are:

A) $$\left[Co^{II}(HS)\right] = \gamma_0\left(1 - e^{-t/\tau_0}\right)$$

B) $$\left[Co^{II}(HS)\right] = \gamma_0\left(1 - e^{-t/\tau_1}\right)$$

C) $$\left[Co^{II}(LS)\right] = \gamma_0 \frac{\tau_2}{\tau_0 - \tau_2}\left(e^{-t/\tau_0} - e^{-t/\tau_2}\right)$$

$$\left[Co^{II}(HS)\right] = \gamma_0\left(1 - \frac{e^{-t/\tau_0} / \tau_2 - e^{-t/\tau_2} / \tau_0}{1/\tau_2 - 1/\tau_0}\right)$$

The thermally-activated back electron transfer to the ground state was omitted since the lifetime of the charge-separated Ru^{III}=$^4Co^{II}(HS)$ is 40 ns (18), i.e. three orders of magnitude longer than

the temporal window studied in this work. The time evolution of the XES signals was then modelled by convoluting the transient concentrations introduced above with a Gaussian MRF. Taking model A as an example, the resulting kinetics were given by:

$$I(\Delta t) = I(t - t_0) = \gamma_0 \int_{-\infty}^{\infty} \frac{1}{\sigma\sqrt{2\pi}} e^{-y^2/2\sigma^2} H(t - t_0 - y)\left(1 - e^{-(t-t_0-y)/\tau_0}\right) dy$$

where σ is the width of the Gaussian broadening, t_0 is time-zero, γ_0 is the full amplitude of the difference signal and H is the Heaviside step function.

The corrected Akaike Information Criterion (AICc) is then used to compare the relative goodness of the fit weighted by the model complexity (49). Briefly, the AIC is introduced as:

$$AIC = 2k - 2\ln(L)$$

where k is the number of fit parameters and L is the maximized likelihood value of the fit defined as:

$$\ln(L) = c - \frac{1}{2}\sum_{i=1}^{N} \frac{(y_i - f(x_i))^2}{\sigma_i^2} = c - \frac{\chi^2}{2}$$

where N is the number of data points, y_i is the measured value, $f(x_i)$ is the fit-value, σ_i is the standard deviation of the measured values, and c is a constant. It has been shown that, for small data-sets, the bias-corrected AIC value (AICc) should be used for model comparison:

$$AICc = AIC + \frac{2k(k+1)}{n-k-1}$$

The direct relation of the AIC value to the maximized likelihood, entails that it can be directly determined from the reduced χ^2:

$$AIC = \chi^2 + 2k$$

Considering two fitting models (1 and 2) of AICc values $AICc_1$ and $AICc_2$, the probability p that model 1 is the most-likely of the two models is given by:

$$p = \frac{e^{-\Delta_{AICc}/2}}{1 + e^{-\Delta_{AICc}/2}}$$

where $\Delta_{AICc} = AICc_1 - AICc_2$.

The best fit parameters for the 3 models A,B,C introduced above are listed in Table S1, along with their AICc-derived probabilities p_A, p_B and p_C, taking B as reference. Considering these 3 probabilities, there is substantial evidence for rejecting A in favor of B and C. C seems to perform significantly better than B, but outright rejection of B over C would necessitate $p_C > 0.95$. On the basis on the XES kinetics alone, with the reported MRF, this would require an improvement in the signal to noise by more than an order of magnitude.

Model	t_0	γ_0	τ	σ	p
A	2.2	0.66	[0.24 ps]	1.5 ps	0.04
B	-0.35	0.67	1.7 ps	0.55 ps	0.5
C	0.05	0.67	[0.24ps] & 1.9 ps	0.52 ps	0.71

Table S1: Summary of the fitting parameters for models A, B and C.

SM7 Determining the MRF and time-zero

During the measurements in June 2012, when SACLA was starting up, we did not have the opportunity to directly measure the MRF of the liquid jet setup. However, comparison between model A and models B or C, within the AICc-framework explicitly acts as a test for the null-hypothesis that the differences in kinetics between XES and TAOS could be an effect of the XFEL MRF. As seen from Table 1 in SM6, this null-hypothesis can be rejected ($p < 0.05$).

Further testing was conducted by constraining the fitted rate constants ($1/\tau_1$ in B, and $1/\tau_2$ in C) to be lower than or equal to the fitted MRF σ, i.e. by setting $1/\tau_1 = \alpha_1 \cdot \sigma$ and $1/\tau_2 = \alpha_2 \cdot \sigma$ with $0 < \alpha_i < 1$. All other parameters were freely varying. In both cases, this led to significantly worse fits ($p < 0.1$), with α_1 and α_2 both taking the maximum value of 1.

Based on this investigation, the fitted MRF σ determined from B and C is representative of the actual MRF, and time-zero t_0 can be extracted from the XES measurements. Since discriminating between B and C is guided by the comparison with the TAOS trace, the average of the two t_0 from B and C was chosen when quoting the pump-probe delays, and plotting the data.

SM8 Is it possible to detect a $Ru^{III}=^{2}Co^{II}$(LS) intermediate with XDS ?

As shown in SM6, a sequential model involving a $Ru^{III}=^{2}Co^{II}$(LS) intermediate state yields the best fit of the XES-DS kinetics. The question of its detectability through XDS can be answered via a simulation that follows the procedure described in "solute term" subsection of SM5. The calculated XDS-DS for $Ru^{II}=^{1}Co^{III}$(LS) → $Ru^{III}=^{4}Co^{II}$(HS) and $Ru^{II}=^{1}Co^{III}$(LS) → $Ru^{III}=^{2}Co^{II}$(LS) are shown in Figure S8.

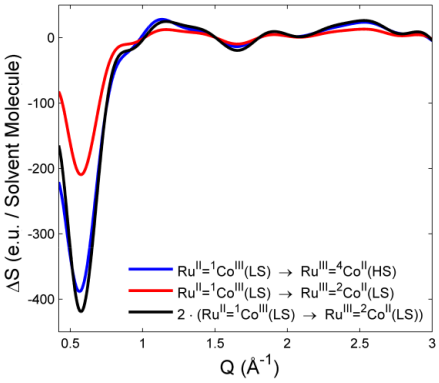

Figure S8: Simulated XDS-DS for $Ru^{II}=^{1}Co^{III}$(LS) → $Ru^{III}=$ $^{4}Co^{II}$(HS) (blue line), for $Ru^{II}=^{1}Co^{III}$(LS) → $Ru^{III}=^{2}Co^{II}$(LS) (red line), and for $Ru^{II}=^{1}Co^{III}$(LS) → $Ru^{III}=^{2}Co^{II}$(LS) multiplied by two to facilitate the comparison (black line).

Their shapes are very similar, with the amplitude of the $^{1}Co^{III}$(LS) → $^{2}Co^{II}$(LS) being approximately half that of the $^{1}Co^{III}$(LS) → $^{4}Co^{II}$(HS) transition. Significant presence of the $^{2}Co^{II}$(LS) species at early times would therefore be manifested in the XDS-DS fits as reduced excitation fraction. Since the fraction of $^{4}Co^{II}$(HS) determined for the 3 ps time-delay is 0.63 ± 0.2 and the final excitation fraction is known to be 0.67 ± 0.04, the presence of $^{2}Co^{II}$(LS) (if any)

must be already very low in the XDS-DS for the first measurement, which is taken at a time delay of 3 ps. This species may become detectable in future combined XES/XDS experiments with better time resolution and higher signal to noise ratio.

Paper V

Direct dynamics studies of a binuclear metal complex in solution: The interplay between vibrational relaxation, coherence decay and solvation effects.

Asmus Ougaard Dohn, Elvar Orn Jonsson, Kasper Skov kjær, **Tim Brandt van driel**, Martin Meedom Nielsen, Karsten Wedel Jacobsen, Niels Engholm Henriksen, and Klaus Braagaard Møller.

Advanced Draft.

Direct dynamics studies of a binuclear metal complex in solution: The interplay between vibrational relaxation, coherence, and solvent effects.

Asmus Ougaard Dohn,[*,†] Elvar Örn Jónsson,[‡] Kasper Skov kjær,[‡] Tim Brandt van Driel,[‡] Martin Meedom Nielsen,[‡] Karsten Wedel Jacobsen,[‡] Niels Engholm Henriksen,[†] and Klaus Braagaard Møller[†]

Department of Chemistry, Technical University of Denmark, Building 207, 2800 Kgs. Lyngby, Denmark, and Department of Physics, Technical University of Denmark, Building 307 2800 Kgs. Lyngby, Denmark

E-mail: asod@kemi.dtu.dk

[*]To whom correspondence should be addressed
[†]DTU Chemistry
[‡]DTU Physics

Abstract

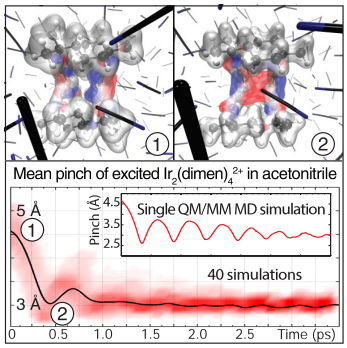

By using a newly implemented QM/MM multiscale MD method to simulate the excited state dynamics of the $Ir_2(dimen)_4^{2+}$ complex, we report on results that support the two experimentally observed coherent dynamical modes in the molecule, but also reveal a third mode, not distinguishable by spectroscopic methods. We directly follow the channels of energy dissipation to the solvent, and report that the main cause for coherence-decay is the initial wide range of configurations in the excited state population. We observe that the solvent can actually extend the coherence lifetime, by decoupling the internal degrees of freedom in the complex.

Introduction

One way of exploring the dynamical nature of chemical reactions has been facilitated through the study of bimetallic d^8-d^8 complexes and their remarkable photochemical properties[1–7], since their first synthesis almost four decades ago[5]. The focus of this work has been on $Ir_2(dimen)_4^{2+}$ (dimen=1,8-diisocyano-*p*-menthane), a type of molecule which has also shown photoconversion functionality for solar energy storage[4].

The electronic configuration of this complex features a σ-antibonding highest occupied molecular orbital (HOMO), while the lowest unoccupied molecular orbital (LUMO) is σ-bonding[1,2]. This causes the complex to undergo large structural changes when photoexcited to the S_1 state with an efficient intersystem crossing to T_1[8], as was experimentally confirmed for the similar $Rh_2(dimen)_4^{2+}$complex in the solid phase using time-resolved x-ray diffraction,

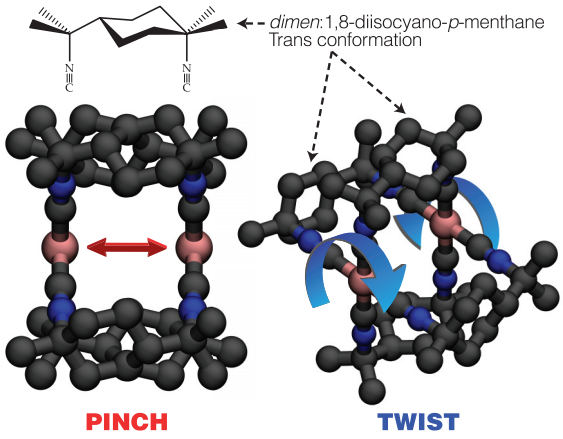

Figure 1: Two of the main dynamic, structural modes of $Ir_2(dimen)_4^{2+}$, here shown without hydrogens for clarity, and in the conformer employed for these studies. The 1,8-diisocyano-*p*-menthane (dimen) ligand provides the optimal compromise between flexibility and rigidity for large, but controllable structural changes e.g. by electronic excitation. Electronically exciting this complex promotes an electron from the antibonding HOMO to the bonding LUMO, effectively forming a chemical bond between the Ir atoms[1–3].

showing a shortening of the metal-metal distance of 0.86 Å[9]. Our group observed a contraction of the Ir variant in solution by 1.4 Å,[10] using ∼100 ps pulsed synchrotron radiation. We have recently gathered data on this system at the Linac Coherent Light Source (LCLS), to directly probe the coherent motion with x-ray methods, utilizing the higher temporal resolution of x-ray free electron lasers, compared to synchrotron radiation. Analysis is ongoing. Hartsock *et al.*[3] has carried out transient spectroscopy measurements on the $Ir_2(dimen)_4^{2+}$ complex, observing excited state (ES) vibrational wavepackets. These are assigned to the previously mentioned contraction on S_1, and also a twist of the metal planes in the complex (see fig. 1). Furthermore, the study reports a deformational isomerism which effectively splits the ground state (GS) population in two main structures. This has previously been observed[6], and is supported by computationally by constrained mappings of the GS energy landscapes[11]. However, to our knowledge, no attempts (including our own) to freely relax the geometry of the molecule into the short conformer has proved successful, when using DFT methods.

With this work, we aim to expand on the pre-existing knowledge about the system using our newly developed QM/MM Born-Oppenheimer MD (QM/MM BOMD) method[12] to obtain an adiabatic version of the vibrational motion in the single molecule. By utilizing the efficiency of the code, we mimic the coherent motion by exciting a host of different GS configurations and analyse the mean properties of these dynamic trajectories, and their relation to individual excitations. By benchmarking these results against experiments, we obtain information not experimentally distinguishable, such as possible dynamics of spectroscopically dark or obscured modes, direct observation of intra- and intermolecular energy transfer and solvent interactions. Since the electronic structure of the QM part is calculated "on the fly", and no full potential energy surfaces are calculated (or needed) in this direct-dynamics method, we focus on simulating the structural dynamics upon excitation of a population of solvated $Ir_2(dimen)_4^{2+}$ from the long GS conformer.

Methodology

The Direct-Dynamics simulations were carried out utilizing the Atomic Simulation Environment (ASE)[13] to interface the QM and MM subsystems. The Grid-based Projector-Augmented Wave Method (GPAW)[14] is used for the QM description. The full details of the method and its interfacing strategy is described elsewhere.[12] The quantum system comprised of the $Ir_2(dimen)_4^{2+}$ complex is described using DFT with the PBE functional.[15] It was placed in a classically pre-thermalized simulation box of 28x28.5x31.5 Å containing acetonitrile at 0.786 g/cm^3. After removal of acetonitrile molecules overlapping with the complex, the total number of classically described acetonitriles was 237. The entire system was then thermalized again, until the temperature was stable at 300 K, as set by the Langevin thermostat applied to the solvent only. For the production run, 18.21 ps of GS trajectory was sampled using 2 fs timesteps.

We simply approximate the experimental excitation by instantaneously promoting a com-

prehensive representation of the GS configuration space to the ES, neglecting effects from finite pulse-widths and bandwidths of real excitation sources (The effect the bandwidth is examined in the SI). The ultrafast ES dynamics take place on S_1, but since similar binuclear d^8-d^8 complexes have previously been shown to have the same triplet and singlet surface shapes, only differing in energy,[16,17] it is possible to carry out T_1 simulations mimicking the S_1 dynamics. Thus, the computational cost is kept within the feasible range for systems of this size by staying within the GS DFT framework on T_1 . This approximation is implied for all the excitations simulated in this work.

Fig 2 shows a GS trajectory from which 40 configurations are promoted to the ES, for a total of 140 ps ES trajectories sampled. The sampling was spaced such as to minimize the correlation between each of the excited state trajectories, while also allowing for comparison of excitations from complexes of similar starting geometries, but with different solvent configurations, and excitations from different starting geometries. The thermostat was turned completely off for these runs. The ES timestep was 1 fs, to allow better resolution and minimize the drift. The maximum observed drift in any of the simulations was 0.40 kJ/mol per atom in the system, over the entire simulation duration.

Results and discussion

The simulations clearly show the Ir-Ir pinch and the dihedral twist (see fig. 3, and videos in SI online), but they reveal more: The ligands expand and contract along the N-C-Ir-C-N directions in the complex. This is best described by plotting the mean of the distances between each carbon in the ligand rings and the one on the opposing side of the entire complex at each time step t. In the following analysis we have incorporated this "breathing mode", and show that it plays an important role in the overall dynamics of this system. The GS trajectory does not exhibit any significant activations of this mode.

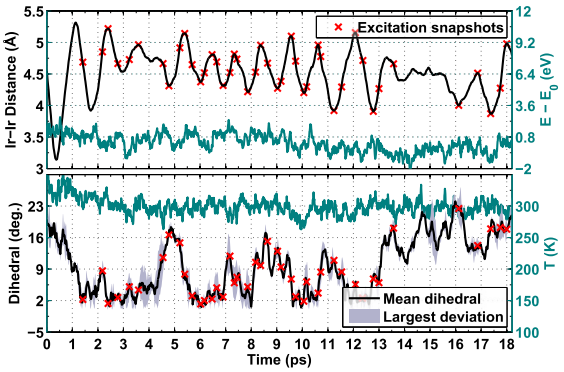

Figure 2: Two of the main structural modes in $Ir_2(dimen)_4^{2+}$ plotted for the GS trajectory. Top: The Ir-Ir distance. Bottom: The dihedral angle. The teal graphs show the total energy difference during the run (where E_0 is the total energy at the start of the production run) and temperature in the top and bottom graph, respectively. The ES runs were started from the configurations marked with red crosses.

Fig. 3 shows how the pinch and twist modes evolve in time, following excitation, and how they relate to the newly discovered breathing mode. The mean Ir-Ir distance in the population when measured over the last ps of the simulation is 2.98 Å, which is in very good agreement with previous experimental results from x-ray scattering[10] of 2.90 Å, given the incomplete basis and the exchange-correlation functional used for the QM part. The second inset in the top figure shows that the pinching motion is limited to the center part of the molecule, affecting the next two atoms adjacent to Ir, but not the outermost parts of the ligands. The mean values of the entire population show oscillatory features, meaning that the motion of each trajectory is in phase with the others, thus showing signs of coherent motion. The excited population loses its mean pinch oscillation amplitude almost before completing a full period, but if the first oscillation period is calculated by doubling the time from the first well to the first top, the period is ∼480 fs, or ∼70 cm^{-1}. In the work by Hartsock *et al.*[3], an observed transient absorption feature with a frequency of 75 cm^{-1} is assigned to the pinching motion, differing only 7 % from the result presented here.

The anharmonicity of the underlying potential, reflected in the direct dynamics, is evident

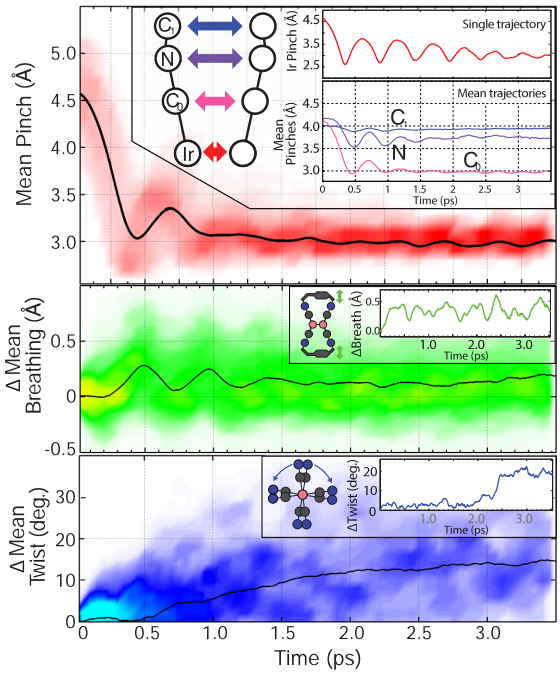

Figure 3: The mean Ir-Ir pinching (top),breathing (middle), and twisting (bottom) as a function of time after excitation. The twist is defined as the change in dihedral angle from the moment of excitation $t = 0$. The shaded background show the binned counts of values from all the trajectories. The bin sizes are 50 fs by 0.1 Å, 0.05 Å, and 2 degrees for the pinching, breathing and twisting, respectively. This population looses its pinch phase within a picosecond, while the single trajectory-pinch oscillation dies out much slower, as can be seen on the top inset. However, the mean phase of the breathing mode is sustained for almost 2 ps. The pinching- and breathing modes share the same oscillation period.
The next inset on the top graph show that the pinch is also affecting the adjacent atoms, but not the ligand ends. The last insets show the breathing and twisting of the same single trajectory as the top inset.

from the oscillation in the single trajectory (top inset in fig. 3): It reflects a steeper potential for the short distances, and gentler slope for the long ones. The oscillation becomes more sinusoidal with time, as the trajectory moves closer to the harmonic approximation limit, deeper in the potential. Similarly, the frequency increases as the molecule dissipates its excess vibrational energy, which is also observed for the single trajectory. This is equivalent to anharmonic potentials with Morse-like characteristics. Therefore, it is also expected that the first oscillation period of the population should be somewhat longer than the experimental result, since the latter is first measured at times $t \geq 0.5$ ps after excitation. Also consistent with experimental results[3], little to no coherent twist oscillation is observed from excitations that start from the long, eclipsed conformation. However, a delayed twist mechanism is observed for the mean motion, with the molecule starting to twist after roughly 500 fs. The simulation coherence decay is faster than the experimental, if only the pinch is taken into account. However, the breathing mode is coherent for almost 1.5 ps. Furthermore, the frequency of the pinching and breathing is similar: The period from the first to the second top is ∼450 fs, or ∼74 cm^{-1}, only 1.3 % slower than the experimental pinch. The first breathing maximum arrives 0.5 ps after excitation, where the experimental fit also starts from[3].

The causes of coherence decay can be either statistical of dynamical in nature, i.e. either a result of the difference in initial configurations from which the system is brought up to the excited state or of (stochastic) energy dissipation in each molecule, either through the solvent or through internal degrees of freedom. Examinations of the individual trajectories (fig. 3, top inset) reveal that vibrational relaxation is much slower than the population mean coherence decay, and not very stochastic in nature. Hence, the fast coherence decay of the population mean must originate from the wide range of initial GS configurations. This is supported by a thorough population-partitioning analysis (see SI for details), which shows that exciting a narrow, phase coherent distribution of GS configurations extends the coherence time on the excited state significantly. Our analysis also shows that introduction of

an effective bandwidth in making the ES population, similar to the one of the experimental excitation source[3], leads to a somewhat longer excited-state coherence time, although there is no strong correlation between the GS metal-metal vibrational amplitude/phase and the excitation energy.

In order to further understand the effect of the solvent on $Ir_2(dimen)_4^{2+}$ dynamics, fig. 4 compares the pinch of the single trajectory from the inset of fig. 3 to a group of additional simulations that have progressively more gas-phase character (from bottom to top in the figure). The first noticeable feature is the large intramolecular vibrational energy redistribution (IVR) in the pure gas phase simulation, which is evidently the *only* possible channel for energy dissipation in that system. In this case, the excess vibrational energy is efficiently transferred to the breathing mode, since there is no solvation-cage effects, as seen in fig. 5.

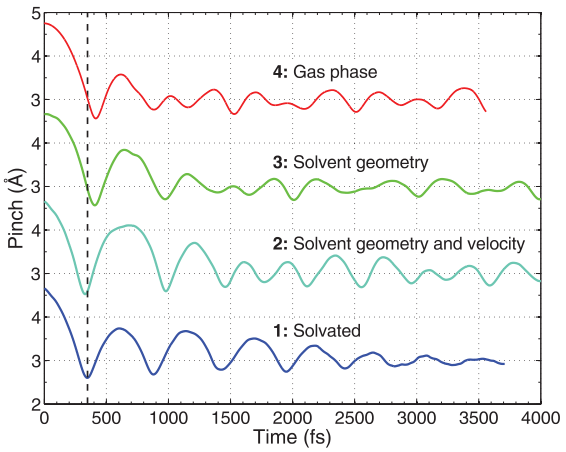

Figure 4: In order to investigate the role of the solvent in the dynamics, three other ES trajectories were also simulated, and shown here, together with a single trajectory from the main production run. **1:** The pinch of the fully solvated complex. **2:** A simulation where the solvent was removed at the time of excitation, but keeping the initial geometry influenced by the solvent, *and* the velocity of the atoms in the complex. **3:** A simulation where only the geometry is kept, while the initial velocities are set to zero. **4:** An excitation started from the gas phase structure of the complex.

Returning to fig. 4, the original trajectory (**1**) was excited from a GS phase space area of already contracting metal atoms, which explains why the first contraction of the metal

atoms in simulations **1** and **2** is faster than in **3** and **4**. The fastest pinch is observed in trajectory **2**, meaning that the solvent interaction of the solvated system must dampen the pinching motion. The second expansion is also shorter in **1**, which is again a cage-effect of the solvent. All in all, for the trajectory of the solvated system, the solvent cage actually facilitates the *extension* of the lifetime of the coherent motion, through decoupling of the internal degrees of freedom in the complex. The flexible dimen ligand can be argued to be

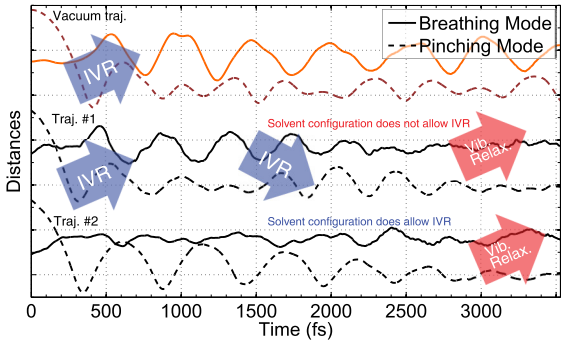

Figure 5: Comparison of the breathing mode in the gas phase trajectory (red) and two trajectories of solvated systems, displaying the energy transfer mechanisms in the system. The two solvate-included trajectories are started from similar GS conditions, but 10 ps apart, so the two accompanying solvent configurations are uncorrelated. The breathing mode amplitude is large compared to the other trajectories, since there is no dampening from the solvent.

the cause of the large amount of IVR observed, delayed by ∼150 fs since the metals atoms need to contract before a coupling of the two modes is made. Since the breathing motion can be heavily dampened by the solvent cage, it can be expected that the main channel of external vibrational dissipation of energy to the solvent is through the ligands. This is further supported by the comparison in fig. 5: In trajectory 2, the solvent configuration does not allow for IVR to the breathing mode, so the excess excitation energy is contained in the pinch, the motion of which is almost free of small perturbations stemming from electrostatic interactions with the solvent. In the first trajectory, the pinch energy is redistributed almost completely to the breathing mode within 1.5 ps, where solvent-induced interactions perturb the oscillation. Some of the remaining energy is then again transferred back into the pinch

before dissipating further. All in all, this means that vibrational relaxation of $Ir_2(dimen)_4^{2+}$ through the solvent can only occur in substantial quantities if the energy is efficiently redistributed into the ligand breathing mode.

That the coherence decay is faster than vibrational cooling is in contrast with the findings of van der Veen *et al.*[16] for the bimetallic d^8-d^8 complex $[Pt_2(P_2O_5H_2)_4]^{4-}$ in various solvents, where the authors observe that coherence decay occurs on the same time scale as vibrational cooling. While the two complexes are different, and different solvents are used (including protic solvents), they both have coordination sites along the metal atom axis, which could facilitate significant electrostatic- and dispersion interactions with the solvent. Nevertheless, the main difference causing the contrasting results is most likely due to the different rigidities of the two distinct ligand types, where the more flexible dimen ligand allows for a wider range of configurations in the GS ensemble. We emphasize that here, the variation of the GS metal-metal distance (fig. 2) is comparable to the amplitude of the excited state vibration (fig. 3).

Both the $Ir_2(dimen)_4^{2+}$ and $[Pt_2(P_2O_5H_2)_4]^{4-}$ experiments represent the formation of a chemical bond in a "scaffolded diatomic". Recently, we have investigated the solvent-induced the bond formation in a true diatomic molecule: The ground-state recombination of I_2, following photo-induced dissociation[18]. In this system, we observed the same behaviour as for $Ir_2(dimen)_4^{2+}$: The coherence decay is much faster than vibrational cooling. However, since I_2 is bound in the ground state, the original GS distribution is very narrow, compared to amplitude of the motion following photo excitation, and it is therefore not a source of decoherence. The cause of I_2 decoherence is still statistical: It is due to the direct interaction with its solvent cage, which lacks in both the order and rigidity compared to the molecular scaffold of the bi-metallic complexes.

Conclusions

In conclusion, this work demonstrates that the implementation using GPAW for the QM description in this multiscale method is capable of producing out-of-equilibrium molecular dynamics with statistical quantities that make it possible to obtain information on the mean dynamics of populations. The experimental Ir-Ir dynamics is reproduced. We observed a, to our knowledge, not previously discovered breathing mode that stays coherent for longer, and helps explain how the energy is transferred to the solvent. We note that the role of the solvent can actually be to *maintain* the coherence, through decoupling of the internal degrees of freedom in the molecule. By looking at the shapes of the individual trajectories, we have argued that the major electrostatic solute-solvent interaction occurs through the ligands for this complex, and that the IVR here is delayed, since the metals need to contract first. At last, the breathing occurs in the ligands, and perpendicular to the pinch axis. As such, the (rigidity of the) ligands play an important role in the complex, both through defining the width of the GS ensemble, which affects the ES population coherence, and as mediators of the solvent interaction.

Acknowledgement

The authors thank Robert W. Hartsock, Kelly Gaffney, & the Center for Molecular Movies for discussion and feedback.
This work was funded by the Lundbeck Foundation.

Supporting Information Available

This material is available free of charge via the Internet at `http://pubs.acs.org/`.

References

(1) Mann, K. R.; Gordon, J. G. I.; Gray, H. B. Characterization of oligomers of tetrakis(phenyl isocyanide)rhodium(I) in acetonitrile solution. *Journal of the American Chemical Society* **1975**, *97*, 3553–3555.

(2) Roundhill, M. D.; Gray, H. B.; Che, C. Pyrophosphito-bridged diplatinum chemistry. *Accounts of Chemical Research* **1989**, *22*, 55–61.

(3) Hartsock, R. W.; Zhang, W.; Hill, M. G.; Sabat, B.; Gaffney, K. J. Characterizing the deformational isomers of bimetallic $Ir_2(dimen)_4^{2+}$ (dimen= 1,8-diisocyno-*p*-menthane) with vibrational wavepacket dynamics. *Journal of Physical Chemistry A* **2011**, *115*, 2920.

(4) Mann, K. R.; Lewis, N. S.; Miskowski, V. M.; Erwin, D. K.; Hammond, G. S.; Gray, H. B. Solar-energy storage - production of hydrogen by 546-nm irradiation of a dinuclear Rhodium(ii) complex in acidic aqueous-solution. *Journal of the American Chemical Society* **1977**, *99*, 5525–5526.

(5) Lewis, N. S.; Mann, K. R.; Gordon, J. G.; Gray, H. B. Oligomerization and 2-center oxidative addition-reactions of a dimeric Rhodium(II) complex. *Journal of the American Chemical Society* **1976**, *98*, 7461–7463.

(6) Exstrom, C. L.; Britton, D.; Mann, K. R. Structures of $[M_2(dimen)_4](Y)_2$ (M = Rh, Ir; dimen = 1,8-Diisocyanomenthane; Y = PF6, Tetrakis[3,5-bis(trifluoromethyl)phenyl]borate, $B(C_6H_5)_4$) crystals featuring an exceptionally wide range of metal-metal distances and dihedral twist angles. *Inorganic Chemistry* **1996**, *35*, 549–550.

(7) Harvey, P. D.; Murtaza, Z. Properties of Pd(i)-Pd(i) Bonds - Theoretical and Spectroscopic Study of Pd2(dmb)2x2 Complexes (Dmb = 1,8-Diisocyano-P-Menthane, X = Cl,br). *Inorganic chemistry* **1993**, *32*, 4721–4729.

(8) Miskowski, V. M.; Rice, S. F.; Gray, H. B. Spectroscopy and Photophysics of $Rh_2(dimen)_4^{2+}$ (dimen = 1,8-Diisocyanomenthane). Exceptional Metal-Metal Bond Shortening in the Lowest Electronic Excited States. *Inorganic Chemistry* **1994**, *33*, 2799–2807.

(9) Coppens, P.; Gerlits, O.; Vorontsov, I. I.; Kovalevsky, A.; Chen, Y.; Graber, T.; Gembicky, M.; Novozhilova, I. A very large Rh-Rh bond shortening on excitation of the $[Rh_2$ (1,8-diisocyano-*p*-mentane$)_4]^{2+}$ ion by time-resolved synchrotron X-ray diffraction. *Chemical Communications* **2004**, *19*, 2144–2145.

(10) Haldrup, K.; Harlang, T.; Christensen, M.; Dohn, A.; van Driel, T. B.; Kjær, K. S.; Harrit, N.; Vibenholt, J.; Guerin, L.; Wulff, M. et al. Bond shortening (1.4 Å) in the singlet and triplet excited states of $[Ir_2(dimen)_4]^{2+}$ in solution determined by time-resolved x- ray scattering. *Inorganic Chemistry* **2011**, *50*, 9329.

(11) Hunter, B. M.; Villahermosa, R. M.; Exstrom, C. L.; Hill, M. G.; Mann, K. R.; Gray, H. B. M-M Bond-stretching energy landscapes for $M_2(dimen)_4^{2+}$ (M = Rh, Ir; dimen = 1,8-Diisocyanomenthane) complexes. *Inorganic Chemistry* **2012**, *51*, 6898–6905.

(12) Jónsson, E. O.; Dohn, A. O.; Ulstrup, J.; Thygesen, K. S.; Jacobsen, K. W. An efficient QMMM scheme to explore electron transfer reactions in solution. *to be submitted* **2014**,

(13) Bahn, S. R.; Jacobsen, K. W. An object-oriented scripting interface to a legacy electronic structure code. *Computing in Science & Engineering* **2002**, *4*, 55.

(14) Mortensen, J. J.; Hansen, L. B.; Jacobsen, K. W. Real-space grid implementation of the projector augmented wave method. *Physical Review B* **2005**, *71*, 035109.

(15) Perdew, J. P.; Burke, K.; Ernzerhof, M. Generalized gradient approximation made simple. *Phys. Rev. Lett.* **1996**, *77*, 3865–3868.

(16) van der Veen, R. M.; Cannizzo, A.; van Mourik, F.; Vlcek, A. J.; Chergui, M. Vibrational relaxation and intersystem crossing of binuclear metal complexes in solution. *Journal of the American Chemical Society* **2011**, *113*, 305.

(17) Stiegman, A. E.; Rice, S. F.; Gray, H. B.; Miskowski, V. M. Electronic spectroscopy of d^8-d^8 diplatinum complexes. $^1A_{2u}(d\sigma^* \rightarrow p\sigma)$, $^3E_u(d_{xz}, d_{yz} \rightarrow p\sigma)$, and $^{3,1}B_{2u}(d\sigma^* \rightarrow d_{x^2-y^2}$ excited states of $Pt_2(P_2O_5H_2)_2^{4-}$. *Inorganic Chemistry* **1987**, *26*, 1112.

(18) lee, J. H.; Wulff, M.; Bratos, S.; Petersen, J.; Guerin, L.; Leicknam, J. C.; Cammarata, M.; Kong, Q.; Kim, J.; Møller, K. B. et al. Filming the birth of molecules and accompanying solvent rearrangement. *Journal of the American Chemical Society* **2013**, *135*, 3255–3261.

Direct dynamics studies of a binuclear metal complex in solution: The interplay between vibrational relaxation, coherence, and solvent effects. Supporting Info

Asmus Ougaard Dohn,[*,†] Elvar Örn Jónsson,[‡] Kasper Skov kjær,[‡] Tim Brandt van Driel,[‡] Martin Meedom Nielsen,[‡] Karsten Wedel Jacobsen,[‡] Niels Engholm Henriksen,[†] and Klaus Braagaard Møller[†]

Department of Chemistry, Technical University of Denmark, Building 207, 2800 Kgs. Lyngby, Denmark, and Department of Physics, Technical University of Denmark, Building 307 2800 Kgs. Lyngby, Denmark

E-mail: asod@kemi.dtu.dk

[*]To whom correspondence should be addressed
[†]DTU Chemistry
[‡]DTU Physics

Computational Details

The QM/MM MD simulations were made using the QM/MM Scheme presented in[1], which interfaces the two regions through the total energy of the system:

$$E_{\mathrm{tot}} = E_{\mathrm{QM}} + E_{\mathrm{MM}} + E_{\mathrm{QM/MM}} \tag{1}$$

where the three terms represent the energy of the QM subsystem, the MM subsystem and their interaction energy, respectively. The interaction energy consists of a Coulomb term between the electronic density and the classical point charges, a Coulomb term between the nuclei in the QM subsystem and the MM point charges, and a Lennard-Jones (LJ) term:

$$E_{\mathrm{QM/MM}} = \sum_{i}^{N_{\mathrm{MM}}} q_i \int \frac{n(\mathbf{r})}{|\mathbf{r} - \mathbf{R}_i|} d\mathbf{r} + \sum_{i}^{N_{\mathrm{MM}}} \sum_{\alpha}^{N_{\mathrm{QM}}} \frac{q_i Z_\alpha}{|\mathbf{R}_\alpha - \mathbf{R}_i|} + E_{\mathrm{LJ}} \tag{2}$$

$$E_{\mathrm{LJ}} = \sum_{i}^{N_{\mathrm{MM}}} \sum_{\alpha}^{N_{\mathrm{QM}}} 4\epsilon_{i\alpha} \left[\left(\frac{\sigma_{i\alpha}}{|\mathbf{R}_\alpha - \mathbf{R}_i|} \right)^{12} - \left(\frac{\sigma_{i\alpha}}{|\mathbf{R}_\alpha - \mathbf{R}_i|} \right)^{6} \right] \tag{3}$$

The LJ parameters are combined using the Waldman-Hagler rule.[2]

The first term in eqn. 1 is evaluated with density functional theory (DFT), using the grid-based projector augmented wave method, implemented in the GPAW package,[3] which is modified so that the total effective potential also contains a term from the MM subsystem. The calculations were performed with a localised atomic orbital basis in combination with the real space grid, allowing for high parallelisation as well as fast diagonalization of the principal matrices.

Preliminary Tests

Preliminary calculations showed that a simulation box with 4 Å of vacuum padding in each dimension was enough to fully eliminate effects from truncating the wave functions, so the cell size for each simulation (both GS and ES) was chosen thusly. Test geometry

calculations were performed in vacuum, and the results are shown in fig. 1. The max Ir-Ir

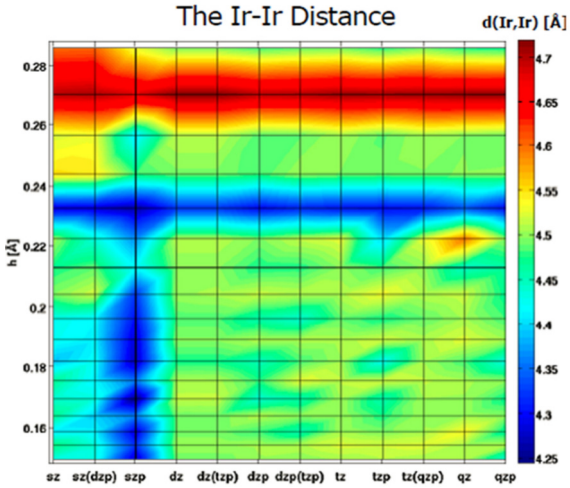

Figure 1: Convergence of the main structural parameter of the complex - the Ir-Ir distance - with respect to the real space grid spacing h, and size of basis set. A stable value for the distance is maintained when employing values of $h < 0.22$ Å with basis sets of at least double-zeta size. The convergence criteria for each individual relaxation was a maximum force of 0.05 eV / Å on any of the atoms in the system.

distance difference in the grid spacing region $0.15 \leq h \leq 0.21$ is less than 3.5 % of the largest distance, so instead of fixing the grid spacing to a definite value, it was possible to speed up the simulation even further by keeping the number of grid points to values divisible by eight, i.e. (112,120,112) for the (x,y,z) dimensions. Since the overall size of the molecule varies for each of the initial GS configurations used in the the ES simulations, so does the QM cell, resulting in grid spacings $0.1571 \leq h \leq 0.1931$, well within the converged region shown in fig. 1. The basis set used was of tzp quality for Ir and dzp for the rest of the molecule. The chosen PBE vacuum description overshoots the Ir-Ir distance (as does the mean QM/MM value), when compared to the experimental value of the solvated complex:[4] 4.3 Å. Crystalline values range from 3.601 Å to 4.414 Å, depending on the type of counter ion.[5]

The Acetonitrile solvent

Since the predominantly used solvent for $Ir_2(dimen)_4^{2+}$ is Acetonitrile (ACN), a classical, rigid, 3-point interaction potential was adapted from Guardia *et al.*[6] A simulation box of 28x28.5x31.5 Å was filled with 290 ACN molecules and thermalized. An MM production run of 0.5 ns was used to obtain radial distribution functions (RDFs). In order to also confirm a proper QM/MM interfacing, RDFs between a single QM ACN and the remaining MM ACNs were produced, and compared to RDFs obtained only using MM MD. Parallel QM/MM runs with a single QM ACN were branched off the production MM trajectory, insterspaced by 500 fs, to avoid any correlation between the new trajectories (see the velocity autocorrelation function inset on fig. 2). A Langevin-type thermostat was used in both the MM and QM/MM runs, with a friction coefficient of 0.05 and 2 fs timesteps. The hydrogens on the QM were constrained using the RATTLE scheme.[7] Each QM/MM trajectory was thermalized again, before sampling the RDFs. A total of 0.5 ns and 0.25 ns of dynamics were sampled for the MM and QM/MM systems, respectively. There is generally a good agreement between the various descriptions. The literature RDFs[6] have been produced in the NPT ensemble, which might be the cause of some of the small differences. Furthermore, the electronic structure description used to create the force field is not the same as the one used in the QM/MM simulations, and the force field is not optimized to work in a QM/MM framework.

Further ES population analysis

In principle, an instantaneous excitation corresponds to an infinite bandwidth. However, a more realistic representation of an experiment can be obtained by including an effective, finite bandwidth[8]. This can be included by estimating the effective bandwidth of our range of ES simulations in fig. 3, and compare the pinch oscillation from different, relevant subsets with similar sampling statistics of the entire ES population in fig. 4, to elucidate how this affects the coherence lifetime.

The simplest way to approximate the excitation energy is simply to subtract a single point

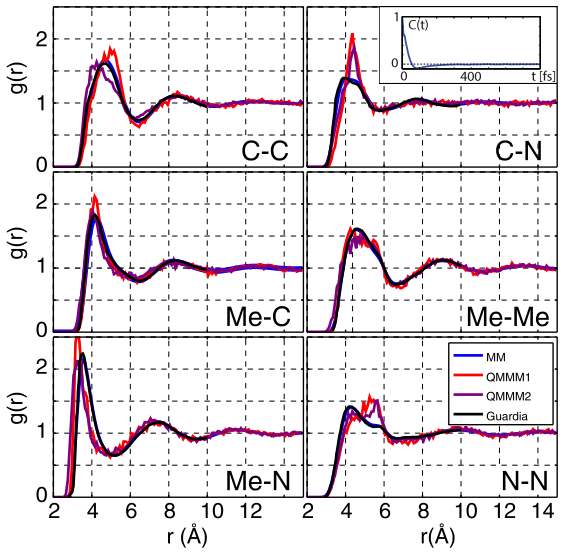

Figure 2: Radial distribution functions (RDFs) of the 6 intermolecular distances of ACN. The RDFs are calculated every 500th fs in trajectories of 0.5 ns and 0.25 ns for the MM and QM/MM systems, respectively. The QM/MM systems are comprised of a single QM ACN in a bath of MM ACN. The QM/MM1 systems are made using methyl-group vdW parameters for the middle Carbon, while QM/MM2 uses aliphatic parameters. There is overall a good agreement between the various description.

energy calculation of the system in T_1 from a single point energy calculation in the S_0. This is of course a very rough approximation within the chosen theoretical framework. Since the T_1 surface is believed to have a similar shape to the S_1, but lower in energy[9,10], utilizing ground state DFT on T_1 can be expected to introduce the error in the energy giving the largest deviation, and give too low excitation energies. The bandwidth, obtained from looking at the excitation energies of all the excitations, should not be as sensitive to this approximation, since the error introduced should be the same for each of the excitations. Since the 40 excitation configurations were specifically chosen to cover as much of the GS phase space as possible, an extrapolation to the excitation energies of each step in the entire GS trajectory is made, although no clear linear correlation between the Ir-Ir distance and excitation energy is observed. The complex is known to have an absorption maximum

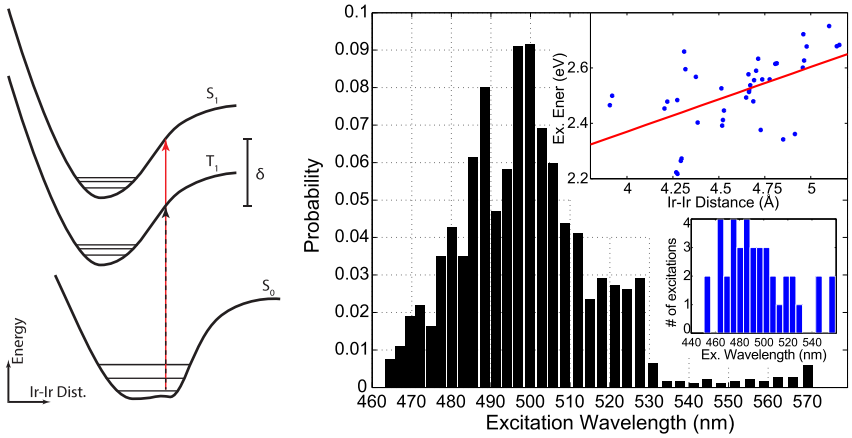

Figure 3: **Left:** Franck-Condon diagram sketching how the experimental excitation is approximated in the simulations, with δ being the error made from exciting to T_1 instead of S_1. **Right:** Approximation of the effective bandwidth used in creating the excited state population. The excitation energy is approximated by subtracting the single point energy of each initial GS configuration from a single point calculation of its ES spin configuration counterpart. The lower inset shows histogram of these energies, converted to wavelengths, and how many times they appear in the ES population. This is extrapolated to the entire GS trajectory, under the (crude) assumption that the excitation energy is linearly dependent on (and only on) the Ir-Ir distance, shown in the top inset. This relation is then used for obtaining the results shown in the main figure.

assigned to the long and eclipsed conformer at 475 nm[11], so it is expected due to the lower

T_1 energy that the simulated excitation peak (fig. 3, left) is located at lower energies. The experimental bandwith is 18.77 nm, and excitation wavelength is 477 nm[11]. The total effective bandwidth of the ES production run simulations can be seen from the figure to be at least 100 nm, or 5 times the experimental bandwidth. Fig. 4 shows the Ir-Ir pinch in four

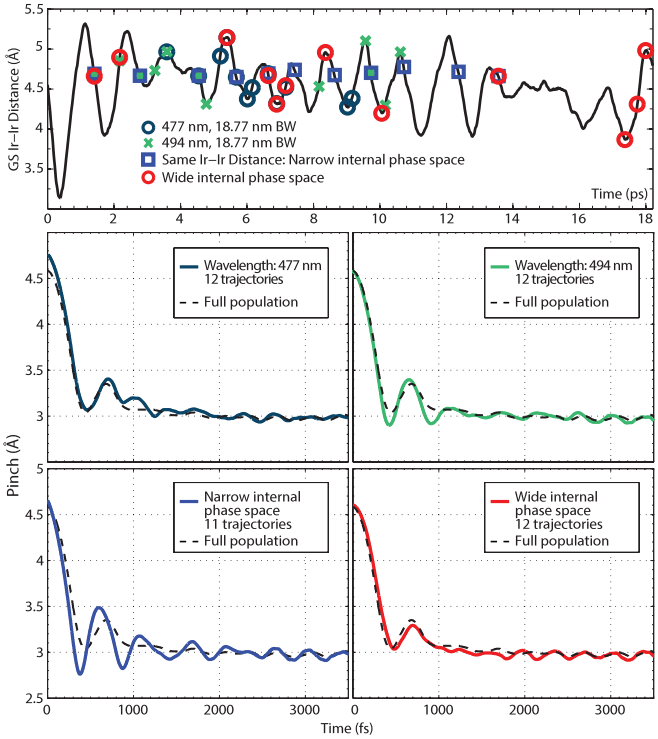

Figure 4: Splitting up the total ES population with respect to excitation energies, or by grouping initial configurations. The top two ES pinch graphs are made from selecting for ES trajectories with excitation energies assumed close to the experimental value and bandwidth. The bottom left subset is made from a narrow internal phase space of initial Ir-Ir distances. The last graph shows the dynamics of a wide phase space, but with the same statistics as the other three subsets.

subsets of the entire phase space of the ES population. The top two are subsets of excitations with energies corresponding to wavelengths of 477 nm and 494 nm, respectively. The first having the same value as in the experiment, and the second is lower in energy to account for the error made in simulating the excitation energies. The bottom left subset is chosen to have the most narrow internal phase space possible, with identical initial Ir-Ir distances,

but different solvent configurations. The last plot shows the pinch in a wide internal phase space, but with similar sampling statistics, allowing for comparison of the four subsets.
As demonstrated in the lower right graph in 4, it is possible to obtain the same coherence-decay time using 12 trajectories as 40, which again means that any changes in coherence time in the other subsets are not simply due to worse statistics. Concentrating on the 477 nm and 494 nm excitation, the coherent pinch amplitude is observed to decay slightly slower than for the full population. Thus, the effective bandwidth in the simulation has, to some extent, an influence on the resulting coherent motion. Therefore, the incoherence in the initial ensemble is the main factor for the coherence decay of the ES population. This result is underpinned by the lower left graph, where the very narrow internal phase space greatly increases the coherence lifetime. This result is not surprising, since the GS pinch oscillation has a similar amplitude as the ES pinch.

References

(1) Jónsson, E. O.; Dohn, A. O.; Ulstrup, J.; Thygesen, K. S.; Jacobsen, K. W. An efficient QMMM scheme to explore electron transfer reactions in solution. *to be submitted* **2014**,

(2) Waldman, M.; Hagler, A. New combining rules for rare gas van der waals parameters. *Journal of Computational Chemistry* **2004**, *14*, 1077.

(3) Mortensen, J.; Hansen, L.; Jacobsen, K. W. Real-space grid implementation of the projector augmented wave method). *Physical Review B* **2005**, *71*, 035109.

(4) Haldrup, K.; Harlang, T.; Christensen, M.; Dohn, A.; van Driel, T. B.; Kjær, K. S.; Harrit, N.; Vibenholt, J.; Guerin, L.; Wulff, M. et al. Bond shortening (1.4 Å) in the singlet and triplet excited states of $[Ir_2(dimen)_4]^{2+}$ in solution determined by time-resolved x- ray scattering. *Inorganic Chemistry* **2011**, *50*, 9329.

(5) Extrom, C. L.; Britton, D.; Mann, K. R. Structures of $[M_2(dimen)_4](Y)_2$ (M = Rh, Ir; dimen = 1,8-diisocyanomenthane; Y = PF_6, Tetrakis[3,5-bis(trifluoromethyl)phenyl]borate, $B(C_6H_5)_4$) crystals featuring an exceptionally wide range of metal-metal distances and dihedral twist angles. *Inorganic Chemistry* **1996**, *35*, 549.

(6) Guardia, E.; Pinzón, R.; Casulleras, J.; Orozco, M.; Luque, F. J. Comparison of different three.site interaction potentials for liquid acetonitrile. *Molecular Simulation* **2001**, *26*, 287.

(7) Andersen, H. C. Rattle: A "velocity" version of the shake algorithm for molecular dynamics calculations. *Journal of Computational Physics* **1983**, *52*.

(8) Petersen, J.; Henriksen, N. E.; Møller, K. B. Validity of the BersohnZewail model beyond justification. *Chemical Physics Letters* **2012**, *539-540*, 234–238.

(9) van der Veen, R. M.; Cannizzo, A.; van Mourik, F.; Vlcek, A. J.; Chergui, M. Vibrational relaxation and intersystem crossing of binuclear metal complexes in solution. *Journal of the American Chemical Society* **2011**, *113*, 305.

(10) Stiegman, A. E.; Rice, S. F.; Gray, H. B.; Miskowski, V. M. Electronic spectroscopy of d^8-d^8 diplatinum complexes. $^1A_{2u}(d\sigma^* \rightarrow p\sigma)$, $^3E_u(d_{xz}, d_{yz} \rightarrow p\sigma)$, and $^{3,1}B_{2u}(d\sigma^* \rightarrow d_{x^2-y^2}$ excited states of $Pt_2(P_2O_5H_2)_2^{4-}$. *Inorganic Chemistry* **1987**, *26*, 1112.

(11) Hartsock, R. W.; Zhang, W.; Hill, M. G.; Sabat, B.; Gaffney, K. J. Characterizing the deformational isomers of bimetallic $Ir_2(dimen)_4^{2+}$ (dimen= 1,8-diisocyno-*p*-menthane) with vibrational wavepacket dynamics. *Journal of Physical Chemistry A* **2011**, *115*, 2920.

Paper VI

Experimental and theoretical investigation of the photoinduced high-spin state of the $[Fe(terpy)_2]^{2+}$ complex.

Amélie Bordage, Kristoffer Haldrup, Pieter Glatzel, Andreas Galler,Wojciech Gawelda, Gilles Doumy, Anne Marie March, Elliot P. Kanter, Asmus Dohn, **Tim B. van Driel**, Kasper S. Kjær, Klaus B. Møller, Henrik T. Lemke, Erik Gallo, Mauro Rovezzi, Mátyás Pápai, Zoltán Németh, Tamás Rozgonyi,Delphine Cabaret, Amélie Juhin, Jens Uhlig, Villy Sundström, Martin M. Nielsen, Stephen Southworth, Linda Young, Christian Bressler and György Vankó.

Advanced Draft.

The photoinduced high-spin state of the $[Fe(terpy)_2]^{2+}$ complex revealed by a time-resolved multitechnique investigation

Amélie Bordage,[*,†,] Kristoffer Haldrup,[‡] Pieter Glatzel,[¶] Andreas Galler,[§] Wojciech Gawelda,[§] Gilles Doumy,[‖] Anne Marie March,[‖] Elliot P. Kanter,[‖] Asmus Dohn,[⊥] Tim B. van Driel,[‡] Kasper S. Kjær,[‡,#] Klaus B. Møller,[⊥] Henrik T. Lemke,[@] Erik Gallo,[¶] Mauro Rovezzi,[¶] Mátyás Pápai,[†] Zoltán Németh,[†] Tamás Rozgonyi,[△] Delphine Cabaret,[▽] Amélie Juhin,[▽] Jens Uhlig,[#] Villy Sundström,[#] Martin M. Nielsen,[‡] Stephen Southworth,[‖] Linda Young,[‖] Christian Bressler,[§] and György Vankó[†]

Wigner Research Centre for Physics, Hungarian Academy Sciences, H-1525 Budapest, P.O.B. 49., Hungary, Centre for Molecular Movies, Technical University of Denmark, Department of Physics, DK-2800, LKgs. yngby, Denmark, European Synchrotron Radiation Facility (ESRF), 6 Rue Jules Horowitz, BP220, 38043 Grenoble Cedex 9, France, European XFEL, Albert-Einstein Ring 19, D-22761 Hamburg, Germany, X-ray Science Division, Advanced Photon Source, Argonne National Laboratory, 9700 S. Cass Ave., Argonne, Illinois 60439, USA, Centre for Molecular Movies, Technical University of Denmark, Department of Chemistry, DK-2800, LKgs. yngby, Denmark, Dept. of Chemical Physics, Lund University, Box 124, 22100 Lund, Sweden, SLAC National Accelerator Laboratory, Linac Coherent Light Source, Menlo Park, California 94025, USA, Institute of Materials and Environmental Chemistry, Research Centre for Natural Sciences, Hungarian Academy of Sciences, H-1025 Budapest, Pusztaszeri ut 59-67, Hungary, and Université Pierre et Marie Curie, IMPMC, UMR CNRS 7590, 4 plave Jussieu, 75252 Paris Cedex 05, France

E-mail: amelie.bordage@u-psud.fr

Abstract

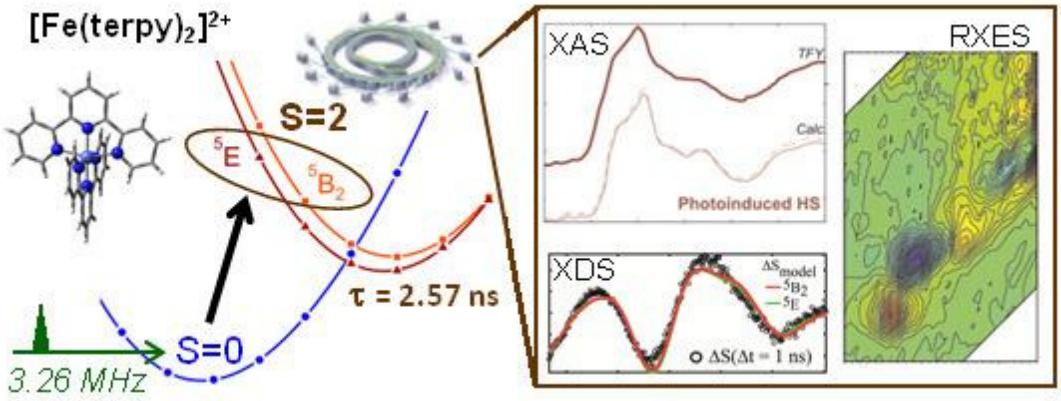

Figure 1: TOC figure

Introduction

Switchable molecular compounds have significant potential as very high-density devices in the areas of data storage systems, molecular switching and display devices. Promising can-

*To whom correspondence should be addressed

†Wigner Research Centre for Physics, Hungarian Academy Sciences, H-1525 Budapest, P.O.B. 49., Hungary

‡Centre for Molecular Movies, Technical University of Denmark, Department of Physics, DK-2800, LKgs. yngby, Denmark

¶European Synchrotron Radiation Facility (ESRF), 6 Rue Jules Horowitz, BP220, 38043 Grenoble Cedex 9, France

§European XFEL, Albert-Einstein Ring 19, D-22761 Hamburg, Germany

‖X-ray Science Division, Advanced Photon Source, Argonne National Laboratory, 9700 S. Cass Ave., Argonne, Illinois 60439, USA

⊥Centre for Molecular Movies, Technical University of Denmark, Department of Chemistry, DK-2800, LKgs. yngby, Denmark

#Dept. of Chemical Physics, Lund University, Box 124, 22100 Lund, Sweden

@SLAC National Accelerator Laboratory, Linac Coherent Light Source, Menlo Park, California 94025, USA

△Institute of Materials and Environmental Chemistry, Research Centre for Natural Sciences, Hungarian Academy of Sciences, H-1025 Budapest, Pusztaszeri ut 59-67, Hungary

▽Université Pierre et Marie Curie, IMPMC, UMR CNRS 7590, 4 plave Jussieu, 75252 Paris Cedex 05, France

Present address: Université Paris-Sud, ICMMO UMR 8182, Equipe de Chimie Inorganique, 91405 Orsay, France

didates are transition metal compounds, in particular octahedral Fe(II) complexes, which can be either in a low-spin (LS) or high-spin (HS) state, depending on parameters such as temperature or pressure.[1] Light[2,3] and X-rays[4–6] can also induce a spin transition in many ferrous compounds, where the resulting HS state can often be stabilized under certain conditions. In octahedral Fe(II) compounds, the spin-state transition occurs from the $^1A_1$ LS ground state to the $^5T_2$ HS state, leading to a spin momentum change of $\Delta S = 2$. Hauser and co-workers suggested a rather simple and apparently complete theoretical framework that for a long time prevailed in explaining the full dynamics of the system.[7–9] This theory describes the transitions along a single configurational coordinate (SCC), typically the breathing mode of the molecule (*i.e.* a symmetric stretch along the Fe-ligand bonds). It was shown to be valid for all complexes with monodentate and bidentate ligands, for instance the $[Fe(bipy)_3]^{2+}$ complex (Fig. 2a). This complex was characterized by a wide range of experimental and theoretical techniques,[10–21] and its photoinduced HS state was shown to be accompanied by a 0.2 Å elongation along the Fe–N bonds.[13,15,17] It was also demonstrated experimentally, using both ultrafast optical and X-rays spectroscopies, that its photocycle upon excitation follows a $^1A_1 \rightarrow {}^1$MLCT $\rightarrow {}^3$MLCT (Metal-to-Ligand Charge Transfer) $\rightarrow {}^5T_2$ sequence.[11,22]

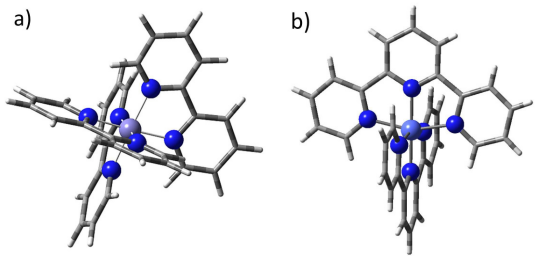

Figure 2: Structure of the $[Fe(bipy)_3]^{2+}$ and $[Fe(terpy)_2]^{2+}$ complexes

The LS↔HS transition, however, cannot be described along a single configuration coordinate for systems with more complex ligands such as the $[Fe(terpy)_2]^{2+}$ system (Fig. 2b),[17] which has two tridentate ligands. The differences with mono- and bidentate ligands are reflected in the longer lifetime of the photoinduced HS state measured in solution[17,23,24] and

also at low temperatures in certain cristalline matrices.[17,25] Only few theoretical attempts to address these anomalies of the HS structure were carried out so far.[17,21] The first Density Functional Theory (DFT)-based study by Hauser and co-workers showed that in the [Fe(terpy)$_2$]$^{2+}$ system, two HS states are created by the removal of the threefold degeneracy of the $t_{2g}(O_h)$ electron orbitals by the axial distortion, corresponding to a different filling of the t_{2g} orbitals d_{xy}, d_{xz} and d_{yz} . These two states, ^{5}B$_2$ and ^{5}E, are not only close in energy but their predicted molecular geometries are also very similar: the corresponding average Fe–N bond length differs about 0.02 Å only, and the angle between the three N atoms of a ligand ($\widehat{NNN}$ angle) differs less than 1°.[17] A more recent DFT investigation by Pápai and co-workers confirm the conclusions of Hauser *et al.*,[17] but they also demonstrated that the most stable structure (^{5}E and ^{5}B$_2$) depends on the particular functional used for the DFT calculations.[21] In order to decipher the energy ordering of the HS ^{5}E and ^{5}B$_2$ states, Pápai and co-workers performed additional multiconfigurational second-order perturbation theory (CASPT2) calculations, which method has proven to yield accurate spin-state energetics of several Fe(II) complexes.[26–29] Starting from the DFT-optimized geometries, the potential energy curves for the LS state and the two HS states were determined : the energy is represented as a function of a combined coordinate that changes both the R(Fe–N$_{ax}$) distance and the ligand distorsion (as measured by the $\widehat{NNN}$ angle). From these results presented in Fig. 3, they thus demonstrated that the electronic difference between the LS state (^{1}A$_1$) and the lowest HS state (^{5}E) is $\Delta E^{\mathrm{el}}_{\mathrm{HS-LS}}$=730 meV, the ^{5}B$_2$ quintet state being higher by 42 meV than the ^{5}E one. However, and despite a recent X-ray Absorption Spectroscopy (XAS) experiment that also concluded that there are more than one Fe–N distance and could give a first estimation of the individual bond lengths,[23] conclusive experimental data validating this hypothesis and these structures are still lacking.

We present in this paper a deep investigation of the [Fe(terpy)$_2$]$^{2+}$ system, aimed at characterizing the photoinduced HS state of [Fe(terpy)$_2$]$^{2+}$ from the LS→HS transition, lifetime, electronic and molecular structure aspects. A combination of experimental X-ray

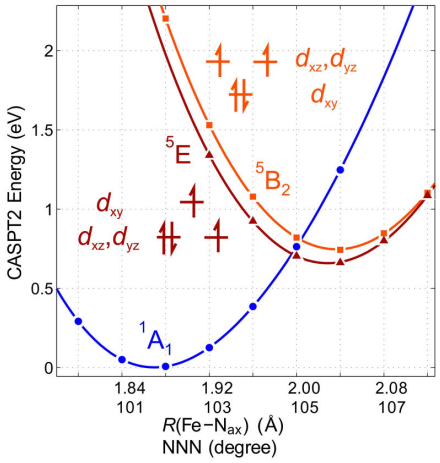

Figure 3: CASPT2 potential potential curves of the LS (^{1}A$_1$) and the two possible HS (^{5}E and ^{5}B$_2$) states of $[Fe(terpy)_2]^{2+}$, extracted from the potential energy surface of Ref. 21. The electronic structure of the corresponding states is schematically represented by the filling of the t_{2g} (d_{xy}, d_{xz} and d_{yz}) orbitals.

tools was used in order to gain a direct access to the most relevant observables characterizing the photoinduced HS state. Using an optical pump/X-ray probe setup with MHz repetition rates, we combined four experimental techniques in a setup that enables highly efficient use of the hard X-ray probe on the 80-100 picosecond time scale:[19,20] X-ray Absorption Near-Edge Structure (XANES) spectroscopy, non-resonant X-ray Emission Spectroscopy (XES), Resonant X-Ray Emission Spectroscopy (RXES; *aka* Resonant Inelastic X-ray Scattering, RIXS) and X-ray Diffuse Scattering (XDS) at the Fe K-edge. Time-resolved techniques based on XDS and XAS have been available for more than a decade, and on the 100 ps time scale both can be considered as mature techniques.[12,30–32] However, application of XES and RXES as tools for time-resolved studies has only recently been started,[19,20] primarily because of the intrinsically low cross-section and the required wavelength-dispersive setups, making them very photon-hungry techniques. The interpretation of XANES spectra is theoretically supported by first-principles calculations. In the case of RXES, support comes from both the determination of the theoretical RXES planes using ligand field multiplet calculations[33–40] and the comparison with the experimental planes of the $[Fe(bipy)_3]^{2+}$ complex, which is a

well-characterized complex.[10,11,14,15,19,22]

After the description of the experimental setup and the theoretical methods used to interpret the experimental data, we present first the characterization of the LS→HS transition by XAS and XES, including the determination of the lifetime of the photoinduced HS state. Then the photoinduced state is characterized in details from both an experimental and theoretical point of view, using XDS, XAS and RXES. For clarity, we use the following nomenclature for the different states : the LS ground state is called *LS state* or *ground state*, the *photoinduced HS state* corresponds the pure HS excited state (that is not fully reached during the experiment), and finally the *laser-pumped* state is the state reached with the laser ON, which has both LS and HS contributions.

Experimental and computational methods

Experimental details

Optical pump/X-ray probe studies with MHz repetition rates were carried out with a setup that combines a crystal spectrometer, a gated area detector and a silicon drift diode. This allows for a simultaneous acquisition of (i) the High-Energy Resolution Fluorescence-Detected and the Total Fluorescence Yield XAS (HERFD-XAS[41] and TFY-XAS) or XES spectrum or RXES plane and (ii) XDS data. This experimental setup with such a high (MHz) repetition rate was successfully implemented for the first time in a study of the [Fe(bipy)$_3$]$^{2+}$ complex.[19,20] In the case of RXES, both the energy of the incident X-ray beam (Ω) and the fluorescence energy (ω) are scanned, and the intensity of the signal is then plotted as a 2D map, one axis being the incident energy (Ω) and the second the transfer energy (Ω-ω).[34] Here the $1s2p$-RXES planes of [Fe(terpy)$_2$]$^{2+}$ and [Fe(bipy)$_3$]$^{2+}$ were recorded over the energy range of the K absorption pre-edge (7110–7120 eV) and the Kα_1 line (6403.84 eV) emission.

The measurements on a 13 mM aqueous solution of [Fe(terpy)$_2$]$^{2+}$ were performed at beamline 7-ID-D of the Advanced Photon Source (APS, Argonne, USA). The capabilities of

7-ID-D beamline for MHz pump-probe experiments and fast shot-to-shot data acquisition were previously described in details in Refs. 19,20,42. The XANES spectra were recorded at the Fe K-edge (7112 eV) both in the TFY and HERFD detection modes; one spherically bent (R=1m) crystal Ge analyzers (100 mm diameter) was used. The XES and XDS data were acquired with a 8200 keV incident monochromatic beam. The repetition rate of the X-ray bunch was 6.52 MHz, and the laser repetition rate 3.26 MHz. The rest of the relevant parameters for the measurements on the $[Fe(terpy)_2]^{2+}$ system are given in Ref. 19.

The RXES planes on a 10 mM solution of $[Fe(bipy)_3]^{2+}$ were acquired on the ID26 beamline[43] of the European Synchrotron Radiation Facility (ESRF, Grenoble, France) using the MHz laser of the FXE beamline of the European X-ray Free Electron Laser (Hamburg, Germany). The repetition rate of the X-ray bunch was 5.68 MHz, and the laser repetition rate 1.42 MHz. The experiments were performed in the 16-bunch mode with the ring current between 90 and 60 mA. A Si(111) double crystal monochromator was used to select the incident energy; X-ray and laser beam size on the sample were 100 x 600 μm^2 (vertical x horizontal). Four (one) spherically bent (R=1 m) crystal Ge analyzers (100 mm diameter) were used. The X-ray detector was an avalanche photodiode (Si with thickness 0.1 mm and 10×10 mm^2 surface area).

Theoretical methods

As input for the simulation of the XDS data and for the calculations of XANES, we use theoretical structural models for the LS and HS states of $[Fe(terpy)_2]^{2+}$ of Ref.[21] These theoretical models results from a DFT calculations performed using the BP86 functional and TZVP basis set, using the ADF 2010.02 program.[44] Details of the structural optimization are given Ref. 21, and the main structural parameters are recalled in table 1:the axial (middle) and equatorial (side) Fe–N bond lengths, and the $\widehat{NNN}$ angle of the terpy ligands.

A first-principles approach based on DFT in the generalized gradient approximation (GGA) was adopted to model the X-ray absorption spectra.[46] The Fe K-edge X-ray absorp-

Table 1: Relevant geometry parameters of the different states of [Fe(terpy)$_2$]$^{2+}$. The experimental data are taken from Ref. 45.

	LS (^{1}A$_1$)		HS (^{5}E)	HS (^{5}B$_2$)
	Exp.[45]	Calc.[21]	Calc.[21]	Calc.[21]
R(Fe–N$_{ax}$)	1.892 Å	1.8859 Å	2.1032 Å	2.1588 Å
R(Fe–N$_{eq}$)	1.988 Å	1.9853 Å	2.1985 Å	2.1866 Å
NNN	102.7°	102.62°	108.35°	107.24°

tion spectrum is calculated in two steps: first the charge-density with a $1s$ core-hole on the absorbing atom is computed and the XANES spectrum is then calculated in the electric dipole ($1s \rightarrow p$), using the broadening parameters given in Ref. 47. These two steps are respectively performed with the PWscf[48] and XSpectra[49] packages of the Quantum-Espresso suite of codes.[50] These codes use a plane-wave basis set and periodic boundary conditions. Therefore the [Fe(terpy)$_2$]$^{2+}$ molecule was included in a cubic cell large enough to avoid interactions between molecules belonging to neighboring cells.[51,52] A 110 Ry cutoff energy was used for the plane-wave expansion, the charge-density with a core-hole on the iron atom was determined at the Γ point and a 2×2×2 (resp. 3×3×3) Monkhorst-Pack grid was chosen for the calculation of the XAS spectrum of the LS ground (resp. photoinduced HS) state. Spin-polarized calculations were performed in the case of the photoinduced HS state (S=2). Norm-conserving pseudopotentials[53] in the Kleinman-Bylander[54] form were used, and the parameters for their generation are given in Ref.[52]

The absorption cross-section of RXES is given by the Kramers-Heisenberg equation[34] and can be simulated using multiplet calculations based on the Ligand Field Multiplet (LFM) theory.[34,55] The $1s2p$-RXES process for [Fe(terpy)$_2$]$^{2+}$ is modeled assuming electric quadrupole transitions from the initial state $1s^2 2p^6 3d^6$ to the intermediate state $1s^1 2p^6 3d^7$, followed by an electric dipole emission to the final state $1s^2 2p^5 3d^7$. The individual absorption and emission transition matrix elements are first calculated using the method developed by Thole,[56] in the framework established by Cowan[57] and Butler,[58] and then combined in a post-processing step. Details about these calculations can be found in Refs. 35,40,55 and 36. The calculations were performed in the approximate octahedral approximation (D_{4h} symmetry),

with a crystal field parameter 10Dq=??? eV for the LS state and ??? eV for the HS state; the transition lines were then convoluted using a Gaussian, accounting for the experimental broadening (??? eV) and a Lorentzian, accounting for the core-hole lifetime broadening (??? for the intermediate state and ??? eV for the final state). The Slater integrals that describe the electronic interactions were scaled down to ??% of their atomic values.

Results and discussion

The low-spin → high-spin transition

In order to characterize the LS→HS transition, XAS and XES spectra of an aqueous solution of $[Fe(terpy)_2]^{2+}$ were taken before and 80 ps after light-excitation. The HERFD-XANES spectra (Fig. 4a) show significant light-induced variations: the B feature intensity increases while the D feature intensity decreases. These changes are similar to those observed for the $[Fe(bipy)_3]^{2+}$ complex,[11,15,19] thus confirming the formation of the photoinduced HS state in this molecular system too. In the case of the XES spectra (Fig. 4b,c), independent of the emission line ($K\alpha$ or $K\beta$), the spectral changes associated with the formation of the photoinduced HS state are obvious and fully consistent with previous studies.[18–20,59] Indeed, from LS to HS states, the intensity of the $K\alpha$ spectral features decreases, and in the case of the $K\beta$ ones, the intensity of the main feature decreases while its energy slightly increases, and a peak rises up around 7045 eV. It is apparent that these variations of both the $K\alpha$ and the $K\beta$ spectra are essentially identical to those of the $[Fe(bipy)_3]^{2+}$ complex:[19] the XES line shapes of $3d$ transition metal ions reflect practically only the spin state; the first coordination shell of Fe in both complexes are distorted octahedra, and the XES spectra are not sensitive to the other relevant differences in symmetry.

The laser ON XAS and XES spectra (Fig. 4, red line) represent the laser-pumped state of the $[Fe(terpy)_2]^{2+}$ complex, which is a combination of both LS and HS contributions. Therefore, to infer the photoinduced HS fraction (γ), we used the spectral differences from LS

and HS references, referred to as the Integrated Absolute Difference (IAD) approach.[19,20,59] The typical photoinduced HS fraction observed during our experiments at 80 ps delay is found to be γ=40%.

The lifetime of the high-spin photoinduced state

The formation and decay of the photoinduced HS state can be characterized by monitoring for different time delays (Δt) the intensity of the spectral features showing the largest variations with the spin transition or the photoexcited fraction (γ). Therefore XAS and XDS data were collected for different time delays between the laser pump and the X-ray probe. To extract the lifetime of the photoinduced HS state, the time evolution of the intensity or the photoexcited fraction is fitted by an expression derived from a Gaussian broadening of an exponential decay and taking into account the photoexcitation fraction, the pulse width (both given by the experimental conditions) and the lifetime of the photoinduced HS state; the general expression is given in equation 1 from Ref. 19. This method was already successfully used to extract the lifetime of the [Fe(bipy)$_3$]$^{2+}$ complex in aqueous solution, using XAS, XES and XDS data.[19]

For the [Fe(terpy)$_2$]$^{2+}$ complex, in the XANES spectrum (Fig. 4a), the B feature at 7125 eV presents the largest variations at the spin transition and therefore was taken to determine the lifetime of the complex; its time evolution is displayed in Fig. 5. The corresponding fit of the kinetics for the B feature results in a photoinduced HS-state lifetime of $\tau_{XAS} = 2.57 \pm 0.07$ ns. In the case of the XDS data, the intensity of the photo-excited fraction (γ) was considered to extract the lifetime of the photoinduced HS state. Fitting γ to an exponential function in analogy with the fit of the XAS signal described above, we find τ_{XDS} = 2.70$\pm$1.50 ns, which is in good agreement with the XAS-derived value; the larger uncertainty arises from the fact that a more important data treatment is required to interpret XDS measurements compared to XAS. These values τ_{XAS} and τ_{XDS} for the lifetime of the [Fe(terpy)$_2$]$^{2+}$ photoinduced HS state are fully consistent with the lifetime of

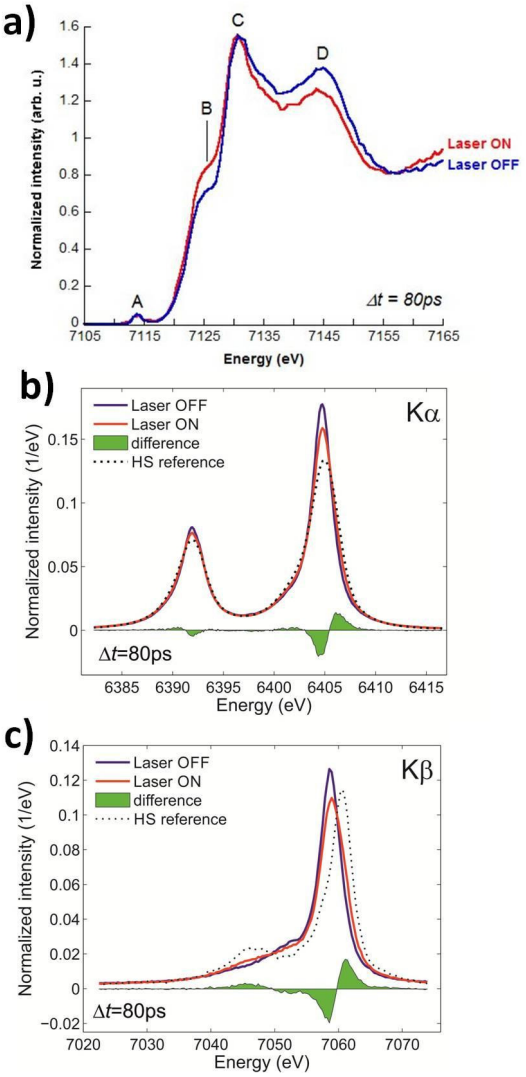

Figure 4: Fe K-edge HERFD-XANES, $K\alpha$ **(b)** and $K\beta$ **(c)** X-ray emisison spectra of a 13mM aqueous solution of $[Fe(terpy)_2]^{2+}$, with (red line) and without (blue line) laser excitation, with a time delay Δt=80 ps for the laser-pumped data. The evolution of the intensity of the B and D features, as well as the changes in the emission lines, are the signature of a change from the LS to HS configuration. The photoinduced HS fraction can be determined from XES by comparing the spectra to LS/HS references, and was found to be γ= 40 % . The HS spectrum (dotted line) could be reconstructed by a linear combination of the LS and laser-pumped spectra, weighted by the experimental photoinduced HS fraction.

τ_{opt} =2.54±0.13 ns previously measured by laser flash-photolysis techniques.[24]

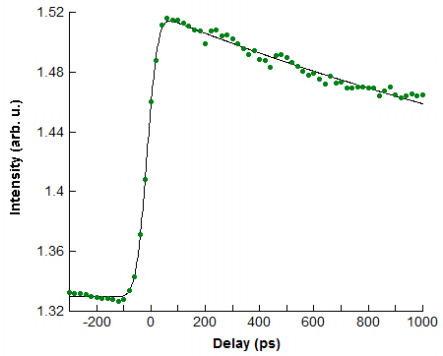

Figure 5: Time scan on the intensity of the 7125 eV (B) feature of the [Fe(terpy)$_2$]$^{2+}$ XANES spectrum (Fig. 4a). The fit with Eq. 1 of Ref.[19] results in a lifetime of τ_{XAS} = 2.57±0.07 ns.

As already observed for the [Fe(bipy)$_3$]$^{2+}$ complex,[19] this consistency of the photoinduced HS state lifetimes extracted from different experimental methods demonstrates the strength of combining these techniques to characterize the dynamics of the complex, as well as the reliability of these methods, given the very good agreement with the lifetime extracted from optical measurements.[24]

Characterization of the photoinduced high-spin state

XDS investigation of [Fe(terpy)$_2$]$^{2+}$

Fig. 6a shows the difference signals ($\Delta S(Q, \Delta t)$) acquired at 6 time delays from Δt = 100 ps to Δt = 25 ns. Qualitatively, the characteristic negative feature around Q = 0.5-1 Å^{-1} corresponds to the immediate (on the 100 ps time scale) appearance of the bond-elongated HS structure and the oscillatory feature around Q=2.2 Å^{-1} arises from temperature (T) and density (ρ) changes in the bulk solvent, as described in detail in Refs. 19for the [Fe(bipy)$_3$]$^{2+}$ complex and 32 for the PtPOP complex. Fig. 6b shows the experimental signal $\Delta S(Q, \Delta t$ = 1 ns) as well as two simulated signals $\Delta S_{Sim} = \gamma * \Delta S_{Solute+Cage} + \Delta T * \Delta S_{\Delta T} + \Delta\rho * \Delta S_{\Delta\rho}$, where γ is the photo-excitation fraction and $\Delta S_{Solute+Cage}$ has been calculated for each of the two proposed HS structures ^{5}E and ^{5}B$_2$. The $\Delta T * \Delta S_{\Delta T}$ and $\Delta\rho * \Delta S_{\Delta\rho}$ parameters

describe the changes in scattering due to bulk-solvent heating and density changes, respectively, and are determined in a separate experiment.[60,61] Fig. 6c displays each of these three contributions to the model difference signal at Δt=1 ns, where the magnitude of the individual contributions are comparable. Separate fits were carried out for each time delay and for both putative HS states, yielding essentially similar results; the time evolution of the magnitude of the photoexcited fraction for the ^{5}E state is visible in the insert of Fig. 6a and discussed in the next section. The time evolution of ΔT and $\Delta\rho$ in general follow what was observed in the analysis of $Fe(bpy)_3$,[19] although the density increase is somewhat smaller in magnitude in the present case ($\sim$ 0.1 kg.m^{-3} vs. $\sim$ 0.4 kg.m^{-3}) and not fully resolvable in the present analysis. The temperature increase is also observed to be lower ($\sim$ 0.3°C vs. $\sim$ 0.6°C), in agreement with the lower concentration of excited-state solutes depositing energy to the solvent through the non-radiative decay processes. Finally, it is evident from Fig. 6b that the expected difference signals from the two putative structures are very similar and that they fit the acquired data almost equally well.

EXAFS spectroscopy

If we add the exafs but with no winning structure, it would come here.

Theoretical and experimental XANES spectroscopy

The XANES spectra were modeled using the optimized structures for the LS and HS states from Ref. 21. The resulting theoretical spectra are compared to those measured for the LS and laser-pumped (Δt=80 ps) states in Fig. 7, where the experimental XANES spectra recorded in both the TFY and HERFD (taken at the maximum of the Kα_1 peak) modes are shown. The improved resolution of the HERFD-XANES spectrum is explained in SI.1.

We are interested here in variations in the spectral features due to changes in the geometry. Therefore only the edge part of the calculated spectra, which arises from electric dipole ($1s \rightarrow p$) transitions, is presented and discussed. In the case of the LS ground state

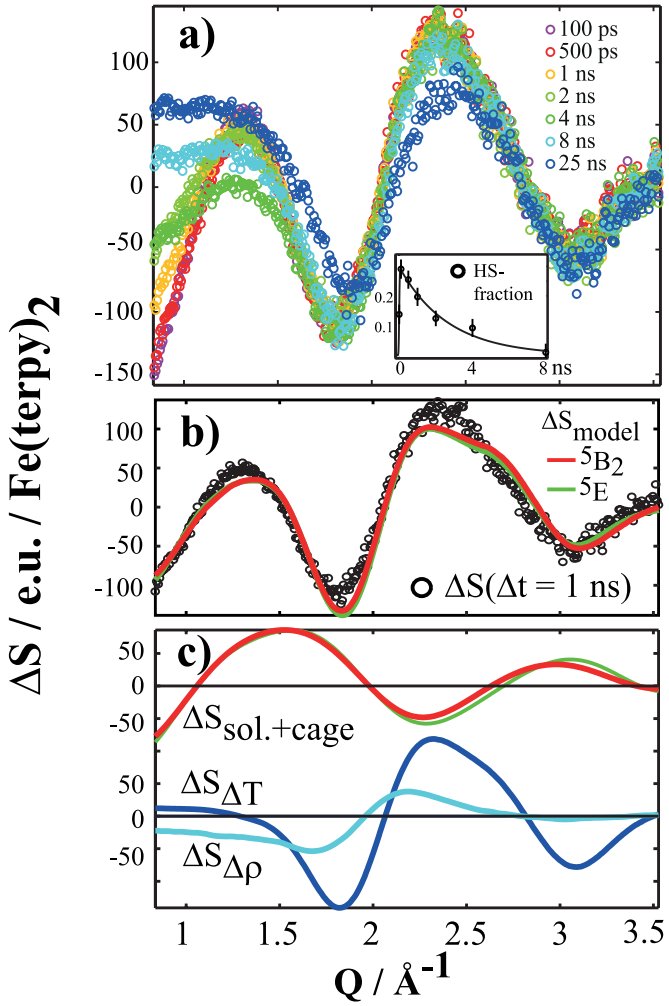

Figure 6: **(a)** The set of difference scattering signals $\Delta S(Q, \Delta t)$ acquired for $[Fe(terpy)_2]^{2+}$, color-coded according to time delay. Insert shows the magnitude of the solute-related contribution to the difference scattering signal as a function of time delay. **(b)** $\Delta S(Q, \Delta t{=}1$ ns) (black circles) and the best-fit simulated difference signal for both of the suggested HS structures (red = $^5B_2$, green = ^5E). **(c)** Each of the three contributions to the simulated difference signal, with the two solute-related difference signal again shown in red ($^5B_2$) and green (^5E). Bulk solvent contributions are shown in light $\Delta\rho * \Delta S_{\Delta\rho}$ and dark blue $\Delta T * \Delta S_{\Delta T}$

.

(Fig. 7a), the DFT-derived spectrum agrees very well with the experiment: both the energy and relative intensity of the spectral features are well reproduced, even the shoulder of peak C that is visible on the experimental HERFD spectrum. In the case of the photoinduced HS state (Fig. 7b), the calculation reproduces all the key spectral features (peaks B, C and D). As discussed above, for the HS structures, no experimental information has so far been available, but simulations exist, and the two possible atomic arrangements predicted by DFT (^{5}E and $^5B_2$) are very similar (Table 1). This strong similarity between the two predicted structures is reflected in their calculated XANES spectra, which are almost identical (Fig. 7b). The simulated laser-pumped spectrum reconstructed from 40% HS and 60% LS contribution (Fig. 7c) compares well with the experimental Δt = 80 ps XANES spectrum, indicating that the description of the HS geometry and electronic structure are good. Independent of the LS and HS populations, the shape of the experimental difference spectra (Fig. 7d) reflects the shape of the theoretical HS–LS difference, only its intensity is scaled by the population of the photoinduced HS state. It is obvious from the very good agreement between experiment and theory shown in Fig. 7 that our HS calculations are reliable, which therefore supports the proposed geometries for the photoinduced HS state of $[Fe(terpy)_2]^{2+}$.

RXES and multiplet calculations

The experimental $1s2p$-RXES planes recorded for the LS and laser-pumped states as well as the difference (HS–LS) planes of the $[Fe(terpy)_2]^{2+}$ and $[Fe(bipy)_3]^{2+}$ complexes are displayed in Fig. 8(a-g). The laser-pumped plane of $[Fe(terpy)_2]^{2+}$ (Fig. 8b) was recorded for a time delay Δt=80 ps, as for the XAS (Fig. 4a)and XES (Fig. 4b,c) spectra; therefore the photoinduced HS plane (Fig. 8d) was reconstructed from the photoinduced HS fraction (γ=40%) determined by XES. Here we represent for each plane the intensity of the signal as a function of the incident (Ω) and transfer (Ω-ω, ω being the emitted energy) energies. The diagonal of these (Ω,Ω-ω) planes corresponds to the resonant $1s$ excitations, *i.e.* the

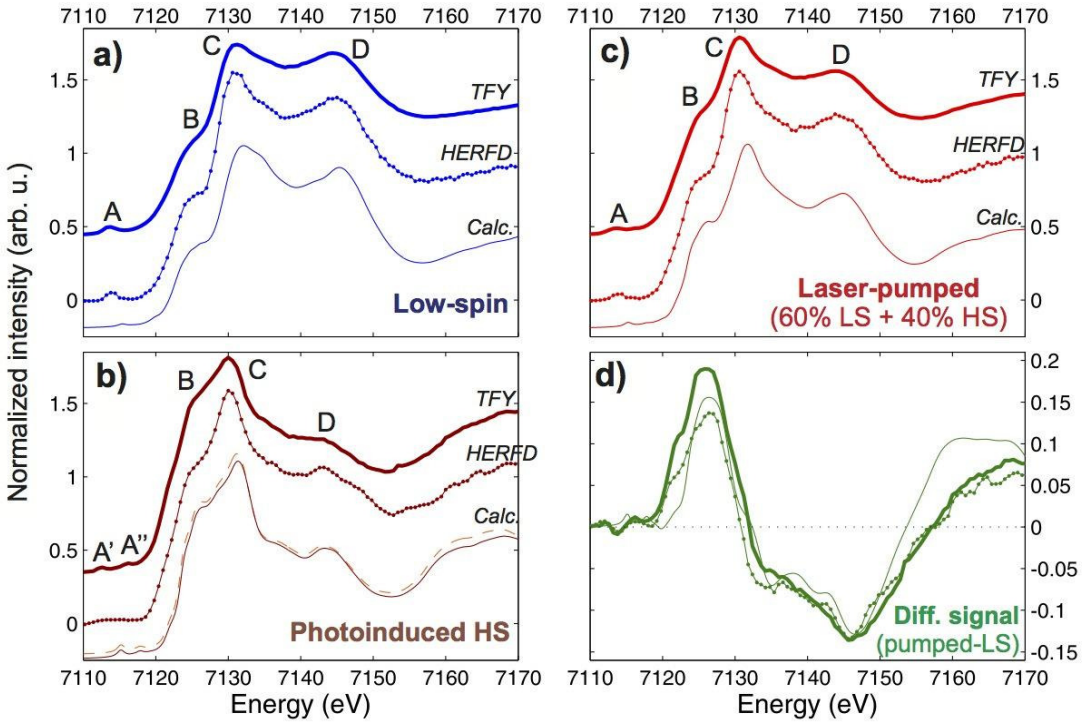

Figure 7: Normalized experimental and calculated Fe K-edge XANES spectra of [Fe(terpy)$_2$]$^{2+}$. In the case of experiments, both detection modes (TFY –thick lines– and HERFD –dotted lines) are represented; for the theoretical spectrum (thin line), only the electric dipole contribution is plotted. **(a)**: LS XANES; the theoretical spectrum was calculated with the ^{1}A$_1$ structure. **(b)**: Photoinduced HS XANES; the experimental spectra were reconstructed from the laser-pumped and LS measurements, and the theoretical spectra were calculated for the possible HS geometries ^{5}E (thin line) and ^{5}B$_2$ (dashed line). **(c)**: Laser-pumped XANES; the theoretical spectrum was reconstructed by a linear combination of the calculated LS (60%) and HS (40%) spectra. For clarity, given the similarity of the two theoretical HS spectra, the reconstruction was done only for the ^{5}E structure. **(d)**: Difference signal (laser-pumped – LS). The very good agreement between experiments and calculations is clear, and thus demonstrates the reliability of the two theoretical geometries of the [Fe(terpy)$_2$]$^{2+}$ HS state.

HERFD-XAS spectrum (Fig. 7), and in the following we describe the features as a function of the incident energy axis (Ω). First, for all the presented experimental RXES planes, the very intense feature observed at 7120 eV corresponds to the beginning of the strong electric dipole 1*s*-*p* resonance, which is the start of the edge rising on the XANES spectrum (Fig. 7). The less intense features between 7112 and 7116 eV are the pre-edge features of the XAS spectrum, and we discuss them in detail now.

In the case of the LS state (Fig. 8a and e), one intense feature is visible at 7114 eV; in an approximate multi electronic picture of the transitions and for an octahedral (O_h) symmetry, this single feature can be interpreted as the signature of the transitions towards the empty $3d(e_g)$ orbitals. However, additional intensity that extends diagonally towards the rising edge indicates that not just one transition forms the pre-edge. Deviation from inversion symmetry in $[Fe(terpy)_2]^{2+}$ (D_{2d} point group) and $[Fe(bipy)_3]^{2+}$ (D_3 point group) allows for *p*-*d* mixing resulting in additional energy levels and dipole contributions to the pre-edge spectral intensity. These effects are highly sensitive to the local geometry and consequently $[Fe(terpy)_2]^{2+}$ and $[Fe(bipy)_3]^{2+}$ show different LS RXES planes. The laser-pumped RXES planes (Fig. 8b and f) show a less intense main feature at 7114 eV and a tail appears at higher energy, corresponding to the HS contribution induced by the laser. Finally, the reconstructed HS plane (Fig. 8d) displays two main features at 7112.2 eV and 7116 eV, with a weaker feature at 7114.3 eV, which are the three dominant spectral features typical for an Fe(II) HS complex in octahedral symmetry.[20,62] In that case, the origin of the features cannot be determined in a simple monoelectronic picture, and a theoretical determination of the RXES plane is necessary in order to extract information on the photoinduced HS state of $[Fe(terpy)_2]^{2+}$ and $[Fe(bipy)_3]^{2+}$. Finally the similarity of the difference RXES planes of $[Fe(terpy)_2]^{2+}$ and $[Fe(bipy)_3]^{2+}$ (Fig. 8c and g) suggests that the same interactions are dominating the spectral shape.

The calculated RXES planes for the LS state and the HS states in the approximate octahedral (D_{4h}) symmetry, as well as the difference signal, are displayed in Fig. 8i-k. The

current level of development of multiplet codes for the determination of the RXES plane can take only the electric quadrupole contribution into account when combining the absorption and emission transition matrix elements. Therefore we do not discuss here the intensity of the peaks, which is affected by the electric dipole contribution, on the contrary to the energy position of the spectral features. When comparing these theoretical planes with the experimental ones of [Fe(terpy)$_2$]$^{2+}$ and [Fe(bipy)$_3$]$^{2+}$, it is obvious that the number of features for each state is well-reproduced. However, their relative position in the plane matches poorly. This small disagreement comes from the use of the approximate D_{4h} symmetry, whereas the local symmetry of Fe in the [Fe(terpy)$_2$]$^{2+}$ ([Fe(bipy)$_3$]$^{2+}$) molecule is D_{2d} (D_3).

Discussion: The photoinduced HS state structure

Our present study based on X-ray techniques brings here the first experimental evidence that the putative structures proposed from DFT calculations by both Hauser and co-workers[17] and Pápai and co-workers[21] are reliable structural models of the lowest energy photoinduced HS state of [Fe(terpy)$_2$]$^{2+}$. The good agreement between *(i)* the different experimental techniques and *(ii)* the experimental and theoretical results, indeed support the theoretical $^5B_2$ and ^5E structures. For both these structures, the Fe–N elongation is more pronounced along the molecular axis (R(Fe–N$_{ax}$)) than in the equatorial plane (R(Fe–N$_{eq}$)), and a bending of the ligand occurs, which differs significantly from the mono- and bidentate ligand complexes suche as the [Fe(bipy)$_3$]$^{2+}$ complex. However, neither the current experimental resolution nor the level of theory for XAS and XDS simulations enable to discriminate between the two structures. Nevertheless our study supports the hypothesis that the elongation of the Fe–N bond during the LS→HS transition is anisotropic, and consequently that the transition must be described by a model taking into account both the distance variations and the bending of the ligands. This corresponds to the theoretical prediction by Hauser and co-workers,[17] *i.e.* the SCC model is inadequate to describe the behavior of [Fe(terpy)$_2$]$^{2+}$. A new LS→HS transition model taking into account this geometrical anisotropy must be defined to cor-

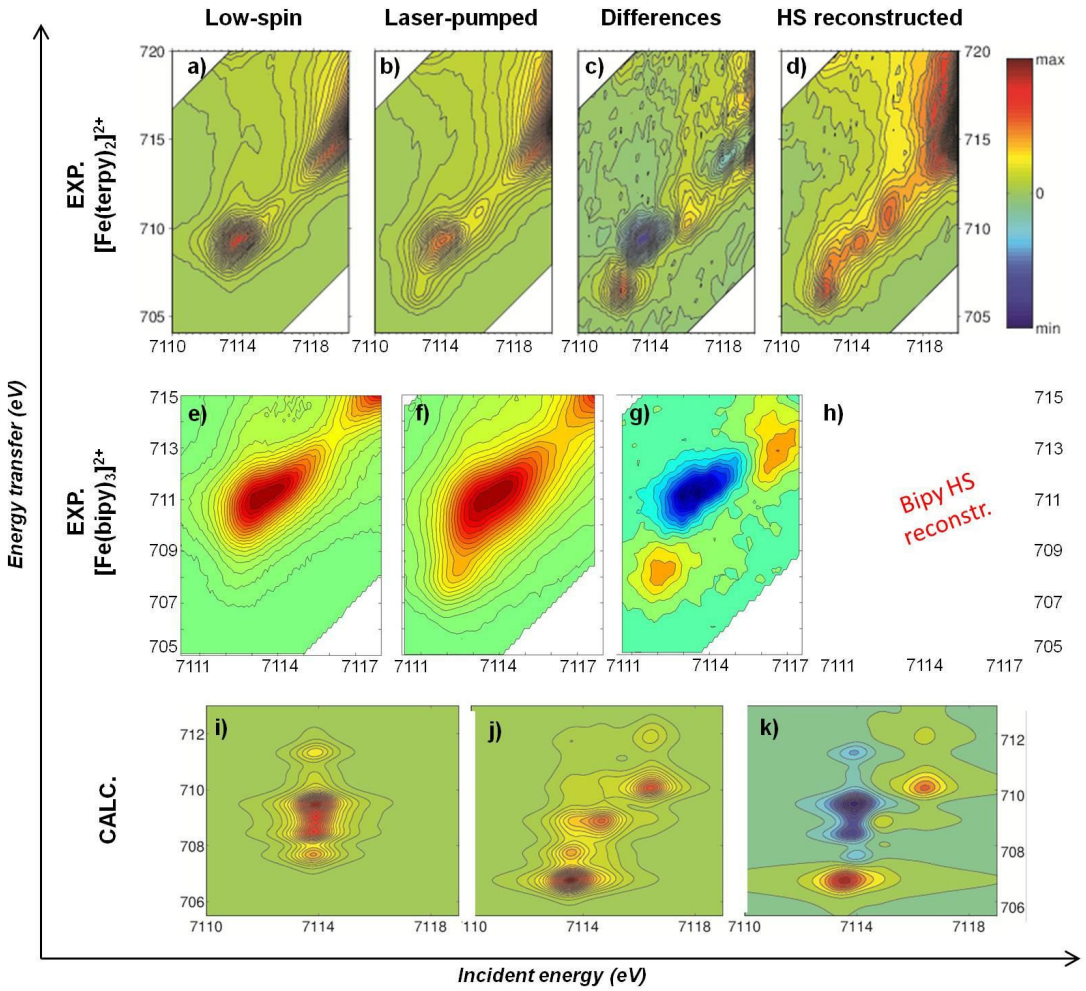

Figure 8: Experimental and theoretical Fe K-edge $1s2p$-(Ω,Ω-ω) RXES planes. The features along the diagonal of the plane corresponds to the HERFD-XANES spectrum. (**a-d**) RXES planes of $[Fe(terpy)_2]^{2+}$ in a 13 mM aqueous solution, showing (a) the LS state plane, (b) the laser-pumped plane, (c) the difference RXES plane (laser-pumped – LS) and (**d**) the photoinduced HS reconstructed plane (γ=40%). (**e-g**) RXES planes of $[Fe(bipy)_3]^{2+}$ in a 10 mM aqueous solution, showing (e) the LS state plane, (f) the laser-pumped plane and (g) the difference RXES plane (laser-pumped – LS). (**h**) RXES planes of $Fe(phen)_2(NCS)_2$ in a 10 mM aqueous solution, recorded as a HS reference. (**i-k**) Multiplet calculations in an approximate D_{4h} local symmetry, showing (i) the LS state, (j) the difference signal and (k) the HS state.

rectly describe the nature and energy of the photoinduced state of [Fe(terpy)$_2$]$^{2+}$ and hence understand its unusual long lifetime.

Conclusions

In the present study, we have used the recently developed MHz laser pump/X-ray probe capability[42] of the 7-ID-D beamline of the APS and ID26 of the ESRF to characterize the photoinduced HS state of [Fe(terpy)$_2$]$^{2+}$ by simultaneously recording XAS, XES and XDS.[19,20] Hence we have measured for the first time by X-ray methods the lifetime of the photoinduced HS state of the [Fe(terpy)$_2$]$^{2+}$ complex ($\tau_{XAS} = 2.57 \pm 0.070$ ns), in good agreement with previous optical measurements.[24] The high quality of the experimental data enabled a direct comparison with a theoretical investigation of the [Fe(terpy)$_2$]$^{2+}$ structure: quantum-chemical DFT-based calculations proposed two structures for the HS states (^{5}B$_2$ and ^{5}E), from which we computed both the X-ray absorption spectrum and the XDS signal. In each case, equally good agreement between experiment and calculation was obtained for both structures. Although the fine details of the HS structure could not be resolved, this is the first experimental evidence that the theoretical structures first proposed by Hauser[17] are representative of the HS structure of the [Fe(terpy)$_2$]$^{2+}$. Since both an elongation of the Fe–N bond length and a bending of the ligand are required to describe the photoinduced HS state structure, it also confirms that the SCC model breaks down and cannot explain the behavior of [Fe(terpy)$_2$]$^{2+}$.

To conclude, we wish to point out the great opportunities of techniques using crystal-analyzer spectrometer as a tool in time-resolved studies, as demonstrated by the improved resolution observed for HERFD-XANES compared to TFY-XANES. Also, our results on RXES open the way to the investigation of the electronic structure of the photoinduced state of switchable molecular compounds on the ultrafast time scale. The newest highly-brilliant X-ray synchrotron sources and X-ray free electron lasers (XFELs), in combination

with synchronized laser systems, indeed offer this possibility. Such an exploration of the geometrical and electronic properties of switchable molecules will permit to identify, and therefore control, the ultrafast elementary steps of light-induced spin-transition processes at the atomic level.

Acknowledgement

This project was supported by the European Research Council via contracts ERC-StG-259709 and ERC-AdvG-VISCHEM-226136, by the German Research Community (DFG) via contract SFB925, the European CRISP project, by the European XFEL, and by the 'Lendület' program of the Hungarian Academy of Sciences under contract no.LP2013-59/2013. K.H., M.N., T. van D., K.K. and H.L. acknowledge support from the Danish National Research Fundation's Centre for Molecular Movies and DANSCATT, S.E.C. funding from the Swedish Research Council. A.M.M., G.D., S.H.S., E.P.K. and L.Y. acknowledge support from the U.S. Department Of Energy (DOE) Office of Science, Division of Chemical, Geological and Biological Sciences under Contract no. DE-AC02-06CH11357. A.B., N.Z., G.V., D.C. and A.J. acknowledge the French Ministry of Foreign Affairs (MAE) and the French Ministry of Higher Education and Research (MESR) for funding through Balaton project no. 27875YK, as well as the Hungarian&French Intergovernmental S&T Cooperation Program (TET11FR-XTHEOEXP). Use of the Advanced Photon Source, an Office of Science User Facility operated for DOE Office of Science by Argonne National Laboratory, was supported by the U.S. DOE under contract no. DE-AC02-06CH11357. We are grateful to Christophe Lapras and the staff of ID26 from the ESRF, the staff of 7-ID from the APS and Sophie Canton (Lund University, Sweden) for help during experiments. D.C and A.J. acknowledge IDRIS for allocation ???.

Supporting Information Available

1. The first observation is the improved resolution of the HERFD-XAS spectra compared to

the TFY ones. This is obvious, for instance, for the LS state (Fig. 7a), where peak C of the TFY spectrum is splitted into a main peak and a shoulder on the HERFD one. This improved spectral resolution of the HERFD mode stems from different lifetimes of the core-holes in the final state of TFY ($1s$ core-hole; lifetime broadening = 1.25 eV[63]) and Kα_1-HERFD ($2p_{1/2}$ core-hole; lifetime broadening = 0.37 eV[63]) and from the narrow bandwidth of the XES spectrometer, as described previously.[34,64] This material is available free of charge via the Internet at `http://pubs.acs.org/`.

References

(1) Gütlich, P.; Goodwin, H. A. *Spin Crossover in Transition Metal Compounds I; Topics in Current Chemistry* **2004**, *233*, 1–47.

(2) McGarvey, J.; Lawthers, I. *Journal of the Chemical Society - Chemical Communications* **1982**, *16*, 906–907.

(3) Decurtins, S.; Gütlich, P.; Köler, C.; Spiering, H.; Hauser, A. *Chemical Physics Letters* **1984**, *105*, 1–4.

(4) Collison, D.; Garner, C. D.; McGrath, C. M.; Mosselmans, J. F. W.; Roper, M. D.; Seddon, J. M.; Sinn, E.; Young, N. A. *Journal of the Chemical Society, Dalton Transactions* **1997**, *22*, 4371–4376.

(5) Vankó, G.; Renz, F.; Molnár, G.; Neisius, T.; Kárpáti, S. *Angewandte Chemie International Edition* **2007**, *46*, 5306–5309.

(6) Renz, F.; Vankó, G.; Homenya, P.; Saadat, R.; Németh, Z.; Huotari, S. *European Journal of Inorganic Chemistry* **2012**, *16*, 2653–2655.

(7) Hauser, A. *Journal of Chemical Physics* **1991**, *94*, 2741–2748.

(8) Hauser, A.; Vef, A.; Adler, P. *Journal of Chemical Physics* **1991**, *95*, 8710–8717.

(9) Hauser, A. *Spin Crossover in Transition Metal Compounds II; Topics in Current Chemistry* **2004**, *234*, 155 – 198.

(10) Gawelda, W.; Cannizzo, A.; Pham, V.-T.; van Mourik, F.; Bressler, C.; Chergui, M. *Journal of the American Chemical Society* **2007**, *129*, 8199–8206.

(11) Bressler, C.; Milne, C.; Pham, V.-T.; ElNahhas, A.; van der Veen, R. M.; Gawelda, W.; Johnson, S.; Beaud, P.; Grolimund, D.; Kaiser, M.; Borca, C. N.; Ingold, G.; Abela, R.; Chergui, M. *Science* **2009**, *323*, 489–492.

(12) Bressler, C.; Chergui, M. *Chemical Reviews* **2004**, *104*, 1781–1812.

(13) Daku, L. M.; Vargas, A.; Hauser, A.; Fouqueau, A.; Casida, M. E. *ChemPhysChem* **2005**, *6*, 1393–1410.

(14) Gawelda, W.; Pham, V.-T.; van der Veen, R. M.; Grolimund, D.; Abela, R.; Chergui, M.; Bressler, C. *The Journal of Chemical Physics* **2009**, *130*, 124520.

(15) Gawelda, W.; Pham, V.-T.; Benfatto, M.; Zaushitsyn, Y.; Kaiser, M.; Grolimund, D.; Johnson, S. L.; Abela, R.; Hauser, A.; Bressler, C.; Chergui, M. *Physical Review Letters* **2007**, *98*, 057401.

(16) Gawelda, W.; Johnson, M.; de Groot, F. F. M. F.; Abela, R.; Bressler, C.; Chergui, M. *Journal of the American Chemical Society* **2006**, *128*, 5001–5009.

(17) Hauser, A.; Enachescu, C.; Daku, M. L.; Vargas, A.; Amstutz, N. *Coordination Chemistry Reviews* **2006**, *250*, 1642 – 1652.

(18) Vankó, G.; Glatzel, P.; Pham, V.-T.; Abela, R.; Grolimund, D.; Borca, C. N.; Johnson, S. L.; Milne, C. J.; Bressler, C. *Angewandte Chemie International Edition* **2010**, *49*, 5910–5912.

(19) Haldrup, K. et al. *Journal of Physical Chemistry A* **2012**, *116*, 9878–9887.

(20) Vankó, G. et al. *Journal of Electron Spectroscopy and Related Phenomena* **2012**,

(21) Pápai, M.; Vankó, G.; de Graaf, C.; Rozgonyi, T. *Journal of Chemical Theory and Computation* **2013**, *9*, 509–519.

(22) Cannizzo, A.; Milne, C.; Consani, C.; Gawelda, W.; Bressler, C.; van Mourik, F.; Chergui, M. *Coordination Chemistry Review* **2010**, *254*, 2677–2686.

(23) Canton, S.; Zhang, X.; Daku, L. M. D.; Smeigh, A. L.; Jianxin, Z.; Carl-Johan, W.; Attenkofer, K.; Jennings, G.; Kurtz, C. A.; Gosztola, D. J.; Warnmark, K.; Hauser, A.; Sundström, V. *Journal of Physical Chemistry C* **2014**,

(24) Creutz, C.; Chou, M.; Netzel, T. L.; Okumura, M.; Sutin, N. *Journal of the American Chemical Society* **1980**, *102*, 1309–1319.

(25) Renz, F.; Oshio, H.; Ksenofontov, V.; Waldeck, M.; Spiering, H.; Gütlich, P. *Angew. Chem. Int. Ed.* **2000**, *39*, 3699–3700.

(26) de Graaf, C.; Sousa, C. *Chem. Eur. J.* **2010**, *16*, 4550–4556.

(27) Fouqueau, A.; Mer, S.; Casida, M. E.; Daku, L. M. L.; Hauser, A.; Mineva, T.; Neese, F. *Journal of Chemical Physics* **2004**, *120*, 9473–9486.

(28) Ordejón, B.; de Graaf, C.; Sousa, C. *Journal of the American Chemical Society* **2008**, *130*, 13961–13968.

(29) Suaud, N.; Bonnet, M.-L.; Boilleau, C.; Labèguerie, P.; Guihéry, N. *Journal of the American Chemical Society* **2009**, *131*, 715–722.

(30) Chen, L. X.; Zhang, X.; Lockard, J. V.; Stickrath, A. B.; Attenkofer, K.; Jennings, G.; Liu, D.-J. *Acta Crystallographica Section A* **2010**, *66*, 240–251.

(31) Kim, T. K.; Lee, J. H.; Wulff, M.; Kong, Q.; Ihee, H. *ChemPhysChem* **2009**, *10*, 1958–1980.

(32) Haldrup, K.; Christensen, M.; Nielsen, M. M. *Acta Crystallographica Section A* **2010**, *66*, 261–260.

(33) de Groot, F. M. F.; Glatzel, P.; Bergmann, U.; van Aken, P. A.; Barrea, R. A.; Klemme, S.; Hävecker, M.; Knop-Gericke, A.; Heijboer, W. M.; Weckhuysen, B. M. *Journal of Physical Chemistry B* **2005**, *109*, 20751–20762.

(34) Glatzel, P.; Bergmann, U. *Coordination Chemistry Reviews* **2005**, *249*, 65–95.

(35) de Groot, F. M. F.; Kotani, A. *Core Level Spectroscopy of Solids*; Taylor & Francis, New York, 2008.

(36) Juhin, A.; Brouder, C.; Arrio, M.-A.; Cabaret, D.; Sainctavit, P.; Balan, E.; Bordage, A.; Seitsonen, A. P.; Calas, G.; Eeckhout, S. G.; Glatzel, P. *Physical Review B* **2008**, *78*, 195103.

(37) Sikora, M.; Juhin, A.; Weng, T.-C.; Sainctavit, P.; Detlefs, C.; de Groot, F.; Glatzel, P. *Physical Review Letters* **2010**, *105*, 037202.

(38) Sikora, M.; Juhin, A.; Simon, G.; Zajac, M.; Biernacka, K.; Kapusta, C.; Morellon, L.; Ibarra, M.; Glatzel, P. *Journal of Applied Physics* **2012**, *111*, 07E301.

(39) Glatzel, P.; Weng, T.-C.; Kvashnina, K.; Swarbrick, J.; Sikora, M.; Gallo, E.; Smolentsev, N.; Alonso Mori, R. *Journal of Electron Spectroscopy and Related Phenomena* **2013**, *188*, 17–25.

(40) Van Schooneveld, M. M.; Kurian, R.; Juhin, A.; de Groot, F. M. F. *Journal of Physical Chemistry C* **2012**, *116*, 15218–15230.

(41) de Groot, F. M. F.; Vankó, G.; Glatzel, P. *Journal of Physics: Condensed Matter* **2009**, *21*, 104207 (7pp).

(42) March, A. M.; Stickrath, A.; Doumy, G.; Kanter, E. P.; Krassig, B.; Southworth, S. H.; Attenkofer, K.; Kurtz, C. A.; Chen, L. X.; Young, L. *Review of Scientific Instruments* **2011**, *82*, 073110.

(43) Gauthier, C.; Solé, V. A.; Signorato, R.; Goulon, J.; Moguiline, E. *Journal of Synchrotron Radiation* **1999**, *6*, 164–166.

(44) ADF2010, SCM, Theoretical Chemistry, Vrije Universiteit, Amsterdam, The Netherlands, http://www.scm.com.

(45) Baker, A. T.; Goodwin, H. A. *Aust. J. Chem.* **1985**, *38*, 207–214.

(46) Taillefumier, M.; Cabaret, D.; Flank, A.-M.; Mauri, F. *Physical Review B* **2002**, *66*, 195107.

(47) Gaudry, E.; Cabaret, D.; Sainctavit, P.; Brouder, C.; Mauri, F.; Goulon, J.; Rogalev, A. *Journal of Physics: Condensed Matter* **2005**, *17*, 5467–5480.

(48) Baroni, S.; de Gironcoli, S.; Dal Corso, A.; Gianozzi, P. *Reviews of Modern Physics* **2001**, *73*, 515–562.

(49) Gougoussis, C.; Calandra, M.; Seitsonen, A.; Brouder, C.; Shukla, A.; Mauri, F. *Physical Review B* **2009**, *79*, 045118.

(50) Giannozzi, P. et al. *Journal of Physics: Condensed Matter* **2009**, *21*, 395502.

(51) Arfaoui, M.; Cabaret, D.; Della Longa, S.; Seitsonen, A. P.; Mauri, F. Firstp-principles full-potential calculations of the Fe K pre-edge and nea-edge structure in carbonmonoxy-myoglobin. AIP Conference Proceedings. 2007; pp 331–333.

(52) Cabaret, D.; Bordage, A.; Juhin, A.; Arfaoui, M.; Gaudry, E. *Phys. Chem. Chem. Phys.* **2010**, *12*, 5619–5633.

(53) Troullier, N.; Martins, J. *Physical Review B* **1991**, *43*, 1993–2006.

(54) Kleinman, L.; Bylander, D. *Physical Review Letters* **1982**, *48*, 1425–1428.

(55) de Groot, F. M. F. *Coordination Chemistry Reviews* **2005**, *249*, 31–63.

(56) Thole, T.; van der Laan, G.; Fuggle, J.; Sawatzky, G.; Karnatak, R.; Estava, J.-M. *Physical Review B* **1985**, *32*, 5107–5118.

(57) Cowan, R. *The theory of atomic structure and spectra*; University of California Press, Berkeley, 1981.

(58) Butler, P. H. *Point group symmetry: Applications, methods and tables*; Plenum, New York, 1981.

(59) Vankó, G.; Neisius, T.; Molnár, G.; Renz, F.; Kárpáti, S.; Shukla, A.; de Groot, F. M. F. *Journal of Physical Chemistry B* **2006**, *110*, 11647–11653.

(60) Cammarata, M.; Lorenc, M.; Kim, T.; Lee, J. H.; Kong, Q. Y.; Pontecorvo, E.; Lo Russo, M.; Schiro, G.; Cupane, A.; Wulff, M.; Ihee, H. *Journal of Chemical Physics* **2006**, *124*, 124504.

(61) Kjaer, K.; van Driel, T. B.; Kehres, J.; Haldrup, K.; Khatchulin, D.; Bechgaard, K.; Cammarata, M.; Wulff, M.; Sorensen, T. J.; Nielsen, M. M. *Physical Chemistry Chemical Physics* **2013**,

(62) Westre, T. E.; Kennepohl, P.; DeWitt, J. G.; Hedman, B.; Hodgson, K. O.; Solomon, E. I. *Journal of the American Chemical Society* **1997**, *119*, 6297–6314.

(63) Krause, M. O.; Oliver, J. H. *J. Phys. Chem. Ref. Data* **1979**, *8*, 329–338.

(64) Hämäläinen, K.; Siddons, D. P.; Hastings, J. B.; Berman, L. E. *Physical Review Letters* **1991**, *67*, 2850.

Paper VII

Fingerprinting and tracking sub-picosecond spin- and solvation dynamics of the spin-crossover complex [Fe(bpy)3]2+ by simultaneous ultrafast X-ray emission and X-ray scattering

Kristoffer Haldrup, Kasper Skov Kjær, Sophie Canton, Robert Hartsock, Tobias Harlang, **Tim Brandt van Driel**, Wojciech Gawelda, Andreas Galler, Asmus Ougaard Dohn, Klaus Braagaard Møller, Amélie Bordage, Zoltan Nemeth, Henrik Lemke, Marco Cammarata, David Mark Fritz, Kelly J. Gaffney, Villy Sundstrom, Gyorgy Vanko, Martin Meedom Nielsen and Christian Bressler.

Advanced Draft.

Fingerprinting and tracking sub-picosecond spin-, structural- and solvation dynamics of the spin-crossover complex $[Fe(bpy)_3]^{2+}$ by simultaneous ultrafast X-ray emission and X-ray scattering

Abstract

INTRODUCTION

From both a fundamental and an applied point of view, transition metal complexes have long been appreciated for the intimate coupling between the electronic and geometric degrees of freedom, a coupling which strongly influences the observed electronic and spin-change dynamics following photo-excitation. In the case of Fe, a particularly interesting class of compounds are the octahedral Fe-N complexes of which the spin-crossover compound $[Fe(bpy)_3]^{2+}$ is probably the most classic and well-studied example [Hauser, McCusker, Gawelda]. Figure 1(A) shows this molecule in schematic form.

Experiments utilizing ultrafast optical spectroscopy techniques have established that photo-excitation of the Low-Spin (S=0) ground state into the singlet Metal-to-Ligand-Charge-Transfer ^{1}MLCT state is followed by a cascade of intersystem crossing steps through singlet and triplet MLCT states, which brings the electronic system with almost unity quantum yield to the lowest-lying excited state in $\sim$ 130 fs. This state is the metal-centered $^5T_2$ High-Spin (HS, S=2) quintet state [Gawelda2007JACS, Cannizzo2010, Consani2009, TheoryRefs]. These electronic transitions are accompanied by a 10% (0.2 Å) increase in Fe-bond lengths and a consequent expansion of the ligand system. From the $^5T_2$ excited state, $[Fe(bpy)_3]^{2+}$ relaxes non-radiatively to the LS ground state within 650 ps in aqueous solutions at room temperature.

The HS ($^5T_2$) state with 4 unpaired electron spins arises from the promotion of two electrons from the lowest crystal field-split t_{2g} orbital to the anti-bonding e_g level. As the ground-state crystal field splitting (10 Dq) of the metal-centered $3d$ orbital is 2.5 eV and as the spin-cross over process can be triggered by excitation at 2.13 eV (580 nm) [References?], it is evident that significant decrease of the crystal field splitting is a key part of the observed dynamics. Such a decrease will result from the lengthening of the Fe-N bonds associated with populating the anti-bonding e_g orbital, but this process becomes energetically accesible only after lowering of the crystal field splitting between the involved orbitals. As such, $[Fe(bpy)_3]^{2+}$ is therefore a case example of a system with strong coupling between the electronic and structural dynamics, and significant theoretical efforts have been devoted to understanding these strongly coupled electronic and structural dynamics [De Groot, Others?].

To complement the results from optical spectroscopy and the efforts in theory and mod-

elling, experimental tools with sensitivity to both electronic and structural changes and with sub-picosecond time resolution are needed. Time-resolved soft[Huse2011, Cho2012] and hard[Gawelda2007, Bressler2009, Lemke2013] X-ray Absorption Spectroscopy studies have yielded significant insights in recent years, but the overlapping contributions to the acquired signals from both electronic and structural degrees of freedom have complicated interpretation, as have limited time resolution. In the present study, simultaneous X-ray Emission Spectroscopy and X-ray Diffuse Scattering with hard X-rays from the LCLS X-ray Free Electron Laser facility were utilized to characterize the fundamental interplay between spin-state transitions, structural changes and solvation dynamics in $[Fe(bpy)_3]^{2+}$ on sub-picosecond time scales. These two X-ray probes are uniquely sensitive to, respectively, electronic and geometric configuration and this complementarity significantly assists in the interpretation of the experimental data [Haldrup2012]. The combined approach provides a widely applicable framework for studying the fundamental couplings between electronic and structural degrees of freedom, as well as the interaction with the environment, on the ultrafast time scales.

EXPERIMENTAL SETUP

Figure 1B shows in schematic form the experimental setup used for the experiment at the XPP end station of the LCLS X-FEL facility, full details are provided in the Supplementary Online Information. The sample was a 50 mM aqueous solution of $[Fe(bpy)_3]^{2+}$, circulating through an open-jet system with a 100 μm nozzle producing a flat sample sheet inclined at 45 degrees to the X-ray beam. The sample was photo-excited at 400 nm with 50 fs long laser pump pulses with 200 μJ/pulse. The X-ray probe beam was produced by the LCLS undulators tuned to an X-ray energy of 8 keV (0.3% bandwidth) with 50 fs pulse length. The number of photons per pulse was on average 10^{11} at the sample position, but with the characteristic large pulse-to-pulse variations also described elsewhere [17]. The laser and X-ray beams were collinear at the sample position, with an X-ray focus spot of 135 μm^2 FWHM and 150 μm FWHM laser focus. Pump/probe frequency was 120 Hz, allowing full sample replenishment between successive pump/probe cycles. Fluorescently emitted X-ray photons were collected by a spherically bent Si(531) analyzer crystal mounted in a 1-m Rowland-circle setup. The collected photons were detected by a Si diode and the energy

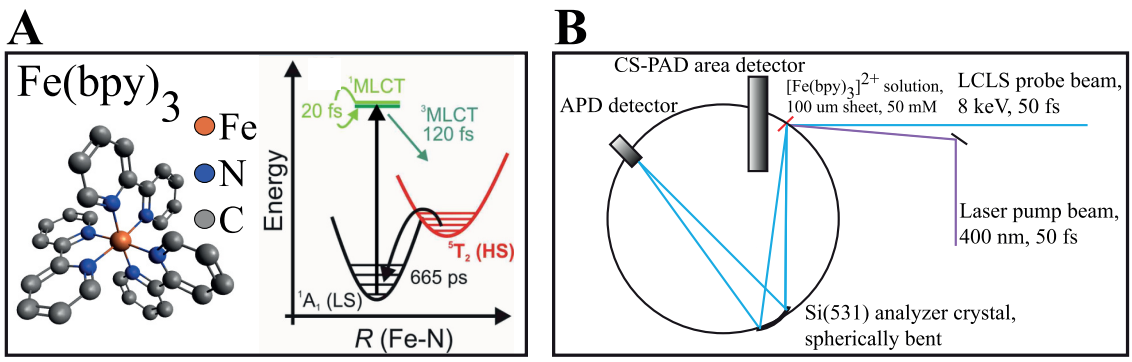

FIG. 1: ***A****: Molecular structure and energy level diagram of* $[Fe(bpy)_3]^{2+}$ *with the* ^1MLCT *to* $^5T_2$ *excited-state conversion indicated. (Prettier version of this figure may arrive later)* ***B****: Schematic illustration of the experimental setup, with the X-ray and laser beams arriving collinearly at the fast-flowing sample sheet. Fluorescently emitted X-ray photons are collected in a Rowland-circle XES setup and scattered X-ray photons are detected by the CS-PAD detector system.*

resolution of the XES spectrometer setup was ∼1 eV. A He-filled plastic bag was installed around the XES setup to minimize absorption losses in air.

The X-ray scattering was detected by a large-area (32 modules) CS-PAD detector mounted on a robot arm behind the sample chamber [12]. The detector was centered on the X-ray beam such that the beam passed through the center-hole of the detector. The detector was read out after each X-ray pulse and the acquired 2D scattering images were azimuthally integrated to yield 1D scattering curves $S(2\theta)$ with $2\theta_{max} = 60^0$, corresponding to a maximum scattering vector $Q_{max} = 4$ Å^{-1}, $Q = \frac{4\pi}{\lambda}\sin(\theta)$.

For the time-resolved data presented here, the laser/X-ray time delay was scanned in 50 fs steps from -2 ps to +2 ps. X-ray emission and scattering data were collected using 240 X-ray pulses (2 s integration time) at each time step.

RESULTS

Figure 2 shows the recorded Fe Kα emission intensity as a function of energy $I(E)$ with and without laser excitation of the sample . The nominal time delay for the laser-on XES signal was $\Delta t = 500$ fs and the acquired difference signal as a function of emission in energy is shown as dark purple points. As described in earlier work [VankoRefs], the total Fe Kα

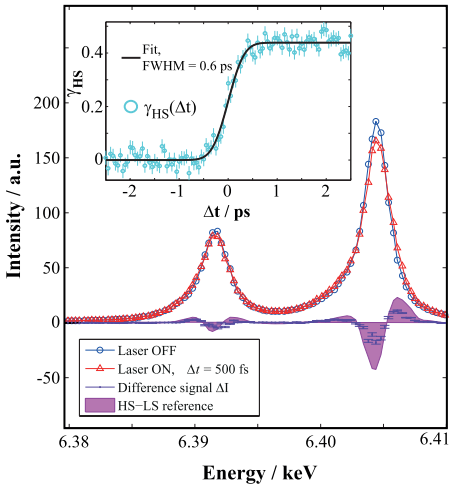

FIG. 2: Fe Kα emission intensity as a function of energy for the 50 mM $[Fe(bpy)_3]^{2+}$ sample with (red) and without (blue) laser excitation before the X-ray probe pulses. Dark purple points show the difference signal between the two measurements, and the light purple area shows the High-Spin minus Low-Spin reference signal for the spin transition. By scaling to this reference, the emission intensity at a given energy point can be directly related to photo-excited High-Spin fraction γ_{HS}; the insert shows this as function of time (light blue points) and the observed kinetics are found to be well described by a broadened step function (fit, black line).

emission intensity is the same for all the involved electronic states, but the line width is proportional to the number of unpaired electrons in the $3d$ orbital through the exchange-interaction with the 2p electrons. Thus the emission intensity at the peak of the Kα line can be used to accurately monitor the total ($3d$) spin momentum of the sample. By scaling to a known High-Spin (HS) reference (light purple area in Figure 2) the HS fraction γ_{HS} can be accurately determined. The insert shows this fraction as a function of nominal time delay, $\gamma_{HS}(\Delta t)$.

As evident from the insert of Figure 2, the time evolution of γ_{HS} is very well captured by a simple model based on a gaussian-broadened step function with a FWHM of 0.60(4) ps. A more complicated model (see SOI) incorporating a gaussian-broadened (FWHM = 0.5(1) ps) exponential grow-in with a time constant of 0.17(8) ps fits the data equally well. As the spin-state transition is known from previous work to be complete in < 0.25 ps [5], we conclude that the large broadening of the XES response is due to the machine/instrument

response function, which is dominated by pulse-to-pulse jitter in the arrival time of the X-ray probe pulses as described in detail elsewhere [2, 11, 17]. This broadening of the time resolution precludes any attempt at fitting and distinguishing between the models proposed to describe the spin-state evolution of $[Fe(bpy)_3]^{2+}$ from the initially excited ^{1}MLCT to the $^5T_2$ state.

The XDS data were recorded simultaneously with the XES signal and the starting point for the analysis of such time-resolved X-ray Diffuse Scattering data is the set of difference signals $\Delta S(Q, \Delta t) = S(Q, \Delta t) - S(Q)_{Off}$ [10]. As discussed in detail in references [10, 13] and below, the set of difference signals $\Delta S(Q, \Delta t)$ contain all the information available from scattering regarding the structural changes in the sample that were triggered by the laser pump pulse. The full procedure for the robust calculation of background-corrected difference signals is provided in the Supplementary Online Information. Background contributions were identified by a Singular Value Decomposition of the set of difference signals acquired at large negative time delays and were individually subtracted from each of the difference signals. Figure 3A shows a 2D-representation of the difference-scattering signals $\Delta S(Q, \Delta t)$. The top part of the insert shows $\Delta S(Q, \Delta t = 1\text{ps})$.

In the following paragraphs, the physics underlying the changes in scattering giving rise to the set of difference signals in Figure 3 are discussed. ΔS contains the signal arising from any structural changes of the solute and its caging solvent molecules as well as from the structural changes in the solvent arising from temperature and density changes.

$$\Delta S_{Model} = \Delta S_{Solute+cage} + \Delta S_{Solvent} \tag{1}$$

Turning first to the difference signal arising from changes in the structure of the solute and its immediate surroundings, this contribution to the difference signal can be directly modelled from DFT-calculated structures for the ground- and excited states of the molecule, see e.g. [9, 15, 16]. In the present case the approach employed in [9] is followed closely, thus assuming the structure of LS and HS $[Fe(bpy)_3]^{2+}$ to be well known and accurately reproduced by the DFT calculations and including the effects of changes in the caging solvent by calculating the difference signal from ensembles of Molecular-Dynamics (MD) simulations.

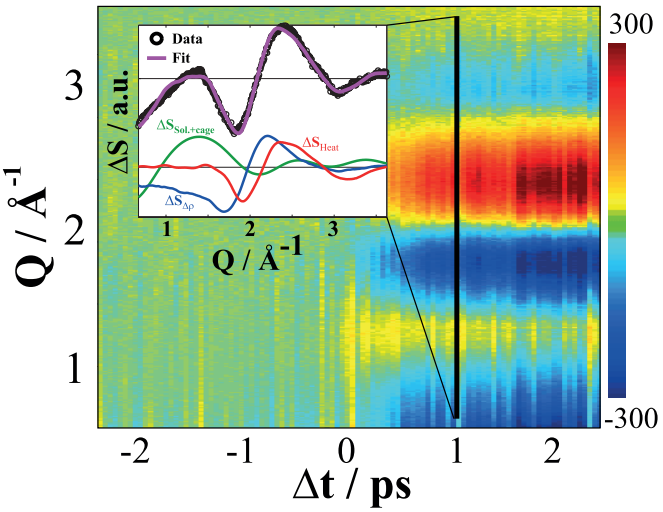

FIG. 3: 2D-representation of the 101 difference scattering signals $\Delta S(Q, \Delta t)$. Insert shows in the top panel a single difference signal for Δt=1 ps (black circles) and the best-fit model signal ΔS_{model} (magenta line). Bottom panel of insert shows the three individual contributions to the difference signal at this time delay as described in detail in the main text.

$$\Delta S_{Solute+cage} = \gamma_{XDS}(\Delta S^{MD}_{HS} - \Delta S^{MD}_{LS}) \tag{2}$$

-Where the scaling parameter γ_{XDS} represents the photo-excitation (HS) fraction. Full details of the calculation of $\Delta S_{Solute+cage}$ are given in the SOI.

For the solvent, changes in temperature or density will change the local structure of the liquid. Such changes in the pair-distribution function will give rise to changes in the X-ray diffuse scattering pattern as described in detail in earlier X-ray studies [4, 14, 18]. For modest temperature changes and when thermodynamic equilibrium has been established, the changes in solvent scattering due to evolution of the hydrodynamic variables can be described at all later time delays by a linear combination of the difference signals arising from changes in temperature and changes in density,

$$\Delta S_{Solvent}(Q) = \Delta T * \Delta S_{\Delta T}(Q) + \Delta\rho * \Delta S_{\Delta T}(Q) \tag{3}$$

-where the solvent difference signals $\Delta S_{\Delta T}(Q)$ and $\Delta S_{\Delta T}(Q)$ are determined in a separate experiment as described in detail in references [4] and [14]. In the present analysis the solvent contribution is this methodology is extended to include second-order effects ($\propto \Delta T^2$) from large temperature changes [20]. However, we note that on the time scales of the present experiment the probed sample volume is far from thermodynamic equilibrium due to the photo-excitation by the intense laser pump pulse, and the interpretation of the analysis results becomes less straightforward as discussed in detail below and in the SOI.

With the contributions to the measured difference signals accounted for, the acquired difference signals from -2.5 ps to 2.5 ps were individually fitted with the model signal ΔS_{Model} and the contributions from a large and highly variable background. These background contributions were characterized by Singular Value Decomposition and included in the fit as $\Delta S_{Bg.}(Q)$ yielding a final fit procedure consisting of minimizing

$$\sum_{Q}([\Delta S(Q)_{Measured} - (\Delta S(Q)_{Solute+cage} + \Delta S(Q)_{Solv.} + \Delta S(Q)_{Bg.})]^2/\sigma(Q)^2)/(N-p-1) \quad (4)$$

-where $\sigma(Q)$ is the estimated error on each data point, N the number of Q-points and p the number of free parameters in the fit [10, 13, 22].

By this fit of a physical model to the acquired difference signals we can for each time step extract the parameter set $(\gamma_{XDS}, \Delta\rho, \Delta T)$ that describe the physical processes in the sample due to the photo-excitation event. Each of these parameters acts as a scaling constant for one of the contributions to the difference signal, which are shown in the insert of Figure 3. We emphasize that these contributing difference signals are not derived from the acquired data, but are either measured in separate experiments or calculated from DFT/MD simulations. There is thus no guarantee that their combination will fit the acquired difference signals, but as is evident from the insert of Figure 3, the quality of the fit provides confidence in the applicability of the underlying physical model.

Figure 4 shows the time evolution of $\gamma_{XDS}, \Delta\rho$ and ΔT as determined by analyzing each of the 101 time steps, along with the HS fraction γ_{HS} determined by the simultaneous measurement of the X-ray emission intensity at 6404 eV. Both the XES analysis and the XDS approach arrives independently at a final value for photo-excitation fraction of ~ 40 %. Further, the XDS analysis finds density- and temperature increases of 2.0(2) kg/m^3 and

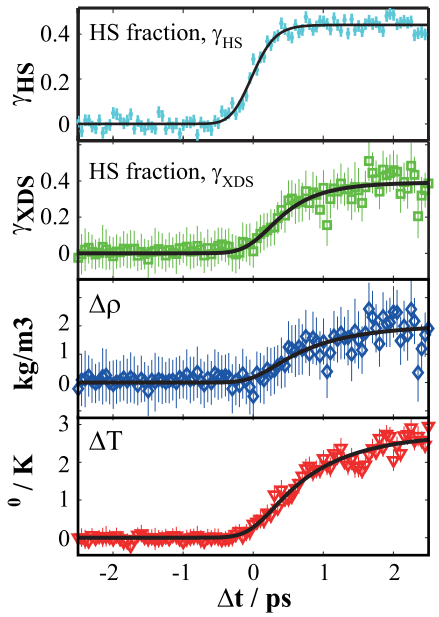

FIG. 4: Solute and solvent kinetics, with the top two panels showing the HS photo-excitation fraction as determined by XES and XDS, respectively. Black lines show fits of kinetic models (broadened exponential grow-ins) to the acquired data as described in the main text. The electronic response from the formation of the HS state is observed to precede the structural response, which in turn is fasther than the bulk-solvent response.

2.75(8) K, respectively. These increases are of the same order of magnitude as observed in our previous synchrotron experiments, but are somewhat larger as discussed in detail below.

From Figure 4, the structural response of the solute as well as the kinetics of the solvent contributions appear to be slower than the electronic response tracked by the XES measurement. As the physical mechanisms underlying the recorded XES signal are known to be significantly faster than the time scale accessible in the present experiment, this spectroscopic measurement allowed the instrument-related parameters (t_0, FWHM) to be fixed to the XES-derived values in the following kinetics analysis, signficantly aiding interpretation. By assuming these two parameters to be accurately determined by the XES measurement, models assuming simple broadened step functions were found to not describe any of the XDS-determined parameter kinetics well (SOI). Assuming kinetics models described by broadened

exponential grow-ins and again with t_0 and the width of the response function determined by the XES measurement, on the other hand, described the observed kinetics well, as indicated by the black fit lines in Figure 4. Denoting the time constants of the grow-in by τ, the best-fit values of the kinetics analysis are $\tau_{\gamma_{XDS}}$=0.50(6) ps, $\tau_{\Delta\rho}$=0.8(2) ps and $\tau_{\Delta T}$=0.86(7) ps. If the instrument-response parameters are determined from an analysis of the XES signal assuming a broadened exponential grow-in as the kinetic model, these time constants increase by ∼20%.

The ∼ 0.8 ps time scale for the solvent response is in good agreement with previous fs- and ps-resolved studies of water heating due to ultrafast energy release and subsequent structural response (e.g. [1, 19, 24]), and the absence of a longer time constant indicate that vibrational relaxation of HS $[Fe(bpy)_3]^{2+}$ is dominated by the 1.1 ps time constant suggested by Consani et al. [6] from optical data.

The value for $\tau_{\gamma_{XDS}}$ as extracted from the fit of the kinetic model incorporating an exponential grow-in is significantly larger than observed by previous spectroscopic measurements in the UV-VIS region as well as by using X-ray spectroscopic methods [3]. As the present measurement is a direct structural probe of the global molecular structure, this indicates that the structural rearrangement in $[Fe(bpy)_3]^{2+}$ takes a few 100 fs longer to be completed after the electronic system has relaxed to the lowest $^5T_2$ excited state. This tentative conclusion is discussed in further detail below.

The observed structural response corresponding to an eventual temperature increase of almost 3 K averaged over the probed volume is larger than expected as follows. The energy released by the ultrafast cascade of internal conversion processes that leads to population of the HS state following excitation at 400 nm is approximately 2.6 eV per excited solute. With a photo-excitation fraction of 40% of the 50 mM sample solution (20 mM HS $[Fe(bpy)_3]^{2+}$), this would be expected to result in a still quite significant temperature increase of 1.2 °C, which is still considerably less than observed. As detailed in the SOI, this seeming discrepancy is resolved by realizing that the sub-50 fs laser excitation pulses have sufficient peak brightness to induce signficant photo-ionization of water through 3-photon absorption processes. As discussed by e.g. Crowell et al. [7] the non-linear nature of these processes leads to a highly anisotropic excitation profile for the ionization, with very significant deposition of energy in the ∼10-20 μm of the liquid sheet facing the incoming laser pump beam. As detailed in the SOI, we find evidence of this through the presence of a second-order term

[20]in the temperature response, indicating that some regions of the probed volume exhibit structural changes consistent with heating by several tens of degrees. We interpret this finding as a combination of the assymetric profile for the third-order absorbtion processes as well as from point-source heating from vibrational relaxation of the photo-excited $[Fe(bpy)_3]^{2+}$ molecules.

As shown in previous synchrotron work on $[Fe(bpy)_3]^{2+}$ on the 100 ps time scale [9], the formation of a significant population of HS $[Fe(bpy)_3]^{2+}$ is accompanied by a rapid increase in the density of the water solvent. This density increase can be tentatively associated with the re-organization of the caging solvent molecules due to the formation of the HS state predicted from high-level modelling [8], a re-organization that results in the expulsion of on average two water molecules which leads to an increase in the density of the bulk solvent. As Figure 4 shows, we also observe this density increase on the ultrafast time scales probed in the present experiments as the density increases by close to 0.2 %, $\Delta\rho = 2$ kg/m^3. This increase is approximately three times more than observed in the synchrotron experiments, in agreement with the higher HS-state concentration in the present study, 20 mM vs. 6-8 mM. The time scale for this density increase appears to be short, close to one picosecond, but with the 0.6 ps time resolution the details of the dynamics are not resolvable. However, the observation of such sub-ps dynamics is in tentative agreement with the time scales observed in a recent MD-based studies of dynamic solvation processes for $Ru(bpy)_3$ in water by Szymczak et al. [23] as well as with a recent study of the I^0 to I^- transition in water [21], where in both cases very fast local dynamics were observed following photo-excitation.

With respect to these solvent-contributions to the measured difference signals, we note that $\Delta S_{\Delta T}$ and $\Delta S_{\Delta T}$ are explicitly measured and calculated for ensembles of solvent molecules in thermodynamic equilibrium, whereas the probed sample volume is in a distinctly non-equilibrium state in the first picoseconds following photo-excitation. However, the changes in scattering that can at longer times be explicitly related to changes in temperature and density are more fundamentally measurements of changes in the local structure and packing of the solvent. The present quality of fit and consistency of results indicate that these structural changes are quite similar on both the ultrafast as well as longer time scales. This can be interpreted as a demonstration of the fact that the observed changes in scattering, both at long and short time scales, are fundamentally related to similar changes in the local structure and packing of the solvent, which at longer time scales may be interpreted in

terms of temperature and density changes. However, we caution that neither temperature or density are well-defined at the spatiotemporal scales probed in the present experiment. The full details of probing locally excited, out-of-quilibrium solvent systems on the ultrafast time scales are beyond the scope of the present paper but are currently being investigated.

From the results presented above, it is evident that the jitter-dominated 0.6 ps broadening of the time resolution precludes determining the nature and time scales of the very first steps in the formation of the HS state, both on an electronic level and from a structural point of view. Also, by close examination of the difference scattering signals acquired with nominal time delays close to $\Delta t = 0$ we find that it is not possible to identify difference signals where only the signal arising from structural changes in the solute and its immediate surroundings are present. At all time delays, we find that jitter leads to a distribution of effective time delays, with some time delays long enough to introduce a significant component from the very large bulk-solvent heating to the averaged signal.

The fact that the solvent signal grows in on a picosecond time scale implies the possibility that on very short time scales the solute+cage signal can be observed without the otherwise dominating signal from solvent heating. This is nevertheless challenging in the results shown above due to the 0.5 ps timing jitter in these measurements. However, the exceptionally bright LCLS pulses offer the opportunity to record single pump/probe events for which only the ∼130 fs geometric time smearing is present. Doing so, the same analysis approach as described above for the 50 fs-binned data can be applied to the individual pump/probe data. Thus, while there is no information available about the actual pump/probe time delay, the individual contributions to ΔS can be used as "structural fingerprints" of the underlying physical processes.

In particular, identifying such difference signals with little or no contribution from the bulk-solvent processes dominant in the 50-fs binned data sets discussed above is essential for disentangling the dynamics on the ultrafast time scales. Such an identification can be accomplished by applying the fit-approach introduced above to individual single-shot difference signals, and subsequently identify the set of ΔS's where the fit yielded ΔT and $\Delta\rho$ essentially zero but with a finite value of the photo-excitation fraction α. Figure 5 shows such a set of solute-only difference signals (black circles), and their average (black line).

For comparison, the solute-only signal from an identical number of pump-probe events but measured at a much-longer nominal time delay of $\Delta t = 1$ ps is with shown with triangles,

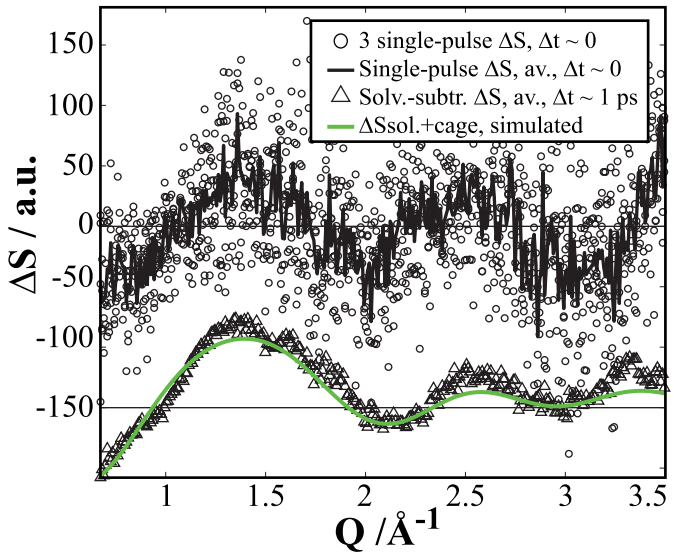

FIG. 5: Four solute-only single-pulse difference signals (black circles) acquired at time delays where little or no contribution from changes in the bulk-solvent structure could be detected. Full black line indicates the average. Below is shown a similarly averaged difference signal (black triangles) for four single-pulse difference signals acquired at long time delays, ∼ 1 ps, and with the bulk-solvent contributions subtracted. For comparison, the full green line shows the DFT/MD-calculated solute+cage difference signal $\Delta S_{Sol.+cage}$.

following subtraction of the solvent contribution, $\Delta S_{Solute+cage} = \Delta S_{Measured} - \Delta S_{Solvent}$. The solute-only signal identified from individual difference signals at very early time delays is observed to be similar, but not identical to the solute-only signal measured following the onset of bulk heating. A full discussion and analysis of these last results are beyond the scope of the present paper, but qualitatively the sharp features of the 1 ps solute-only difference signal appear somewhat indistinct in the short-delay difference signal, as would be expected when the molecules are vibrationally hot.

DISCUSSION AND CONCLUSIONS

By utilization of the complementary techniques of X-ray Emission Spectroscopy and X-ray Diffuse Scattering in a single combined experiment at the LCLS Free Electron Laser, the electronic and structural degrees of freedom in $[Fe(bpy)_3]^{2+}$ were tracked with sub-picosecond

time resolution. Information about the structural changes in the solute and surrounding solvent was obtained by a multi-component fit to 50 fs binned difference signals. The time resolution of the experiment was governed by jitter in the arrival time of the X-ray probe pulses, and was approximately 0.6 ps FWHM. This time resolution was not sufficient to allow distinction between the various models proposed for the Spin Cross-Over processes, but the XDS results indicate that the structural re-arrangement may complete on a longer time scale than the electronic degrees of freedom. We speculate that the higher than expected value of τ_γ determined in the present XDS study (0.5 ps) compared to the simultaneous as well as previous previous spectroscopic investigations (0.2 ps) is related to the initially excited molecule being vibrationally hot. The structural models employed in the present study do not incorporate the structural disorganization associated with a vibrationally hot molecule, and as this would tend to lower the intensity of all features in the difference signals the derived excitation fraction will be lower in turn.

On slightly longer time scales the formation of the HS state is observed to be associated with an increase in the density of the bulk solvent, surmised to be associated with the solvent-cage re-organization proposed from modelling by Daku & Hauser (Daku2010). Significant heating of the bulk solvent was observed to grow in with a time constant of 1 ps. The magnitude of this heating was larger than expected from simple considerations based on energy release from only the photo-excited solute molecules, and was concluded to be due to direct 3-photon ionization of the water molecules. From the volume-averaged temperature increase of $\sim$1 K tentatively associated with the 3-photon absorption processes and conservatively assuming 1 eV excess energy of the electrons after photo-ionization in analogy with Crowell et al., then the concentration of solvated electrons is estimated to be in the range of several tens of mM, in agreement with the results in Crowell et al.[Crowell2004] who reported $[e^{-1}]$=15 mM at significantly lower laser intensity. We note that the presence of a significant concentration of solvated electrons may influence the difference scattering signals, and therefore a more detailed, structural analysis of the acquired difference signals was not attempted, although such an analysis may eventually shed further light on the details of the solvent-cage dynamics.

In an effort to probe the structural response of the sample at very short time scales the multi-component fit approach to difference signals arising from single probe pulses from the LCLS machine. This was possible thanks to the very high intensity of the individual X-ray

pulses, and allowed the identification of difference signals with essentially no bulk-solvent component. This indicates, that even though the re-organization of the solvent shell that manifests as a density increase of the bulk solvent is very fast, the formation of the HS structure does occur first. The slight differences between the short- and long-delay solute-only difference signals (with the latter having somewhat sharper features) are tentatively assigned to the molecules being vibrationally hot immediately after photo-excitation. The ability to measure solute-only signals at very short (but here unknown) time delays also shows that it is possible to conduct such pump/probe measurements on time scales short enough for the measured scattering, and thus structure, to not be influenced by e.g. bulk-solvent heating – a possibility that has been colloquially referred to as "beating the heat".

The approach used here to identify the structural signals corresponding to the very shortest time delays between the pump- and probe pulses relies on the feasibility of applying a model-fit to single difference scattering signals recorded from individual X-ray probe pulses. That this is indeed possible, and also for a molecule comprised mostly of light elements, underscores the potential of the new X-ray Free Electron Lasers with 10^{11} ph/pulse as powerful tools for studying fundamental chemical reactions in solution. In particular, the recent implementation of pulse-to-pulse time delay diagnostics with 10-fs time resolution offers exciting new opportunities for combined studies of the type presented here to unravel the interplay between electronic structure and molecular geometry in unprecedented detail.

ACKNWOLEDGEMENTS

---

* hald@fysik.dtu.dk

[1] Satoshi Ashihara, Nils Huse, Agathe Espagne, Erik T. J. Nibbering, and Thomas Elsaesser. Ultrafast structural dynamics of water induced by dissipation of vibrational energy. *JOURNAL OF PHYSICAL CHEMISTRY A*, 111(5):743–746, FEB 8 2007.

[2] Mina R. Bionta, H. T. Lemke, J. P. Cryan, J. M. Glownia, C. Bostedt, M. Cammarata, J.-C. Castagna, Y. Ding, D. M. Fritz, A. R. Fry, J. Krzywinski, M. Messerschmidt, S. Schorb, M. L. Swiggers, and R. N. Coffee. Spectral encoding of x-ray/optical relative delay. *Opt. Express*, 19(22):21855–21865, Oct 2011.

[3] Ch. Bressler, C. Milne, V.-T. Pham, ElNahhas, R. M. van der Veen, W. Gawelda, S. Johnson, P. Beaud, D. Grolimund, M. Kaiser, C. N. Borca, G. Ingold, R. Abela, and M. Chergui. Femtosecond xanes study of the light-induced spin crossover dynamics in an iron(ii) complex. SCIENCE, 323:489–492, 2009.

[4] M. Cammarata, M. Lorenc, T.K. Kim, J. H. Lee, Q. Y. Kong, E. Pontecorvo, M. Lo Russo, G. Schiro, A. Cupane, M. Wulff, and H. Ihee. Impulsive solvent heating probed by picosecond x-ray diffraction. *Journal of Chemical Physics*, 124:124504 1–9, 2006.

[5] A. Cannizzo, C. J. Milne, C. Consani, W. Gawelda, Ch. Bressler, F. van Mourik, and M. Chergui. Light-induced spin crossover in Fe(II)-based complexes: The full photocycle unraveled by ultrafast optical and X-ray spectroscopies. *COORDINATION CHEMISTRY REVIEWS*, 254(21-22, SI):2677–2686, NOV 2010. 18th International Symposium on the Photochemistry and Photophysics of Coordination Compounds (ISPPCC), Sapporo, JAPAN, JUL 04-09, 2009.

[6] Cristina Consani, Mirabelle Premont-Schwarz, Amal ElNahhas, Christian Bressler, Frank van Mourik, Andrea Cannizzo, and Majed Chergui. Vibrational Coherences and Relaxation in the High-Spin State of Aqueous [Fe-II(bpy)(3)](2+). *ANGEWANDTE CHEMIE-INTERNATIONAL EDITION*, 48(39):7184–7187, 2009.

[7] RA Crowell, R Lian, IA Shkrob, J Qian, DA Oulianov, and S Pommeret. Light-induced temperature jump causes power-dependent ultrafast kinetics of electrons generated in multiphoton ionization of liquid water. *JOURNAL OF PHYSICAL CHEMISTRY A*, 108(42):9105–9114, OCT 21 2004.

[8] Latevi Max Lawson Daku and Andreas Hauser. Ab initio molecular dynamics study of an aqueous solution of [fe(bpy)3](cl)2 in the low-spin and in the high-spin states. *Physical Chemistry Letters*, 1:1830–1835, 2010.

[9] K. Haldrup, G. Vanko, W. Gawelda, A. Galler, G. Doumy, A. M. March, E. P. Kanter, A. Bordage, A. Dohn, T. B. van Driel, K. S. Kjaer, H. T. Lemke, S. E. Canton, J. Uhlig, V. Sundstrom, L. Young, S. H. Southworth, M. M. Nielsen, and C. Bressler. Guest-Host Interactions Investigated by Time-Resolved X-ray Spectroscopies and Scattering at MHz Rates: Solvation Dynamics and Photoinduced Spin Transition in Aqueous Fe(bipy)(3)(2+). *JOURNAL OF PHYSICAL CHEMISTRY A*, 116(40):9878–9887, OCT 11 2012.

[10] Kristoffer Haldrup, Morten Christensen, and Martin Meedom Nielsen. Analysis of time-resolved x-ray scattering data from solution-state systems. *Acta Crystallographica Section A*,

A66:261–260, 2010.

[11] M. Harmand, R. Coffee, M. R. Bionta, M. Chollet, D. French, D. Zhu, D. M. Fritz, H. T. Lemke, N. Medvedev, B. Ziaja, S. Toleikis, and M. Cammarata. Achieving few-femtosecond time-sorting at hard X-ray free-electron lasers. *NATURE PHOTONICS*, 7(3):215–218, MAR 2013.

[12] Philip Hart, Sebastien Boutet, Gabriella Carini, Mikhail Dubrovin, Brian Duda, David Fritz, Gunther Haller, Ryan Herbst, Sven Herrmann, Chris Kenney, Nadine Kurita, Henrik Lemke, Marc Messerschmidt, Martin Nordby, Jack Pines, Don Schafer, Matt Swift, Matt Weaver, Garth Williams, Diling Zhu, Niels Van Bakel, and John Morse. The CSPAD megapixel x-ray camera at LCLS. In Moeller, SP and Yabashi, M and HauRiege, SP, editor, *X-RAY FREE-ELECTRON LASERS: BEAM DIAGNOSTICS, BEAMLINE INSTRUMENTATION, AND APPLICATIONS*, volume 8504 of *Proceedings of SPIE*. SPIE, 2012. Conference on X-Ray Free-Electron Lasers - Beam Diagnostics, Beamline Instrumentation, and Applications, San Diego, CA, AUG 13-16, 2012.

[13] Sunhong Jun, Jae Hyuk Lee, Jeongho Kim, Joonghan Kim, Kyung Hwan Kim, Qingyu Kong, Tae Kyu Kim, Manuela Lo Russo, Michael Wulff, and Hyotcherl Ihee. Photochemistry of HgBr2 in methanol investigated using time-resolved X-ray liquidography. *Physical Chemistry Chemical Physics*, 12(37):11536–11547, 2010.

[14] Kasper Skov Kjaer, Tim B. van Driel, Jan Kehres, Kristoffer Haldrup, Dmitry Khakhulin, Klaus Bechgaard, Marco Cammarata, Michael Wulff, Thomas Just Sorensen, and Martin M. Nielsen. Introducing a standard method for experimental determination of the solvent response in laser pump, X-ray probe time-resolved wide-angle X-ray scattering experiments on systems in solution. *PHYSICAL CHEMISTRY CHEMICAL PHYSICS*, 15(36):15003–15016, 2013.

[15] Q. Kong, J. H. Lee, A. Plech, M. Wulff, H. Ihee, and M. H. J. Koch. Ultrafast x-ray solution scattering reveals an unknown reaction intermediate in the photolysis of ru_3co_{12}. *Angewandte Chemie Int. Edition*, 47:5550–5553, 2008.

[16] Qingyu Kong, Kasper S. Kjaer, Kristoffer Haldrup, Stephan P. A. Sauer, Tim Brandt van Driel, Morten Christensen, Martin M. Nielsen, and Michael Wulff. Theoretical study of the triplet excited state of PtPOP and the exciplexes M-PtPOP (M = Tl, Ag) in solution and comparison with ultrafast X-ray scattering results. *CHEMICAL PHYSICS*, 393(1):117–122, JAN 17 2012.

[17] Henrik T. Lemke, Christian Bressler, Lin X. Chen, David M. Fritz, Kelly J. Gaffney, Andreas Galler, Wojciech Gawelda, Kristoffer Haldrup, Robert W. Hartsock, Hyotcherl Ihee, Jeongho Kim, Kyung Hwan Kim, Jae Hyuk Lee, Martin M. Nielsen, Andrew B. Stickrath, Wenkai Zhang, Diling Zhu, and Marco Cammarata. Femtosecond X-ray Absorption Spectroscopy at a Hard X-ray Free Electron Laser: Application to Spin Crossover Dynamics. *JOURNAL OF PHYSICAL CHEMISTRY A*, 117(4):735–740, JAN 31 2013.

[18] AM Lindenberg, Y Acremann, DP Lowney, PA Heimann, TK Allison, T Matthews, and RW Falcone. Time-resolved measurements of the structure of water at constant density. *JOURNAL OF CHEMICAL PHYSICS*, 122(20), MAY 22 2005.

[19] D Madsen, CL Thomsen, J Thogersen, and SR Keiding. Temperature dependent relaxation and recombination dynamics of the hydrated electron. *JOURNAL OF CHEMICAL PHYSICS*, 113(3):1126–1134, JUL 15 2000.

[20] J. Neuefeind, C. J. Benmore, J. K. R. Weber, and D. Paschek. More accurate X-ray scattering data of deeply supercooled bulk liquid water. *MOLECULAR PHYSICS*, 109(2):279–288, 2011.

[21] Van-Thai Pham, Thomas J. Penfold, Renske M. van der Veen, Frederico Lima, Amal El Nahhas, Steve L. Johnson, Paul Beaud, Rafael Abela, Christian Bressler, Ivano Tavernelli, Christopher J. Milne, and Majed Chergui. Probing the Transition from Hydrophilic to Hydrophobic Solvation with Atomic Scale Resolution. *JOURNAL OF THE AMERICAN CHEMICAL SOCIETY*, 133(32):12740–12748, AUG 17 2011.

[22] W. H. Press, B. P. Flannery, T. A. Teukolsky, and W. T. Vetterling. *Numerical Recipes – The Art of Scientific Computing.* Cambridge University Press, 1986.

[23] Jaroslaw J. Szymczak, Franziska D. Hofmann, and Markus Meuwly. Structure and dynamics of solvent shells around photoexcited metal complexes. *PHYSICAL CHEMISTRY CHEMICAL PHYSICS*, 15(17):6268–6277, 2013.

[24] Haidan Wen, Nils Huse, Robert W. Schoenlein, and Aaron M. Lindenberg. Ultrafast conversions between hydrogen bonded structures in liquid water observed by femtosecond x-ray spectroscopy. *The Journal of Chemical Physics*, 131(23):234505, 2009.